



HAL
open science

Analysis of the climate controls of the surface mass balance of Zongo glacier (Bolivia) and Little Ice Age climate reconstruction by application of a distributed surface energy balance model

Philémon Autin

► To cite this version:

Philémon Autin. Analysis of the climate controls of the surface mass balance of Zongo glacier (Bolivia) and Little Ice Age climate reconstruction by application of a distributed surface energy balance model. *Glaciology*. Université Grenoble Alpes [2020-..], 2022. English. NNT : 2022GRALU021 . tel-03814680

HAL Id: tel-03814680

<https://theses.hal.science/tel-03814680v1>

Submitted on 14 Oct 2022

HAL is a multi-disciplinary open access archive for the deposit and dissemination of scientific research documents, whether they are published or not. The documents may come from teaching and research institutions in France or abroad, or from public or private research centers.

L'archive ouverte pluridisciplinaire **HAL**, est destinée au dépôt et à la diffusion de documents scientifiques de niveau recherche, publiés ou non, émanant des établissements d'enseignement et de recherche français ou étrangers, des laboratoires publics ou privés.



THÈSE

Pour obtenir le grade de

DOCTEUR DE L'UNIVERSITÉ GRENOBLE ALPES

Spécialité : Océan, Atmosphère, Hydrologie

Arrêté ministériel : 25 mai 2016

Présentée par

Philémon AUTIN

Thèse dirigée par **Jean Emmanuel SICART**, Chargé de Recherche, IRD - IGE, co-dirigée par **Antoine RABATEL**, Physicien, Université Grenoble Alpes - IGE, co-encadrée par **Regine HOCK**, Professeure, University of Alaska, Oslo University

préparée au sein de l'**Institut des Géosciences de l'Environnement**

dans l'**École Doctorale : Sciences de la Terre, de l'Environnement et des Planètes**

Analyse des facteurs climatiques contrôlant le bilan de masse d'un glacier tropical et étude de sensibilité aux changements climatiques lors du Petit Âge Glaciaire par application d'un modèle de bilan d'énergie distribué

Analysis of the climate controls of the surface mass balance of Zongo glacier (Bolivia) and Little Ice Age climate reconstruction by application of a distributed surface energy balance model

Thèse soutenue publiquement le **10 juin 2022**

devant le jury composé de :

Mme Valentina Radic, Professeure associée, University of British Columbia, Rapporteur

M. Mathias Vuille, Professeur, State University of New York at Albany, Rapporteur

M. Hugues Goosse, Directeur de recherche, FRS-FNRS, Examineur

M. Ben Marzeion, Professeur, University of Bremen, Examineur

M. Olivier Gagliardini, Professeur des universités, UGA, Président

M. Jean Emmanuel SICART, Chargé de recherche, IRD-IGE, Directeur de thèse

M. Antoine Rabatel, Physicien, UGA-IGE, Co-directeur de thèse

Abstract

This PhD thesis was dedicated to the understanding of processes that control the temporal variability of the surface mass balance of a tropical glacier: Zongo Glacier, Bolivia. Over the glacier, the year can be split into three seasons: a wet season (austral summer) during which most of the accumulation occurs, a dry season (austral winter) where limited melt rates are observed and a transition season (September-November) characterized by increasing melt rates. The end of the transition season is the period where the highest annual melt rates occur.

The first part of this study consisted in evaluating the atmospheric controls of the surface mass balance through the application of a distributed surface energy balance model (DEBAM, Hock and Holmgren, 2005). The model was applied to nine years at the hourly time step over a digital elevation model of the glacier surface with a 20 x 20 m resolution. The model was validated by comparing measured and simulated discharge at the catchment outlet, albedo at the weather station, surface type (snow/ice), annual glacier-wide surface mass balance and surface mass balance by altitude. Analysis of the mean monthly energy fluxes revealed the importance of the meteorological conditions during the transition season on the interannual variability of the surface mass balance. Two sensitivity analyses over this period were carried out. The first looked at the impact of the temporal distribution of precipitation events on the surface mass balance. For this study, in order to maintain physical consistency between the measured variables, the scenarios were obtained by shuffling days to obtain the desired changes in temporal precipitation distribution. The second sensitivity analysis investigated the impact of a prolonged cloud cover on the surface mass balance. To do this, the presence of clouds was mimicked by lowering the incoming shortwave radiation and increasing the incoming longwave radiation. These sensitivity analyses showed that, *via* an albedo feedback effect, the temporal distribution of precipitation and its associated amounts were the main drivers of the interannual surface mass balance variability. Besides, extended periods of sustained cloud cover, particularly during November, had a strong ability to reduce melt.

The last part of this thesis looked at the climate conditions that allowed the glacier to reach its Little Ice Age maximum extent (LIA, late 17th century). Considering a digital elevation model of the glacier LIA maximum extent, the surface energy balance model was used to perform a sensitivity analysis of the annual surface mass balance to different paleoclimate scenarios. Emphasis was put on the seasonal changes in precipitation and cloud cover which may have occurred during the LIA *via* the generation of four paleoclimate scenarios. To ensure physical consistency between the meteorological variables, the scenarios were built by shuffling measurements carried out over the glacier between 1999 and 2017. The scenarios were considered plausible if near equilibrium conditions were obtained (ie., an annual glacier-wide surface mass balance close to 0 m w.e.). Results showed that both a 1.1°C cooling and a ~20% increase in annual precipitation relative to current conditions were required. In addition, two changes in precipitation seasonality provided near-equilibrium conditions: an increase in precipitation between September and November or an early wet season onset.

Résumé

Cette thèse de doctorat est consacrée à la compréhension des processus qui contrôlent la variabilité temporelle du bilan de masse de surface d'un glacier tropical : le glacier Zongo, en Bolivie. Sur le glacier, l'année peut être divisée en trois saisons : une saison humide (été austral) pendant laquelle la plupart de l'accumulation a lieu, une saison sèche (hiver austral) où la fonte est faible et une saison de transition (septembre-novembre) caractérisée par une fonte croissante. La fin de la saison de transition est la période où l'on observe les débits de fonte annuels les plus élevés.

La première partie de cette étude a consisté à évaluer les contrôles atmosphériques du bilan de masse de surface par l'application d'un modèle de bilan énergétique de surface distribué (DEBAM, Hock et Holmgren, 2005). Le modèle a été appliqué sur neuf ans au pas de temps horaire sur un modèle numérique de terrain de la surface du glacier d'une résolution de 20 x 20 m. Le modèle a été validé en comparant le débit mesuré et simulé à la sortie du bassin versant, l'albédo à la station météorologique, le type de surface (neige/glace), le bilan de masse annuel et le bilan de masse par altitude. L'analyse des flux d'énergie mensuels moyens a révélé l'importance des conditions météorologiques pendant la saison de transition sur la variabilité interannuelle du bilan de masse de surface. Deux analyses de sensibilité sur cette période ont été réalisées. La première a porté sur l'impact de la distribution temporelle des événements de précipitations sur le bilan de masse. Pour cette étude, afin de maintenir une cohérence physique entre les variables mesurées, les scénarios ont été obtenus en mélangeant les jours afin d'obtenir les changements de précipitation souhaités. La deuxième analyse de sensibilité a étudié l'impact d'une couverture nuageuse prolongée sur le bilan de masse en surface. Pour ce faire, la présence de nuages a été imitée en diminuant le rayonnement solaire incident et en augmentant le rayonnement thermique incident. Ces analyses de sensibilité ont montré que, à travers un effet de rétroaction de l'albédo, la distribution temporelle des précipitations et les quantités associées étaient les principaux moteurs de la variabilité interannuelle du bilan de masse en surface. En outre, les périodes prolongées de couverture nuageuse, en particulier pendant le mois de novembre, ont eu une forte capacité à réduire la fonte.

La dernière partie de cette thèse analyse les conditions climatiques qui ont permis au glacier d'atteindre son extension maximale du Petit Âge Glaciaire (PAG, fin du 17^{ème} siècle). En considérant un modèle d'élévation numérique de l'étendue maximale du glacier pendant le PAG, le modèle de bilan énergétique de surface a été utilisé pour effectuer une analyse de sensibilité du bilan de masse annuel à différents scénarios paléoclimatiques. L'accent a été mis sur les changements saisonniers des précipitations et de la couverture nuageuse qui ont pu se produire pendant le PAG *via* la génération de quatre scénarios paléoclimatiques. Pour assurer la cohérence physique entre les variables météorologiques, les scénarios ont été construits en mélangeant les mesures effectuées sur le glacier entre 1999 et 2017. Les scénarios ont été considérés comme plausibles si des conditions proches de l'équilibre étaient obtenues (c'est-à-dire un bilan de masse annuel proche de 0 m eq. eau). Les résultats ont montré qu'un refroidissement de 1,1°C et une augmentation de ~20% des précipitations annuelles par rapport aux conditions actuelles étaient nécessaires. En outre, deux changements dans la saisonnalité des précipitations ont permis d'obtenir des conditions proches de l'équilibre : une augmentation des précipitations entre septembre et novembre ou un début précoce de la saison humide.

Table of Content

General introduction and PhD objectives	1
Chapter 1 - Andean tropical glaciers	4
1.1 Tropical glaciers climate	4
1.1.1 General features of tropical glaciers and climate	4
1.1.2 Climate over Zongo Glacier	7
1.2 Glacier-climate interactions in the tropics	12
1.2.1 Tropical glaciers across the world	12
1.2.2 Surface energy balance studies on Zongo Glacier	13
1.2.3 Other current climate studies of interest for this study	15
1.3 Tropical glaciers and paleoclimate studies	18
1.4 Concluding remarks	19
Chapter 2 - Datasets	21
2.1 Glacier monitoring network	21
2.2 Model input data	27
2.2.1. Existing gap-filled dataset	28
2.2.2 Extension and presentation of the dataset	31
2.2.3 Model calibration and validation data	34
2.3 Cloud radiative properties dataset	37
2.3.1 Definition of the cloud radiative properties	37
2.3.2 Calibration of the cloud longwave emission factor for measurement at PLATAFORMA (4750 m a.s.l.)	38
2.4. Summary	41
Chapter 3 - Model setting, calibration and validation for the current climate	42
3.1 Model description	42
3.1.1 Energy balance	42
3.1.2 Incoming shortwave radiation	43
3.1.3 Albedo	47
3.1.4 Longwave radiation	48
3.1.5 Estimation of turbulent energy fluxes	48
3.1.6 Multi-layer snow model to calculate the subsurface heat flux	49
3.1.7 Glacier surface temperature	51
3.1.8 Precipitation	52
3.1.9 Accumulation	52
3.2 Model initialization and calibration	52
3.2.1 Model initialization	52
3.2.2 Model calibration	55
3.3 Model validation	57
3.4 Main sources of modeling errors	61

3.5 Attempts at calibrating the multi-layer snow model	63
3.6 Summary	66
Chapter 4 - Current climate-glacier relationships	69
4.1 Temperature and surface mass balance	70
4.2 Cloud links with precipitation and surface mass balance	71
4.2.1 Linking clouds and precipitation events	71
4.2.2 Clouds and surface mass balance	72
4.3. Links between precipitation and surface mass balance	75
4.4 Impact of the wet season onset on the annual surface mass balance	80
4.4.1 Methods used to define the wet season	80
4.4.2 Impact of the wet season onset on the surface mass balance	85
4.5 Climate controls of the interseasonal and interannual variability of the surface mass balance.	89
4.6 Summary	111
Chapter 5 - Assessment of the climate which allowed the glacier to reach its Little Ice Age maximum extent	113
5.1 Little Ice Age climate reconstruction	114
5.2 Comment on the results of Jomelli et al. (2011) on the LIA climate	138
5.3 Sensitivity analyses carried out for the model initialization of LIA simulations	138
5.3.1 Sensitivity of the simulated surface mass balance to the altitude up to which the precipitation gradient is applied	139
5.3.2 Impact of the surface temperature gradient on the simulated surface mass balance	142
5.4 Summary	146
General conclusion and perspectives	147
Current climate (1991-2017)	147
Seventeenth century climate	150
Perspectives	152
References	155
List of figures	169
List of tables	176
Glossary and acronyms	179
Supporting Information	182
S1. Seasonal patterns of meteorological measurements	182
S2. Seasonal cloud radiative properties	185
Supporting information for the Chapter 4.5	189
Appendix A - Scientific diffusion and training	195
Appendix B: Data availability	196

General introduction and PhD objectives

Over the last decades, worldwide glacier retreat has been widely documented (e.g., Zemp et al., 2019; Gärtner-Roe et al., 2019; Hugonnet et al., 2021). This retreat strongly impacts freshwater availability in some parts of the world (e.g., Kaser et al., 2010). Using glaciological and geodetic data from the World Glacier Monitoring Service (WGMS) between 1961 and 2016, Zemp et al. (2019) showed that this retreat is uneven across the world. The highest cumulative mass losses were in the Southern Andes, Alaska and tropical glaciers, whereas mass gains were observed in Western South Asia. When considering the 2006-2016 period, Western South Asian glaciers were close to equilibrium as opposed to South American glaciers which showed the highest average mass loss rates.

Using digital elevation models derived from ASTER images between 2000 and 2018, Dussaillant et al. (2019) corroborated the findings of Zemp et al. (2019) and showed that the highest mass losses were observed in the Patagonian Andes (-0.78 ± 0.25 m w.e. yr^{-1}), followed by the tropical Andes (-0.48 ± 0.24 m w.e. yr^{-1}). Such a rapid shrinkage of tropical South American glaciers is concerning as they play an important role in freshwater regulation and availability throughout the year whether it is for human consumption, irrigation or hydroelectricity (e.g., Soruco et al., 2015; Buytaert et al., 2017). This is especially true in the outer tropics as these are characterized by a long dry season with scarce precipitation events. For example, in Bolivia, Soruco et al. (2015) estimate that glacier meltwater contributes to about 15% of the annual water consumption in La Paz and up to 27% during the dry season.

In addition to the potential threat of water scarcity induced by the rapid disappearance of these glaciers, glacier retreat can result in increasing risks of natural hazards such as glacial lake outburst floods. These can have devastating effects on both human lives and infrastructures (e.g., Lliboutry et al., 1977; Cook et al., 2016; Kougkoulos et al., 2018).

Glacier surface mass balance and melt are controlled by the climate *via* energy and mass fluxes between the atmosphere and the glacier surface. A way to assess these forcings is to use distributed energy balance models which provide insights into the mechanisms that control interseasonal and interannual surface

mass balance variability. Hence, these models can be used to identify the key meteorological variables that control the glacier evolution and to estimate past and future glacier evolutions.

Here, we focus on Zongo Glacier, located in the outer tropical Andes of Bolivia ($16^{\circ}15'S$, $68^{\circ}10'W$), where diverse long-term observations are available from the GLACIOCLIM monitoring program maintained within the framework of a collaboration between France (IRD, Université Grenoble Alpes, CNRS) and Universidad Mayor de San Andrés in La Paz (<https://glacioclim.osug.fr/>). The glacier's meltwater is of particular importance to the local population as it is at the head of the Zongo river along which are eleven hydropower plants, and hydropower is expected to represent 74% of the country's electricity production by 2025 (Morato et al., 2019).

A number of studies on the present-day climate controls of the glacier surface mass balance have already been carried out over short time periods (e.g., Francou et al., 1995; Wagnon et al., 1999; Sicart et al., 2005; 2007; 2011; Rabatel et al., 2013) leading to different hypotheses on the controls of the surface mass balance interannual variability (discussed in Chapter 1).

Studies of past advances of the Zongo Glacier have also been carried out (e.g., Rabatel et al., 2008; Jomelli et al., 2009). Rabatel (2005) reconstructed the glacier's maximum extent during the Little Ice Age, a multiseccular cold period during which glaciers across the world advanced (~ 1350 to ~ 1850 AD, e.g., Solomina et al., 2015; 2016). Studying this period is of interest because the climate was significantly different than today. Besides, since it is a relatively recent period, a number of paleoclimate proxies such as ice cores or speleothems provide information on changes in precipitation amounts and/or temperature down to the annual scale (e.g., Apaéstegui et al., 2014; Hurley et al., 2016, 2019).

In this context this PhD aims at:

- Contributing to the understanding of present-day climate controls of the glacier surface mass balance *via* the application of a surface energy balance model (Distributed Energy Balance Model - DEBAM, Hock & Holmgren, 2005) over several contrasting years.

- Reconstructing the climate which allowed the glacier's last significant advance (during the late seventeenth century, Rabatel et al., 2008). This allows an assessment of the hypotheses on the climate controls of the surface mass balance *via* the construction of climate scenarios. In addition, the use of a surface energy balance provides insights on potential seasonal variations of meteorological variables which may have occurred in the past. Hence, this allows us to carry out a paleoclimate study at a finer temporal scale than what has already been done in the tropical Andes (e.g., Rabatel et al., 2005, 2008, Jomelli et al., 2009, 2011; Malone et al., 2015). Besides, the long hourly measurement dataset available for modeling allows the construction of physically consistent scenarios by shuffling months of measurements. Finally, accurately representing past glacier variations provides valuable information for the prediction of future glacier evolutions and associated water availability.

To investigate these questions, the first part of this study consisted in analyzing the measurements from the glacier and its catchment to obtain a multi-annual continuous hourly dataset of on-glacier meteorological measurements which was used to apply the distributed energy balance model DEBAM (Chapter 2). The next step was to calibrate and validate the model (Chapter 3).

We then used measurements and simulated energy fluxes to assess the climate controls on the surface mass balance at different time scales (hourly to annually). The importance of the forcings on the surface mass balance were assessed *via* sensitivity analyses on the glacier surface mass balance (Chapter 4).

The final part of this study consisted in assessing the climate which allowed the seventeenth century glacier extent. This analysis was carried out based on the combination of information obtained from paleoclimate proxies/studies and information on the current climate controls of the surface mass balance (Chapter 5).

Chapter 1 - Andean tropical glaciers

This chapter presents Andean tropical glaciers and their climate before zooming in on the climate specificities of Zongo Glacier, Bolivia. Then, a selective literature review on glacier-climate interactions in the tropics is presented. Finally, a focus is put on why these glaciers are suitable paleoclimate proxies and on studies which have used them to assess the Little Ice Age climate.

1.1 Tropical glaciers climate

1.1.1 General features of tropical glaciers and climate

Kaser (1999) defined tropical glaciers as those located at the junction of three distinct zones: they must be between $28^{\circ}5'$ N and $28^{\circ}5'$ S (astronomical tropics, so that the sun reaches its zenith position once a year). The annual thermal amplitude of the region must be smaller than the diurnal one and, they have to be within the Intertropical Convergence Zone (ITCZ) annual oscillation extent (Fig. 1.1). The ITCZ is a belt of minimum pressure and intense low-level convergence of the tradewinds over the equatorial oceans. Precipitation within it is mostly of convective nature (Garreaud et al., 2009).

According to this definition, the vast majority of tropical glaciers are located in South America (over 99% of the total tropical ice surface, Kaser, 1999), the rest is in equatorial East Africa and Indonesia (Fig. 1.1). A major characteristic of these glaciers is that the seasonality of their surface mass balance is mostly explained by the annual moisture cycle (e.g., Hastenrath, 1991; Mölg et al., 2008).

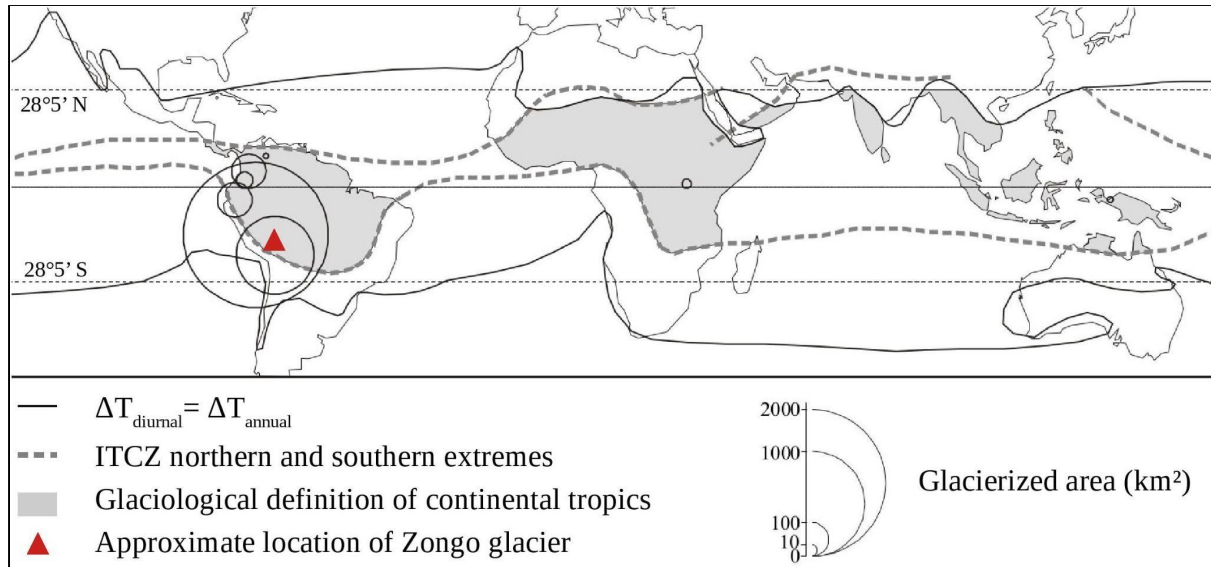


Figure 1.1 Worldwide tropical glacier distribution, adapted from Kaser & Osmaston (2002).

Tropical glaciers can be divided into two groups. Those of the inner tropics, which are characterized by prevailing wet conditions all year round (9 % of the total tropical glacier surface, which is distributed between Colombia, Venezuela, Ecuador, East Africa and Indonesia). For these glaciers, accumulation and ablation are concomitant all year round (Kaser, 1999).

The second group is the glaciers of the outer tropics which are found in Peru and Bolivia (71 and 20 % of the total tropical ice surface area, respectively, Rabatel et al., 2013). Over such glaciers, the year can be split into a wet and a dry season. The wet season (austral summer) is characterized by frequent precipitation events (about 70% of the annual amounts) and glaciers are subject to both melt and accumulation. During the dry season, few precipitation events occur and, generally, limited glacier mass loss is observed (austral winter, Kaser, 1999; Wagnon et al., 1999).

South American climate is strongly influenced by the Andes which acts as a climatic wall resulting in moist eastern Andes and dry western Andes. The Andes also encourage extratropical interactions at tropical and subtropical latitudes. Besides, the large continental mass at low latitudes (10°N-25°S) allows the development of intense convective storms (Garreaud et al., 2009).

The interannual and interdecadal variability of the climate is largely controlled by large-scale climate phenomena such as El-Niño Southern Oscillation (ENSO).

ENSO is a coupled ocean-atmosphere phenomenon over the tropical Pacific Ocean marked by its warm and cold phases (El Niño and La Niña, respectively, summarized in Fig. 1.2). El Niño phases are associated with decreased precipitation over tropical South America whilst the opposite is observed during La Niña phases (e.g., Garreaud et al., 2009; Vuille 1999). Another notable large-scale control is the sea surface temperature anomalies in the tropical Atlantic ocean which have a strong impact on the eastern South American climate (e.g. Marengo et al., 2011). To a lesser extent, the Pacific Decadal Oscillation and North Atlantic Oscillation also play a role in South American climate variability (Garreaud et al., 2009).

Analysis of the Climate Hazards group InfraRed Precipitation with Stations , a gridded precipitation product based on a combination of ground measurements and satellite images (CHIRPS; Funk et al., 2015), showed that the South American tropics can be subdivided into two groups. A region close to the equator (5°S-8°S) which has a bimodal precipitation regime and the Southern tropics (8°S-20°S) which have a unique wet season during the austral summer (unimodal precipitation regime, Fig. 1.3a, b, respectively, Segura et al., 2019).

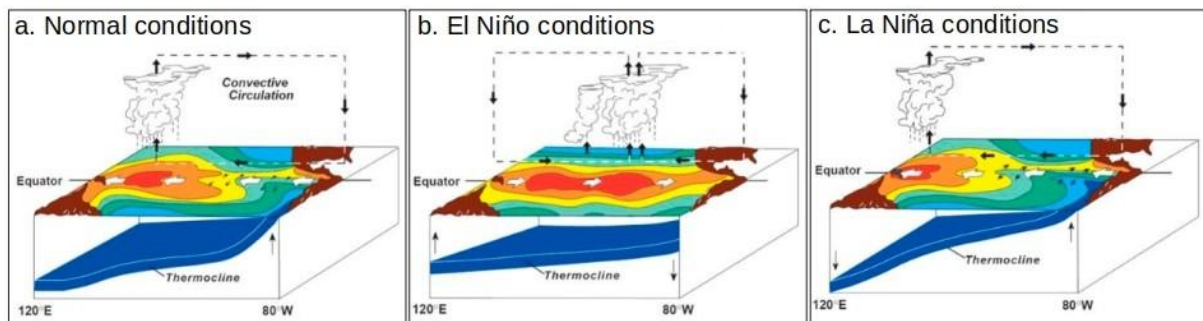


Figure 1.2 The three phases of ENSO: normal conditions (a), warm El Niño phase (b) and cold La Niña phase (c). The left side of the diagram is the western pacific ocean (Asian side) and the right side shows eastern Pacific ocean towards South America. Red and orange colors show warm sea surface temperatures (SSTs) and the yellow and green ones show cooler SSTs. The blue band shows the approximate location of the thermocline (water at about 20°C). Rain clouds form over the warmest SSTs. Source: Pacific Marine Environmental Laboratory: <https://www.pmel.noaa.gov/elnino/schematic-diagrams>

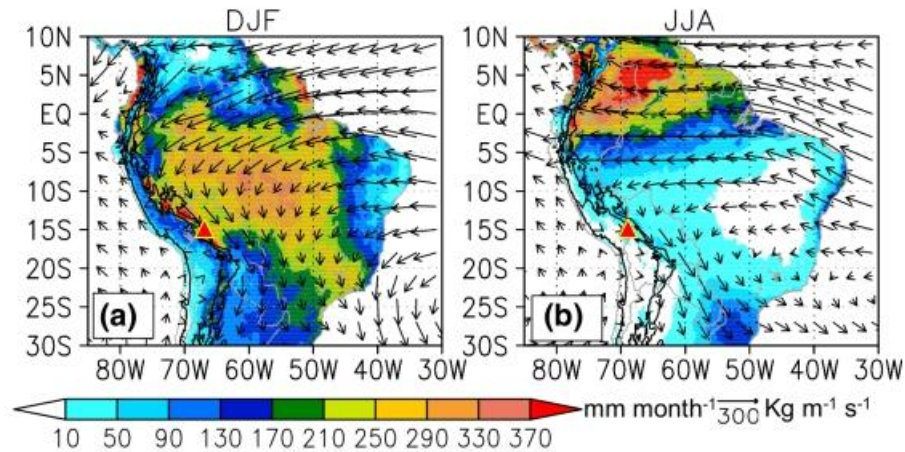


Figure 1.3 Average CHIRPS precipitation (shaded) and vertically integrated water vapor flux (vectors) between December and February (DJF, plot a) and between June and August (JJA, plot b). The red triangle with a yellow outline shows the approximate position of Zongo Glacier. Source: Segura et al. (2019).

1.1.2 Climate over Zongo Glacier

Zongo Glacier is a small glacier of the outer tropics (1.7 km² in 2016), on the southern side of Huayna Potosi Peak in the Cordillera Real, Bolivia (red triangle on Fig. 1.3, Fig. 1.4 shows a panoramic view of the glacier). The hydrological year starts in September and ends the following August. A unimodal precipitation regime is observed with the wet season taking place during the austral summer (Fig 1.3a, Fig 1.5a). Conversely, the austral winter (June-August) is characterized by predominant clear-sky conditions and dry air (Fig 1.3b, Fig 1.5a, Troll, 1941). Figure 1.5b illustrates the small temperature variability observed across the year on Zongo Glacier, a typical feature of tropical glaciers.



Figure 1.4. Panoramic view of Zongo Glacier on the 15th of July 2015. Photo courtesy: Maxime Harter

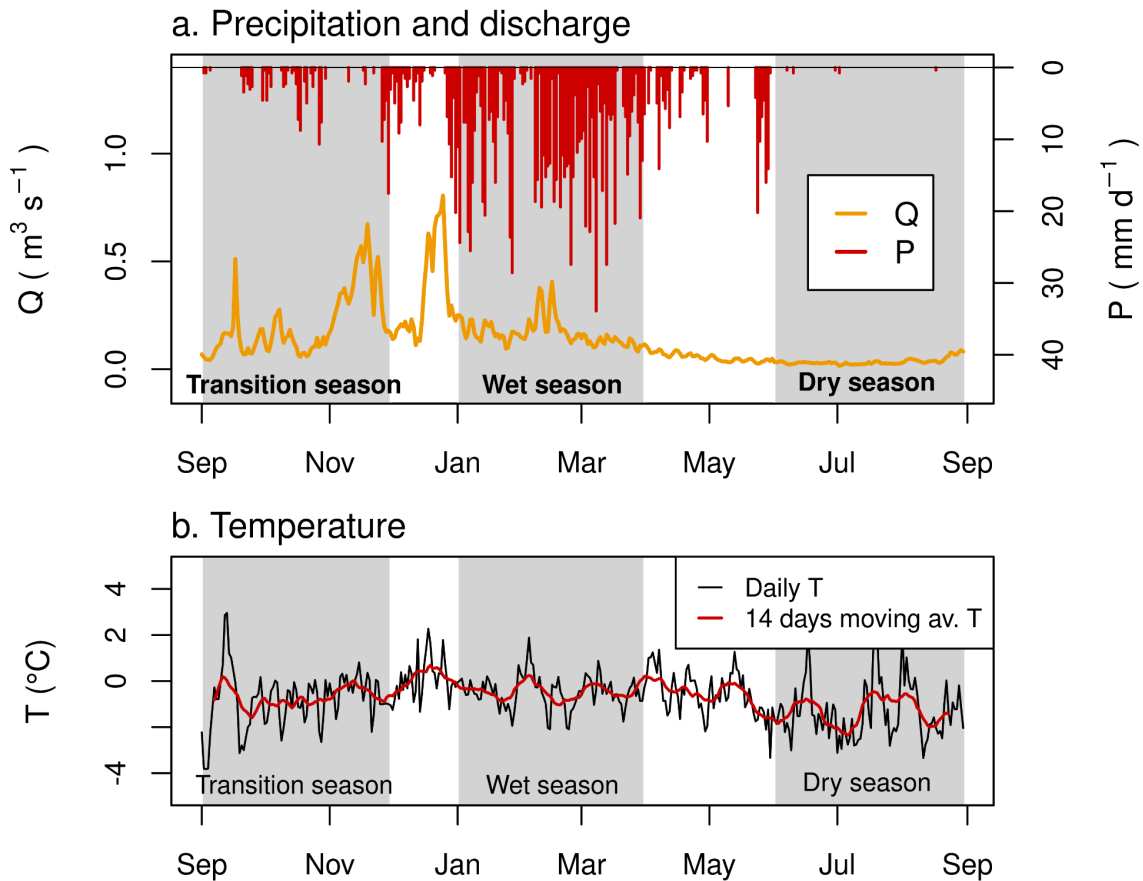


Figure 1.5. Daily precipitation and discharge (a) and temperatures (b) over the year 2016/17. The gray rectangles show the seasons following the definition provided in Sicart et al. (2011). On plot b, the 14 days moving average temperature highlights the low seasonal temperature variability. Daily precipitation and temperature measurements were carried out on the glacier (SAMA Automatic Weather Station, 5050 m a.s.l.), discharge measurements were carried out at the glacier outlet (TUBO gauging station, 4850 m a.s.l.).

A number of studies over the glacier led to finer definitions of the seasons and their respective controls on the melt rates. For example, Sicart et al. (2011) identified seasons based on a combination of surface temperature, precipitation occurrences and measured discharge at the glacier outlet (Fig. 1.5a). Similarly, Rabatel et al. (2012, 2013) defined seasons based on the interannual variability of the measured surface mass balance in the ablation zone. Both methods result in three main seasons: a transition season (September–November), a core wet season (January to

March) and a dry season (June-August). The description of the seasons below is inspired from Sicart (2021).

The transition season is characterized by large mass losses in the ablation area and increasing melt rates. Besides, there is a gradually increasing frequency of precipitation events as the wet season approaches (Fig. 1.5a). Previous studies (e.g., Sicart et al., 2011) showed that this period is a key control of the annual glacier mass loss. Based on 19 years of daily discharge measurements, Ramallo (2013) showed that 31 ± 6 % of the annual discharge flows through the proglacial stream at the glacier's outlet over this season.

On average, 20 ± 5 % of the annual precipitation amounts fall over the transition season (Ramallo, 2013) and 80% of the thickest cloud events are linked to cold surges in the East of the Cordillera (Sicart et al., 2016). These climatic events, known as *Surazos*, are one of the two main synoptic conditions which bring precipitation events over the glacier. They are a destabilization of the tropical atmosphere by extra tropical cold air intrusion related to low level southern wind incursion (Fig. 1.6, Ronchail, 1989). Garreaud & Wallace (1998) showed that *Surazos* were responsible for up to a quarter of the summer precipitation in central Amazonia. Over Zongo, they are marked by the arrival of cold high-altitude clouds which can bring snow events that last for a few days.

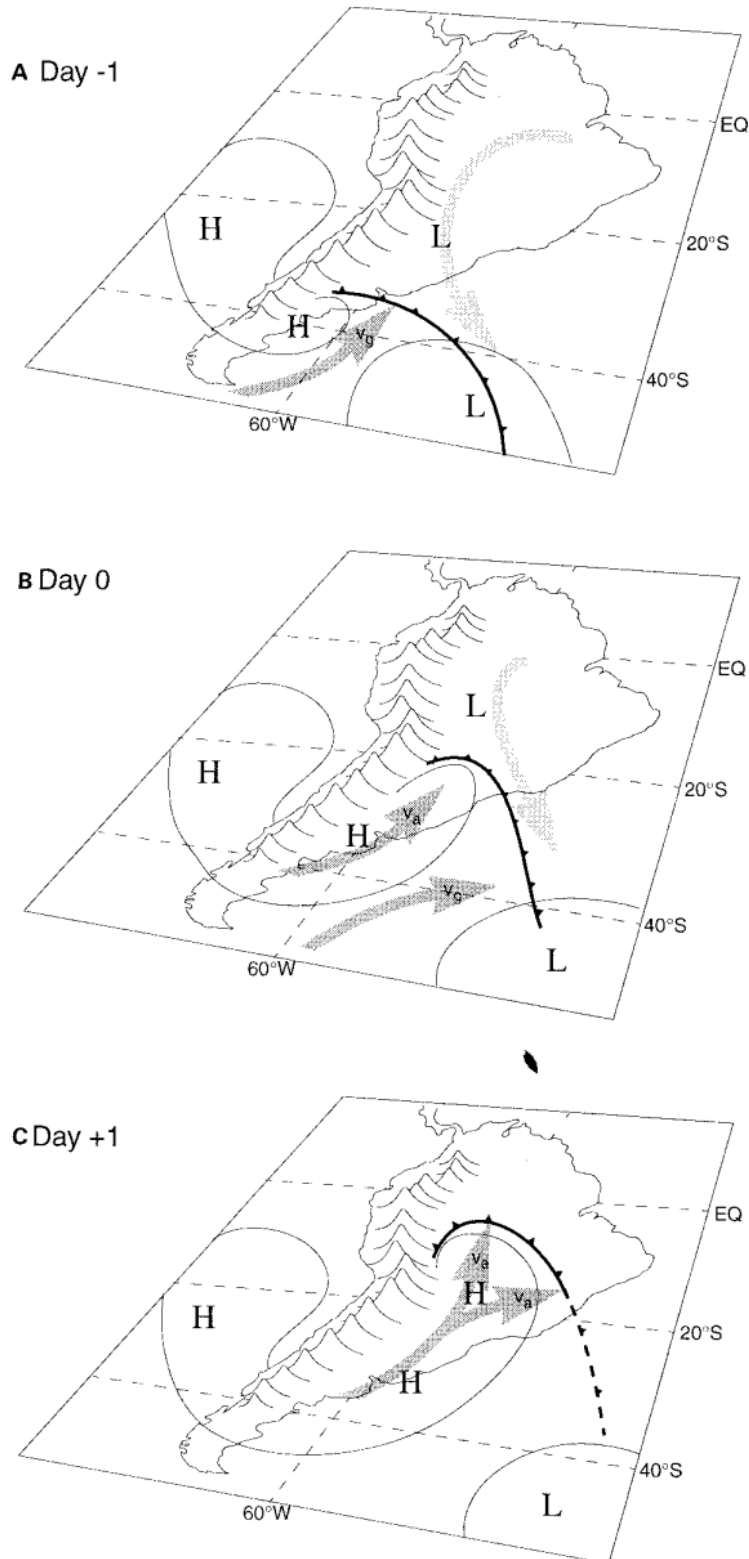


Figure 1.6. Schematics of the synoptic conditions of *Surazo* events. Thick dark arrows represent low-level wind advecting cold air whilst the light gray ones represent the low level advection of warm air. Thin contour lines represent surface isobars. Source: Garreaud (2000)

The core wet season is a period during which the mass loss in the ablation area of the glacier is limited and frequent precipitation events occur. It corresponds to the mature phase of the South American Monsoon System (SAMS, e.g., Vera et al., 2006). Vuille and Werner (2005) describe the SAMS as a period of large-scale land-ocean temperature gradient combined with low pressure in the continent and high pressure over the Bolivian Altiplano leading to intense moisture influx towards the continent. As the SAMS develops, the diabatic heating over the western Amazon leads to the formation of the upper troposphere anticyclonic system known as the Bolivian High (Lenters and Cook, 1997). Meanwhile, in the lower troposphere, the southward displacement of the South American Low Level Jet (SALLJ) favors mean easterly winds on the northern arc of the Bolivian High. The SALLJ is a result of the entrapment of the Northeastern tradewinds between the Brazilian plateau to the east and the Andes to the West (between 10 and 20° S, e.g. Garreaud et al., 2009). These upslope winds transport moisture from the Amazon Basin to the tropical Andes (Fig. 1.3a). The solar heating of the surface leads to strong afternoon convective events in the Bolivian Andes and Altiplano (Garreaud et al., 2003).

Over this season, 33 ± 5 % of the annual discharge at the glacier outlet and 70 ± 6 % of the annual precipitation on Zongo Glacier are observed (Ramallo, 2013) and 46% of the cloud events can be linked to *Surazo* conditions (Sicart et al., 2016). Hence, the remaining 54% of the precipitation events are linked to the southward displacement of the SALLJ. As a result, small changes of the SALLJ direction with respect to the Andes lead to high precipitation variability (e.g., Espinoza et al., 2015; Junquas et al., 2017).

The dry season (June to August) is characterized by low melt rates, rare precipitation events and prevailing clear-sky conditions over Zongo Glacier (Fig. 1.5a). Over the glacier, Wagnon et al. (1999) attribute the limited melt rates to the prevailing clear sky and dry air conditions which favor sublimation whilst Sicart et al. (2005, 2011) showed that it is mainly due to the low clear-sky longwave irradiance due to the high altitudes at which tropical glaciers are found. This reduces the amount of energy available for melt. About 9% of the annual discharge and 10% of the annual precipitation falls during this period (Ramallo, 2013). In addition, 87% of the cloud events can be linked to *Surazo* conditions (Sicart et al., 2016).

1.2 Glacier-climate interactions in the tropics

Glacier surface mass balance is controlled by the climate via energy and mass fluxes between the atmosphere and the glacier surface (e.g., Cuffey and Paterson, 2010). Although the study of tropical glaciers started later than those of mid and high latitude glaciers (e.g., Lliboutry, 1977; Hastenrath and Ames, 1995; see the synthesis of Rabatel et al., 2013), numerous studies of the climate forcing on tropical glaciers have been conducted in different continents.

1.2.1 Tropical glaciers across the world

Prinz et al. (2016) applied a surface energy balance (SEB) model to the Lewis Glacier (Mount Kenya, 0°9'S, 37°18'W) over 2011/12 and found that incoming shortwave radiation dominated the surface energy balance and that 25% of the ablation was a result of sublimation and the remaining 75% were due to melt.

Mölg and Hardy (2004) applied a SEB model on a flat glacier at the summit of Mount Kilimanjaro where melt is negligible (3°4'S, 37°2'E, 5794 m a.s.l., Tanzania) and showed that net shortwave radiation governed the energy exchanges at the surface-atmosphere interface and that the second largest energy flux was the continuously negative latent heat flux (i.e., sublimation conditions). The important role of sublimation at this site (around 90% of the ablation) was confirmed by Cullen et al. (2007) who applied a SEB model over the same glacier using Eddy Covariance measurements to calibrate the turbulent heat fluxes. Similarly, Mölg et al. (2008) applied a SEB model on a glacier on the slopes of Kilimanjaro and found that sublimation was responsible for up to 65% of the total ablation. *Via* sensitivity analyses, the authors show that the glacier is two to four times more sensitive to a 20% change in precipitation than to a 1 °C change in air temperature. The important role of sublimation on the ablation processes of the glaciers of Mount Kilimanjaro is explained by their high altitude which implies that melt rates are limited.

Permana et al. (2019) studied glaciers near Puncak Jaya (previously known as Irian Jaya) in Papua, Indonesia (4°1'S, 137°2'E, 4 884 m a.s.l.) using satellite images and a 32 m deep ice core. They showed that these glaciers are rapidly disappearing and strongly influenced by the ENSO signal: strong positive ENSO

phases result in increased temperatures, decreased precipitation and hence faster glacier shrinkage.

In tropical South America, both field observations and remote sensing have shown a trend of rapid glacier retreat over the last decades (e.g., Kaser, 1999; Soruco et al., 2009; Rabatel et al., 2013; Vincent et al., 2018; Dussailant et al., 2019; Zemp et al. 2019, Seehaus et al., 2020; Masiokas et al., 2020). These observations led to a large number of studies on the climate controls of the surface mass balance variability of tropical glaciers. Some studies have linked these mass changes to the high sensitivity of tropical glaciers to changes in moisture-related variables which control the climate at low latitudes, such as precipitation and cloudiness (e.g., Sicart et al., 2005). Conversely, considering 50 years of Temperature reanalysis, Bradley et al. (2009) found statistical correlations between mass changes and air temperature for the Quelccaya Ice Cap. However, according to other authors (e.g., Gurgiser et al., 2013) these correlations might result from the indirect effect of air temperature on the precipitation phase whereby warmer temperatures affect the rain-snow altitude and it is the latter that affects melt rates. In addition, most studies conducted to understand the complex climate-glacier relationships in the tropics have been carried out with data acquired over a short period (less than two to three years, e.g., Wagnon et al., 1999; Sicart et al., 2005; Mölg et al., 2008, 2009; Litt et al., 2014; Maussion et al., 2015; Hurley et al., 2015; Prinz et al., 2016).

1.2.2 Surface energy balance studies on Zongo Glacier

A number of surface energy balance studies have been carried out on Zongo Glacier over short temporal scales. Wagnon et al. (1999) calculated the surface energy balance over one point (at 5150 m a.s.l.) using 18 months of data and found that the main source of melt energy is the net all-wave radiation whose variability is primarily controlled *via* albedo feedback effects. Furthermore, they attribute the melt rate seasonality to the specific humidity which defines the ablation mechanisms (moist air during the wet season leads to melting and dry air during the dry season to sublimation).

Similarly, Sicart et al. (2005) analyzed surface energy balance using measurements from two automatic weather stations in the ablation zones between 1998 and 2000. The analysis of the turbulent heat fluxes revealed that apart from the dry season, the sensible heat flux supplied to the ice offsets the loss of energy *via* the latent heat fluxes. The authors also show that during the wet season, most of the melt comes from the melting of the snowpack due to the frequent alternation of accumulation and melt. In addition, they found that the main source of fusion is the shortwave radiation and that the incoming longwave radiation plays an important role on melt rate seasonality due to the low latitude and very high altitude. For example, the melt rates are maintained throughout the wet season *via* the incoming longwave radiation which compensates for the reduced incoming shortwave radiation. Conversely, during the dry season, the predominant clear sky conditions cause a large longwave energy deficit which reduces melt rates.

Lejeune et al. (2007) applied the Météo-France CROCUS-ISBA model to a lateral moraine of the Glacier Charquini North (around 2 km east-southeast of Zongo Glacier) between May 2002 and July 2003 to assess the snow melt mechanisms and showed the predominant control of incoming solar radiation. Lejeune (2009) applied this model setting over the Zongo Glacier catchment between September 2004 and March 2006 and found that at the annual scale, sublimation exceeds melt above 5600 m a.s.l. Besides, he found that sublimation plays a key role in the glacier-wide ablation processes during the dry season (29% of the ablation) when it is negligible during the wet season (6-10% of the ablation). Finally, *via* sensitivity analyses, he found that the glacier was more sensitive to changes in temperature than to changes in precipitation.

Sicart et al. (2011) analyzed the glacier seasonal mass balance variations by applying the distributed surface energy balance model (DEBAM, Hock & Holmgren, 2005) over one year (1999/00) and found that changes in melt rate were linked to a combination of snow fall and cloud radiative properties. They attribute increasing melt rates during the transition season to a gradually increasing amount of incoming shortwave radiation as the summer solstice approaches. During the wet season, the decreasing melt rates are linked to the frequent snowfall events which increase the surface albedo. The low melt rates observed during the dry season are due to reduced incoming longwave radiation linked to prevailing clear-sky conditions.

Finally, the authors suggest that the onset of the wet season around December is a key control on the annual glacier-wide surface mass balance. An early wet season onset will result in strong cloud cover which will reduce the amount of energy reaching the surface over the period where potential solar radiation is close to its maximum (summer solstice). Coupled to the associated snowfall events which increase the surface albedo, this reduces the period of maximum melt.

1.2.3 Other current climate studies of interest for this study

In addition to surface energy balance studies, a large number of glaciological and hydrological studies have been carried out to understand melt mechanisms of the Zongo Glacier. The aim here is not to list them all but only the ones which were used during this PhD.

Francou et al. (1995) published one of the first studies on the interannual variability of the surface mass balance of the glacier. Based on two years of data (1991-1993), the authors point out the important role of the El-Niño Southern Oscillation on the annual mass loss *via* a control on the wet season onset and duration.

Caballero (2001, 2004) modeled the discharge of the Zongo river (Zongo Glacier is at the head of its catchment) using the ISBA flow model to assess the relationship between hydrological processes and hydraulic dynamics over the valley and to optimize water management strategies. They showed that to accurately reproduce observed discharge, glacier meltwater had to be accounted for as these provide extra runoff during the wet season and sustain discharge during the dry season.

Sicart et al. (2007) compared the hydrological and glaciological methods used to calculate the surface mass balance. They found large measurement errors with the glaciological method (about ± 0.4 m w.e. yr^{-1}) due to the overestimation (underestimation) of highly negative (positive) surface mass balance. They showed that the hydrological method consistently underestimated the mass loss (by 0.6 m w.e. yr^{-1}). The authors revealed that the measurement errors in the hydrological method (in undercatch, evaporation or water storage) cannot by themselves explain

this difference. They concluded that the bias is due to spatialization errors (linked to the absence of precipitation measurements at high altitudes).

Soruco et al. (2009) used photogrammetric and hydrological data to assess specific net surface mass balance derived from the glaciological method. They also reconstructed the annual surface mass balance using the hydrological method between 1975 and 2006. Their study revealed that 80% of the interannual glacier-wide surface mass balance variability can be explained by the surface mass balance in the ablation zone.

Ramallo (2013) analyzed 18 years of daily precipitation amounts measured below the glacier (at 4750 m a.s.l.) and linked them to the observed discharge at the glacier outlet. She found that the wet season duration and precipitation amounts are well linked to the discharge. In addition, she showed that the El-Niño Southern Oscillation was poorly linked to the interannual variability of both annual precipitation amounts and surface mass balance.

Vincent et al. (2018) developed a non-linear statistical model which accounts for spatial and temporal changes in point mass balance which, combined with geodetic data, allows precise evaluation of the glacier-wide surface mass balance. They applied the model to Zongo Glacier, resulting in 25 years of accurately reconstructed glacier surface mass balance. This dataset is considered to be the reference (measured) surface mass balance in this study.

Tropical glaciers are characterized by a marked longwave radiation seasonality as cloud emission during the wet season strongly enhances the low emissivity of the otherwise thin and dry clear-sky atmosphere found at high altitudes. Thus, Sicart et al. (2010) analyzed incoming longwave radiation cycles and found that cloud emission was responsible for up to 55% increase in measured incoming longwave radiation during the wet season and by 20% on average.

Similarly, Sicart et al. (2016) analyzed seasonal cloud radiative properties over the glacier between 2005 and 2013 and linked them to regional atmospheric circulation. They showed that cloud shortwave attenuation and longwave emissivity were higher during the wet season than during the dry season. They attribute these differences to the warm and thick clouds observed during the wet season as

opposed to the high altostratus clouds in the dry season. Using wind and geopotential height anomalies along with outgoing longwave radiation satellite reanalysis data, they showed that 46, 87 and 80% of the thickest cloud covers observed during the wet, dry and transition seasons, respectively were due to cold surges which lasted 2-3 days (*Surazo* events). Part of this study consisted in building up on their dataset to investigate the links between clouds, precipitation and surface mass balance (Chapters 2 and 4).

Rabatel et al. (2012) analyzed satellite imagery over Zongo Glacier between 1992 and 2012 and found that the highest snow line altitude recorded between May and August was representative of the annual equilibrium-line altitude. Their methodology was used to identify the annual firn lines in the simulations (Chapter 3).

Studies on the turbulent fluxes, which are the least known fluxes over the glacier, have also been carried out. For example, Litt et al. (2014) using data from an eddy-covariance (EC) measurements campaign (July/August 2007), studied the predominant downslope wind and found that in low wind conditions, a maximum wind speed was observed around 2 m above the surface and that the low wind oscillations resulted in erratic sensible heat fluxes. On the contrary, during periods of high winds, no wind speed maximum was observed and wavelet analysis revealed that coherent structures enhanced the turbulent sensible heat fluxes. Sicart et al. (2014) studied mean wind and temperature profiles and glacier surface (roughness lengths) considering two eddy covariance measurement campaigns and found katabatic wind maximum heights around 2-3 m above the surface during low wind conditions. This, coupled to strong inversions, led to reduced surface layer depths.

Litt et al. (2015) analyzed the turbulent fluxes and their measurement errors for different wind regimes during the dry season. Their study showed that for night density-driven katabatic flows or for strong downslope flows related to large-scale forcing, the sensible heat flux (H) was positive and the latent heat flux (LE) negative. In addition, because both have similar magnitudes they tend to cancel each other out. Their study revealed that most of the energy losses through turbulence occurred in day-time with upslope flow conditions. They showed that the bulk aerodynamic method underestimates the fluxes due to vertical flux divergence at low heights and non-stationarity of the turbulent flow. In addition, the mean random errors on the sum

of the turbulent fluxes (H+LE, 6%) were mainly due to the roughness height estimation. They also showed that the method is highly sensitive to the way surface temperature is derived from outgoing longwave radiation measurements. These studies highlight the difficulty in estimating turbulent fluxes over the Zongo Glacier, making it a source of modeling error (Chapter 3).

1.3 Tropical glaciers and paleoclimate studies

Tropical glaciers are characterized by steep vertical mass balance gradient in the ablation zone ($\partial B/\partial z$) due to frequent changes in snow cover throughout the long ablation season (Sicart et al., 2011). Kaser (2001) showed that in the Cordillera Blanca, $\partial B/\partial z > 2$ m w.e./100 m. Thus, tropical glaciers have a rapid response time to climate perturbations (from one to a few years, Rabatel, 2005) which makes them suitable proxies to assess past climate variations (e.g., Jomelli et al., 2009).

Using lichenometry techniques on the moraines of Zongo Glacier, Rabatel et al. (2005, 2008) dated the Little Ice Age (LIA) glacier extent to 1680 ± 28 AD. They applied both the Kaser (2000) model and Hastenrath and Ames (1996) approach to estimate climate differences between the LIA and now at a multi-annual scale. They suggest that for the glacier to have reached its maximum extent, temperatures had to decrease by 1.1 to 1.2 °C and that precipitation and cloudiness should have increased by 20-30 % and 0.1 to 0.2, respectively.

Other past climate reconstruction study in the region include Jomelli et al. (2011) who dated and reconstructed glacier extents over the past 11,000 years on the Telata Glacier in the Zongo Valley using the ^{10}Be dating technique and applied simplified surface energy and ice flow models to the Telata Glacier (about 5 km East of Zongo) providing information on potential past climate temperatures. For example, their findings suggest a cooling of 2.1 ± 0.8 °C during the Little Ice Age associated with about 15% less precipitation at the annual scale.

Malone et al. (2015) proposed a paleoclimate reconstruction over the Huancané outlet Glacier of the Quelccaya Ice Cap (Peru) using a 1D numerical flowline model. Their results suggest that for the glacier to have reached its LIA maximum extent, a cooling of 0.69 °C (contemporary lapse-rate: 1 °C / 1000 m) or

0.74 °C (temperature dependent lapse-rate 1 °C / 900 m) coupled with a ~21% precipitation increase (+ 0.28 m w.e.) was required.

1.4 Concluding remarks

Thus, despite a large number of studies carried out over tropical south American glaciers and more specifically on Zongo Glacier, a number of questions remained unanswered as some studies emit different hypotheses, for example, on the role of ENSO on the mass balance. Besides, as all the surface energy balance studies have been carried out over short periods (one to two years at most), some of the hypotheses on the climate controls on the surface mass balance variability have not yet been verified (e.g., the role of the wet season onset). In this context applying a surface energy balance model over several years is of particular interest as it allows a better oversight of the climate controls and the long dataset enables the testing and validation of different hypotheses.

Additionally, as seen in the previous section, the paleoclimate studies carried out over tropical glaciers have all provided information at a pluriannual scale. Here, using the surface energy balance model and the long measurement dataset available over the glacier provides an opportunity to create scenarios which can be used to assess the LIA climate at the seasonal scale.

Besides, understanding the climate controls of the surface mass balance and past glacier variations is important to better predict future glacier evolutions. This is of primary importance as its meltwater is an important resource for the local populations.

Main characteristics of Zongo Glacier

3 seasons:

- **Transition season (September to November):** Period of annual maximum melt rates in the ablation area, making it a key control period on the annual surface mass balance.
- **Core wet season (January-March):** over 70% of the annual precipitation falls during this period. Most of the seasonal melt comes from the frequent snowfall events as a result the glacier loses little mass over this period
- **Dry season (June-August).** Prevailing clear sky conditions and increased wind speed favor sublimation over melt. The associated incoming longwave radiation deficit leaves limited amounts of energy available for melt. As a result, the glacier loses little mass over this period.

Main precipitation synoptic forcings:

- **Surazos:** a destabilization of the tropical atmosphere due extra tropical cold air intrusion because of low-level southern wind incursion - occurs all year round
- **South American Monsoon System:** strong afternoon/early evening convection events - during the wet season

Main drivers of melt and of surface mass balance interannual variability:

- **Net shortwave radiation** is the main source of fusion (controlled *via* an albedo feedback effect). **Incoming longwave radiation** plays an important role in the seasonal variability of melt rates.
- **Wet season onset:** an early onset will interrupt the period of highest melt

Chapter 2 - Datasets

This chapter presents (1) the measurement program over Zongo Glacier; (2) the gap-filling methodology applied to obtain complete hourly scale time series for the seven variables required as model input: wind speed, precipitation, air temperature, relative humidity, incoming short and longwave radiation and outgoing longwave radiation along with the model calibration and validation data considered and (3) the cloud radiative dataset used to build on the analysis carried out over the glacier by Sicart et al. (2016).

2.1 Glacier monitoring network

The Bolivian authorities (Universidad Mayor de San Andrés, UMSA, Instituto de Hidráulica e Hidrología, IHH), in collaboration with the *Institut de Recherche pour le Développement* (IRD), started a meteorological, glaciological, and hydrological observation program on Zongo Glacier in 1991 (Francou et al., 1995; Ribstein et al., 1995, Fig. 2.1). In 2002, the program integrated the GLACIOCLIM observatory (GLAciers, An Observatory of CLIMate) as it answers the following criteria: surface mass and energy balance measurement, long observation periods and because it is representative of tropical glacier climate characteristics (Rabatel, 2015). GLACIOCLIM is a research program whose aim is to establish long term glacial meteorological databases to understand climate forcings on glacier mass balance in the Alps, Andes and Antarctica (<https://glacioclim.osug.fr/?lang=en>).

The mass balance measurement network on Zongo Glacier is composed of about 20 ablation stakes and a few snow pits whose positions have moved from year to year, storage rain gauges and a discharge gauging station at the glacier outlet composed of a triangular weir and a limnigraph (TUBO, 4830 m a.s.l., Fig. 2.2). In addition, there are three automatic weather stations: on the glacier (SAMA, 5050 m a.s.l.), on the moraine (ORE, 5050 m a.s.l.) and at the pass below the glacier (MEVIS/PLATAFORMA, 4750 m a.s.l.).

The AWS at the pass has changed over time, between 1991 and 2011 it was the MEVIS AWS however, in the years prior to 2011, various measurement and data download problems occurred. Consequently, in 2011, the Servicio Nacional de

Meteorología e Hidrología (SENAMHI) installed the PLATAFORMA AWS about 50 m away from the MEVIS AWS. This AWS, operational since the 7th of October 2011 was financed by the Proyecto de Adaptación al Impacto del Retroceso Acelerado de Glaciares en los Andes Tropicales (PRAA) of the andean community (CAN) and the World Bank (Lehmann et al., 2013). The MEVIS AWS was dismantled four months later (on the 31st of January 2012) to allow comparison of the measurements at the two AWS. At the daily time scale, all the measurements are significantly correlated ($R^2 > 0.7$, Lehmann et al., 2013). For simplicity, from Chapter 3 onwards, we use PLATAFORMA AWS for both MEVIS and PLATAFORMA.

All four automatic weather stations measure wind speed and direction, air temperature, relative humidity, precipitation, incoming and outgoing radiation fluxes (short and long wave components, tables 2.1 to 2.4 list the equipment for each AWS and photos are shown on Fig. 2.3). A number of studies have been carried out to quantify the measurement uncertainties over the Zongo Glacier. For example, Sicart et al. (2007) published a comparative study of the totalizing rain gauges and found measurement differences of about 20% linked to both undercatch due to wind exposure and altitude. The authors attribute the larger amounts at lower altitudes to the rain/snow limit as solid precipitation increases under-catch (Larson and Peck, 1974).

For modeling purposes, only the years from 1999 onwards are considered as it is when reliable hourly measurements started. However, due to the difficulty in maintaining fully operational automatic weather stations at such high-altitudes, there are a large number of measurement gaps (Fig. 2.4) specifically at the glacier AWS (SAMA). To maximize the number of years which could be used with the surface energy balance model (DEBAM), we continued the work started by Guillaumin (2014) which consisted in comparing measurements from the three AWS (over overlapping operating periods) to fill in measurement gaps at SAMA.

In addition to this permanent monitoring network, a number of specific measurements campaigns have also been carried out for example eddy-covariance measurements (over two dry seasons: 2005 and 2007, Litt et al., 2014) providing data on the sensible and latent heat fluxes. Other types of field measurement have

included, for example, an 18.5 m firn core from the accumulation zone (5800 m a.s.l., Gautier, 2012).

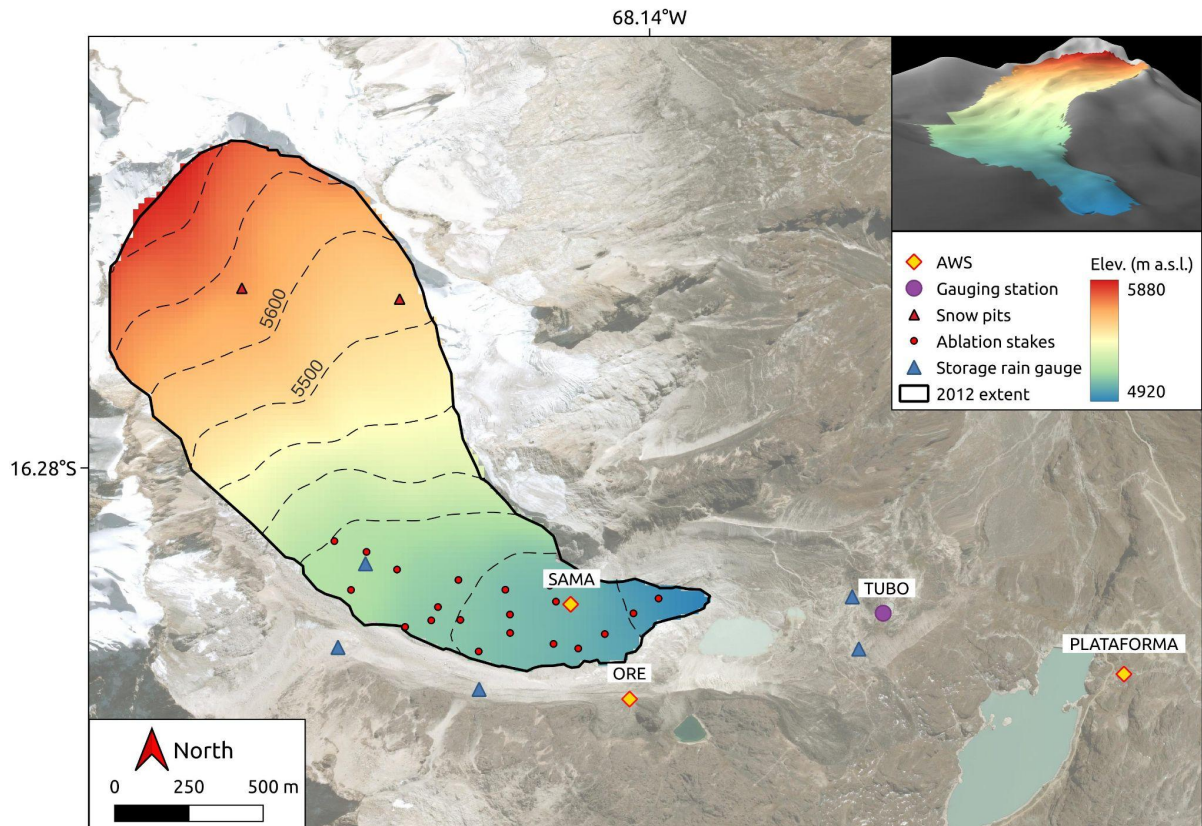


Figure 2.1 Monitoring network on and around the Zongo Glacier. The diamonds show the three automatic weather stations, the purple dot shows the position of the discharge gauge, the red dots and triangles show the ablation stakes and snow pit positions respectively. The blue triangles show the positions of the storage rain gauges. The glacier contour shown is the 2012 glacier extent and the top right inset is a 3D representation of this extent. Background image acquired by the Pléiades satellite in 2016, © CNES - Airbus D&S.



Figure 2.2. TUBO gauging station in 2019, photo courtesy: Victor Ramsayer

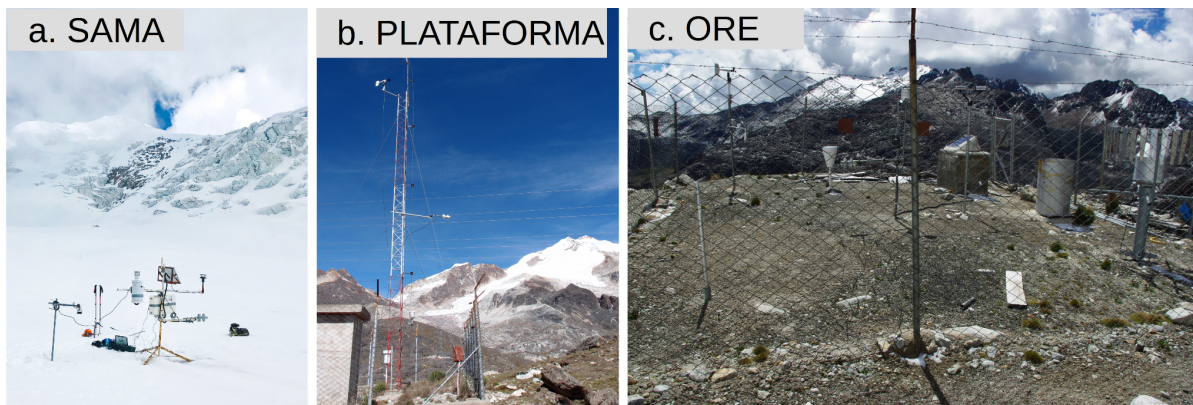


Figure 2.3. Photos of the three AWS on and around the glacier. Photographs a and b were taken in 2019 by Victor Ramsayer, photograph c. was taken in 2014 by Maxime Harter.

Table 2.1. SAMA AWS equipment (on the glacier at 5050 m a.s.l., 1991 - Now)

Variable	Sensor	Sensor Height	Precision (according to the manufacturer)
Temperature (K)	CS2115 (since 02/23/2011)	1.00 m	± 0.2 °C
	Vaisala HMP45C (up to 02/23/2011)	1.57 m	± 0.9 °C
Relative humidity (%)	CS2115 (since 02/23/2011)	1.00 m	± 2 %
	Vaisala HMP45C (up to 02/23/2011)	1.57 m	± 4 %
Wind speed (m s^{-1}) and direction (°)	Gill Solent (since 02/23/2011)	1.74 m	± 5 %
	Young 05103 (up to 02/23/2011)	2.50 m	± 0.3 m s^{-1}
Incoming and outgoing shortwave radiation (W m^{-2})	Kipp&Zonen CM3 $0.305 < \lambda < 2.8$ μm	1.00 m	± 3 %
Incoming and outgoing longwave radiation (W m^{-2})	Kipp&Zonen CG3 $5 < \lambda < 50$ μm	1.00 m	± 3 %
Snow height, ultrasonic measurements (m)	Campbell, SR50AT	1.15 m	± 1 cm or 0.4 % of the distance

Table 2.2. ORE AWS equipment (on the moraine at 5050 m a.s.l., 25th August 2003 - 12th March 2015)

Variable	Sensor	Sensor Height	Precision (according to the manufacturer)
Temperature (K)	CS2115	2.05 m	± 0.2 °C
Relative humidity (%)	CS2115	2.05 m	± 4 %
Wind speed (m s^{-1}) and direction (°)	Young 05103	2.50 m	± 0.3 m s^{-1} / ± 3 °
Incoming and outgoing shortwave radiation (W m^{-2})	Kipp&Zonen CM3 ($0.3 < \lambda < 2.8$ μm)	0.90 m	± 10 % of daily amount
Incoming and outgoing longwave radiation (W m^{-2})	Kipp&Zonen CG3 ($5 < \lambda < 50$ μm)	0.90 m	± 10 % of daily amount
Precipitation (mm)	Geonor T-200B, $\Phi = 0.39$ m	1.70 m	± 0.1 mm
	Storage rain -gauge	1.40 m	Max accu = 1150 mm
Snow height, ultrasonic measurements (m)	Campbell, SR50AT (up to 02/28/2012)	1.15 m	± 1 cm / ± 0.4 % of the distance
	Campbell, SR50AT (since 02/28/2012)	1.15 m	± 1 cm / ± 0.4 % of the distance

Table 2.3. MEVIS AWS equipment (at the pass, 4750 m a.s.l., 1991 up to the 31st of January 2012)

Variable	Sensor	Sensor Height	Precision (according to the manufacturer)
Temperature (K)	THIES Hygro-Thermogeber	1.90 m	NA
Relative humidity (%)	THIES Hygro-Thermogeber	2.05 m	NA
Wind speed (m s^{-1}) and direction ($^{\circ}$)	Windgeber 4.3303.10.007	1.55 m	NA
Incoming shortwave radiation (W m^{-2})	Kipp&Zonen CM3 ($0.3 < \lambda < 2.8 \mu\text{m}$)	1.55 m	$\pm 10\%$ of daily amount
Precipitation (mm)	Cobee rain gauge (22cm wide), daily measurements carried out by an observer every day at 7 am	?	± 1 mm
Ground temperature ($^{\circ}\text{C}$)	Pt100, Thermogeber 2.1235.00.000	1m deep	NA

Table 2.4. PLATAFORMA AWS equipment (at the pass, 4750 m a.s.l., 7th October 2011 - Now)

Variable	Sensor	Sensor Height	Precision (according to the manufacturer)
Temperature (K)	Vaisala HMP45C	1.93 m	± 0.2 $^{\circ}\text{C}$
	Campbell T108	0.45 m	± 0.3 $^{\circ}\text{C}$
Relative humidity (%)	Vaisala HMP45C	1.93 m	$\pm 4\%$
Wind speed (m s^{-1}) and direction ($^{\circ}$)	Young 05103	10.00 m	± 0.3 $\text{m s}^{-1} / \pm 3^{\circ}$
Incoming and outgoing shortwave radiation (W m^{-2})	Kipp&Zonen CM3 ($0.3 < \lambda < 2.8 \mu\text{m}$)	5.00 m	$\pm 10\%$ of daily amount
Incoming and outgoing longwave radiation (W m^{-2})	Kipp&Zonen CG3 ($5 < \lambda < 50 \mu\text{m}$)	5.00 m	$\pm 10\%$ of daily amount
Precipitation (mm)	Met one instruments, $\Phi = 0.3$ m (12" heated rain gauge)	1.00 m	± 0.1 mm

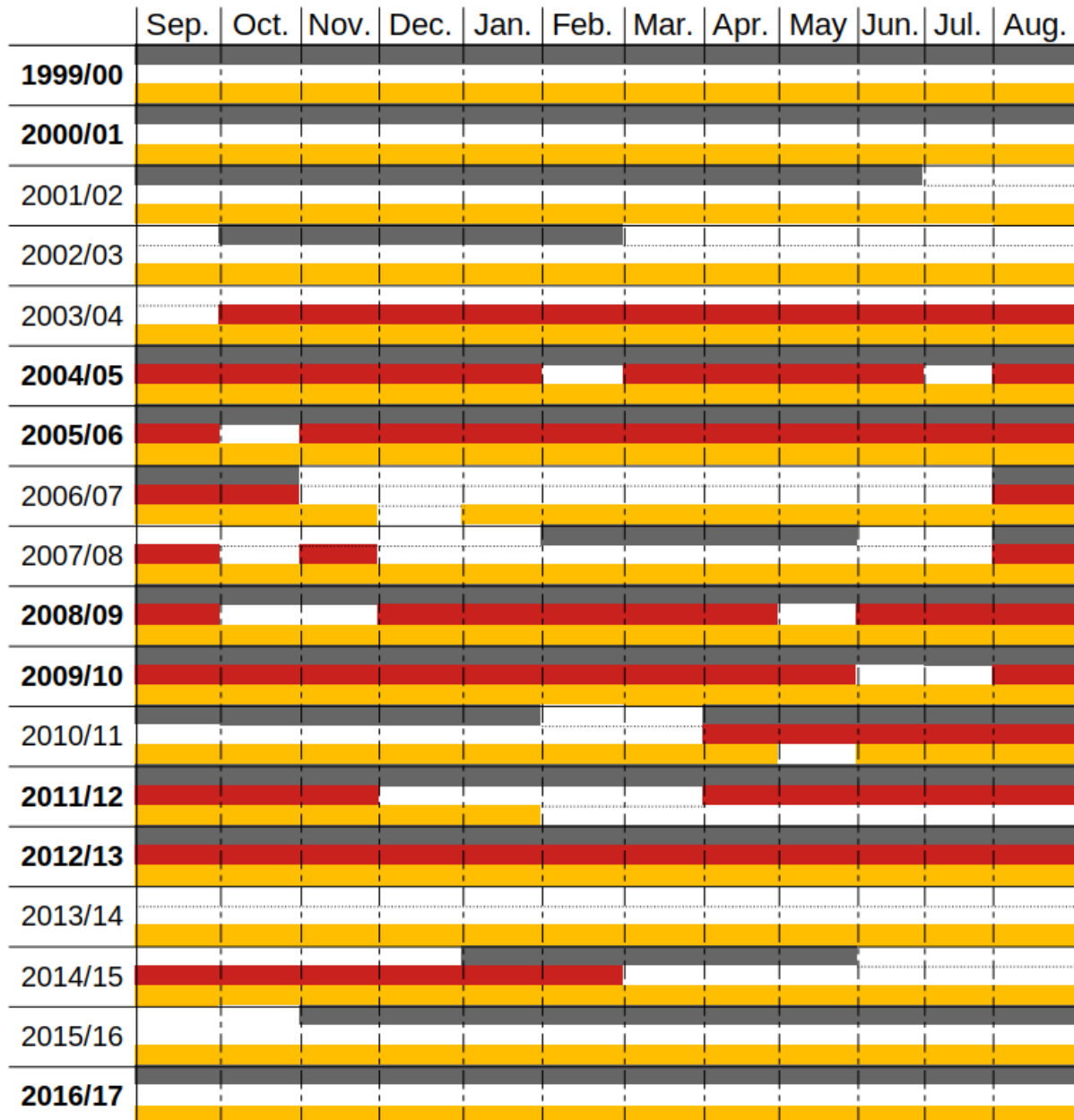


Figure 2.4. Operating periods of the three automatic weather stations located on and around the glacier (SAMA measurements are in gray, ORE measurements in red and MEVIS & PLATAFORMA measurements in yellow). Note that the displayed operating periods correspond to periods with at least one variable measured for over 15 days in the corresponding month. The years in bold are those for which hourly data was available for the whole hydrological year after filling the measurement gaps.

2.2 Model input data

In order to apply DEBAM over the glacier, we need gap-free hourly radiation (incoming short and longwave radiation and outgoing longwave radiation), air

temperature, precipitation, wind speed and relative humidity measurements from the SAMA AWS. To fill in measurement gaps at SAMA, some of the variables measured at the ORE and PLATAFORMA can be used.

2.2.1. Existing gap-filled dataset

Prior to this PhD, Guillaumin (2014) filled a number of glacier measurement gaps for several hydrological years (2005/06, 2008/09, 2009/10, 2011/12 and 2012/13) using the methodology described below (based on comparison of the ORE and SAMA AWSs). Table 2.5 summarizes all the measurement gaps (≥ 1 day) which were filled. Section S1 in the Supporting Information provides an analysis of the seasonal patterns of the meteorological measurements at the three AWS.

Incoming shortwave radiation (SW_{in})

- If a few hours are missing, and if it is a clear-sky day, then SW_{in} is considered to be the same as it was the previous day (if the latter is also a clear-sky day). Otherwise, data from the ORE is used as the two are well correlated ($R^2 = 0.82$, Fig. 2.5a).
- If data gaps > 1 day, ORE data is considered

Incoming longwave radiation (LW_{in}) - Missing data was replaced with data from the ORE if available. Else, data from the MEVIS/PLATAFORMA was considered ($R^2 = 0.91$ and 0.8 , when considering ORE and MEVIS/PLATAFORMA measurements, respectively, Fig. 2.5b).

Outgoing longwave radiation (LW_{out})

- If ORE measurements were available, then it was used to fill in the gaps but the maximum admissible value was set to 315.6 W m^{-2} as when doing so, the measurements are well correlated (Fig. 2.5c)
- In the absence of ORE data, the gaps cannot be filled, however, this is of limited importance as it is possible to run the model without these measurements.

Temperature, relative humidity and temperature

When SAMA is operating there is a limited number of data gaps of these three variables, and, when it occurs, it is over a short period (2-3 days).

- Relative humidity gaps were filled using ORE measurements when available ($R^2 = 0.93$, Fig. 2.5d) or gaps were filled by either linear interpolation between two measurements (gaps less than a few hours).
- Temperature and wind speed gaps were filled by linear interpolation or by copying and pasting values of previous days if gaps were larger than half a day and if no changes in weather were observed.

Precipitation

In this study hourly precipitation is calculated using the measured snow heights at SAMA (using the ultrasonic sensor) as observations show that most precipitation falls in the form of snow over the glacier. This method is accurate at the sub-daily timescale because at the AWS, fresh snow has a high density (~220 to 250 kg m^{-3}) and during snowfall events, moderate wind conditions are observed which limits snowdrift conditions (Sicart et al., 2002).

The snow height changes are converted into water equivalent according to the method presented by Sicart et al. (2002): snow events are characterized by a decrease in measured sensor-surface distance. If three consecutive measurements spread over one hour at 3-hour intervals show height changes $\Delta h \geq 0.01$ m, then it is considered that a precipitation event has occurred. The snow height changes are converted into water equivalent by multiplying Δh by the fresh-snow density and re-distributed evenly over the three hours. Based upon on-site measurements, we consider a fresh snow density of 250 kg m^{-3} during the core wet season and one of 220 kg m^{-3} for the rest of the year (Sicart et al., 2002).

The precipitation gaps were filled as follows:

- During a measurement gap, to ensure that a precipitation event took place, albedo and discharge plots are analyzed: if the albedo rises / discharge decreases or if precipitation is measured at the other AWS, then we consider that a precipitation event occurred. In the absence of precipitation, the values are set to zero.

- If the data gap during the transition season is too large (> one month), the year cannot be modeled as during these months, precipitation events are a key control of melt (e.g., Sicart et al., 2011).
- If data gaps are over a few days, in the absence of large melt rate differences, values of the previous day are considered. If that is not possible, then ORE or measurements are used and increased by 40% (a result of the comparison of the two AWS, Sicart et al., 2002).

Table 2.5. Detailed summary of the data gaps which were filled considering measurements carried out on the moraine (ORE). Note 2004/05 is in bold and italic as for this year we identified a problem with the measured incoming longwave measurements. We corrected them following the methodology described in the next section.

Year	Period with missing data	Missing data completed by ORE measurements
<i>2004/05</i>	Less than a month	4 th to 21 st Jan. 2005
2005/06	Less than a month	31 st Jan. to 3 rd Feb. 2006 1 st to 18 th Apr. 2006
2008/09	Less than a month	1 st to 24 th Sept. 2008
2009/10	About 4 months	1 st to 8 th Sept. 2009 1 st March to 4 th May 2010 19 th May to 11 th June 2010 4 th to 31 st Aug. 2010
2011/12	About 2 months	20 th to 30 th Sept. 2011 9 th to 15 th Oct. 2011 4 th to 7 th Nov. 2011 27 th Jan. to 16 th Feb. 2012 21 st to 28 th Feb. 2012 1 st to 16 th March 2011 1 st to 5 th & 13 th to 19 th Apr. 2012 3 rd to 9 th Aug. 2012
2012/13	Less than a month	25 th Dec. 2012 to 16 th Jan. 2013 21 st to 24 th Jan. 2013

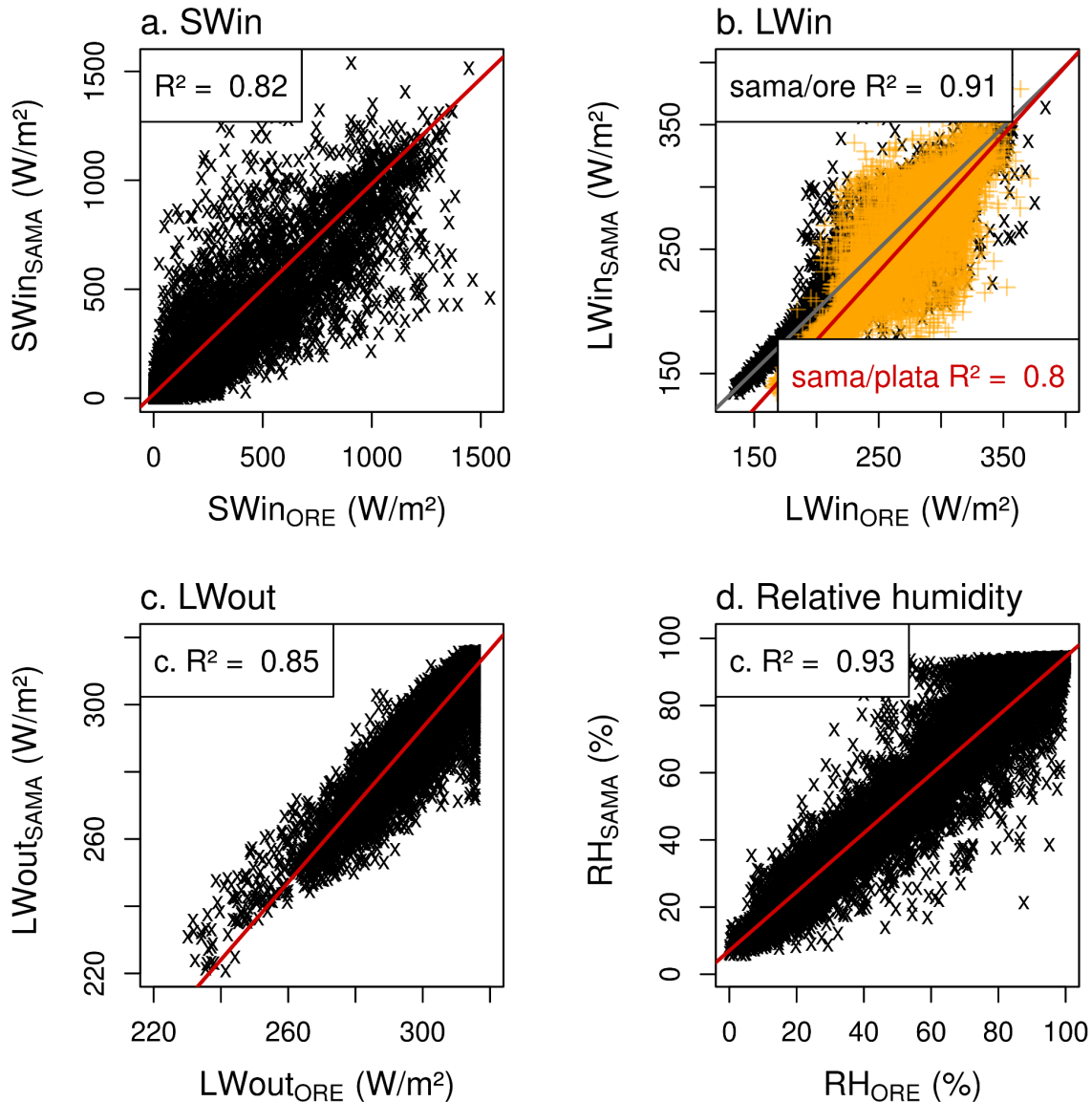


Figure 2.5. Correlations between hourly incoming shortwave radiation measured at SAMA and ORE (a), incoming longwave radiation at SAMA and both ORE (black) and PLATAFORMA (yellow, plot b), outgoing longwave radiation at SAMA and ORE (c) and (d) shows the 30 minutes relative humidity measurements at SAMA and ORE. The measurements were carried out during 2012/13.

2.2.2 Extension and presentation of the dataset

Altogether, we were able to fill in gaps for another two years: 2004/05 and 2016/17. In 2004/05, the measured incoming longwave radiation was erroneous between September and December and April-May. The data was replaced by daily values calculated using the formula calibrated over the glacier by Sicart et al. (2010, Eq. 2.1)

$$LW_{in} = C \left(\frac{e}{T} \right)^{1.7} \left(1.67 - 0.83 \tau_{atm} \right) \sigma T^4 \quad (2.1)$$

With $C = 1.24$, $\tau_{atm} = \frac{SW_{in}}{S_{extra}}$, e the vapor pressure (hPa), T the temperature (K), S_{extra} the top of atmosphere radiation (calculated according to Paltridge and Platt, 1976) and σ the Stefan-Boltzmann constant ($5.67 \cdot 10^{-8} \text{ W m}^{-2} \text{ K}$).

During 2016/17 incoming longwave radiation measurements were missing for 10 days in January and were replaced considering Equation 2.1. In addition, SAMA precipitation measurements were missing between June and August and were replaced with those from the PLATAFORMA considering a 50% increase based on the analysis of the differences in monthly amounts over the period. We followed the methodology applied by Guillaumin (2014) to see if a precipitation event occurred.

The resulting 9 years of continuous hourly dataset (1999/00, 2000/01, 2004/05, 2005/06, 2008/09, 2009/10, 2011/12, 2012/13 & 2016/17, available at: <https://glacioclim.osug.fr/335-Energy-balance-on-a-tropical-glacier-in-Bolivia>) is composed of highly contrasting years as the annual glacier-wide surface mass balance calculated by Vincent et al. (2018, B_{GW}) ranges between -1.90 m w.e. and 0.48 m w.e. (Fig. 2.6a) providing an opportunity to assess climate controls on the annual surface mass balance.

At the annual scale, important variability in precipitation amounts (1.3 to 1.9 m w.e.) and mean annual temperature (-1 to 0.8 °C) are observed (Fig. 2.6b&c, respectively). Conversely, relative humidity and wind speed show little year-to-year variability (Fig. 2.6d&e, respectively). Similarly, the annual mean radiation components show little interannual variability (Fig. 2.6f-h for SW_{in} , LW_{in} and LW_{out} , respectively). The highest year-to-year radiative variability is on the measured incoming longwave radiation (standard deviation: $\pm 8 \text{ W m}^{-2}$) which is a result of the cloud cover associated with the precipitation events. Finally, annual mean outgoing longwave radiation suggests that, on average, the surface temperature at SAMA is close to 0°C for all years ($\overline{LW_{in}}$ close to 315.6 W m^{-2} , Fig. 2.6h).

In addition to the hourly dataset for the simulations, we also considered the 18 years long daily precipitation and temperature measurements at MEVIS/PLATAFORMA provided by Ramallo (2013). This dataset was not used for the simulations but to assess the long term links between precipitation and temperature and the surface mass balance (Chapter 4).

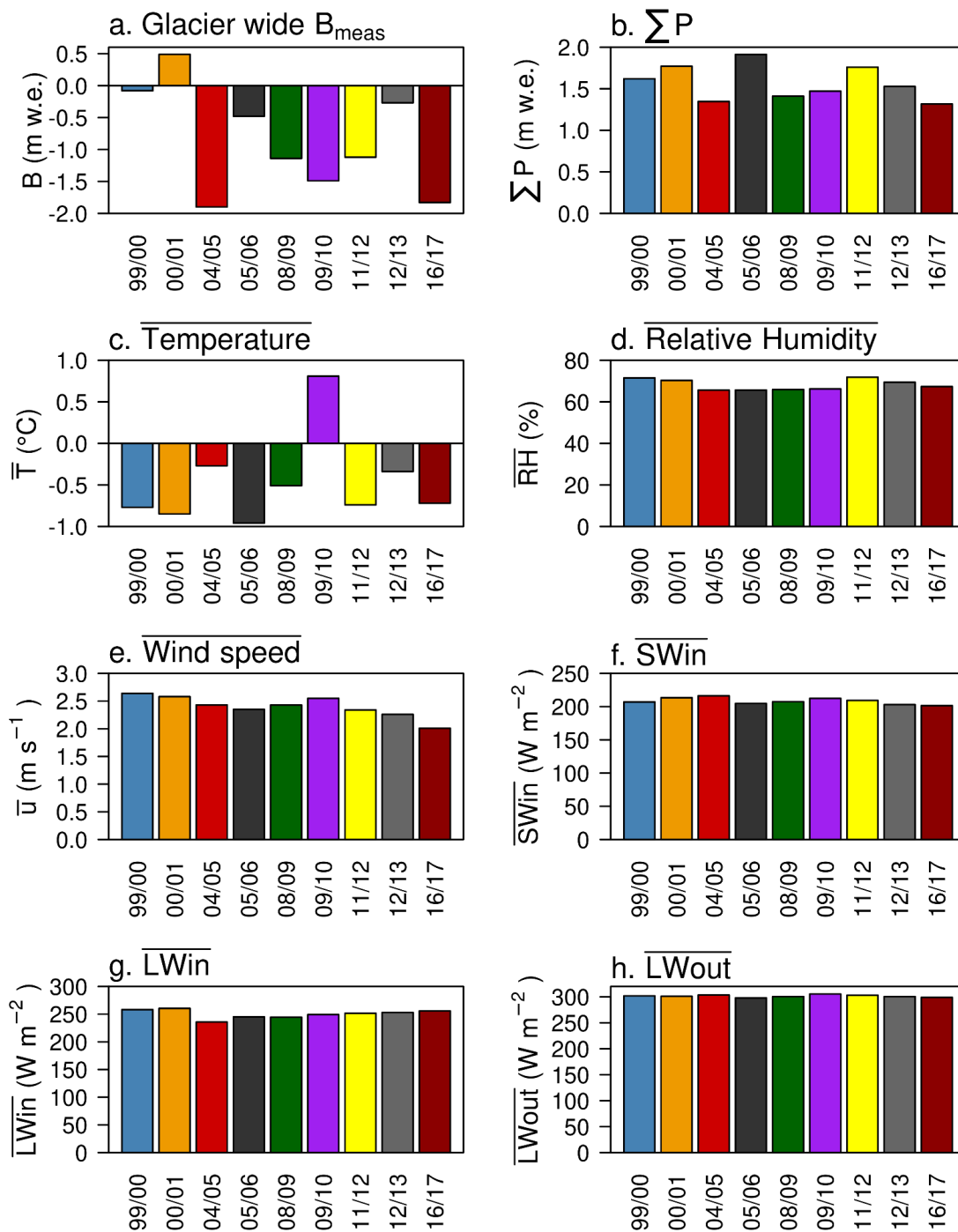


Figure 2.6. Annual glacier-wide surface mass balance (B_{GW} , plot a), precipitation amounts (b), mean temperature (c), relative humidity (d), wind speed (e), annual mean incoming

shortwave (f), and longwave (g) radiation and outgoing longwave radiation (h), for the nine years with on-glacier hourly data.

2.2.3 Model calibration and validation data

To calibrate and validate our simulations, we analyzed the measured albedo at the glacier AWS (SAMA). Similarly, we compared the discharge simulations with the measurements at the proglacial stream (TUBO, Fig. 2.1). The measurement gaps in this dataset (~25 % when considering the 9 years), were not filled as no reliable information was available to do so.

To validate the simulation results, we also considered visual information of the glacier surface collected during bimonthly field visits (Table 2.6). Photographs of the glacier ablation zone are taken at each field visit from the ORE meteorological station (Fig. 2.1. and 2.8). These are useful calibration and validation information as once elevations of the observed different surface types (snow/ice) are extracted, it can be used to assess the simulated glacier surface of specific days in the year. Figure 2.7 illustrates the way snow cover information from photographs is converted into maps .

Although Corripio (2004) developed a method to accurately reproduce the snow line by projecting terrestrial photographs on a Digital Elevation Model (DEM), we chose not to use it as we aimed at obtaining qualitative rather than quantitative information. See Dumont et al. (2011) for an example of this method's application over the Saint-Sorlin Glacier.

Finally, for the calibration and validation of the simulations, we used, as reference, the glacier-wide surface mass balance and altitudinal gradient of mass balance calculated by Vincent et al. (2018).

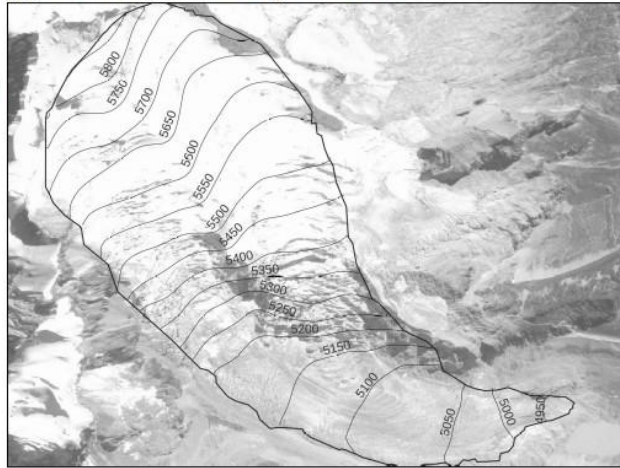
Table 2.6. Example of the site visit information used to validate modeling over the year 2000/01

Date	Observed glacier surface between the glacier terminus and 5100 m a.s.l.
09/08/2000	Large snow grains over 7 cm + penitent formation
09/19/2000	Salt-like snow
10/12/2000	25 cm deep fresh snow
10/24/2000	20-30 cm of transforming snow
11/10/2000	10 cm of large grain, transformed snow
11/21/2000	Dirty ice with crevasses forming around the AWS (at 5050 m a.s.l.)
12/07/2000	15-20 cm of fresh snow over the whole glacier
12/18/2000	5 cm of fresh snow
01/04/2001	40-50 cm of fresh snow
01/19/2001	1 m of fresh snow
01/30/2001	Fresh snow
02/08/2001	Crusted snow over a few cm
02/22/2001	2 cm of transforming fresh-snow
03/08/2001	Transformed snow
03/20/2001	Wet transformed snow
03/29/2001	Fresh snow in the morning, transformed in the afternoon
04/20/2001	1 cm of sleet covering transformed snow
05/17/2001	Transformed snow
05/29/2001	Transforming snow
06/13/2001	Rough surface
06/23/2001	25 cm of fresh snow
07/10/2001	10-15 cm high penitents
07/24/2001	Alternating zones of fresh snow (30 cm thick), formation of penitents (10 cm high)
08/03/2001	10-15 cm high penitents
08/08/2001	2-3 cm of fresh snow
08/21/2001	50 cm of fresh snow
08/29/2001	30 cm of transforming snow

(1) Identification of the snow limit from a field photo



(2) Use of DEM to identify its altitude



(3) Assignment of snow and ice values over DEM altitudes

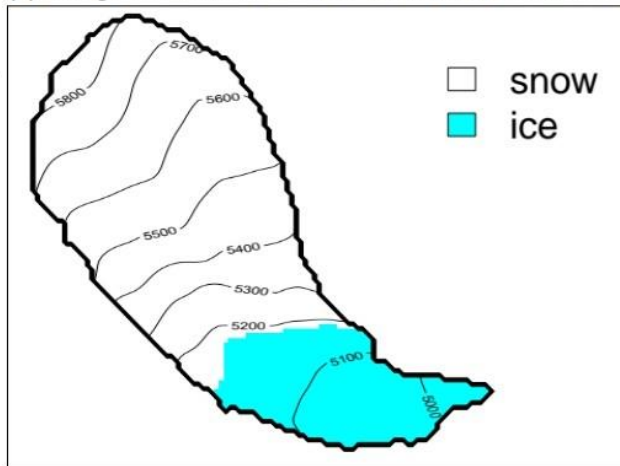


Figure 2.7. Methodology used to estimate snow lines from photographs illustrated over the 25th of August 2009. Photo courtesy: Maxime Litt

2.3 Cloud radiative properties dataset

To assess the impact of cloud cover on the surface energy balance, we extended the cloud radiative properties dataset constructed by Sicart et al. (2016) between 2005 and 2012. Information on the type of cloud which passes over the AWS can be derived from the cloud radiative properties: attenuation of incoming shortwave (solar) radiation (SW_{in}) and increase in longwave emissivity (LW_{in}). To extend the dataset (14 years between 1999/00 and 2018/19), we considered data from all three AWS as analysis of measured radiation at the three locations showed that a cloud which passes over one AWS generally passes over the other two (the measured incoming radiation at all three stations is well correlated $R^2 \geq 0.8$).

2.3.1 Definition of the cloud radiative properties

Calculation of the cloud radiative properties requires daily incoming radiation (LW_{in} and SW_{in}), air temperature and relative humidity measurements. Following the methodology presented by Sicart et al. (2016), we calculated the cloud bulk shortwave transmissivity and longwave emission factors (T_n and F , respectively) which represent the cloud ability to reduce (increase) SW_{in} (LW_{in}). From these parameters it is possible to define the impact the cloud has on the incoming radiation fluxes (the cloud radiative forcing, CF in $W m^{-2}$) and to differentiate clouds types (e.g., warm/thick or cold/high) *via* the cloud cover index (CI) which is the difference between F and T_n .

Cloud bulk short-wave transmissivity factor (T_n , Eq. 2.2) is obtained by comparing measured incoming shortwave radiation (SW_{in}) to clear-sky incoming shortwave radiation (S_{clear}). Note, $0 < T_n \leq 1$ because clouds cannot increase the amount of solar radiation reaching the surface.

$$SW_{in} = T_n S_{clear} = T_n T_{clear} S_{extra} \quad (2.2)$$

With $T_{clear} = 0.87$ is the bulk clear-sky transmissivity derived from measurements on Zongo glacier by Sicart et al. (2016) and S_{extra} is the calculated top of atmosphere shortwave radiation ($W m^{-2}$).

Similarly, the cloud longwave emissivity factor (F , Eq. 2.3) is obtained by comparison of measured incoming longwave radiation (LW_{in}) and clear-sky incoming

longwave radiation (L_{clear} , Eq. 5.4) calculated from Brutsaert (1975)'s formula. $F \geq 1$ as clouds cannot reduce the amount of LW_{in} reaching the surface.

$$LW_{in} = \varepsilon_{clear} F \sigma T^4, \varepsilon_{clear} = C \frac{e^{1/m}}{T} \quad (2.3)$$

$$L_{clear} = \varepsilon_{clear} \sigma T^4 \quad (2.4)$$

σ is the Stefan-Boltzmann constant ($5.67 \cdot 10^{-8} \text{ W m}^{-2} \text{ K}^{-4}$), T the air temperature (K), ε_{clear} the apparent clear-sky emissivity and e is the vapor pressure (hPa). Finally, m and C are two constant parameters: m relates to the integration of the emission level of a slab of water vapor with carbon dioxide in the atmosphere; it was set to 7 regardless for all three AWS following the original equation formulation (Brutsaert, 1975). C represents the relationship between vapor pressure and temperature near the ground and their atmospheric profile (it varies with altitude). For SAMA and ORE measurements (at 5050 m a.s.l.), Sicart et al. (2016) calibrated equation 2.3 and found $C = 1.14$ (Sicart et al., 2016). Because Plataforma AWS is 300 m lower (at 4750 m a.s.l.), C was recalibrated and set to 1.2 (explained below).

The cloud cover index (CI) is the difference between the two factors and is high for warm low and/or thick clouds and low for high clouds.

$$CI = F - T_n \quad (2.5)$$

Finally, cloud radiative forcing (CF) is calculated as follows :

$$\begin{aligned} CF &= CF_{SW} + CF_{LW} = (SW_{in} - S_{clear}) + (LW_{in} - L_{clear}) \\ &= S_{clear}(T_n - 1) + L_{clear}(F - 1) \end{aligned} \quad (2.6)$$

2.3.2 Calibration of the cloud longwave emission factor for measurement at PLATAFORMA (4750 m a.s.l.)

The calibration of C for the PLATAFORMA measurements was carried out by trial and error with values of C ranging between 1.14 and 1.24. We tested increments of 0.01 and validated the C value by comparing the resulting clear-sky atmospheric emissivity (ε_{clear} , Eq. 2.3) to the measured one (Fig. 2.8a). To account for radiation measurement errors ($\sim 10\%$, Sicart, 2002), up to 10 % of daily clear-sky LW_{in}

measurements were allowed to reach lower values than the theoretical L_{clear} curve (Fig. 2.8b).

The calibration of C over Plataforma measurements resulted in a 14 years dataset of daily cloud radiative properties (spanning between 1999 and 2019) with data originating from:

- Measurements at SAMA between September 1999 and June 2002 i.e., hydrological years 1999/00, 2000/01 and 2001/02 (up to June for the latter)
- Mix of SAMA and ORE measurements for 2004/05, 2005/06, 2008/09,2009/10, 2011/12, 2012/13
- Measurements from the pass (PLATAFORMA AWS) between 2013/14 and 2018/19

Cloud radiative forcing and its components (CF_{SW} , and CF_{LW}) show that in terms of energy amounts, clouds reduce more incoming solar radiation (up to - 300 $W m^{-2}$) than they increase incoming longwave radiation (by up to 100 $W m^{-2}$, Fig. 2.8c). As analyzed by Sicart et al. (2016), globally clouds reduce the amount of energy reaching the surface (negative cloud radiative forcing, Fig. 2.8c). Section S2 in the supporting information provides an analysis of the seasonal cloud radiative properties.

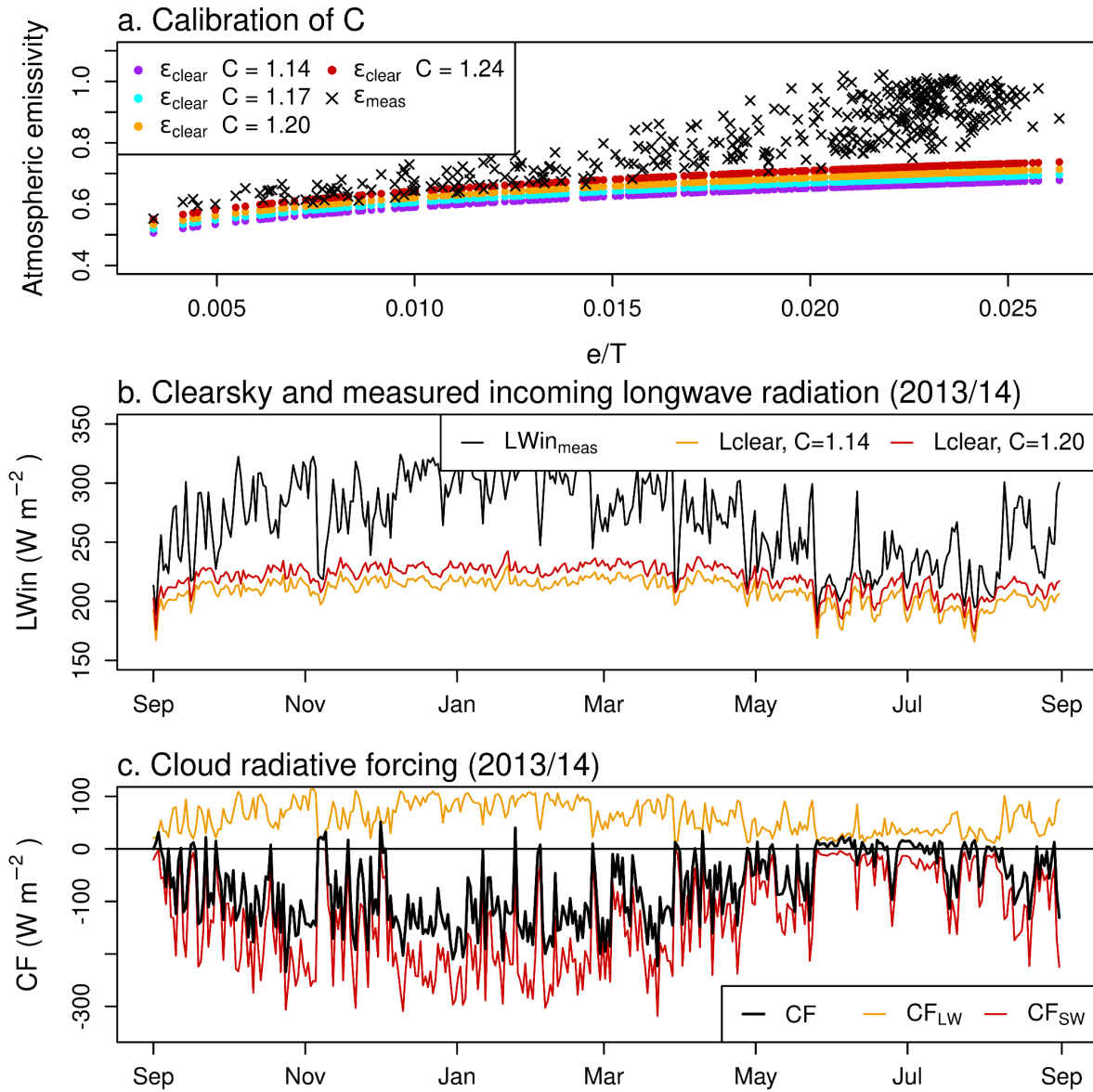


Figure 2.8. Illustration of the calibration of C on atmospheric emissivity (a) and L_{clear} (b) over Plataforma measurements for the year 2013/14. (c) shows the cloud radiative forcing (CF) and its components (CF_{SW} & CF_{LW}).

2.4. Summary

Datasets

- **Simulation dataset:** 9 years of continuous hourly precipitation, temperature, relative humidity, incoming short and longwave radiation, and outgoing longwave radiation measurements spanning between 1999 and 2017: 1999/00, 2000/01, 2004/05, 2005/06, 2008/09, 2009/10, 2011/12, 2012/13, 2016/17
- **Calibration/validation material:** discharge at the glacier's outlet, measured albedo at SAMA, field observations and photographs
- **25 years** (1991-2017) of daily precipitation measurements at the MEVIS/PLATAFORMA
- **14 years** between 1999 and 2019 of daily cloud radiative properties

Chapter 3 - Model setting, calibration and validation for the current climate

We apply the open source distributed surface energy balance model DEBAM (Hock and Holmgren, 2005; <https://regine.github.io/meltmodel/>) on a 20 x 20 m grid of the Zongo catchment at the hourly time step. This model has been applied to glaciers in the Northern Hemisphere (e.g., Hock and Holmgren, 2005; Reijmer and Hock, 2008; Østby et al., 2017) or the Sub-Antarctic region (Braun and Hock, 2004). Sicart (2002) adapted the model to the conditions of the high altitudes and low latitudes of Zongo Glacier. First a detailed presentation of the model is provided followed by how it was initialized, calibrated and validated. Finally, the main source of simulation errors are briefly discussed.

3.1 Model description

3.1.1 Energy balance

Melt energy (ΔQ_M) is derived from the following surface energy balance equation (Fig. 3.1 illustrates the energy balance equation):

$$SW_{in}(1 - \alpha) + LW_{net} + H + LE + Q_G + Q_R = \Delta Q_M + \Delta Q_s \quad (3.1)$$

$$\Delta Q_s = \int_0^{z^*} \frac{d(\rho c T)}{dt} dz$$

SW_{in} the the measured incoming shortwave radiation ($W m^{-2}$), α the surface albedo, LW_{net} the net longwave radiation ($LW_{in} - LW_{out}$, $W m^{-2}$), H and LE the sensible and latent heat fluxes respectively ($W m^{-2}$), Q_G the subsurface heat flux ($W m^{-2}$) and Q_R the sensible heat supplied by rain ($W m^{-2}$, negligible on Zongo Glacier, Sicart et al., 2005). The model convention is such that energy fluxes are positive if they supply energy to the control volume (surface) and negative otherwise.

ΔQ_s is the heat content change in a control volume of snow or ice, c is the specific heat capacity of the control volume and ρ its density. T is the ice temperature and z^* the depth at which the energy flux is null. If ΔQ_M is positive, then melt occurs,

if it is negative, freezing occurs. When Q_M is positive then it is converted into meltwater equivalent (m w.e. h^{-1}) and is routed through the glacier *via* three linear reservoirs with storage constants of 30, 350 and 16 hours representing snow, firn and ice, respectively (Sicart et al., 2011). Firn is considered to be snow which remains from the previous year.

Zongo Glacier covers 70% the catchment's surface area, the 30% non-glacierized part of the catchment contributes to about 10% of the discharge at the glacier outlet during the wet season, its runoff is estimated with a constant runoff coefficient of 0.8 (Ribstein et al., 1995, Sicart et al., 2007; 2011).

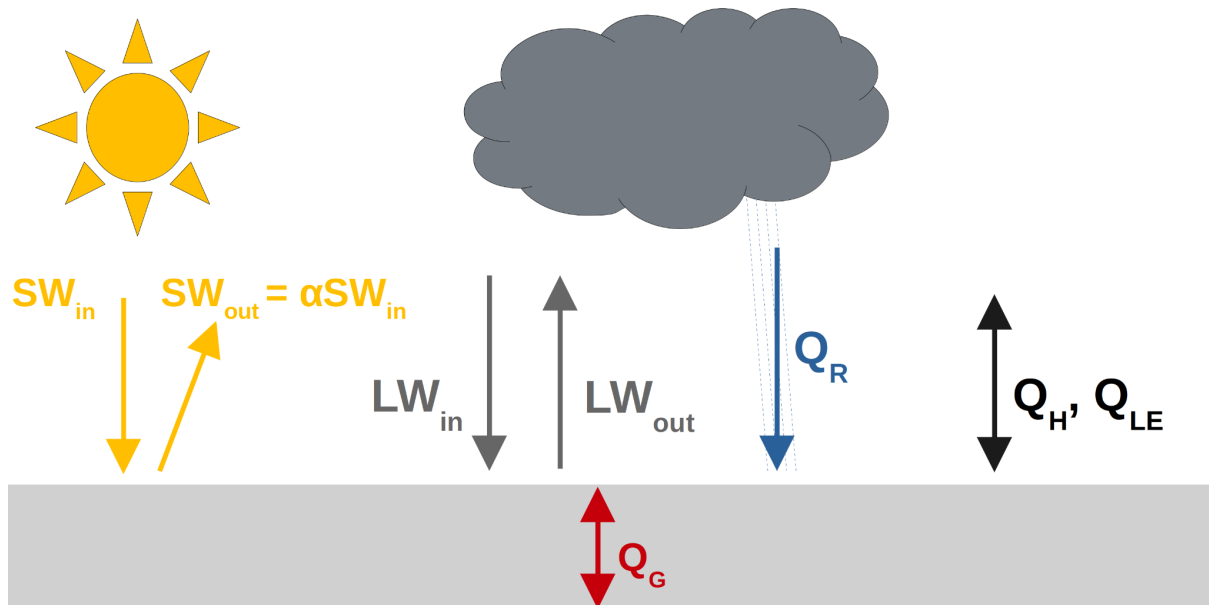


Figure 3.1. Illustration of the different energy fluxes considered in the energy balance.

3.1.2 Incoming shortwave radiation

Incoming shortwave radiation (SW_{in}) is split into direct and diffuse components which requires the calculation of the potential clear-sky solar radiation (I, Oke, 2006):

$$I = I_0 \times \left(\frac{r_m}{r}\right)^2 \times \Psi_a^{\frac{p}{P_0}/\cos(Z)} \times \cos(Z) \quad (3.2)$$

I_0 is the solar constant (1368 W m^{-2}), r the sun-earth distance and r_m the mean sun-earth distance, p is the atmospheric pressure and P_0 the standard atmospheric

pressure (1013.25 hPa) whilst Z is the zenith angle. Calculations are done using the altitude and latitude of the approximate center of the area. For this to work, a small surface area (S) must be considered (valid here as $S_{\text{Zongo}} < 1.7 \text{ km}^2$). Thus, the calculated values only vary according to the grid elevation (h) which is expressed in terms of air pressure: $p = e^{-0.000184 \times h \times P_0}$.

The ratio $\frac{p}{P_0}$ accounts for the effect of altitude: a higher elevation yields a lower air pressure which results in higher solar radiation. $\cos(Z)$ expresses the variation of the path length with the sun's altitude. The atmospheric transmissivity accounts for the bulk effect of reflection, scattering and absorption of solar radiation by droplets, particles and gasses in the atmosphere.

The Sun to Earth radius is calculated as follows:

$$\theta = \frac{2\pi jd}{365} \quad (3.3)$$

$$\begin{aligned} \text{radius2sun} = & 1.000110 + 0.034221 \cos(\theta) + 0.00128 \sin(\theta) + \\ & 0.000719 \cos(2\theta) + 0.000077 \sin(2\theta) \end{aligned} \quad (3.4)$$

The zenith angle (in degrees) is calculated according to Oke (1987):

$$\cos(Z) = \sin(\Phi) \sin(\delta) + \cos(\Phi) \cos(\delta) \cos(h) \quad (3.5)$$

$$\delta = -23.4 \cos(360(t_j + 10)/365), \quad h = 15 \times (12 - t) \quad (3.6)$$

Φ is the latitude (-16° here), δ the angle between the sun's ray and the equatorial plane which is a function of the day of the year, h is the angle through which the earth must turn to bring the meridian of Zongo directly under the sun, t_j is the julian date and t the local apparent time, calculated by subtracting 4 minutes for each longitude degree east of the meridian.

Because the equation for the potential clear sky radiation (Eq. 3.2) applies to a horizontal surface, the clear sky radiation is corrected using a factor which accounts for grid shading, slope and aspect. These three factors are calculated for each grid and each time step. Slope and aspect are accounted for as follows:

$$I_{slope} = I \times \frac{\cos(\theta)}{\cos(Z)} \quad (3.7)$$

$$\text{with } \cos(\theta) = \cos(\beta) \times \cos(Z) + \sin(\beta) \times \sin(Z) \times \cos(\Omega - \Omega_{slope})$$

$$\text{considering: } -\cos(\Omega) = \frac{\sin(\delta) \times \cos(\Phi) \times \cos(h)}{\sin(Z)} \quad \text{for } t < 12 \text{ pm}$$

$$-\cos(\Omega) = 360 - \frac{\sin(\delta) \times \cos(\Phi) - \cos(\delta) \times \sin(\Phi) \times \cos(h)}{\sin(Z)} \quad \text{for } t > 12 \text{ pm.}$$

With θ the angle of incidence between the normal to the slope and the solar beam, β the slope angle, Ω the solar azimuth angle and Ω_{slope} the slope azimuth angle, I_{slope} the direct-beam solar radiation on a slope in terms of the beam radiation received on the horizontal surface (S).

Shading is calculated according to the Schulla algorithm (1996) for the center of each grid cell every fifteen minutes. The result is considered true for the entire grid cell and length of the sub-timestep (15 minutes). If the grid cell is in the shade, the correction factor is set to 0 as there is no direct radiation and, to avoid unrealistic values, the correction factor cannot exceed 5 (Zenith angle = 78°). The mean correction factor for one time step (of n subintervals) is defined as follows:

$$\frac{\cos(\theta)}{\cos(Z)} = \frac{\sum I \times \cos(Z) \times \frac{\cos(\theta)}{\cos(Z)}}{\sum I \times \cos(Z)} \quad (3.8)$$

Therefore, the mean potential direct radiation for one time step is given by:

$$I = \frac{\sum I \times \cos(Z) \times \frac{\cos(\theta)}{\cos(Z)} \times \Delta T}{\sum \Delta T} \quad (3.9)$$

Extrapolation of direct solar radiation (I)

I is extrapolated for each grid cell by accounting for topography effects and by calculating the ratio of actual direct solar radiation (I) to potential clear-sky radiation at the AWS (I_{sc}) as follows:

$$I = \frac{I_s}{I_{sc}} \times I_c \quad (3.10)$$

I_s being the direct radiation at the AWS and I_c the clear-sky conditions. In the calculations, it is assumed that $\frac{I_s}{I_{sc}}$ is spatially constant, I_c is calculated for each grid cell to account for the effects of its slope and aspect.

Diffuse solar radiation (D)

Total diffuse radiation is computed using the sky-view factors to account for the fraction of the hemisphere which is obstructed by surrounding topography and the additional reflected diffuse radiation from adjacent slopes:

$$D = D_0 F + \alpha_m SW_{in} (1 - F) \quad (3.11)$$

With D_0 being the diffuse radiation for an unobstructed sky, α_m the surrounding terrain mean albedo, SW_{in} the incoming shortwave radiation, F the sky-view factor (i.e., a normalized quantification of sky obstruction at a location) defined by Oke (2006):

$$F = \frac{1}{2\pi} \int_0^{2\pi} \cos(\gamma)^2 d\phi \quad (3.12)$$

γ is the elevation angle of the horizon and $d\phi$ the azimuth integration (steps of 15° in the model).

In the input file, the parameters used to split incoming shortwave radiation into its direct and diffuse components are as follows (adapted from Sicart, 2002):

- number of shade calculation per time step = 1
- Clear-sky transmissivity = 0.8
- first ratio of global radiation and direct radiation = 1 (simulations are started on a clear-sky day, this is quickly adjusted by the model)
- first ratio of direct and clear-sky direct radiation = 0.95
- direct radiation is read from files
- slope at the AWS is derived from the DEM information

3.1.3 Albedo

Because DEBAM was originally developed to model glaciers in the Northern Hemisphere, we use a key adaptation to the albedo calculations of tropical glaciers implemented by Sicart (2002). It is a modified version of Oerlemans and Knap (1998)'s albedo parameterization which accounts for the rapid alternation of accumulation and melt periods during the wet season as well as the impact of ice albedo below shallow snow depths on the surface albedo.

In the absence of precipitation, the snow albedo decreases as follows:

$$\alpha_{snow} = \alpha_{firn} + (\alpha_{fresh\ snow} - \alpha_{firn})e^{-\frac{n_j}{n^*}} \quad (3.13)$$

$$\alpha = \alpha_{snow} + (\alpha_{ice} - \alpha_{snow})\left(1 + \frac{e_s}{e_s^*}\right)^{-3} \quad (3.14)$$

n_j is the number of days since the last snowfall, n^* is the time constant of decrease in albedo which is an important parameter as it defines the decay rate of the albedo after a snowfall event. Based on albedo measurement, $n^* = 10$ days (Sicart, 2002, Sicart et al., 2011, Fig. 3.2). e_s is the snow depth and e_s^* the critical snow height below which the ice starts to influence the modeled albedo, considered here to be 6 mm w.e. (Sicart et al., 2011). This last parameter is much more difficult to estimate as the influence of the surface beneath thin snow layers depends on the snow density and dust concentration (Sicart, 2002).

During precipitation events, the albedo increases proportionally to precipitation rate (Pr):

$$\Delta\alpha = c_p Pr \quad (3.15)$$

Based on observations, $c_p = 0.02$ h/mm (Fig. 3.2, Sicart, 2002)

We chose to keep the same parameters values (n^* , e_s^* and c_p) as those found by Sicart (2002) and applied by Sicart et al. (2011) as they were derived from observations, consequently, they have a physical explanation. In addition, Beeman (2015) carried out an automatic calibration of these parameters and found that it did

not significantly improve the results due to error compensations in the model. In addition, albedo measurements should be taken with caution as their measurements over the glacier are highly sensitive to the surface slope. Besides, hourly measurements are mostly unreliable (Sicart et al., 2001).

Initial albedo values (snow, firn and ice) are allocated by providing snow and firn maps at the beginning of each simulation and the admissible values were derived based on observations (section 2.2).

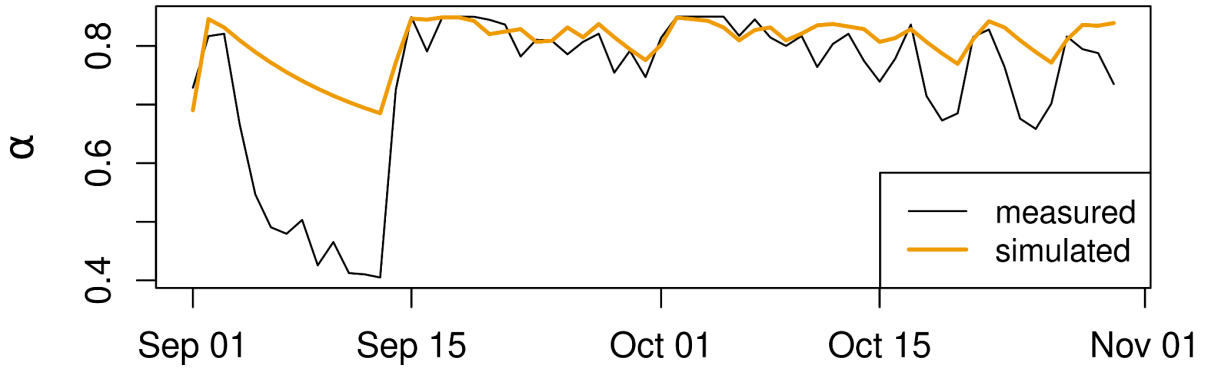


Figure 3.2. Observed and simulated albedo between September and October 1999. A time constant, $n^* = 10$ days, is selected in the simulation.

3.1.4 Longwave radiation

Both incoming and outgoing longwave radiation are considered uniform across the glacier and equal to the AWS measurements.

3.1.5 Estimation of turbulent energy fluxes

The sensible and latent turbulent heat fluxes were calculated according to the profile aerodynamic approach between the surface and the measurement level (equations 3.16 and 3.17) considering atmospheric stability based on the Monin-Obukhov similarity theory (for more details, see Hock and Holmgren, 2005).

$$H = \rho c_p \frac{k^2}{[\ln(z/z_{0w}) - \Psi_M(z/L)][\ln(z/z_{0T}) - \Psi_H(z/L)]} u(T_z - T_0) \quad (3.16)$$

$$LE = L_v \frac{0.623\rho_0}{P_0} \frac{k^2}{[\ln(z/z_{0w}) - \Psi_M(z/L)][\ln(z/z_{0e}) - \Psi_H(z/L)]} u(e_z - e_0) \quad (3.17)$$

where c_p is the specific heat capacity of air at constant pressure (1005 J/kg/K), k is the Von Karman constant (0.41), P_0 the standard atmospheric pressure, ρ_0 is the air density at P_0 , T_0 the surface temperature, e_z is the water vapor pressure at the instrument height and e_0 the surface water vapor pressure. z_{0w} , z_{0T} , z_{0e} are the surface roughness lengths of wind, temperature and water pressure respectively, and z is the instrument height. L_v is the latent heat of evaporation (2.514×10^6 J kg⁻¹).

The model considers the latent heat flux in the following way:

- LE towards the surface ($e_z - e_0 > 0$):
 - $T_s = 0 \Rightarrow$ condensation, $L =$ latent heat of evaporation ($2.514 \cdot 10^6$ J kg⁻¹)
 - $T_s < 0 \Rightarrow$ re-sublimation, $L =$ latent heat of sublimation ($2.849 \cdot 10^6$ J kg⁻¹)
- LE away from the surface ($e_z - e_0 < 0$):
 - sublimation, $L =$ latent heat of sublimation ($2.849 \cdot 10^6$ J kg⁻¹)

3.1.6 Multi-layer snow model to calculate the subsurface heat flux

This model, which is applied to the snowpack, was inspired by Greuell and Konzelmann (1994) and developed by Reijmer and Hock (2008). It was made available in 2012 (Hock and Reijmer, 2012). It solves the following thermodynamic energy equation on a vertical grid extending from the surface to a user-defined depth where the subsurface heat flux is considered to be null:

$$\rho c_{pi} \frac{\partial T}{\partial t} = \frac{\partial}{\partial z} \left(K \frac{\partial T}{\partial z} \right) + \frac{\partial Q_t}{\partial z} - \frac{\partial ML_f}{\partial z} + \frac{\partial FL_f}{\partial z} \quad (3.18)$$

With ρ the density (kg m⁻³), $c_{pi} = 2009$ J kg⁻¹ K⁻¹ the heat capacity of ice, ∂t the sub timestep considered (user-defined), Q_t the energy coming from the atmosphere (W m⁻²), M the melt rate (kg m⁻² s⁻¹), F the re-freezing rate (kg m⁻² s⁻¹), L_f the latent heat of fusion ($0.334 \cdot 10^6$ J kg⁻¹) and K the effective conductivity which can be defined according to five different parameterizations:

1. Van Dusen (1929), presented in Sturm et al. (1997):

$$K = 0.21 \cdot 10^{-1} + 0.42 \cdot 10^{-3} \rho + 0.22 \cdot 10^{-6} \rho^2 \quad (3.19)$$

2. Sturm et al. (1997):

$$K = 0.138 \cdot 10^{-1} - 1.01 \cdot 10^{-3} \rho + 3.233 \cdot 10^{-6} \rho^2 \quad (3.20)$$

3. Douville et al. (1995): $K = 2.2 \left(\frac{\rho}{\rho_{ice}} \right)^{1.88}$ (3.21)

4. Jansson (1901) presented in Sturm et al. (1997):

$$K = 0.02093 + 0.7953\rho + 1.512\rho^4 \quad (3.22)$$

5. Östin and Andersson (1991) presented in Sturm et al. (1997):

$$K = -0.00871 + 0.439\rho + 1.05\rho^2 \quad (3.23)$$

The model is driven at the surface from the energy coming from the atmosphere and at the bottom (10 m deep in our simulations) it is considered that the heat flux is null. The temperature profile is the first variable calculated by the snow model using the first two terms on the right hand side of the thermodynamics equation. Once the surface temperature reaches 0°C, the excess amount of energy in the layer is transformed into melt energy.

The water content consists of two parts: the irreducible water content (θ_{mi}) which, in this case is calculated according to Schneider and Jansson (2004) and of slush (a snow layer saturated with water). When the water content in a layer exceeds θ_{mi} , the excess percolates downwards until it reaches an impermeable layer where it is converted into runoff. Refreezing is allowed by the model if water is present in the layer and the temperature drops below 0 °C but is limited by either of the following:

- Temperature which cannot be raised above 0 °C.
- The amount of melt water available.
- The amount of pore space available.

Densification occurs even without water in the snowpack (age-dependent). This process is described in the model using the empirical relations of Herron and Langway (1980) and is dominated by the melting and refreezing in the snowpack.

On the use of the multi-layer snow model on Zongo Glacier

Over the Zongo Glacier, several studies have shown that most of the melt occurs between September and March (e.g., Sicart et al., 2011). The 25 years of measured surface mass balance in the ablation zone (between 5000 and 5200 m a.s.l.) show that the glacier lost an average of -1.32 ± 0.91 m w.e. over this period when the annual mean loss is -2.04 ± 1.31 m w.e. In addition, during these months, the surface temperatures in the ablation zone are close to the melting point making the subsurface heat flux negligible (Sicart et al., 2005, 2011; Wagnon et al., 1999).

During the dry season, the only season for which the sub-surface heat flux is non negligible as important night cooling of the surface occurs, only 9% of the annual discharge volume is observed at TUBO (based on Ramallo, 2013). This corroborates the findings of a number of studies which show that this season plays a limited role in the interannual variability of the surface mass balance (e.g. Sicart et al., 2005; 2011).

Thus, to understand the annual surface mass balance variability, it is possible to run the model over the glacier without considering the sub-surface heat flux. However, this limits our understanding of the processes which occur during the dry season: sublimation (Wagnon et al., 1999) and limited melt due to the large incoming longwave radiation deficit (Sicart et al., 2011). Not considering the sub-surface heat flux implies a systematic melt rate overestimation during the dry season which causes a bias on the annual surface mass balance.

We attempted to apply the snow module over the glacier to have a more complete representation of the surface energy balance and accurately represent the ablation processes of the dry season. However, we found errors in the spatialization routine and not enough measurements were available to validate the parameterisation of the subsurface temperature and density profiles (in both firn and snow). Therefore, we decided not to use it (detailed in section 3.6).

3.1.7 Glacier surface temperature

Because we chose not to use the snow model, glacier surface temperature is calculated at the AWS from the measured outgoing longwave radiation considering

the surface as a black body emitter and, for the current climate, it is considered constant across the glacier. Although not ideal due to the large altitudinal range of the glacier, the absence of surface temperature measurements in the upper reaches of the glacier led us to consider that it was the best option. It is worth noting that this choice implies uncertainties on the simulated turbulent fluxes and contributes to melt rate overestimations in cold periods (during the dry season).

The error linked to considering a constant surface temperature is partly compensated because both incoming and outgoing longwave radiation are considered constant across the glacier. Indeed, the incoming longwave radiation should decrease with altitude (by about 10% over the glacier, Sicart, 2002) and outgoing longwave radiation should also be lowered due to colder surface temperatures at higher altitudes.

3.1.8 Precipitation

Based on previous works (e.g. Beeman, 2015), a linear altitudinal precipitation gradient of + 10 % / 100 m is considered between 4900 and 5400 m a.s.l. Rain and snow are discriminated using an air temperature threshold of 1 °C. If the air temperature is less than or equal to 0 °C, the whole of the precipitation is considered to be snow, whereas if it gets greater than or equal to 2°C it is considered to be rain. Between the two air temperatures, a linear gradient is used to define the proportion of rain and snow.

3.1.9 Accumulation

Accumulation is accounted for by adding snowfall (in m w.e.) from the previous time step to the snow cover grid provided at the model initialization.

3.2 Model initialization and calibration

3.2.1 Model initialization

To initialize each simulation, the model must be provided with the glacier digital elevation model and corresponding topographical information (aspect, slope and sky-view factor) along with the firn limit and a snow cover map.

The nine years modeled span over 18 years (1999-2017 AD), a period during which the glacier retreated largely: it lost 12% of its surface area (Fig. 3.3) and the altitude at September 2016's glacier terminus was 55 m thinner than in 1999. To improve the simulation results, we reconstructed annual glacier extents and elevations (digital elevation models - DEM). Glacier retreat was accounted for using the annual topographical measurements except for 2011 and 2016. The 2011 glacier contour was interpolated between the measured 2010 and 2012 contours and the 2016 contour was derived from Pléiades images. Annual glacier elevations were obtained by linearly interpolating (extrapolating) the elevations from two digital elevation models (DEMs): one from 1997 based on aerial photographs (Soruco et al., 2009) and one from 2013 created from Pléiades satellite stereo-images (Cusicanqui et al., 2015).

Initial snow cover was estimated using field photographs from the beginning of the hydrological year. To limit the impact of the resulting uncertainty (precise elevation definition), each simulation was initiated considering a day at the beginning of September where the glacier was as dry as possible (between the 1st and the 8th of September depending on the year). Annual firn line altitude was obtained by comparing two different sources: Landsat images (following Rabatel et al., 2012) or field photographs taken during periods of high melt rates (which implies a small glacier snow-cover extent which provides a better estimate of the firn limit). Due to the lack of firn depth measurements, the initial firn layer was considered homogeneous and 2 m deep (Table 3.1).

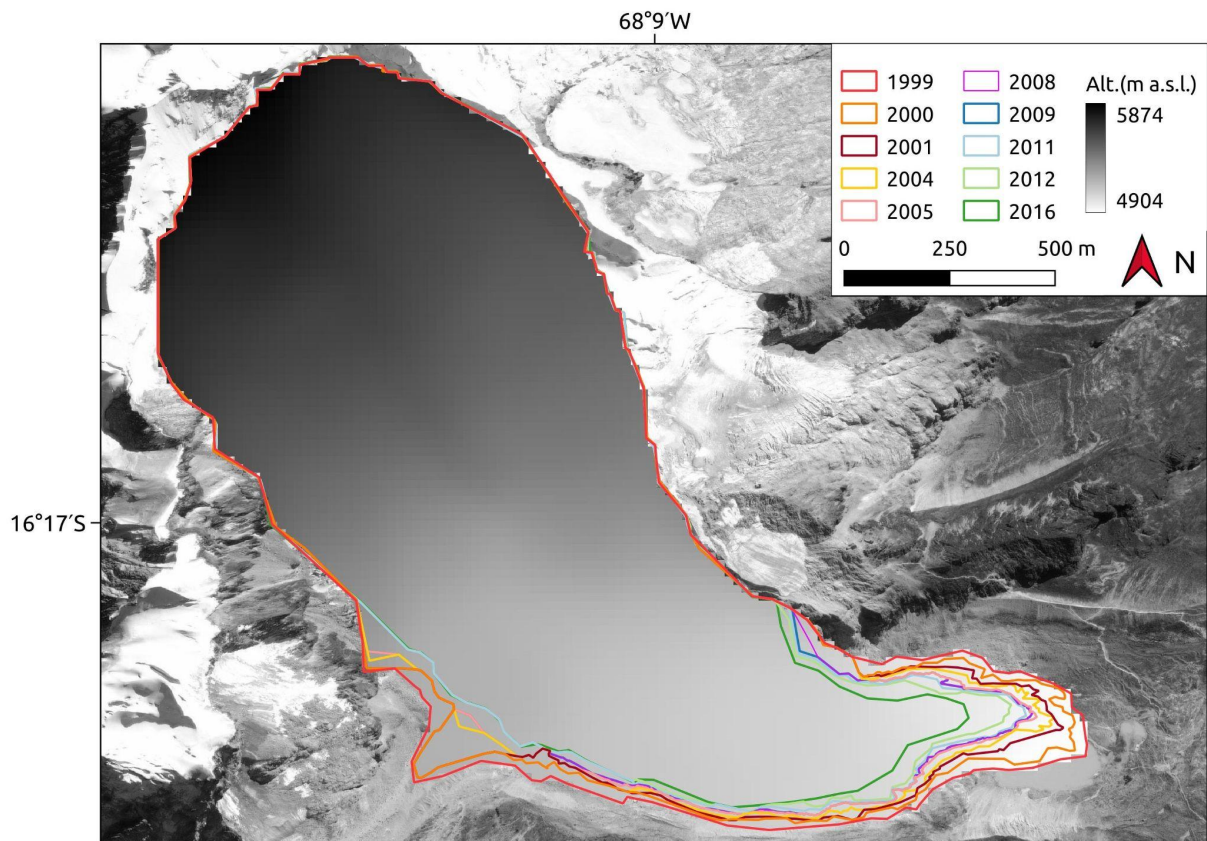


Figure 3.3. Changes in Zongo Glacier surface area between 1999 and 2016. Data comes from *in situ* topographical measurements performed within the framework of the GLACIOCLIM observatory.

Table 3.1. Simulation period and firn-line altitude for each modeled year

Year	Start date	End date	Firn altitude (m a.s.l.)	Source
1999/00	09/02/1999	08/29/2000	5100	Landsat (07/02/1999)
2000/01	09/05/2000	08/31/2001	5080	Landsat (08/05/2000)
2004/05	09/04/2004	08/30/2005	5350	Photo (12/23/2004)
2005/06	09/02/2005	08/30/2006	5250	Landsat (09/03/2005)
2008/09	09/01/2008	08/29/2009	5107	Landsat (08/27/2008)
2009/10	09/01/2009	08/30/2010	5127	Landsat (08/30/2009)
2011/12	09/01/2011	08/30/2012	5250	Photo (01/12/2012)
2012/13	09/01/2012	30/08/2013	5250	Photo (11/24/2012)
2016/17	09/01/2016	08/30/2017	5250	Landsat (08/01/2016)

3.2.2 Model calibration

We use a constant set of parameters for the whole dataset. Special emphasis was put on representing the transition period (September-November) as accurately as possible as it is a key period in controlling the annual surface mass balance (Sicart et al., 2011; Autin et al., 2022). This process implied a trade-off between accurately representing a year with little melt and one with large mass loss. Moreover, we calibrated physical parameters separately to avoid error compensation.

For the calibration we considered two contrasting years: 1999/00 ($B_{\text{meas}} = -0.08$ m w.e.) and 2004/05 ($B_{\text{meas}} = -1.90$ m w.e., which is the highest measured mass loss in the dataset). Because the model had already been calibrated over the glacier (Sicart, 2002, Sicart et al., 2011, Beeman, 2015), only the parameters described below were re-evaluated.

Maximum fresh-snow albedo values were changed as a larger observation dataset was available. The optimal value was estimated by trial and error and set to $\alpha_{\text{fresh-snow}} = 0.85$ as it allows the best fit between observed and simulated discharge during the transition season. Besides, this value is in agreement with the albedo broadband calculation (Gardner and Sharp, 2010). This value is 0.05 lower than the value considered by Sicart et al. (2011) because we calibrated the model over two contrasting years as opposed to a single year.

Turbulent fluxes were also calibrated by re-evaluating the roughness heights of momentum over ice and snow and those of temperature and humidity. The calibration was carried out over a period where eddy-covariance (EC) measurements were available and validated over another such period (July-August 2007 and June 2011, respectively). We found that the best results were found by considering roughness height of momentum ice was 26 mm and the other three to be 2.6 mm in agreement with the values found in Sicart et al. (2014). The roughness height of momentum over ice we calibrated differs largely from the value considered by Sicart et al. (2011, $z_0 = 10$ mm) because as opposed to calibrating the fluxes based on the observed discharge, we considered the turbulent fluxes derived from EC measurements. Table 3.2 summarizes the main parameters values issued from the calibration process.

Table 3.2 Summary of the retained parameter values.

Parameter	Value
Fresh snow albedo	$\alpha_{\text{fresh-snow}} = 0.85$
Firn albedo	$\alpha_{\text{firn}} = 0.6$
Ice albedo	$\alpha_{\text{ice}} = 0.3$
Clear sky attenuation	$\tau_{\text{clear-sky}} = 0.8$
Roughness height of momentum over ice	$z_{0\text{ice}} = 0.026$ m
Roughness heights of temperature, humidity and momentum over snow/firn	$z_{0\text{snow}} = z_{0\text{T}} = z_{0\text{q}} = 0.0026$ m
Precipitation gradient	$\frac{\partial P}{\partial z} = + 10\%/100\text{m}$ between 4900 and 5400 m a.s.l.

3.3 Model validation

The model was validated over the seven remaining years of the dataset by comparing simulated albedo at the AWS location, discharge, surface mass balance (both glacier-wide and by altitude) and snowline altitudes to their respective observations/measurements.

Figure 3.4 shows the simulated and observed albedo at the AWS (first column) and simulated and observed discharge (second column) for the nine years modeled. During the transition and wet seasons (September to March), globally, albedo is well-simulated resulting in acceptable melt rates and hence, simulated discharge at the outlet (Fig. 3.4, right column). In 2016/17 the simulated albedo is off, which may be because of erroneous precipitation measurements.

During the dry season (JJA), the model does not capture the intense night cooling which delays diurnal melt (Sicart, 2002; 2011) leading to a systematic melt overestimation over this period (Fig. 3.4, right column, see section 3.1). This melt rate overestimation leads to a fast disappearing snow pack which results in simulated albedo values which decay faster than the observations.

In order to assess if the melt mechanisms of the transition and wet seasons were accurately reproduced, we analyzed the contribution of the three reservoirs (snow, firn and ice) used to route meltwater to the glacier outlet. Considering the 9 year average, during the transition season, ice melting contributes to most of the simulated discharge (60%) and controls its daily variability (Fig. 3.5a). This shows that the glacier loses substantial mass during this season. Over this period, the contribution of snow and firn gradually increases as precipitation events become more frequent (as the wet season onset approaches, Fig. 1.5a) .

Conversely, during the core wet season, the discharge variability is mainly due to snowmelt and the main discharge contributors are firn and snow (77%, Fig. 3.5c, d) showing limited glacier mass loss. It is interesting to see that it is once again the melting of ice which controls the daily discharge variability. This is because it is the reservoir with the shortest storage time constant (16 hours). These results match field observations and findings of previous studies (e.g., Sicat et al., 2011). Thus, the

model seems to accurately reproduce the melt mechanisms of the transition and wet seasons.

Simulated annual glacier-wide mass balance shows a near constant mass loss overestimation compared to the measurements (Fig. 3.6). This overestimation is mostly explained by the melt overestimation during the dry season (Fig. 3.4, left column). Consequently, on average, the model overestimates the annual mass loss by 0.18 m w.e. (with $\overline{B}_{meas} = -0.88$ m w.e.).

To assess the accuracy of the simulations in the ablation and accumulation zones, we compared measured and simulated mass balance by altitude profiles (Fig. 3.7). Overall, the simulations are in agreement with the observations, in some years the simulated and observed ELA match with elevation differences ≤ 50 m (e.g., 1999/00, Fig. 3.6a) whilst for others the ELA is off by over a 100 m (e.g., 2000/01, Fig. 3.6b). Besides, depending on the year, melt is overestimated in the ablation zone (e.g., 2004/05, Fig. 3.6c) whilst on others it is underestimated (e.g., 2005/06, Fig. 3.6d). Such differences can be explained by both the constant model parameterisation and the accuracy of the precipitation measurements at the hourly time step (Sicart, 2002).

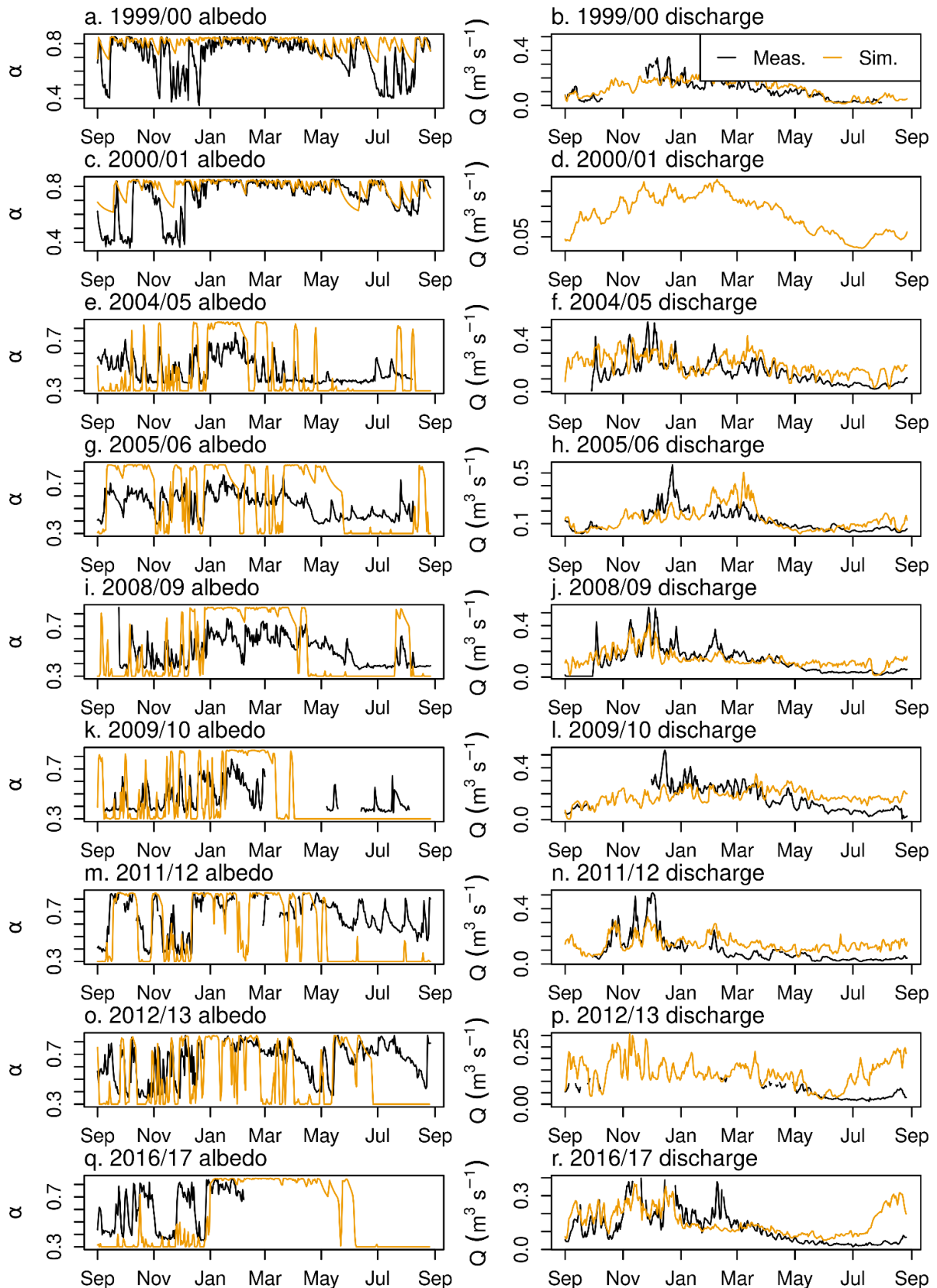


Figure 3.4 Observed (black) and simulated (orange) albedo at the AWS (first column) and discharge at the outlet (second column) for the whole simulation dataset.

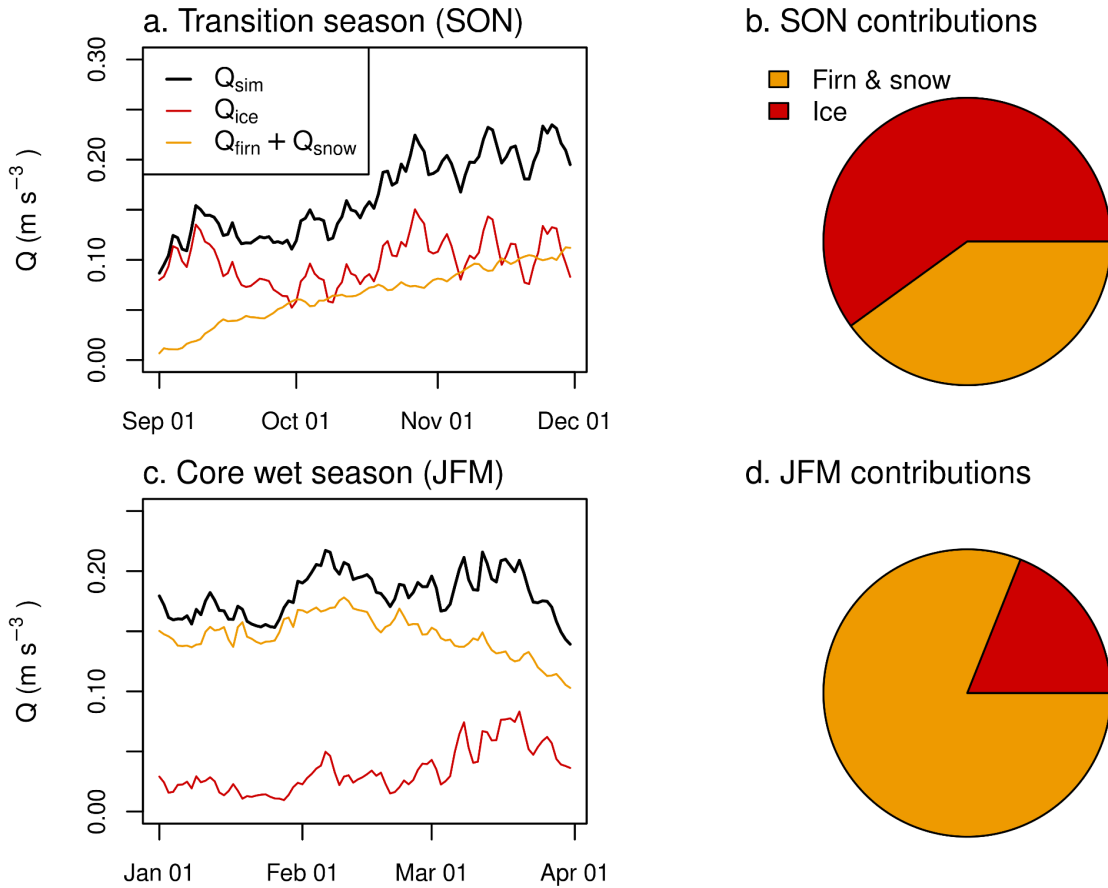


Figure 3.5 Nine year averaged simulated discharge and its components and mean contribution of each reservoir to the simulated discharge over the transition season (a and b, respectively), c and d show the same for the wet season.

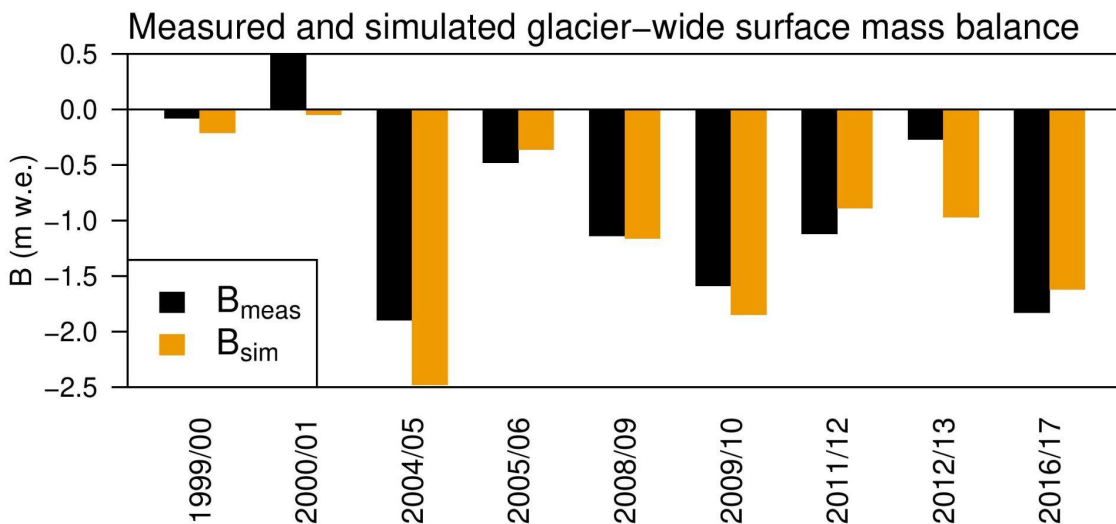


Figure 3.6 Annual measured (in black) and simulated (in orange) glacier-wide surface mass balance (B_{GW}) for the nine years studied.

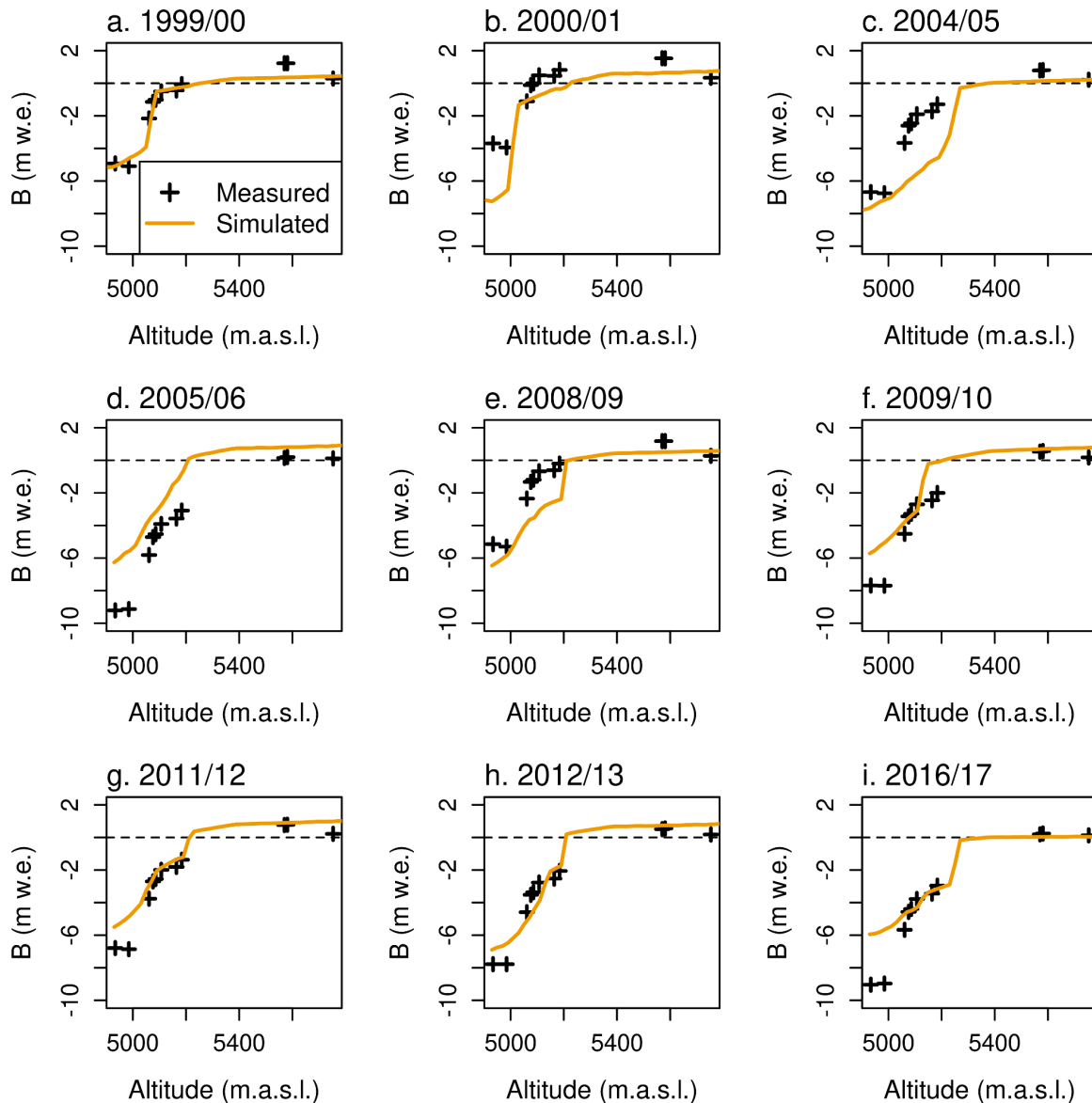


Figure 3.7 Measured (crosses) and simulated surface mass balance by altitude for the nine years studied.

3.4 Main sources of modeling errors

Due to the model's complexity, a wide variety of sources of errors can occur in the simulations. The aim here is to point out the main ones which are linked to our calibration.

Various tests carried out during the calibration process revealed that the simulated melt rates were particularly sensitive to the albedo calibration. As a whole, the model is able to represent albedo variations but the amplitude of these is sometimes off, suggesting that precipitation events are well represented but not

necessarily their intensity (Figure 3.4 right column). This is due to both albedo parameterization errors and precipitation measurement uncertainty at the hourly time scale (Sicart et al., 2002). In addition, using the same set of parameters for the whole year causes a simulation error as the snow melts faster during the wet season than during the dry season leading to different albedo decay rates which are not accounted for by the model (Sicart et al., 2011).

Inexact albedo parameterization strongly impacts simulated snow melt which leads to errors on the simulated glacier surface state (*i.e.* snow or ice, Fig. 3.8). This has a significant impact on the melt rate, as solar irradiance is often the main source of energy and its impact is mostly controlled *via* a positive albedo feedback effect (Sicart et al., 2005). In addition, errors on the simulated surface type lead to erroneous turbulent flux simulations *via* the roughness height of the momentum over the surface applied by the model.

Other sources of errors include the surface temperature, which is considered constant across the glacier. As a result, the model is not able to capture the intense night cooling of the surface in the accumulation zone, which delays the diurnal melting period, leading to a melt rate overestimation.

Furthermore, imprecise surface temperatures affect the simulated turbulent fluxes, which in turn, should affect the surface temperature, leading to rapid uncertainty propagation. This process is particularly important in the dry season when nighttime cooling of the glacier surface is at its highest.

During the dry season, turbulent fluxes may play an important role in controlling the melt rates in the accumulation zone (Wagnon et al., 2003) but these are poorly known due to the scarcity of measurements at such high altitudes and the simulation uncertainties linked to the bulk aerodynamic method (Litt et al., 2015). The model considers a constant wind speed across the glacier which results in an imprecise quantification of the sensible and latent heat fluxes. Besides, the model considers constant stability functions when these depend on the meteorological forcing (Sicart et al., 2011). Besides, not accounting for the sub-surface heat flux implies that all of the meltwater reaches the outlet as re-freezing does not occur, adding to the melt overestimation during the dry season (Sicart et al., 2011).

Another non-negligible source of error are the temperature and precipitation elevation gradients as well as the temperature threshold used to discriminate between rain and snow which are poorly known. Furthermore, the precipitation gradient is not well known as the comparison of measured amounts between rain gauges at different altitudes is complicated (due to wind exposure, precipitation phase and varying undercatch, Sicart et al., 2005; 2011). To avoid unrealistically high precipitation amounts over the upper reaches of the glacier, we decided not to apply it beyond 5400 m a.s.l.

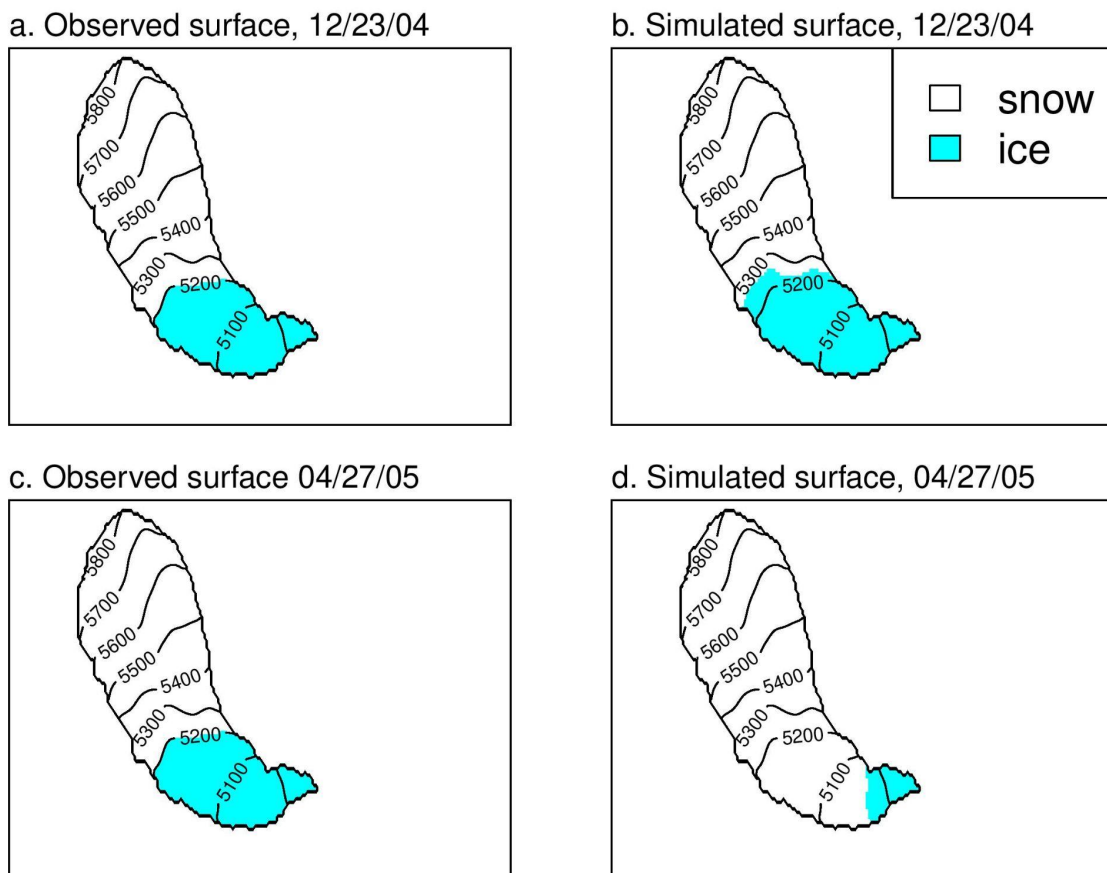


Figure 3.8 Observed and simulated glacier surface for two days in 2004/05.

3.5 Attempts at calibrating the multi-layer snow model

Using the snow module would have been of interest over the glacier as there is a buildup of cold content in the snow during dry season nights *via* the sub-surface heat flux. This cold content reduces the diurnal melting period, consequently, it has a large control on the melt rates over the dry season. Thus, despite spatialization errors in the snow model routine and the lack of information to accurately parameterize sub-surface temperature and density profiles, an attempt was made to

run a point simulation at the automatic weather station SAMA at the glacier surface (5050 m a.s.l.) to estimate the sub-surface heat fluxes in the ablation zone.

Simplified sub-surface temperatures and density gradients configuration were considered: constant snow and firn densities of 220 kg m^{-3} and 400 kg m^{-3} , respectively, and a constant initial temperature of $0 \text{ }^{\circ}\text{C}$ in the sub-surface (as various tests showed that this was corrected within a few time steps by the model and thus, had a negligible impact at the annual scale). The thermal conductivity of snow and ice was parameterized according to Östin and Andersson (presented in Sturm et al., 1997) and the irreducible water content according to Schneider and Jansson (2004).

To ensure numerical stability of the model, the uppermost layer of the vertical grid was 2 cm thick and the model was run at a 1 minute time step. In addition, to limit simulation errors, we ran simulations over a period where a lot of measurements were available (Eddy-covariance -EC measurement campaign, June 2012, Litt et al., 2014; Sicart et al., 2014). This allowed us to force the model with measured outgoing shortwave radiation (to bypass albedo parameterization errors) and, we compared the simulated turbulent fluxes to the ones derived from EC measurements.

The snow module was able to match the surface temperature derived from the outgoing longwave measurements (Fig. 3.9a) however, a number of unexplained features occurred: using the snow model largely reduces the direct and diffuse components of incoming shortwave radiation by 120 W m^{-2} (with respect to running simulations without the snow model, Fig 3.9b, c) resulting in reduced amounts of energy available for melt.

Cumulative energy balance components of the two simulations (with and without the snow model) show that the snow model does not impact the net longwave energy balance (blue lines) which is reasonable as the model is forced with the same measurements (Fig. 3.9d and e for the run without and with the snow model, respectively). However, the net shortwave energy balance is reduced with the snow model (orange lines), due to the unexplained reduced amount of solar energy reaching the surface mentioned above.

The larger spike in turbulent energy fluxes (green line) observed at the beginning of the simulation for the run with the snow model is due to the initialization

of the surface temperatures (much more negative in the first few hours of the simulation, Fig. 3.9a). Large differences are visible when considering the sum of the energy fluxes (red lines): the snow model drastically reduces the amount of melt energy (positive portion of the energy fluxes sum).

The main differences between the two runs is the simulation of the sub-surface heat flux in the latter case (cyan line, Fig. 3.9e). This flux seems to be inverted as it should be positive during night-time (the subsurface heats the surface due to the cold night $T_{\text{subsurface}} > T_{\text{surface}}$) and negative during the day ($T_{\text{surface}} > T_{\text{subsurface}}$).

As a result, with the snow model, the simulated energy balance is too small and snow does not melt at the AWS (Fig 3.9f). When the model is run for a whole year (not shown), once snow falls at the AWS, it never disappears when observations show otherwise.

Due to this unexplained behavior of the snow model, despite a large number of tests on all possible parameters (subsurface temperature and density profiles, pore space parameterization, thermal conductivity parameterizations and various vertical grid and time steps sensitivity studies) and the lack of measurements to accurately initialize density and temperature profiles, we decided not to use it. This was deemed reasonable as the aim of the first part of this PhD was to understand the climate forcings which control the inter-seasonal and inter-annual variability of the surface mass balance and, a number of studies point out that the dry season (when the sub-surface heat flux plays an important role on the melt rates) is a period of limited melt and control of the interannual surface mass balance variability (e.g., Sicart et al., 2005, 2011; Wagnon et al., 1999).

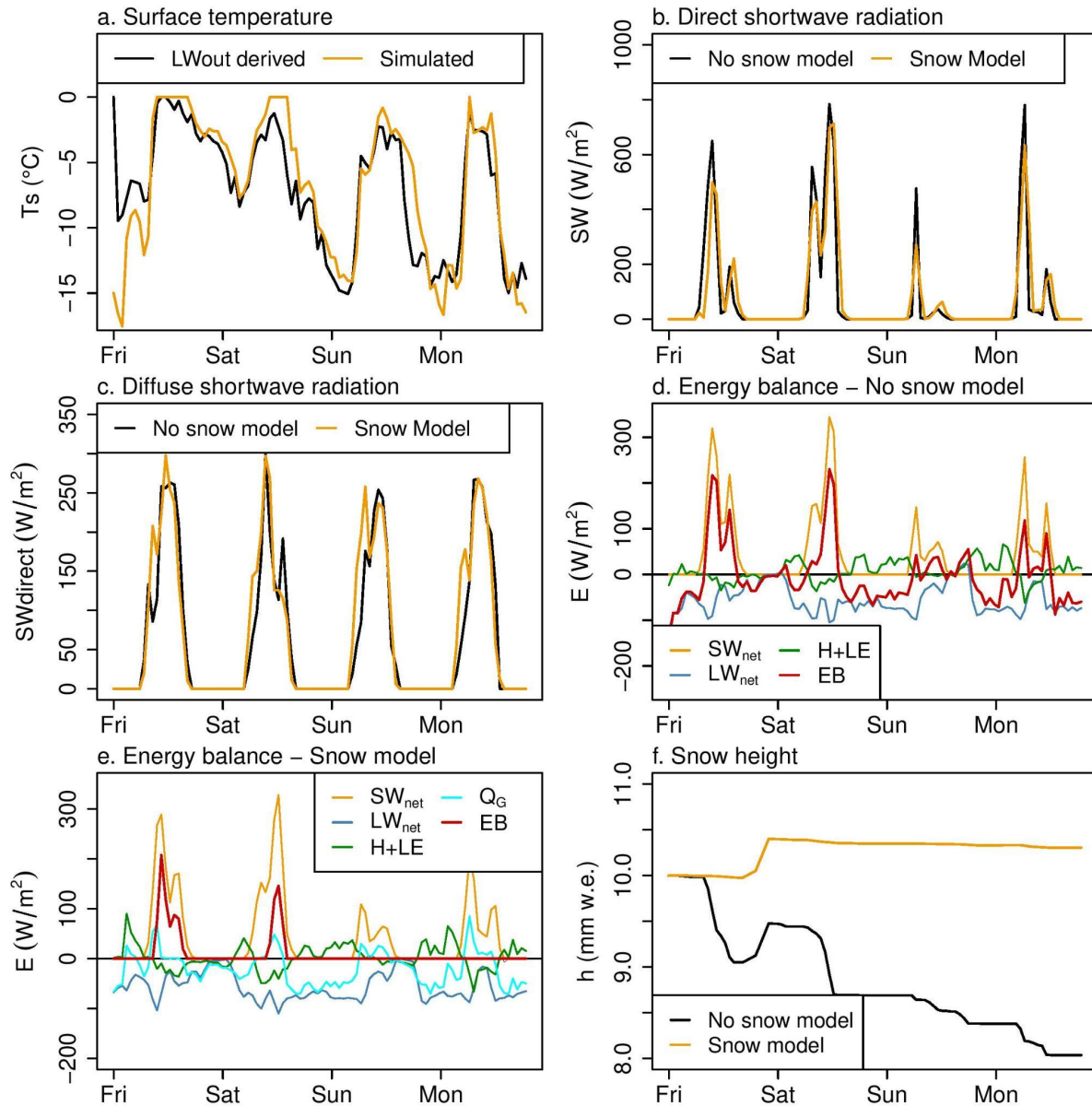


Figure 3.9 Comparison of the simulation results with or without the snow module when the model is run only at the AWS between 06/08/2012 and 06/12/2012. The results shown are surface temperature derived from LW_{out} measurements and calculated by the snow model (a), direct and diffuse shortwave radiation (b and c), energy balance without and with the snow module (d and e) and simulated snow heights at the AWS (f).

3.6 Summary

The calibration of the energy balance model was carried out over two contrasting years (little and large mass losses) and validated over the remaining 7 years of the dataset. The calibration concerned mainly the fresh snow albedo and the roughness lengths of momentum over the surface. Due to the model

complexity, to avoid error compensation, we chose a parsimonious approach with a manual calibration. The validation was carried out considering discharge, albedo, surface type and mass balance (glacier-wide and by altitude).

At the annual scale, the model systematically overestimates the mass loss primarily because the sub-surface heat flux is accounted for, as a result, the intense-night cooling which reduces the diurnal melt period during the dry season is not captured by the model.

Up to the beginning of June, the model can accurately represent albedo variations (but not necessarily their amplitude) and runoff at the outlet.

A systematic melt rate overestimation during the dry season is not problematic as observations show that only 9% of the annual discharge flows through the weir over this period. In addition, several studies have shown that this period plays a limited control on the interannual variability of the surface mass balance as little melt occurs due to a large deficit in incoming longwave radiation (Sicart et al., 2011) and because meteorological conditions favor sublimation (Wagnon et al., 1999). Thus, despite the fact that the model setting cannot fully explore the physical processes which occur during the dry season, it is still possible to study the climate controls on the seasonal and interannual surface mass balance variability.

The main sources of simulation errors come from the combined effect of the albedo parameterization and the uncertainties in hourly precipitation measurements as the main source of energy for melt is net solar radiation whose seasonal variations are controlled *via* the albedo feedback effect (Sicart et al., 2005). A consequence of the albedo simulation errors is that the simulated snow line altitude is often higher than the observations. This also affects the simulation of the turbulent fluxes (*via* roughness heights of momentum over the surface). The knowledge of the model's weaknesses allows us to assess the climate controls of Zongo Glacier intra and interannual surface mass balance variability despite a global annual-scale overestimation of the simulated melt rates.

DEBAM application over Zongo Glacier

Applied at the hourly scale over a 20 x 20 m resolution digital elevation model of the Zongo catchment (70% glacierized)

Model setting

- Constant glacier surface temperature is considered for the whole glacier
- A +10 %/100m precipitation gradient is applied between 4900 and 5400 m a.s.l.
- The sub-surface heat flux is neglected
- Based on topographic measurements, the glacier extent and surface elevation are adapted for each hydrological year.
- Initial firn and snow maps provided based on field/satellite observations

Turbulent fluxes and albedo calibration

- Calibration was carried out over two contrasting years: 1999/00, $B_{\text{meas}} = -0.08$ m w.e. and 2004/05, $B_{\text{meas}} = -1.90$ m w.e.
- Special emphasis was put on accurately reproducing the transition and wet seasons

Model validation - Comparison of modeled and observed:

- Discharge
- Albedo at the AWS
- Surface state (snow or ice)
- Glacier-wide surface mass balance and mass balance gradient with altitude

Main sources of error

- Systematic melt over-estimation during the dry season because the sub-surface heat flux is not accounted for and large uncertainties in the simulated turbulent fluxes. As a result, the observed surface cooling at night is not captured by the model.
- The simulated albedo variations follow those of the observations; however, the amplitude of these changes is sometimes off (linked to albedo parameters and precipitation measurement uncertainties).

Chapter 4 - Current climate-glacier relationships

The first part of this chapter (up to section 4.4) addresses the relationships between climate and glaciers based on the long-term data available at Zongo Glacier. Figure 4.1 shows the applied methodology to study the relationships at different time scales and considering the annual glacier-wide surface mass balance (B_{GW}) and the monthly, seasonal and annual surface mass balance values in the ablation zone (B_{Abla} , measured between 5,000 and 5,200 m a.s.l.).

Section 4.1. presents an assessment of the controls that air temperature exerts on the surface mass balance. In section 4.2, because previous studies suggest that clouds and precipitation are key drivers of melt (e.g., Sicart et al., 2005; 2011), we investigated the relationship between clouds and both precipitation and surface mass balance (Section 4.2). Section 4.3 analyzes the links between precipitation and surface mass balance considering the two precipitation datasets presented in Chapter 2.

Next, because some studies conclude that the wet season onset is a key driver of the annual surface mass balance variability (e.g., Francou et al., 1995; Sicart et al., 2011), we present an analysis of the wet season onset and duration defined by both local and regional methods (Section 4.4). We also looked at the impact of considering mean precipitation of the wet season defined according to the regional and local methods on the surface mass balance. This was done to see if it improved their relationship with the surface mass balance compared to considering a core wet season between January and March.

Section 4.5 presents the climate controls of the seasonal and interannual variability of the surface mass balance based on measurements, the multi-year application of DEBAM and cloud and precipitation sensitivity analyses. This section is presented in the form of an article that is published in the Journal of Geophysical Research: Atmospheres.

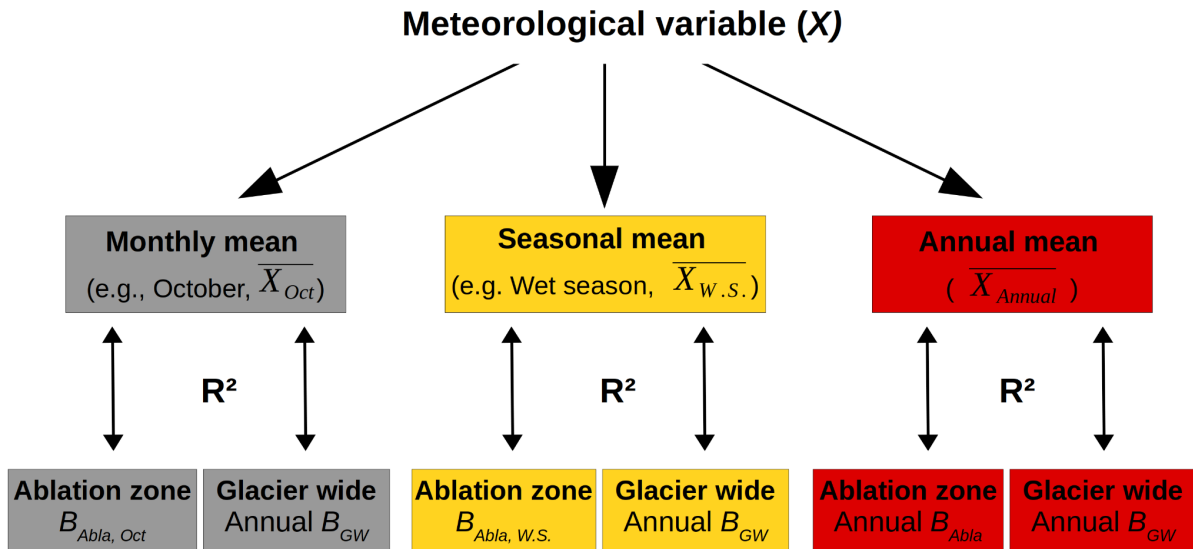


Figure 4.1. Methodology used to assess the links between measured meteorological variables and surface mass balance.

4.1 Temperature and surface mass balance

We applied the method presented in Figure 4.1 to two temperature datasets (9 years of hourly measurements at SAMA and 14 years of daily measurements at PLATAFORMA).

Monthly mean temperatures measured at SAMA in March and April share a common variance with their corresponding ablation zone surface mass balance values ($R^2 = 0.73$ and 0.64 , respectively, which passes the Student test with an error risk lower than 5%). The wet season (January-March) mean temperature is the only one which shares a significant percentage of variance with the surface mass balance in the ablation zone of the corresponding season ($R^2 = 0.58$). Annual mean temperature explains a large portion of the annual ablation zone surface mass balance variability as $R^2 = 0.62$. The mean July temperature measured at SAMA is the only one which shares a significant portion of variance with the annual glacier-wide surface mass balance ($R^2 = 0.49$).

Considering PLATAFORMA measurements, mean monthly temperature shares a significant percentage of variance (considering the Student test with an error risk lower than 5%) with monthly B_{Abla} values for seven months (September-October and December to April, $0.3 \leq R^2 \leq 0.65$). As for SAMA measurements, the wet season mean temperature is the only one which shares

significant common variance with its corresponding B_{Abla} values ($R^2 = 0.69$). Similarly, annual mean temperature shows a clear link with the annual B_{Abla} ($R^2 = 0.46$). At the glacier-wide scale, compared to temperature measurements at SAMA, the only difference is that the wet season mean temperature shares a common variance with the annual B_{GW} ($R^2 = 0.31$).

Mean temperature shares significant percentages of variance with the surface mass balance in the ablation zone during the wet season and at the annual scale because they impact the rain-snow limit. Warmer temperatures may result in rain over the lower reaches of the glacier, thereby increasing melt. Conversely, colder temperatures will lower the rain-snow limit causing snow over the lower reaches thereby reducing mass loss (*via* an albedo feedback effect).

Regardless of the time scale considered, limited shared variance between mean temperature and annual glacier-wide surface mass balance was expected as it is a typical feature of tropical glaciers (e.g. Kaser, 1999; 2000, see Chapter 1). For instance, because Zongo Glacier is at high altitudes (~4,950-6,000 m a.s.l.), temperatures are negative almost all year round over most of the glacier (see Fig. 1.5).

4.2 Cloud links with precipitation and surface mass balance

4.2.1 Linking clouds and precipitation events

Previous studies show that cloud cover and precipitation play an important role on the surface mass balance (e.g., Sicart et al., 2011). To understand how clouds and precipitation are linked, we considered the cloud radiative properties on days with precipitation ($P > 0 \text{ mm d}^{-1}$) and compared them to cloudy days without precipitation (*i.e.*, $P = 0 \text{ mm d}^{-1}$ and $F \geq 1.15$).

On days with precipitation ($P > 0 \text{ mm d}^{-1}$), precipitation and cloud cover index follow similar monthly distribution patterns (Fig. 4.2a, b). Higher precipitation amounts are linked to higher monthly CI as both occur during the wet season. Since high CI values imply low CF values, precipitation and cloud radiative forcing show opposite patterns (Fig. 4.2a, c). T_n and F follow the CF and CI patterns, respectively (not shown).

To further investigate the relationship between precipitation events and cloud radiative properties, we considered three precipitation characteristics (amounts, mean intensity and number of events $3 \geq \text{mm d}^{-1}$) at different time scales (monthly, seasonal and annual). This analysis revealed that mean cloud cover index (CI) and cloud emission factor (F) share large proportions of common variance with annual mean precipitation intensities ($R^2 = 0.65$ and 0.53 , respectively, both pass the Student test with an error risk lower than 5%). It is worth noting that the globally limited observed shared variance between cloud radiative properties and precipitation is because the cloud radiative properties are calculated at the daily scale whereas precipitation may only occur over a few hours during the day. Hence, the daily cloud radiative properties may not be representative of those which occur during the precipitation event.

Comparison of cloud radiative properties on cloudy days with and without precipitation events revealed that, on average, F and CI are higher than on days without precipitation (by 27 and 57%, respectively). Conversely, T_n and CF are lower (11% and 49%, respectively). This suggests that most precipitation events are due to warm and thick clouds, a reasonable finding as most of the precipitation events occur during the wet season.

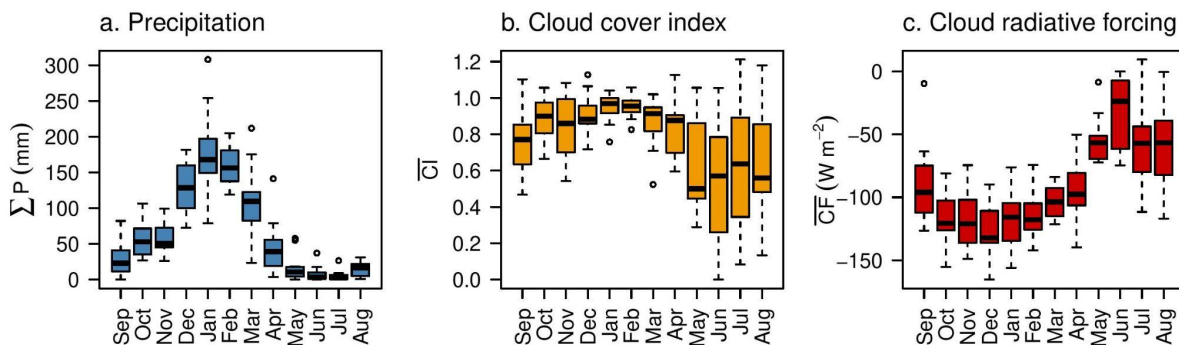


Figure 4.2. Boxplots of monthly precipitation amounts (a), mean cloud radiative forcing (b) and cloud index (c) when considering only days with precipitation.

4.2.2 Clouds and surface mass balance

This section investigates the link between the different mean cloud radiative properties and the surface mass balance following the methodology presented in Figure 4.1.

At the monthly scale, cloud radiative properties do not explain significant percentages of the variance of the two surface mass balance datasets considered ($R^2 < 0.5$, Table 4.1). March is the only month for which one of the cloud radiative properties (F) shares a large portion of common variance with both datasets. ($R^2 = 0.68$ for both monthly B_{Abla} and annual B_{GW} values). Despite poor correlations, the variables which explain the largest portion of common variance with surface mass balance are the intrinsic cloud radiative properties (F and T_n).

During the transition season cloud radiative properties do not share a common variance with B_{Abla} as opposed to those of the wet season (Table 4.2). Mean T_n values over the dry season share 55 % of common variance with B_{GW} ($R^2 = 0.55$). This may be because during this season, precipitation events are mainly due to cold air incursion which tend to bring stratospheric-type clouds which impact T_n more than F .

At the annual scale, F , T_n and CI explain large proportions of both the glacier-wide and ablation zone surface mass balance variance ($0.44 \leq R^2 \leq 0.75$). Thus, as opposed to shorter timescales, clouds play an important role on the surface mass balance variability.

Table 4.1. Determination coefficient (R^2) values obtained between the monthly mean cloud radiative properties and the monthly mass balance in the ablation zone, B_{abla} , and annual glacier-wide surface mass balance B_{GW} . The values in bold are those which are trustworthy as they pass the Student test with an error risk lower than 5% (i.e. $R^2 \geq 0.29$).

$R^2_{B \sim X}$	Monthly B in the ablation zone ($B_{Ab\Delta}$)				Annual glacier-wide B (B_{GW})			
	\bar{F}	\bar{T}_n	\overline{CF}	\overline{CI}	\bar{F}	\bar{T}_n	\overline{CF}	\overline{CI}
September	0.24	0	0	0.08	0	0.24	0.23	0.02
October	0.24	0.12	0	0.22	0.25	0	0	0.13
November	0	0	0	0	0	0.39	0.41	0.19
December	0.16	0	0.18	0	0	0.05	0.13	0
January	0.35	0	0.24	0.24	0.08	0	0.18	0
February	0.38	0	0	0.26	0.03	0	0	0
March	0.68	0.67	0	0.73	0.68	0.67	0	0.05
April	0.17	0.46	0	0.34	0.07	0	0.18	0
May	0.01	0.16	0	0.12	0.25	0	0	0.17
June	0.19	0.34	0	0.32	0.21	0.13	0	0.21
July	0.39	0.46	0.19	0.52	0.21	0.12	0	0.21
August	0	0	0	0	0.64	0.38	0	0.59

Table 4.2. Determination coefficient (R^2) values obtained between the monthly mean cloud radiative properties and the seasonal to annual mass balance in the ablation zone, $B_{ab\Delta}$, and annual glacier-wide surface mass balance B_{GW} . The values in bold are those which are trustworthy as they pass the Student test with an error risk lower than 5 % (i.e. $R^2 \geq 0.29$).

$R^2_{B \sim X}$	Seasonal/annual B in the ablation zone ($B_{Ab\Delta}$)				Annual glacier-wide B (B_{GW})			
	\bar{F}	\bar{T}_n	\overline{CF}	\overline{CI}	\bar{F}	\bar{T}_n	\overline{CF}	\overline{CI}
SON	0.07	0	0	0.03	0.17	0	0.15	0
JFM	0.51	0.20	0.03	0.62	0.20	0	0.05	0.20
JJA	0.20	0.16	0	0.26	0.24	0.55	0	0.46
Annual	0.67	0.51	0	0.75	0.47	0.14	0.18	0.44

4.3. Links between precipitation and surface mass balance

A number of studies have identified that solar radiation is often the main source of energy for fusion (e.g., Sicart et al., 2005). The amount of melt energy available is controlled by an albedo feedback effect. Hence, precipitation not only impacts the surface mass balance *via* accumulation but also *via* its impact on the albedo.

To investigate how precipitation impacts surface mass balance, we applied the method presented in Figure 4.1 to two precipitation datasets: nine years of hourly precipitation at SAMA between 1999 and 2017 and 18 years of daily precipitation at PLATAFORMA between 1992 and 2011 (Ramallo, 2013). For each dataset we considered three precipitation characteristics: precipitation amounts (P , Eq. 4.1), mean intensity (\bar{I} , Eq. 4.2) and number of events $\geq P$ mm/time step (# Events).

$$P = \sum_{t=x}^{t=x+y} P_t \quad (4.1)$$

$$\bar{I} = \frac{P}{\#Events > 0 \text{ mm.w.e.}} \quad (4.2)$$

A threshold value $P \geq 1$ mm w.e. h^{-1} was picked for the SAMA dataset because of the way on-glacier precipitation is derived (ultrasonic sensor, Chapter 2), it implies that at least 3 mm w.e. has fallen during the day. Considering a fresh-snow density of 220-250 kg m^{-3} , implies the formation of a minimum of 1.4 cm of snow over the glacier which is sufficient to impact the albedo (Sicart et al., 2002).

For the PLATAFORMA dataset, different threshold values were analyzed at the annual scale, $P \geq 3$ mm w.e. d^{-1} was retained as it is the value which resulted in the highest proportion of common variance between the number of events and the annual glacier-wide surface mass balance ($R^2 = 0.57$).

Links with the annual glacier-wide surface mass balance (B_{GW})

Because the results were similar for both precipitation datasets (with lower correlations for the longer PLATAFORMA dataset), we present the results obtained with SAMA measurements.

At the monthly scale, the number of events and monthly amounts share significant proportions of common variance with B_{GW} for June and August ($R^2 > 0.5$) as they are colder months during which glacier fresh snow cover lasts longer. Conversely, mean monthly precipitation intensities do not share common variance with the annual glacier-wide surface mass balance (maximum $R^2 = 0.35$ in November).

At the seasonal scale uneven determination coefficients are observed (Table 4.3). During the transition period the precipitation characteristics share little common variance with B_{GW} ($0.16 < R^2 < 0.30$). This is due to the large interannual variability of the precipitation over this season ($\overline{P_{SON}} = 0.39 \pm 0.14$ m w.e.). The limited common variance observed during the core wet season ($R^2 < 0.15$) is explained by the large precipitation amounts which have a small interannual variability ($\overline{P_{JFM}} = 0.81 \pm 0.1$ m w.e.). Finally, the dry season is the only season for which significant shared variance between B_{GW} and all the assessed precipitation characteristics is observed (*i.e.* the R^2 obtained pass the Student test with an error risk lower than 5%).

At the annual scale, all the precipitation characteristics share significant proportions of common variance with B_{GW} as all the determination coefficients pass the Student considering an error risk lower than 5% (Fig. 4.3). This highlights the strong potential precipitation control on the surface mass balance (*via* accumulation and albedo feedback effects).

Table 4.3. Summary of the determination coefficients (R^2) obtained between the annual glacier-wide surface mass balance and seasonal precipitation characteristics.

R^2_{B-X}	Transition period	Core wet season	Dry season
#Events ≥ 1 mm/h	0.30	0.13	0.60
P_{Season} (m w.e.)	0.20	0.05	0.59
\bar{i} (mm/h)	0.16	0.03	0.72

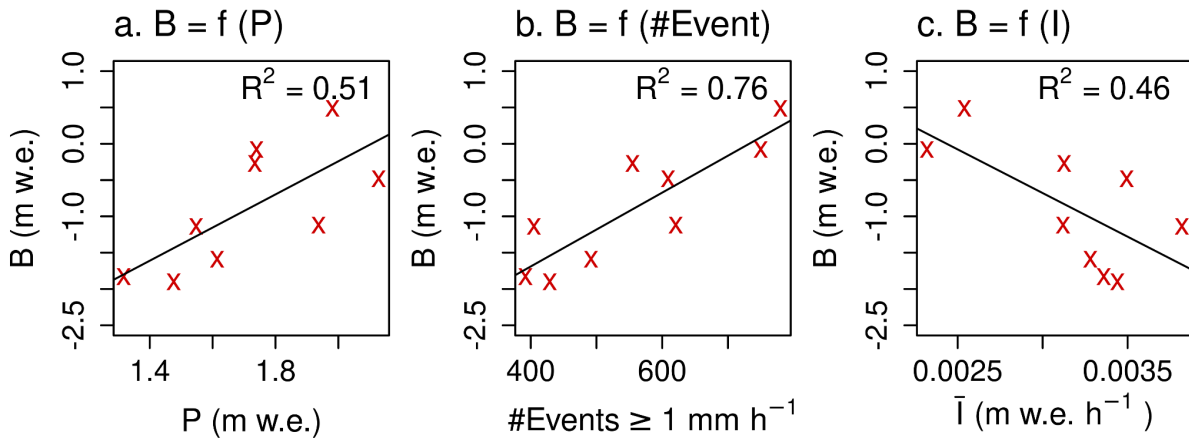


Figure 4.3. Glacier-wide annual surface mass balance as a function of annual precipitation amounts (a), #events ≥ 1 mm/h (b) and mean annual intensity (c) along with their corresponding determination coefficients (R^2).

Links with the surface mass balance in the ablation zone (B_{Abla})

The results presented here are those obtained with the daily precipitation measured at PLATAFORMA. Over 50% of the observed monthly variability of B_{abla} can be explained by the monthly precipitation amounts for September, October, March, June and August (Fig. 4.4a, b, g, j & i, $R^2 > 0.5$, which passes the Student test with an error lower than 5%). Similarly, for these months, the number of events $\geq 3 \text{ mm d}^{-1}$ can explain up to 70% of the interannual variability of monthly B_{abla} (not shown).

In contrast, the mean monthly precipitation intensities do not share much common variance with B_{abla} ($R^2 \leq 0.37$) which may be because it is a derived precipitation characteristic which is highly sensitive to the uneven rain gauge undercatch (undercatch is higher when precipitation events occur under windy conditions especially for solid precipitations, eg., Sicart et al., 2007). Similarly, all the studied monthly precipitation characteristics do not share a common variance with the annual surface mass balance in the ablation zone.

The dry season is the only season for which seasonal precipitation characteristics explain most of the variance of the seasonal surface mass balance values in the ablation zone ($R^2 \geq 0.58$). The highest percentage of common variance obtained is when considering mean precipitation intensities ($R^2 = 0.72$). As for the glacier-wide surface mass balance, the precipitation events explain large portions of

the variance of B_{Abla} since it is a cold period of the year with scarce precipitation events. Besides, when they occur, they usually are due cold surges (Sicart et al., 2016) which result in large amounts of snow falling over the glacier. Because melt rates are low over this season (e.g. Sicart et al., 2005), snow cover lasts longer than in other seasons resulting in a sustained albedo feedback effect. As a result, precipitation events during the dry season have the capacity of lowering melt rates over a longer time than when they occur in the other seasons.

When considering seasonal precipitation characteristics and annual B_{Abla} , the highest percentages of common variance are obtained with the number of events above 3 mm d^{-1} and the precipitation amounts of the core wet season ($R^2 = 0.45$ and 0.37 , respectively).

At the annual scale the variable showing the largest proportion of shared variance is the number of events ($R^2 = 0.62$, Fig. 4.5a) followed by precipitation amounts ($R^2 = 0.59$, Fig. 4.5b) highlighting the importance of precipitation events and associated amounts on the surface mass balance. Mean precipitation intensities are, on the other hand, not correlated to the annual B_{Abla} (Fig. 4.5c).

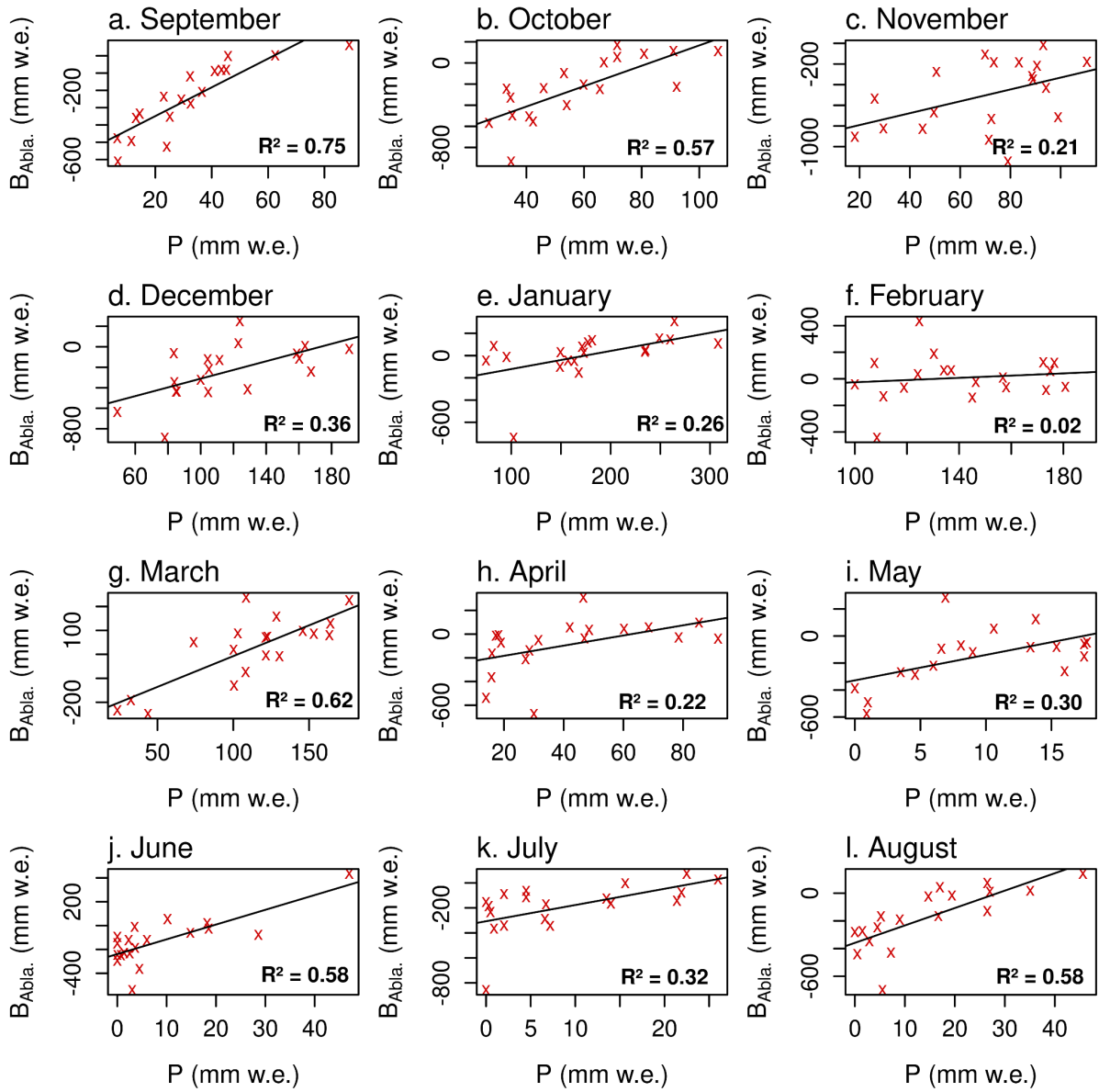


Figure 4.4. Correlation between monthly precipitation amounts and measured surface mass balance in the 5000-5200 m a.s.l. elevation range considering 19 years of data (1991/92 - 2009/10).

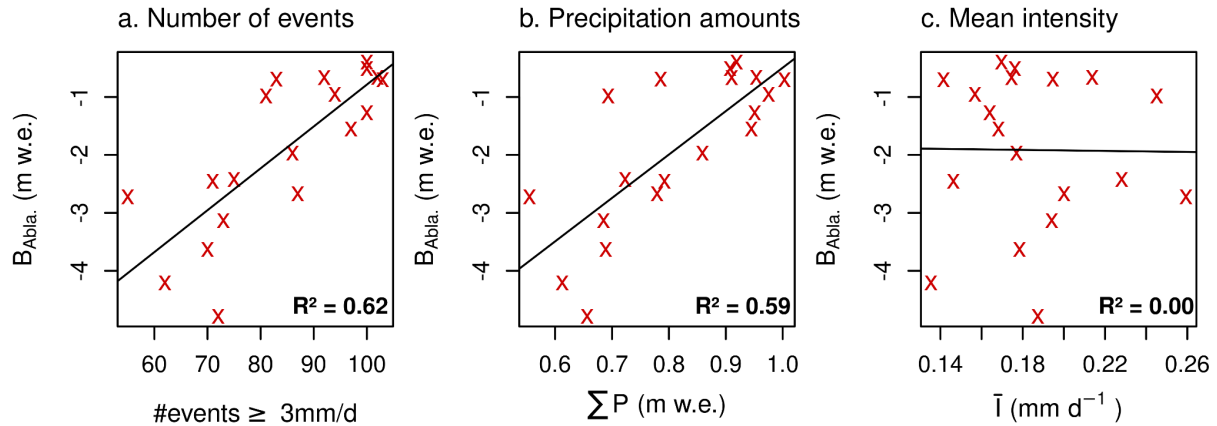


Figure 4.5. Linear regression between the annual surface mass balance in the ablation zone (B_{Abla}) and annual number of events $\geq 3 \text{ mm d}^{-1}$ (a), precipitation amounts (b) and mean precipitation intensity (c).

4.4 Impact of the wet season onset on the annual surface mass balance

Because some studies suggest that it is a key control of the annual surface mass balance variability (e.g., Francou et al., 1995; Sicart et al., 2011), we investigated the relationship between the wet season onset and the surface mass balance. The arrival date (onset) of the wet season can be defined by a number of methods both local (considering measurements carried out in the vicinity of the glacier) and regional (considering larger geographical domains). A comparative study of the onset and durations defined by both local and regional methods is presented. It is followed by an assessment of the seasonal precipitation characteristics calculated over the wet season defined by the methods and over a transition season which ends the day before the wet season onset date.

4.4.1 Methods used to define the wet season

Regional methods

The two regional methods used follow the methodology proposed by Fu et al. (2013): the wet season onset is when the first pentad (5 days average) for which the precipitation amount is greater than the annual mean precipitation and for which the precipitation amount is above the annual pentad mean for the following 6 out of 8

pentads. The demise date of the wet season is the first pentad for which this condition is not respected anymore.

The first dataset (method 1) is the result of the application of the method over the Porto Velho and Madeira catchment (Gutierrez-Cori et al., 2021, Fig. 4.6, blue outline) considering the following precipitation data:

- Improved 1° gridded historical precipitation analysis over the Brazilian and Bolivian Amazon for the period 1978-2007 provided by the National Oceanic and Atmospheric Administration Climate Prediction Center (NOAA - CPC)
- 1° gridded daily precipitation data over the Brazilian and other northern Amazonian countries for the period 1940-2011 from the NOAA Climate Diagnostics center (NOAA - CDC)
- Two regional daily rainfall datasets based on a network of 300-450 rain (1979-2013)
- TRMM satellite data for overlapping periods

The second dataset (method 2, Arias et al., 2015) considers a different domain over Tropical South America (50-70°W, 15-5°S, Fig. 4.6, red outline). As opposed to method 1, it considers that if the condition of 6 out of 8 pentads cannot be met, then 5 out of 6 pentads is considered. The method was applied considering 1° gridded daily precipitation data from the NOAA CPC between January 1978 and December 2007 (Silva et al., 2007) and the SA24 version of the NOAA CDC between January 1940 and December 2011 (Liebmann & Allured, 2005).

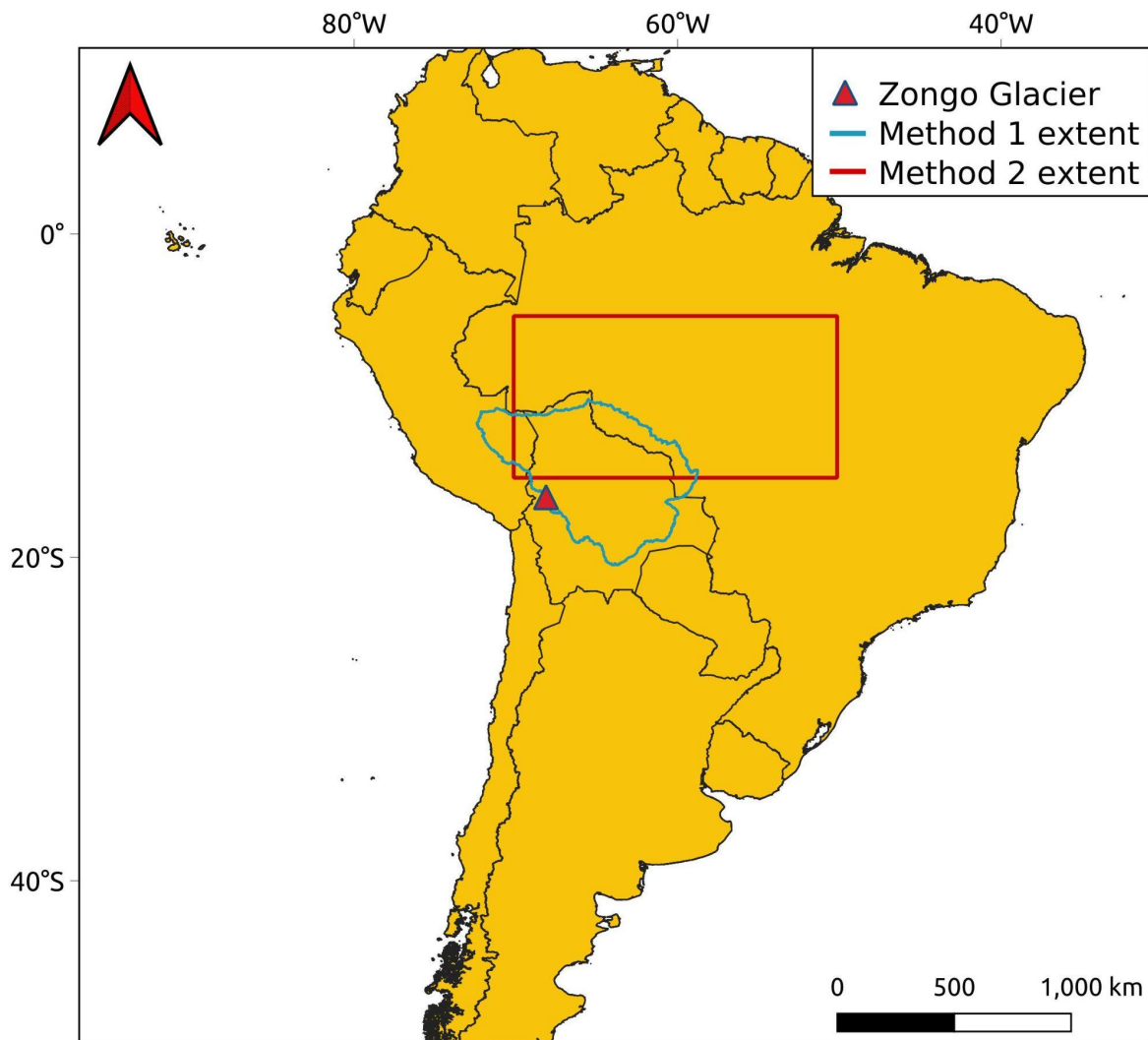


Figure 4.6. Geographical extents over which the two regional methods are applied.

Local methods

Two of the local methods used are from Ramallo (2013) and are applied over daily precipitation measurements from PLATAFORMA between 1992 and 2010 (18 years):

- The pentad method, considering the onset date when 3 out of 4 pentads are above 4 mm/5d and 4 out of 6 below 1 mm/5d for the demise date (Fig. 4.7a).
- Number of rainy days over a 21-day moving window (NoR) considering onset and demise dates when there are 13 days out of 21 with $P \geq 1 \text{ mm d}^{-1}$ and 5 out of 21 days, respectively (Fig. 4.7b).

The third method is based on the cloud cover index values as it is a suitable indicator of the wet season (section 4.2.1). Following Beeman (2015), the onset is defined by considering the 66th percentile of the cloud cover index threshold ($CI = 0.84$). When the 14-days moving average of CI values cross it, we consider that the wet season starts. The demise is when the 14-days average significantly drops (usually between March and April, Fig. 4.8). The threshold is the 66th percentile of CI because it is considered that at least a third of the cloudiest days in the year should be concentrated in the core wet season (Beeman, 2015).

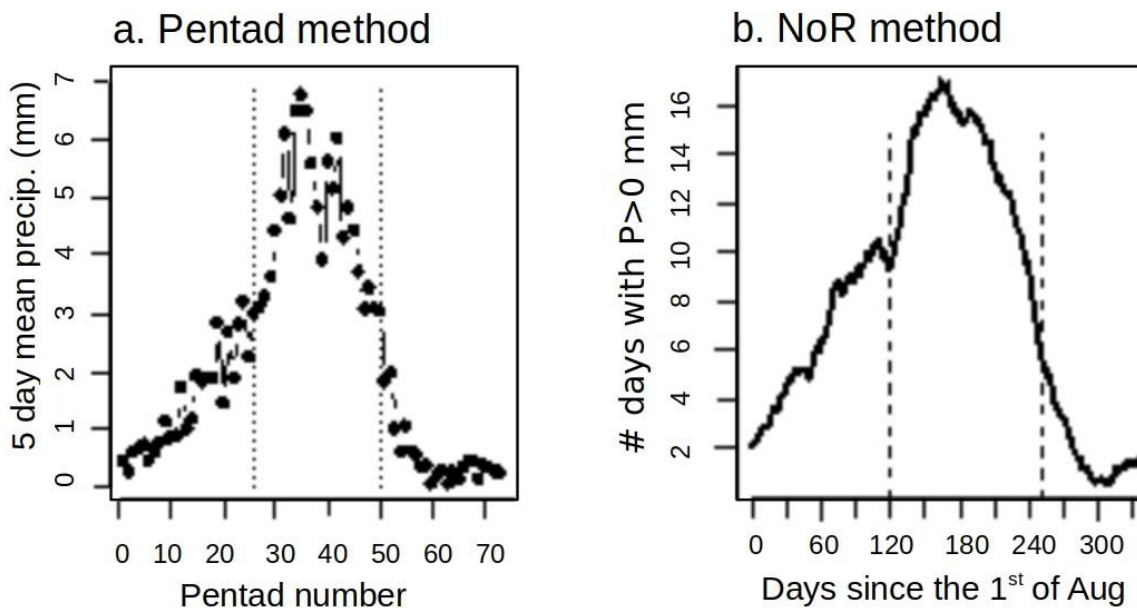


Figure 4.7. Wet season onset and demise dates considering the 19 year measured cycle (1992-2010) at PLATAFORMA with the pentad (a), number of rainy days (b). The dashed lines represent the onset and demise dates of the mean cycles. Source: Ramallo (2013).

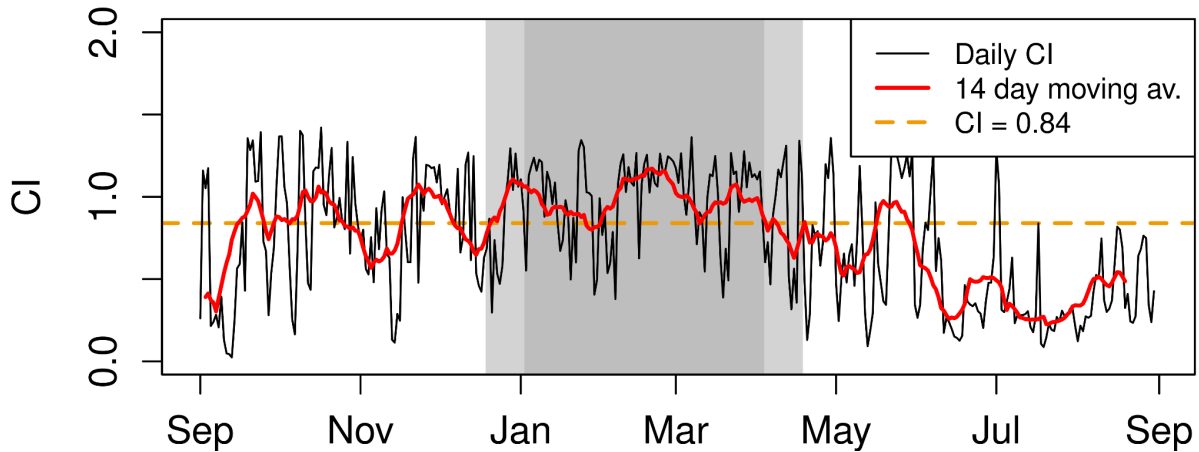


Figure 4.8. Daily Cloud cover index (CI) for the year 2016/17 (in black) along with the 14 days centered moving average (red line). The dashed orange line shows the threshold value and the gray rectangle shows the wet season defined according to the CI method. The light gray rectangles on each side show the 7 days error bars linked to the method.

Comparison of regional methods

On average, according to method 1, the wet season starts around mid-October and lasts about 6.5 months whereas with method 2, it starts early November and lasts about 5 months. They show large onset date differences (their respective distributions hardly overlap, Fig.4.9a) with a larger variability observed with method 2. Method 1 yields longer wet seasons which have a large interannual variability (Fig. 4.9b). Hence, the comparison of onset dates and duration over 16 years revealed that the two do not share a common variance ($R^2 = 0$). Such large discrepancies are probably linked to the domain sizes considered by each method.

Comparison of local methods

The Pentad method is the local method which results in the highest interannual variability of onset and duration (Fig. 4.9c, d). The two methods from Ramallo (2013) have a similar mean arrival date - towards the beginning of November but do not share a common variance ($R^2 = 0.03$). The cloud cover index method shows a much later onset (December 4th on average) but is the method for which the highest onset date correlations are observed ($R^2 = 0.18$ when considering the NoR method). Finally, they all yield similar wet season mean durations (115-120 days, Fig. 4.9d).

Comparison of local and regional methods

Comparison of the monsoon onset and duration between regional and local methods has shown that they are mostly poorly linked. The highest percentage of common variance (obtained over 15 years) is between the cloud index method and method 1 ($R^2 = 0.52$) which suggests that local clouds are better linked to large scale conditions than local precipitation. This is probably because clouds cover a larger spatial extent and have a higher occurrence than precipitation events.

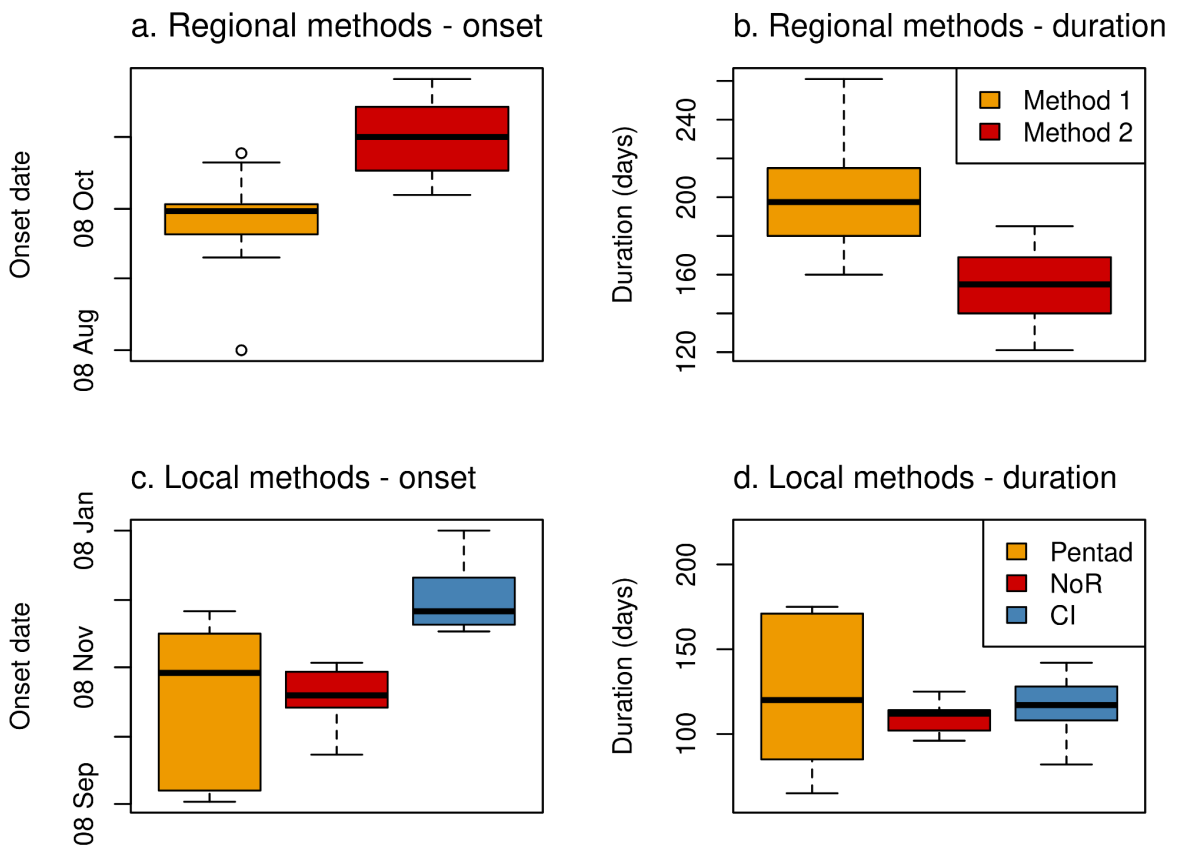


Figure 4.9. Wet season onset (a.) and duration (b.) for the two regional methods assessed. On plot a, the axis ranges between August 8 and December 6. The onset date and duration obtained with the local methods are shown on plots (c) and (d), respectively.

4.4.2 Impact of the wet season onset on the surface mass balance

A number of authors state that the wet season onset is a key control of the annual surface mass balance variability (e.g., Francou, 1995; Sicart et al., 2011). To test this hypothesis, we looked at how the wet season onset impacts seasonal

precipitation characteristics and how these were linked to the glacier-wide surface mass balance.

Onset date and glacier-wide surface mass balance (B_{GW})

Wet season onset dates and B_{GW} share little common variance. For local methods, the highest determination coefficient obtained is $R^2 = 0.4$ when considering the cloud cover index method over 14 years. Onset dates determined from regional methods do not share a common variance with the surface mass balance ($R^2 = 0.02$ with method 1 over 14 years).

Wet season precipitation and B_{GW}

In order to see if seasonal precipitation characteristics calculated over a wet season defined by the methods presented above result in an increased percentage of common variance with the annual glacier-wide surface mass balance, we considered the PLATAFORMA precipitation dataset.

A significant percentage of common variance was found between the mean number of events $\geq 3 \text{ mm d}^{-1}$ and the wet season onset determined with method 1 ($R^2 = 0.43$). This is probably because this method splits the year in two, leading to up to 90 % of the annual number of events taking place during the wet season. When considering local methods, the cloud cover index method is the only one for which seasonal precipitation characteristics share a common variance with the annual glacier-wide surface mass balance ($R^2 = 0.64$ and 0.33 when considering the #events $\geq 3 \text{ mm d}^{-1}$ and the seasonal amounts, respectively, Table 4.4).

Impact of seasonal precipitation calculated over a transition season which ends the day before the wet season onset on B_{GW}

The wet season onset has an impact on the transition season's demise. We analyzed the impact of considering precipitation characteristics between the 1st of September and the day before the wet season onset defined by local methods. Regional methods were not considered as they shortened the transition season by more than a month.

Considering a transition season with a varying demise date (linked to the interannual variability of the wet season onset) does not yield statistically significant

relationships (Table 4.5). The only relationship which passes the Student test with an error risk lower than 5% is when considering the #events $\geq 3 \text{ mm d}^{-1}$ and the wet season onset defined using the cloud cover index method ($R^2 = 0.23$).

Thus, compared to considering fixed transition and core wet seasons, annually varying seasons based on methods such as the ones presented here does not significantly increase the percentage of common variance between seasonal precipitation characteristics and annual surface mass balance. Besides, the wet season onset dates do not share a common variance with the annual glacier-wide surface mass balance. Therefore, we considered the following seasons:

- A transition season between the 1st of September and the 30th of November (SON).
- A core wet season between the 1st of January and the 31st of March (JFM). We consider the onset to be January as it is the first whole month for which the wet season has started (Fig. 4.10).
- April and May are considered to be a transition period between the wet and dry seasons. The high interannual precipitation variability observed during this period is linked to the interannual variability of the wet season demise date (Fig. 4.15).
- A dry season between the 1st of June and the 31st of August (JJA).

Table 4.4. Summary of the determination coefficients obtained for three precipitation characteristics over the wet seasons whose onset and demise dates are defined according to different methods (both local and regional). For the regional methods, only the results obtained with method 1 are presented as it is with this method that the highest R^2 values were found.

Method		$R^2_{B \sim P_{amounts}}$	$R^2_{B \sim \#Events \geq 3 \text{ mm } d^{-1}}$	$R^2_{B \sim \bar{I}}$
Regional	Method 1	0	0.43	0.35
Local	Pentad	0.13	0.11	0.07
	# rainy days (NoR)	0.22	0.25	0.07
	CI	0.33	0.64	0.29

Table 4.5. Summary of the determination coefficients obtained for seasonal precipitation amounts, number of events $\geq 3 \text{ mm } d^{-1}$ and mean seasonal intensity (\bar{I}) over the transition seasons whose demise date is defined as the day before wet season onset derived from different methods (local methods only).

Method	$R^2_{B \sim P_{amounts}}$	$R^2_{B \sim \#Events \geq P}$	$R^2_{B \sim \bar{I}}$
Pentad	0.01	0.02	0.06
# rainy days (NoR)	0.03	0.04	0.08
CI	0.13	0.23	0.04

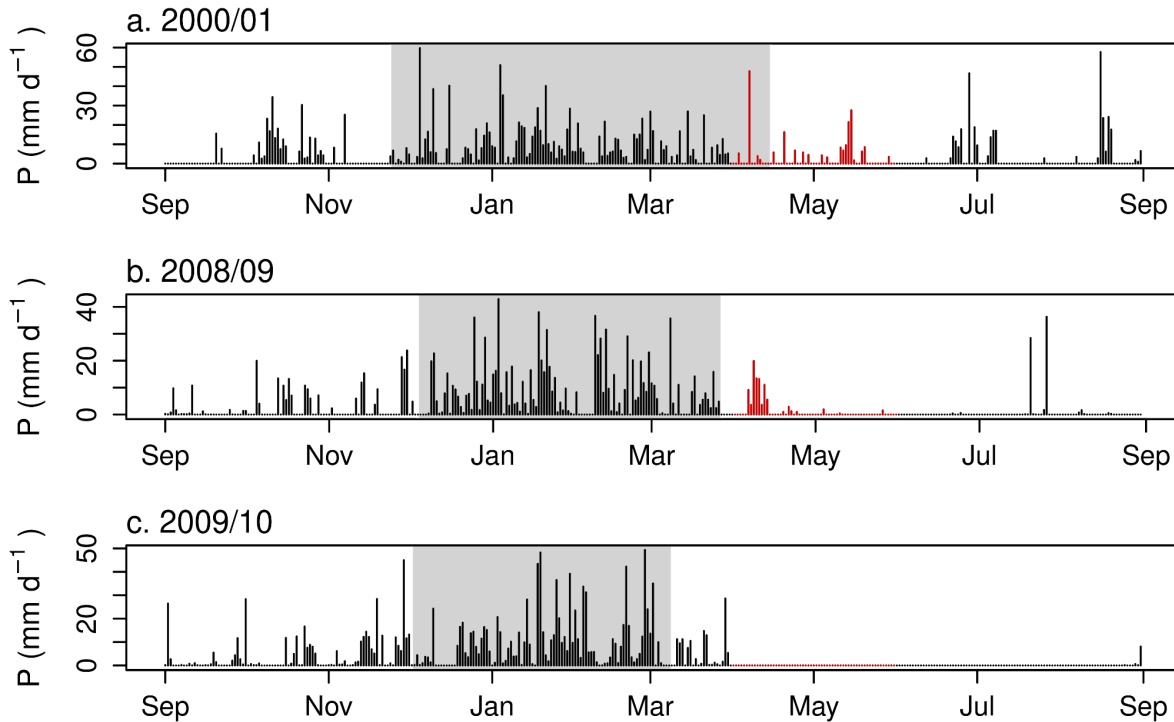


Figure 4.10. Illustration of the wet season's demise for three contrasting years. In red at the April-May precipitation events. The gray boxes show the monsoon onset and duration for each year defined using the cloud cover index method.

4.5 Climate controls of the interseasonal and interannual variability of the surface mass balance.

This section summarizes all the findings on the climate controls of the surface mass balance at both seasonal and annual scales. It is presented in the form of the article published in the *Journal of Geophysical Research: Atmospheres*. The full reference list used in the article has been integrated into the reference list at the end of the manuscript.

JGR Atmospheres

RESEARCH ARTICLE

10.1029/2021JD035410

Key Points:

- Seasons over Zongo Glacier can be identified using the distribution of the cloud radiative forcing
- October and November play a strong control on the interannual surface mass balance variability of Zongo Glacier
- Distribution of the precipitation events in time is key in controlling the melt rate

Supporting Information:

Supporting Information may be found in the online version of this article.

Correspondence to:

P. Autin,
philemon.autin@univ-grenoble-alpes.fr

Citation:



Autin, P., Sicart, J. E., Rabatel, A., Soruco, A., & Hock, R. (2022). Climate controls on the interseasonal and interannual variability of the surface mass and energy balances of a tropical glacier (Zongo Glacier, Bolivia, 16°S): New insights from the multi-year application of a distributed energy balance model. *Journal of Geophysical Research: Atmospheres*, 127, e2021JD035410. <https://doi.org/10.1029/2021JD035410>

Received 14 JUN 2021
Accepted 22 MAR 2022

Author Contributions:

Conceptualization: P. Autin, J. E. Sicart, A. Rabatel
Data curation: A. Soruco
Methodology: P. Autin, J. E. Sicart, A. Rabatel
Software: R. Hock
Supervision: J. E. Sicart, A. Rabatel, R. Hock
Validation: P. Autin
Visualization: P. Autin
Writing – original draft: P. Autin
Writing – review & editing: P. Autin, J. E. Sicart, A. Rabatel, R. Hock

Climate Controls on the Interseasonal and Interannual Variability of the Surface Mass and Energy Balances of a Tropical Glacier (Zongo Glacier, Bolivia, 16°S): New Insights From the Multi-Year Application of a Distributed Energy Balance Model

P. Autin¹ , J. E. Sicart¹, A. Rabatel¹, A. Soruco², and R. Hock^{3,4} 

¹University Grenoble Alpes, CNRS, IRD, Grenoble-INP, Institut des Géosciences de l'Environnement (IGE, UMR 5001), Grenoble, France, ²Facultad de Ciencias Geológicas, Universidad Mayor de San Andrés, La Paz, Bolivia, ³Department of Geoscience, Oslo University, Oslo, Norway, ⁴Geophysical Institute, University of Alaska, Fairbanks, AK, USA

Abstract The application of a distributed energy balance model over nine years at an hourly time step to a 20 × 20 m grid cell over Glacier Zongo (Bolivia, 16°S) enabled assessment of the climate factors that control the interseasonal and interannual variability of its surface mass balance. The model was validated by comparing the measured and simulated discharge at the outlet, albedo at the Automatic Weather Station, surface state and annual mass balance both glacier-wide and as a function of altitude. Analysis of the mean monthly energy fluxes highlighted the importance of the meteorological conditions over October and November on the variability of the annual surface mass balance. Two sensitivity analyses are presented, one of the distribution of precipitation over time which maintains a physical coherence between the different meteorological variables and one of the impact of prolonged periods of intense cloud radiative forcing on the surface mass balance. The distribution of precipitation events over time and their associated amounts are the main drivers of the interannual variability of the surface mass balance via an albedo feedback effect. Additionally, prolonged periods of negative cloud radiative forcing, specifically over the month of November, notably reduce the melt rate.

Plain Language Summary This study aimed at identifying the meteorological variables which control the seasonal and annual melt rates of a tropical glacier in Bolivia considering nine years of measurements at the hourly timescale. The analysis of the energy fluxes at the weather station has shown that the period between the austral winter and summer is the period during which most melt can be generated making it key in defining the annual melt rates. The analysis of the impact of measured meteorological variables on the melt rate has shown that it is the solar energy that controls most of it. The amount of solar energy available for melt is defined by the state of the glacier surface (snow, ice, debris) which controls the amount of reflected energy. In this context, the frequency of the snowfall events plays a key role in controlling the melt as frequent events imply a whiter glacier which is able to reflect most of the incoming solar energy. Similarly, because clouds can block large portions of solar energy, sustained cloud periods can play an important role in reducing the melt rate.

1. Introduction

In recent decades, both field observations and remote sensing have shown a trend of glacier retreat in tropical South America (e.g., Dussailant et al., 2019; Kaser, 1999; Masiokas et al., 2020; Rabatel et al., 2013; Seehaus et al., 2020; Soruco et al., 2009; Vincent et al., 2018), with specific mass losses over the last decades even larger than the global mean (e.g., Rabatel et al., 2013; Zemp et al., 2019). Previous studies have linked these mass changes to the high sensitivity of tropical glaciers to changes in moisture-related variables including precipitation, albedo, and cloudiness rather than directly to air temperature (e.g., Sicart et al., 2005). Bradley et al. (2009) found statistical correlations between mass changes and air temperature for the Quelccaya Ice Cap, however, these might result from the indirect effect of air temperature on the phase of precipitation (e.g., Gurgiser, Marzeion, Nicholson, Ortner, & Kaser, 2013). Hence, air temperature increase does not increase melt directly, but it may change the local hygric regime. In addition, most studies conducted to understand the complex climate-glacier

relationships in the tropics have been carried out with data acquired over a short period (Hurley et al., 2016; Litt et al., 2014; Maussion et al., 2015; Mölg et al., 2008, 2009; Prinz et al., 2016; Sicart et al., 2005; Wagon et al., 1999).

Glacier surface mass balance is controlled by the climate via energy and mass fluxes between the atmosphere and the glacier surface (e.g., Cuffey & Paterson, 2010). These fluxes are modulated by conditions specific to tropical glaciers, including small seasonal air temperature variations, marked cloud and precipitation seasonality, very high elevations, and pronounced sublimation (e.g., Nicholson et al., 2013; Prinz et al., 2016; Sicart et al., 2011). Understanding the relationship between mass and energy balances and identifying the key meteorological variables that control the glacier surface mass balance is crucial to better estimate past and future changes of these glaciers and their consequences, for example, on water availability for human consumption, irrigation, or hydroelectricity production (e.g., Soruco et al., 2015).

Several studies put forward different atmospheric/meteorological factors as being responsible for the interannual variability of the surface mass balance of tropical glaciers in the Andes (e.g., Abermann et al., 2014; Gurgiser, Marzeion, et al., 2013; Gurgiser, Mölg, Nicholson, & Kaser, 2013; Hastenrath, 1997; Maussion et al., 2015; Vuille et al., 2008). Some highlighted the importance of the onset of the wet season (Francou et al., 1995; Sicart et al., 2011). However, Ramallo (2013) found poor correlations between the surface mass balance and the onset or end of the wet season primarily due to the difficulty in precisely identifying the latter which generally starts between mid-November and January in the eastern Andes of Bolivia. Other studies (e.g., Francou et al., 2004; Rabatel et al., 2013) considered the role of large-scale climatic indices like El Niño Southern Oscillation (ENSO) that promote increased surface mass loss due to reduced precipitation and increased air temperatures. However, poor correlations have also been reported between the ENSO and precipitation: based on 18 yr of data, Ramallo (2013) finds that the two variables have less than 10% of common variance at interannual scale on the Altiplano and less than 30% in the Zongo Valley.

In this context, distributed energy balance models (DEBAMs) are useful tools as they provide insight into the mechanisms that control interseasonal and interannual surface mass-balance variability of entire glaciers. Here, we focus on Zongo Glacier, located in the outer tropical Andes of Bolivia, where diverse long-term observations are available from previous studies.

Wagon et al. (1999) calculated the surface energy balance of Zongo Glacier at the automatic weather station (AWS) in the ablation area over one hydrological year (1997/1998). This was the first study of the annual surface energy balance over the glacier; it showed that the main driver of mass loss is the net all-wave radiation, which is primarily controlled by an albedo feedback effect. The authors also pointed out that because the meteorological conditions favor sublimation during the austral winter (between May and August, also known as the dry season) the melt rate over this period is lower than over the rest of the year, a process already identified by Kaser et al. (1990). Using data acquired between 1999 and 2000, Sicart et al. (2011) applied the physically-based DEBAM, (Hock & Holmgren, 2005) to the whole glacier in order to study the seasonal variability of the surface mass balance. This study highlighted the notable influence of processes that occur during the transition period between the dry (June–August) and wet season (January–March) on the annual surface mass balance. In addition, they show that at the glacier scale sublimation does not play an important role in controlling seasonal melt rate changes.

Lejeune et al. (2007) applied the CROCUS-ISBA model forced by meteorological data from an AWS on the moraine of Zongo Glacier. These authors showed that the rapid melting of snow on the moraine is mainly driven by incident shortwave radiation.

In this study, we applied DEBAM to Zongo Glacier over nine years to obtain deeper insights into the atmospheric/meteorological factors that control the interannual variability of the surface mass balance. The long data set available at Zongo Glacier provides a unique opportunity to investigate the climate factors that control both interannual and seasonal variabilities of the surface mass balance. Model experiments are performed to investigate the role of precipitation frequency and cloud cover on mass balance based on synthetic climate scenarios constructed from reorganized climate observations.

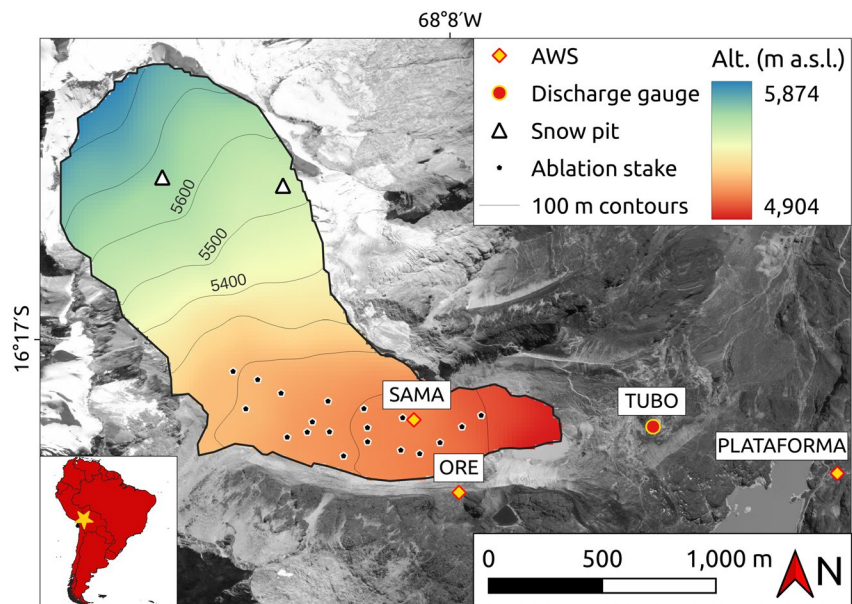


Figure 1. Location of Zongo Glacier and its monitoring network. SAMA is the on-glacier AWS, ORE is the AWS on the moraine and PLATAFORMA is the one at the pass. TUBO is a discharge gauging station. The bottom left inset map shows the location of the glacier in South America. The thick black line is the glacier outline in 1999. Thin black lines are elevation contours every 100 m from the 1999 digital elevation model (the first elevation contour being 5,000 m a.s.l.). The image in the background was acquired by the Pléiades satellite in 2013, © CNES–Airbus D&S.

2. Study Area and Climate Setting

2.1. Zongo Glacier

Zongo Glacier ($16^{\circ}15'S$, $68^{\circ}10'W$) is located on the southern side of Huayna Potosi peak (Cordillera Real, Bolivia). It is a valley-type glacier extending 2.8 km from about 6,000 m a.s.l. down to about 4,950 m a.s.l. and had a surface area of 1.7 km² in 2016. In collaboration with the French Research Institute IRD, the Bolivian authorities started a meteorological, glaciological, and hydrological observation program on Zongo Glacier in 1991 (Francou et al., 1995; Ribstein et al., 1995). The location of the AWS s on and around the glacier as well as the ablation stakes have varied over time but measurements have continued uninterrupted since the beginning of the program; see Rabatel et al. (2013) for a detailed overview of the monitoring network, and Figure S1 in Supporting Information S1 for the operating periods of the three AWS s. Figure 1 shows the location of the glacier along with its monitoring network.

2.2. Tropical Climate and Glaciological Regime

Since Zongo Glacier is located in the outer tropics, its climate is characterized by marked seasonality with frequent cloud cover and precipitation events primarily during the austral summer and a pronounced dry season during the austral winter (Troll, 1941). The glaciological regime over this region was described by Kaser (2001): most accumulation occurs during the wet season (austral summer) whereas during the dry season (austral winter) predominant clear-sky conditions and dry air favor sublimation. This overall pattern has been well established from in situ monitoring, for instance by Kaser et al. (1990) over glaciers in the Cordillera Blanca, Hardy et al. (1998) on Sajama Ice cap and by Wagnon et al. (1999) at Zongo Glacier. Sicart et al. (2011) found that the low ablation rate during the dry season is linked to the large longwave emission deficit during this period. Note that the hydrological year for Zongo Glacier begins in September and ends the following August.

We analyzed the mass-balance record (1992–2017, Vincent et al., 2018) to characterize the glaciological regime of the glacier. As shown in Figure 2, the ablation zone of Zongo Glacier experiences the highest net mass losses from September to November (-0.21 to -0.50 m w.e./month). This period is considered as the transition period

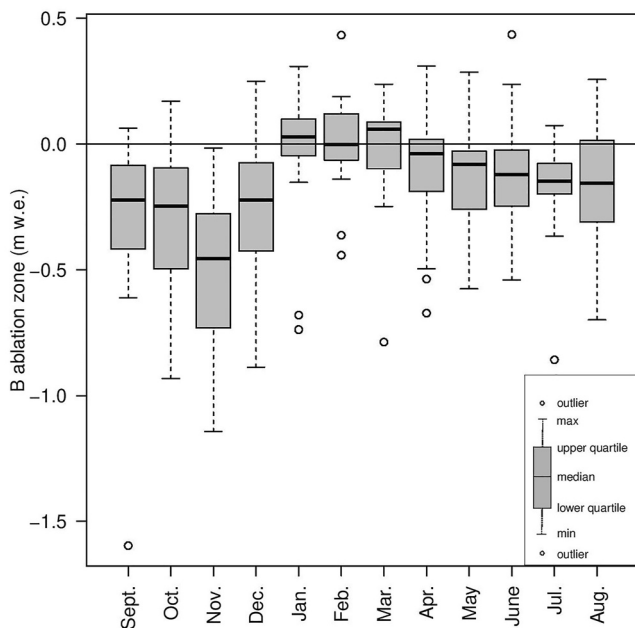


Figure 2. Box plot showing the monthly surface mass balances of the ablation zone of Zongo Glacier calculated from 20 ablation stakes (between 5,000 and 5,200 m a.s.l.) for the 27 mass balance years 1990/1991–2016/2017.

between the dry and the wet seasons. It is also characterized by very high interannual variability of the surface mass balance (standard deviation of 0.29 m w.e./month on average for the three months). Ramallo (2013) reported that about 20% of annual precipitation occurs during this period. Most cloud events during this period (80%, Sicart et al., 2016) are linked to northward propagating wind incursions to the east of the Cordillera (Surazos) that lead to deep convection events (Garreaud, 2000). Previous studies (e.g., Sicart et al., 2011) have shown that this period plays a key role in explaining the annual surface mass balance.

During the wet season (January–March), the surface mass balance in the ablation area is either slightly negative or positive. This period corresponds to the core of the wet season linked to the mature phase of the South American Monsoon System (SAMS). As the SAMS develops, the diabatic heating over the western Amazon leads to the formation of the anticyclonic system known as the Bolivian High in the upper troposphere (Lenters & Cook, 1997). Meanwhile, in the lower troposphere, the southward displacement of the South American Low-Level Jet favors mean easterly winds on the northern arc of the Bolivian High, which in turn, allow the formation of strong heat-driven easterly winds on the eastern slopes of the Cordillera Real. These upslope winds transport moisture from the Amazon Basin to the tropical Andes. The solar heating of the surface leads to strong afternoon/early evening convection events in the Bolivian Andes and Altiplano (Garreaud et al., 2003). According to Sicart et al. (2016), nearly half the cloud events during this period can be linked to Surazo conditions. These correspond to a destabilization of the tropical atmosphere by extra tropical cold air intrusion

related to low-level southern wind incursion (Ronchail, 1989). In the Bolivian lowlands, Espinoza et al. (2013) found an average of 3.4 such events lasting 2.7 days for each austral winter (JJA) between 1975 and 2002. Over this region, such events can cause sudden drops in temperature associated with deep convection events (Sicart et al., 2016). These events are responsible for up to a quarter of the summer precipitation in central Amazonia (Garreaud & Wallace, 1998). Over Zongo Glacier, they are marked by the arrival of cold high-altitude clouds which bring snow events which usually last for a few days. These events differ from the monsoon events which are convective events (i.e., thick and warm clouds) resulting from moist air advection from the Amazon Basin toward the eastern Andes due the destabilization of the boundary layer via the intense heating of the Altiplano between December and March (Sicart et al., 2016).

Throughout this period (wet season), there is little net mass loss since most of the melt energy goes to melting fresh snow (70% of the annual melt; Ramallo, 2013). Indeed, as shown by Sicart et al. (2011), throughout this season at the glacier snout, periods of snow melt during cloud events alternate with periods of ice melt during clear sky periods.

Finally, between April and August, surface mass-balance in the ablation area becomes increasingly negative, and both the top of atmosphere shortwave and incoming longwave radiation fluxes are low. The large incoming longwave deficit leaves little energy available for melt (Sicart et al., 2005). In addition, the negative latent heat fluxes during this period favor strong sublimation (Wagnon et al., 1999). About 10% of the annual precipitation occurs during this period (Ramallo, 2013), and 87% of the cloud events can be linked to Surazo conditions (Sicart et al., 2016).

While the top of atmosphere shortwave radiation peaks between September and November (Figure 3a), incoming shortwave radiation is at its maximum during the dry season (May–August). In contrast, the incoming longwave radiation is highest during the core wet season (January–March) and minimal during the dry season (Figure 3b). Sicart et al. (2010) showed that clouds increased the longwave radiation by up to 55% during the wet season and by about 20% on average. This effect contributes to the significant mass loss in the ablation area during the transition period (September–November, Figure 2).

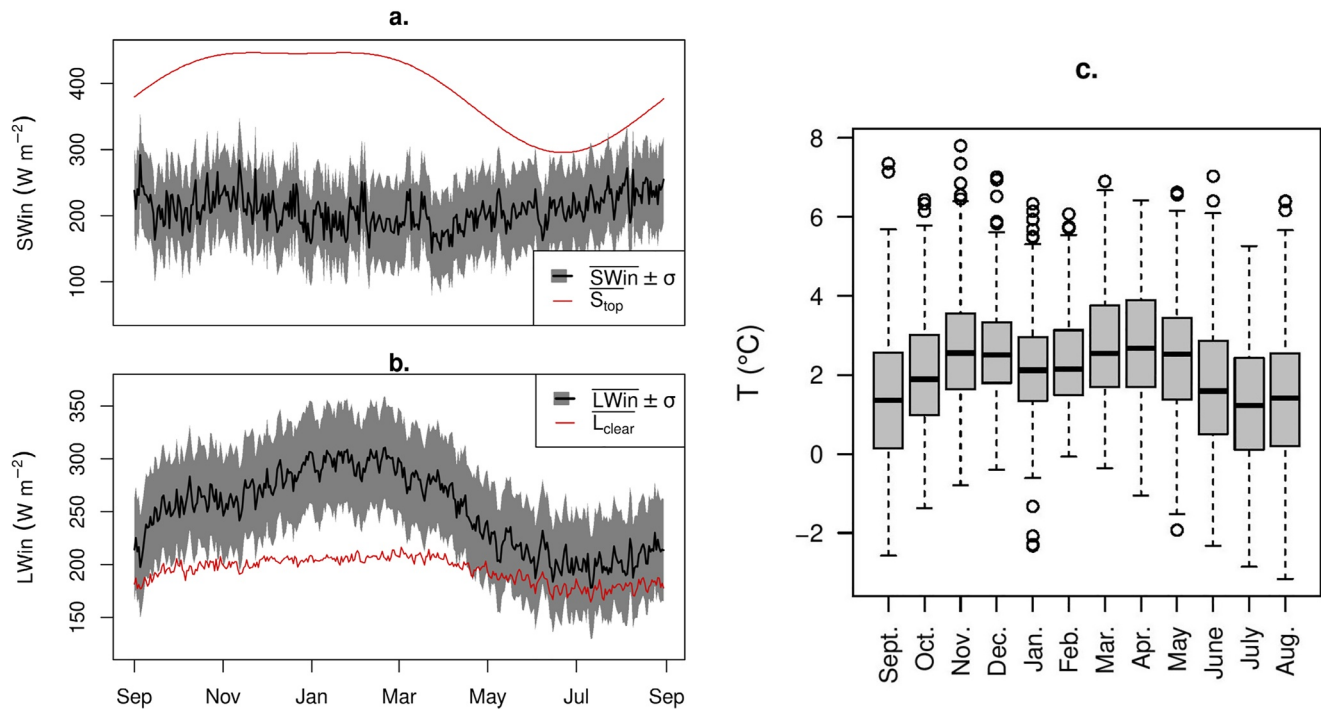


Figure 3. Annual cycle of (a) incoming shortwave radiation (SWin) and top of the atmosphere shortwave radiation (S_{top}) and (b) incoming longwave radiation (LWin) at the on-glacier weather station (SAMA) and theoretical clear-sky incoming longwave radiation (L_{clear}). L_{clear} was derived by dividing LWin by the cloud longwave emission factor (F). Daily mean station data are averaged over the nine simulated years between 1999 and 2017. (c) Boxplot showing the interannual variability of the monthly mean near-surface air temperature at the PLATAFORMA weather station (Figure 1).

Both incoming short and longwave radiation fluxes (averaged over each mass-balance year) are rather poorly correlated with the annual surface mass balance ($R^2 = 0.28$ and 0.0 , respectively) for the nine study years.

Figure 3c shows the interannual variability of the monthly mean temperatures at PLATAFORMA over a period of 14 yr (between 1999 and 2017): as expected the seasonal variability of the monthly average is low (the median temperatures vary between $1.5^{\circ}C$ and $2.2^{\circ}C$). We correlated monthly mass balances to monthly mean air temperatures at the on-glacier weather station (SAMA) and found the best correlation during the core wet season (up to $R^2 = 0.69$). The best correlations with glacier-wide surface mass balance derived from extrapolating the point balances across the glacier using a nonlinear statistical model (Vincent et al., 2018) were obtained at the annual scale but remained low ($R^2 = 0.18$).

Seasons can also be defined by looking at the distribution of the cloud radiative properties and more specifically at cloud radiative forcing, that is, the combined effect of clouds on the incoming radiation fluxes resulting from an increase in longwave radiation and a reduction in incoming shortwave radiation, the latter being dominant. Following the methodology of Sicart et al. (2016), we calculated the cloud radiative forcing of cloudy days for each month of 13 yr between 1999 and 2017, and analyzed the monthly probability density functions (Figure 4). Results indicate that cloud radiative forcing is distinctly different for the core wet season (January–March), the dry season (June–August) and the transition period (September–November), and therefore can be used as a criterion to identify these three seasons.

Between September and November (transition period, Figure 4a), the bimodal distribution of the cloud radiative forcing suggests the presence of two different types of clouds: those with little impact on the radiation budget (cold high-altitude thin clouds), and clouds with a considerable impact on the radiative budget as evidenced by the peak around $-120 W m^{-2}$; that is, thick clouds typical of convective events. During the core wet season (January–March, Figure 4b) the cloud distribution is unimodal, and the peak is centered around $-150 W m^{-2}$, suggesting predominantly thick clouds. Finally, the distribution is again unimodal during the dry season, centered around $-20 W m^{-2}$, indicating predominantly thin clouds at high altitude with a small impact on the radiation budget.

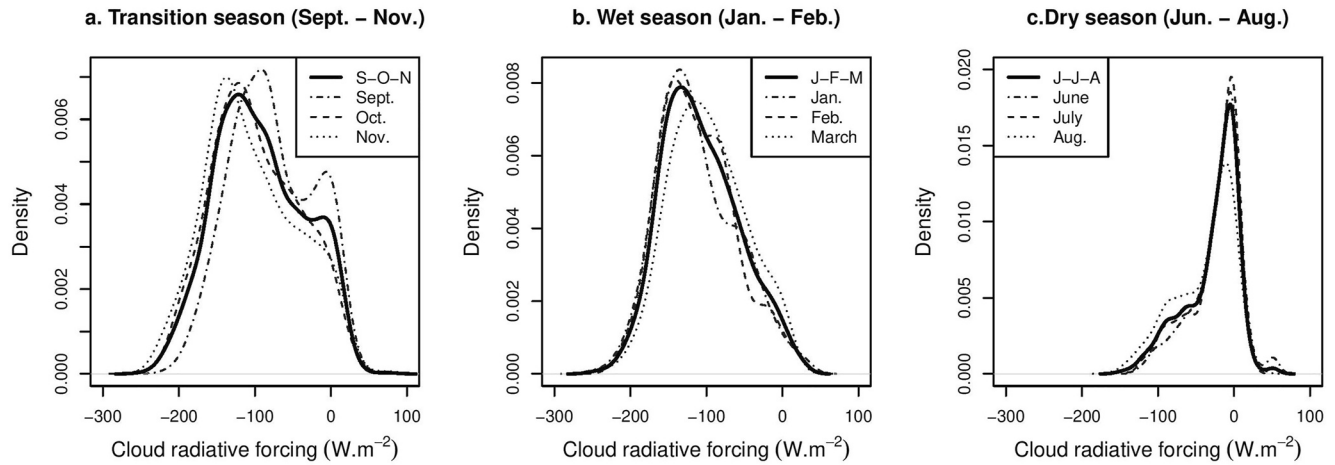


Figure 4. Probability distribution functions of cloud radiative forcing for the transition period (a), the core wet season (b) and the dry season (c) based on 13 yr of data (between 1999 and 2017) at both the on-glacier and PLATAFORMA weather stations.

3. Mass-Balance Modeling

We apply the open-source mass-balance model DEBAM (Hock & Holmgren, 2005; <https://regine.github.io/melt-model/>) to nine non-consecutive years between 1999 and 2017 when weather station data were available to reliably simulate the energy and mass fluxes over the glacier surface at the hourly time step. Although less complex than other physically based models (e.g., CROCUS-ISBA), DEBAM requires less meteorological input variables, and therefore is well suited to study the interannual variability of Zongo Glacier surface mass balance. This model has been applied to glaciers in the Northern Hemisphere (Hock & Holmgren, 2005; Østby et al., 2017; Reijmer & Hock, 2008), the Sub-Antarctic (Braun & Hock, 2004) and on Zongo Glacier (Sicart, 2002; Sicart et al., 2011).

3.1. Input Data Sets

The model is forced with seven meteorological input variables at hourly resolution: air temperature, precipitation, incoming shortwave and longwave radiation, outgoing longwave radiation, relative humidity, and wind speed. Due to the difficulty of maintaining a fully operational AWS on the glacier, sufficient data were only available for nine non-consecutive years within an 18 yr period from 1999 to 2017: 1999 to 2001, 2004 to 2006, 2008 to 2010, 2011 to 2013, and 2016/2017.

We use the data from the SAMA AWS located on the glacier surface at 5,050 m a.s.l (Figure 1, Table 1). Text S1 in Supporting Information S1 details the gap-filling methodology used.

Table 1
List of the Equipment at SAMA Along With the Sensor Heights and Precision According to the Manufacturer

Variable	Sensor	Sensor height	Precision (according to the manufacturer)
Temperature	CS2115 (since 23/02/2011)	1.00 m	±0.2°C
	Vaisala HMP45C (up to 23/02/2011)	1.57 m	±0.9°C
Relative humidity	CS2115 (since 23/02/2011)	1.00 m	±2%
	Vaisala HMP45C (up to 23/02/2011)	1.57 m	±4%
Wind speed (m/s)	Gill Solent (since 23/02/2011)	1.74 m	±5%
	Young 05103 (up to 23/02/2011)	2.50 m	±0.3 m/s
Incoming and outgoing shortwave radiation (W/m ²)	Kipp & Zonen CM3 0,305 < λ < 2,8 μm	1.00 m	±3%
Incoming and outgoing longwave radiation (W/m ²)	Kipp & Zonen CG3 5 < λ < 50 μm	1.00 m	±3%
Snow height, ultrasonic measurements	Campbell, SR50AT	1.15 m	±1 cm or 0.4% of the distance

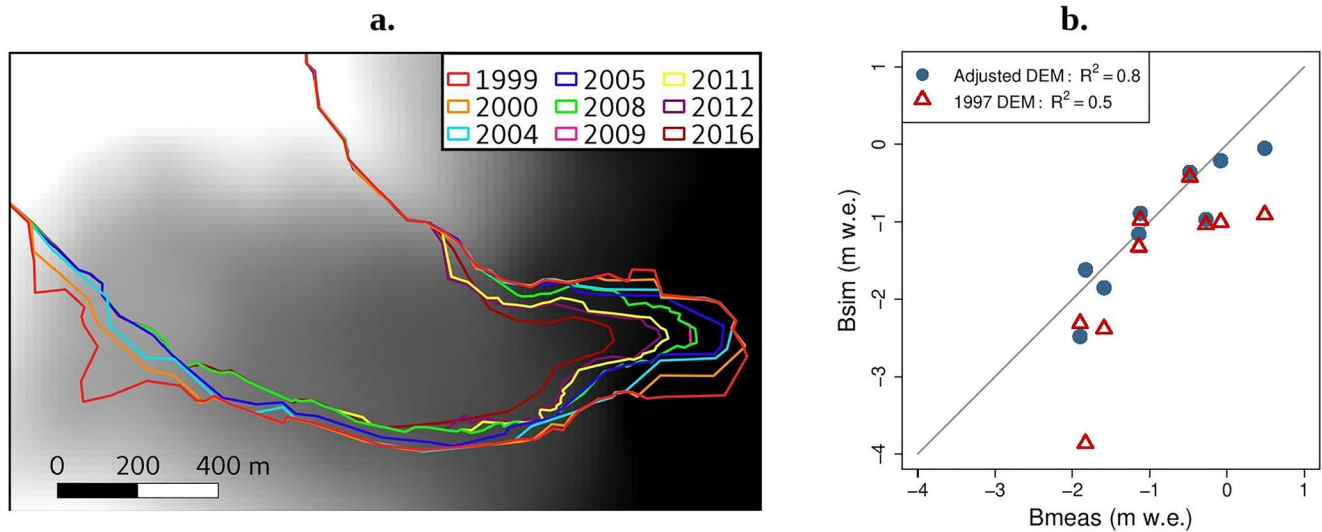


Figure 5. (a) Zongo glacier front positions between the first (1999) and the last modeled year (2016). (b) Simulated glacier-wide annual surface mass balance (B_{sim}) vs. balances derived from stake observations and geodetic balances (B_{meas} , Vincent et al., 2018), including the 1:1 line. Simulations using annually adjusted DEMs are compared to those keeping the 1997 DEM and outline constant.

Precipitation was derived from the ultrasonic gauge measurements following Sicart et al. (2002): precipitation amounts were obtained by comparing the means of three consecutive measurements spread over one hour at 3 hr intervals, in order to identify changes in surface height of at least 1 cm. The amounts in water equivalent were then derived by applying a fresh snow density of 220 kg m^{-3} for the transition period and the dry season and a higher density of 250 kg m^{-3} for the wet season due to slightly higher temperatures during the austral summer.

Between 1999 and 2016, the glacier lost 12% of its surface area (Figure 5a) and thinned considerably (the altitude of the grid points making up the glacier front in 2016 were 55 m lower in 2016 than in 1999). To account for the changing geometry, digital elevation models (DEMs) were generated for each modeled year. The glacier topography was interpolated (or extrapolated) linearly between two measured DEMs: one from 1997 based on aerial photographs (Soruco et al., 2009) and one from 2013 made from Pléiades satellite stereo-images (Cusicanqui et al., 2015). The glacier contours were based on differential GPS measurements made each year during field campaigns.

Figure 5a illustrates the glacier retreat during the modeled period while plot 5b shows the impact of accounting for changing surface elevations compared to the use of the 1997 DEM on the simulated annual surface mass balance (B_{meas} , Vincent et al., 2018). Accounting for the glacier retreat improved the correlation between the simulated glacier-wide annual surface mass balances and those derived from observations (R^2 went from 0.5 to 0.84). This is because accounting for glacier retreat adjusts the size of the ablation zone thereby significantly reducing the overall melt.

In addition, when keeping the glacier topography constant, the simulated snowline is at a higher altitude than what observations indicate. Therefore, simulated glacier-wide albedo is too low which in turn increases both melt and total mass loss.

Hourly discharge data from the TUBO gauging station (Figure 1), a V-shaped weir with an automatic limnigraph, were used for validation as it is representative of the overall amount of melt water. In addition, surface mass balance observations at 20 ablation stakes distributed over the ablation area were used. Finally, photos taken during field campaigns were used to compare the modeled and observed snow line positions.

3.2. Model Description

DEBAM (Hock & Holmgren, 2005) solves the following surface energy balance equation:

$$Q_M = G(1 - \alpha) + LW_{net} + H + LE + Q_G + R \quad (1)$$

where Q_M is the energy available for melt, G is the global (or shortwave incoming, SW_{in}) radiation, α the albedo, LW_{net} the net longwave radiation balance, H and LE are the sensible and latent heat fluxes, respectively, Q_G is the ground heat flux and R the sensible heat supplied by rain (negligible over Zongo as shown by Sicart et al., 2011). The model convention is such that energy fluxes directed toward the surface are positive and those away from the surface are negative.

The model also includes a runoff module which routes glacier melt and rain water through the glacier using three linear reservoirs representing firn, snow and ice. We use storage constants of 350, 30, and 16 hr, respectively, according to Sicart et al. (2011).

3.2.1. Incoming Radiation Fluxes

To extrapolate global radiation across the glacier, measured radiation was split into its direct and diffuse components using a calibrated empirical relationship between the ratio of global radiation at the top of the atmosphere and the potential diffuse radiation considering a clear sky attenuation of 13% at the daily time scale (Sicart et al., 2011). The diffuse radiation component was considered to be spatially variable and extrapolated according to topographic shading based on the sun's path, the effective horizon and sky view factor of the grid cell (Hock, 1998). The direct component of incoming shortwave radiation was extrapolated according to the slope and orientation of the grid cells. The incoming longwave radiation was taken from the weather station measurements and assumed to be spatially constant over the glacier, a reasonable assumption given the small glacier surface area (1.7 km²).

3.2.2. Parameterization of Albedo

Because DEBAM was originally developed to model glaciers in the Northern Hemisphere, a key adaptation to tropical glacier on the albedo calculation was implemented in the model by Sicart (2002), and was used here. It consists of a modified version of Oerlemans and Knap (1998)'s albedo parameterization that accounts for the rapid alternation of accumulation and melt in the wet season as well as the impact of ice on the albedo over shallow snow depths.

In the absence of precipitation, the snow albedo decreases as follows:

$$\alpha_{snow} = \alpha_{firn} + (\alpha_{fresh-snow} - \alpha_{firn}) e^{-nj/n^*} \quad (2)$$

$$\alpha = \alpha_{snow} + (\alpha_{ice} - \alpha_{snow}) (1 + e_s/e_s^*)^{-3} \quad (3)$$

where n^* is the time constant of decrease in albedo (10 days), nj is the number of days since the last snowfall, e_s the snow depth and e_s^* the critical snow depth below which the ice starts to influence the modeled albedo, considered here to be 6 mm w.e. according to Sicart (2002).

During precipitation events, the albedo increases proportionally to precipitation rate (Pr) (Sicart, 2002):

$$\Delta\alpha = cpPr \text{ with } cp = 0.02 \text{ h/mm} \quad (4)$$

3.2.3. Surface Temperature

Surface temperature was derived from measured outgoing longwave radiation and assumed constant across the glacier. The subsurface snow module (Hock & Tijm-Reijmer, 2012) was not used to evaluate the surface temperature spatial evolution due to lack of data to constrain the model (i.e., subsurface temperature and density profiles). In addition, most of the melt occurs between September and March when the surface temperatures in the ablation area remain close to the melting point (Sicart et al., 2011). Thus its application would significantly increase the model uncertainty and hence the risk of error compensation.

3.2.4. Turbulent Energy Fluxes

The sensible and latent turbulent heat fluxes were calculated according to the aerodynamic profile method between the glacier surface and measurements as a function of 1.57 m air temperature, relative humidity, and wind speed based on the Monin-Obukhov similarity theory (see Hock & Holmgren, 2005 for more details). Stability functions were assumed constant across the glacier and based on Beljaars and Holtslag (1991) for stable conditions and on the Businger-Dyer expressions from Paulson (1970) for the less frequent unstable cases.

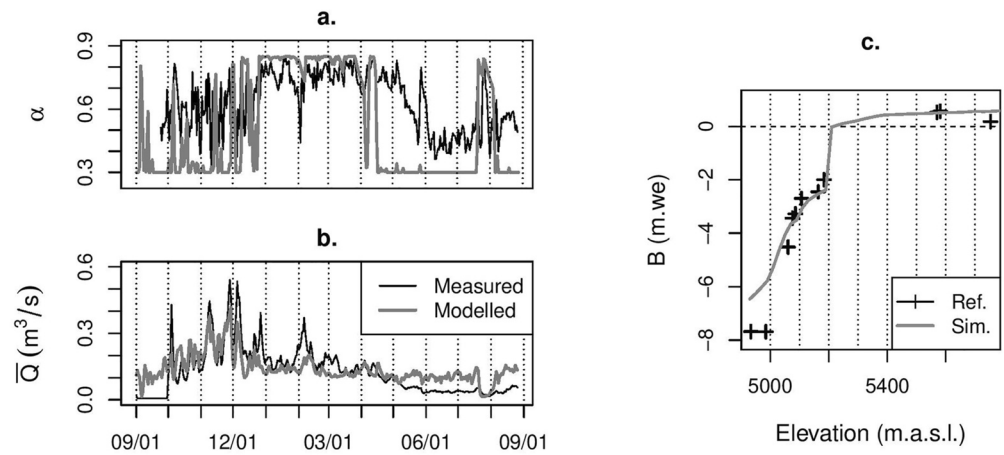


Figure 6. Validation of the model results exemplified for the hydrological year 2008/2009. Modeled and measured (a) daily mean albedo (α), (b) daily discharge (Q) and (c) annual specific surface mass balance (B) profiles.

3.2.5. Model Application and Calibration

The model was run with hourly resolution and on a 20×20 m grid. Air temperature was extrapolated across the glacier using a constant lapse rate of -0.55 K/100 m. A precipitation gradient of $+10\%/100$ m was applied up to 5,400 m a.s.l., above which it remained constant (based on an analysis of measurements at different altitudes). Relative humidity and wind speed were assumed constant across the glacier. At the beginning of each hydrological year (1 September), the model was initialized with a map of the extent of the firn zone estimated from in situ terrestrial photographs or LANDSAT images and a map of snow cover derived from field photographs, and snow depth derived from observations.

First, the melt rate was calculated at the AWS. The energy fluxes were then extrapolated across the glacier.

We chose to use a constant set of parameters for the nine years to guarantee robust calibration, the calibration process involved a trade-off between very precise modeling of specific years (e.g., years with high precipitation) and obtaining a globally efficient parameter set. Special emphasis was placed on reproducing the transition periods as accurately as possible as they play an important role in the interannual variability of the surface mass balance (Sicart et al., 2011). We focused on two main sets of parameters: albedo and roughness lengths.

The albedo was calibrated using measurements at SAMA for two contrasting years (1999/2000, $B = -0.08$ m w.e. and 2004/2005, $B = -1.90$ m w.e.). It implied a trade-off between the simulated albedo for these two years. It was validated over the remaining years. Accordingly, the following albedo values were assumed: 0.85 for fresh snow, 0.6 for firn and 0.3 for ice.

The roughness length for momentum over ice was calibrated using eddy covariance (EC) measurements in June 2011 and set to 0.026 m. Those of momentum over snow and of temperature and humidity were considered constant and set to a tenth of the roughness length of momentum over ice (i.e., 0.0026 m). These values were then validated over the other period where EC measurements were available (July–August 2007, Litt et al., 2014).

3.3. Model Validation

To validate model performances, we focus on the following observations: albedo at SAMA, discharge at TUBO gauging station, observations of surface type (snow, ice) from terrestrial photographs, glacier-wide surface mass balances derived from observations, and point surface mass balances as a function of altitude.

Figure 6 illustrates the results for the year 2008/2009, a year with high albedo variability at the AWS. Overall, variations in albedo are well simulated but the amplitude is sometimes off (Figure 6a), suggesting that precipitation events are well represented, but not always their intensity. This is due to both the precipitation measurements uncertainties (Sicart et al., 2002) and the assumption of a constant value for the time constant of decrease in albedo (10 days, Equation 2) although snow ages faster in the wet season than in the dry season (Sicart et al., 2011).

Errors in modeled albedo have a significant impact on modeled melt rate, since solar irradiance is often the main source of energy for melt (Sicart et al., 2005) and its effect on melt is controlled via an albedo feedback effect (and hence the glacier surface state). In addition, errors in simulated surface state lead to erroneous turbulent flux simulations as different roughness lengths are used over snow and ice.

Simulated discharge is in good agreement with the measurements up to the end of the wet season (Figure 6b) although the model underestimates some peaks probably due to errors in accurately modeling the snow line on a daily scale. During the dry season, the discharge is systematically overestimated likely because the model does not account for the ground heat flux. Hence, the glacier surface does not cool enough and cannot delay the diurnal melt.

Figure 6c compares modeled and observed surface mass-balance as a function of altitude. The model underestimates mass loss close to the glacier front however, this has little impact on the glacier-wide surface mass balance since this region represents only a very small fraction of the ablation area. The mass balance for the remaining glacier area is well simulated.

Measured and simulated surface mass balance profiles for all nine simulated years are shown in Figure S2 in Supporting Information S1. Overall, the simulated equilibrium-line altitude is in good agreement with the measurements.

One of the main drawbacks of calibrating a single parameter set for all the modeled years is that the model is not equally accurate for each of the years modeled: in some years, melt in the ablation zone is underestimated (e.g., 2005/2006) whereas in others, it is overestimated (e.g., 2004/2005). Considering the nine-year average, the overall mass loss is overestimated by 0.18 m w.e. with an average surface mass balance of -0.88 m w.e. The simulation errors for years with significant net mass loss tend to be higher than for years with limited mass loss.

Overall, a variety of error sources can explain the differences between measured and simulated variables (Sicart et al., 2011). In the model, the surface temperature is calculated using the measured outgoing longwave radiation at the weather station and considered constant. As a result, the model is not able to capture the intense night cooling of the surface in the firn area, which in turn, delays the diurnal melting period of the surface, leading to potential overestimation of the melt rate. Furthermore, erroneous surface temperatures affect the simulated turbulent fluxes which in turn, affect the surface temperature, leading to rapid uncertainty propagation. This process is particularly important in the dry season when nighttime cooling of the surface in the accumulation area is at its highest.

3.4. Generation of Scenarios for Precipitation Sensitivity Analysis

We perform a series of sensitivity experiments to analyze the impact of the timing of precipitation amounts during the transition season (September–November) on the annual surface mass balance. Three scenarios (S1–S3) were generated by shuffling the time series of daily meteorological data during the transition season:

1. S1: All days with precipitation events ≥ 2 mm/d were evenly distributed in time. For example, if there are 30 such days, then, in the scenario, such a day occurred every third day as there are 91 days in the season. Days were shuffled manually so that each day was moved as little as possible (maximum was 12 days). The threshold was chosen because it allows the formation of at least 1 cm of snow, which in turn, enables considerable changes in albedo and hence has a notable impact on the melt rate
2. S2: Same as S1 except the threshold was 9 mm/d (to assess the threshold impact)
3. S3: All precipitation events exceeding 2 mm/d within a given month were moved to the beginning of that month

The procedure guarantees that precipitation amounts in the transition period are conserved (i.e., only the temporal distribution of the events changes).

To guarantee physical coherence between the different meteorological variables for each day, all the other meteorological input data for the corresponding day were shuffled as well.

Table 2
Summary of the 66th Percentile Value of the Cloud Radiative Forcing (CF) Per Month and the Corresponding Cloud Longwave Emission Factor (F^{cloud}) and Bulk Cloud Shortwave Transmissivity (Tn^{cloud}) Values Retained for the Scenario

Month	66th percentile value of CF (W m^{-2})	F^{cloud}	Tn^{cloud}
September	-109	1.42	0.47
October	-128	1.30	0.51
November	-136	1.23	0.53

Scenarios S1–S3 were generated for three contrasting years: 1999/2000 represents a year with little melt ($B_{\text{meas}} = -0.08$ m w.e.), 2008/2009 represents a mass balance close to the nine-year average ($B_{\text{meas}} = -1.14$ m w.e.). The year 2004/2005 had the highest recorded net mass loss of the nine years studied ($B_{\text{meas}} = -1.90$ m w.e.).

Moving days around also impacts the daily total incoming radiation at the glacier surface via cloud radiative forcing as moving precipitation events also involve displacing clouds. But, as melt was generally limited during precipitation events, the cloud radiative forcing induced by moving the clouds was of little importance.

3.5. Generation of Scenarios for Cloud Sensitivity Analysis

To assess the impact of the cloud cover on the annual surface mass balance, we constructed three scenarios that change the cloud radiative forcing (which is the net effect of clouds on the incoming radiation fluxes) to mimic a cloud cover sustained over an entire month. In practice, we changed the incoming shortwave and longwave radiation for each time step, separately for each of the three months of the transition period (September–November) for all nine simulated years resulting in three scenarios: Sce_S, Sce_O, and Sce_N. The radiative forcing of all other months and all other meteorological data for the entire period remained unaltered.

To achieve this we used the cloud emission factor F which represents the increase in sky longwave emission due to clouds and the bulk cloud shortwave transmissivity Tn which represents the attenuation of incoming shortwave radiation linked to the presence of clouds (Sicart et al., 2010, 2016).

Thus, the incoming longwave radiation flux in each scenario ($LW_{\text{in}}^{\text{Sce}}$) was calculated by:

$$LW_{\text{in}}^{\text{Sce}} = (F^{\text{cloud}}/F^{\text{meas}}) LW_{\text{in}}^{\text{meas}} \quad (5)$$

where LW_{in} is the measured longwave incoming radiation, F^{meas} is the measured cloud emission factor and F^{cloud} is the emission factor needed to construct the scenario.

Similarly, the incoming shortwave radiation ($SW_{\text{in}}^{\text{Sce}}$) was calculated by scaling measured $SW_{\text{in}}^{\text{meas}}$ by the ratio of the bulk shortwave transmissivity representing cloudy conditions (Tn^{cloud}) and the measured transmissivity (Tn^{meas}):

$$SW_{\text{in}}^{\text{Sce}} = (Tn^{\text{cloud}}/Tn^{\text{meas}}) SW_{\text{in}}^{\text{meas}} \quad (6)$$

F^{cloud} and Tn^{cloud} were derived from the long-term (nine-year) monthly 66th percentile of cloud radiative forcing. We assume that the 66th percentile of daily values over the nine simulated years represents thick cloud cover. Table 2 lists the cloud radiative properties for each month. The F and Tn values are typical of thick warm clouds: regardless of the month considered, the clouds reduce the incoming shortwave radiation by at least 47% and increase the incoming longwave radiation by at least 23% (Sicart et al., 2016 considered that clouds have a strong impact on the radiative budget when $F \geq 1.15$).

Although changing the incoming radiation fluxes values led to a loss of physical coherence between radiation fluxes and the other meteorological variables (temperature, relative humidity, and wind speed), the loss was considered acceptable since the main impact is on the turbulent fluxes which, according to Sicart et al. (2011), tend to be small during the transition period.

In order to assess the impact of generating the cloud cover scenarios compared to measured conditions, the mean number of cloud events per month over 13 yr was calculated based on the methodology defined in Sicart et al. (2016). Accordingly, there were 20 cloudy days in September, 25 in October, and 24 in November. Hence, on average the scenarios implied adding 10 cloudy days in September and six cloudy days in both October and November.

It is worth noting that the cloud radiative forcing values applied were significantly lower than the measured values: for each month, the mean cloud radiative forcing was 34% more negative than the nine-year average (as the 66th

Table 3

Simulated Annual Glacier-Wide Surface Mass Balance, Melt and Precipitation in the Nine Simulated Years, Along With the Differences From Their Respective Mean Values

Years	Simulated variable X			Difference from mean values ($X - \bar{X}$)		
	B (m w.e.)	Melt (m w.e.)	Precipitation (m)	B (m w.e.)	Melt (m w.e.)	Precipitation (m)
<i>1999/2000</i>	-0.21	1.93	1.74	0.85	-0.64	0.13
<i>2000/2001</i>	-0.04	2.03	1.98	1.02	-0.53	0.37
2004/2005	-2.47	3.49	1.35	-1.41	0.93	-0.26
<i>2005/2006</i>	-0.36	2.25	1.91	0.70	-0.32	0.31
<i>2008/2009</i>	-1.14	2.38	1.41	-0.08	-0.19	-0.20
2009/2010	-1.84	3.00	1.47	-0.79	0.43	-0.14
<i>2011/2012</i>	-0.88	2.55	1.76	0.18	-0.01	0.15
<i>2012/2013</i>	-0.97	2.51	1.53	0.09	-0.06	-0.80
2016/2017	-1.62	2.96	1.32	-0.56	0.39	-0.29
\bar{X}	-1.06	2.60	1.61	NA	NA	NA
σ	0.81	0.50	0.25	0.81	0.50	0.25

Note. The three years in italics are years in which the mass loss is considerably less than the average ($B > B_{\text{mean}} + \sigma/2$). The three years in bold are years with considerable mass loss ($B < B_{\text{mean}} - \sigma/2$).

percentile of the absolute cloud radiative forcing was used to build the scenarios). In terms of intrinsic cloud radiative properties, this increased the cloud longwave emission factor (F) by 12%, 1%, and 6% in the September, October, and November scenarios, respectively. Similarly, it reduced bulk cloud shortwave transmissivity (Tn) by 33%, 14%, and 9% in September, October, and November, respectively. Therefore, this scenario generation method allows the assessment of the impact of strong sustained cloud cover on the surface mass balance.

4. Results and Discussion

4.1. Analysis of the Interannual Variability of the Simulated Energy Fluxes

Simulated annual glacier-wide surface mass balances range between 0.49 and -1.90 m w.e. indicating contrasting climate conditions between the nine simulated years. The average annual balance is strongly negative (-0.88 m w.e.) suggesting that the glacier is not at equilibrium with climate.

Table 3 shows the modeled annual surface mass balance, melt, precipitation and their differences to the nine-year average. Years with limited net mass loss are years when the precipitation amounts were well above average ($P > P_{\text{mean}} + \sigma/2$). Similarly, years with high net mass losses were years with a precipitation deficit ($P < P_{\text{mean}} - \sigma/2$).

The monthly mean energy fluxes at the automatic weather station (SAMA) averaged over all nine years and for two contrasting years are presented in Figure 7. The AWS fluxes are presented rather than glacier-wide average fluxes in order to avoid simulation errors that are due to spatial extrapolation (e.g., temperature and precipitation gradients).

On average the sum of radiative and turbulent fluxes is lower during the dry season (June–August, Figure 7a). During this period, net longwave radiation deficit is greatest due to the absence of longwave radiation emitting clouds (Sicart et al., 2011). Conversely, during the transition period, the increase in surface temperatures combined with the increased frequency of cloud events and the increase in incoming solar radiation combined with a relatively low albedo result in large amounts of energy available for melt.

Figure 7b shows that much more energy is available for melt in the strongly negative mass-balance year. This is due to a significantly higher shortwave energy budget, while the longwave budget is less different than the long-term average.

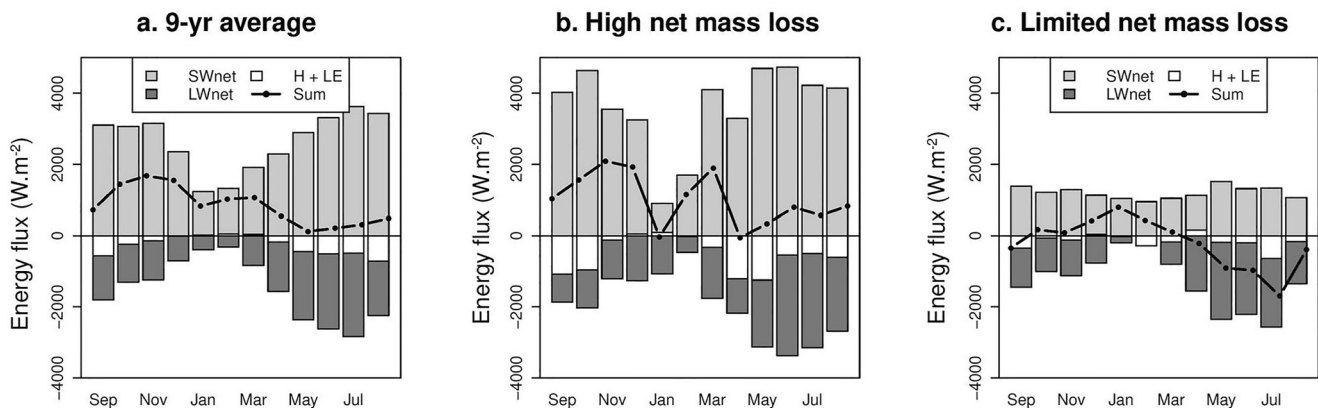


Figure 7. Monthly mean energy fluxes (a) averaged over the nine simulated years, (b) for a year with a highly negative surface mass balance (2016/2017, -1.62 m w.e.) and (c) for a year with limited net mass loss (1999/2000, -0.21 m w.e.). The cumulative energy fluxes shown are the simulated fluxes at the automatic weather station (SAMA). Note, a positive sum implies that energy is available for melt, whereas a negative one implies surface cooling via the ground heat flux.

For a year with a limited net mass loss (Figure 7c), some energy was available for melt during the wet season, but the sum of the radiative and turbulent fluxes was mostly negative, resulting in surface cooling rather than melting. The differences to the long-term average are mainly explained by a lower net shortwave radiation budget due to a higher glacier-wide albedo.

Overall Figure 7 illustrates that the transition period controlled most of the annual surface mass balance as, both on average and for the year with significant mass loss, the transition period is when most energy is available for melt. When the sum of the energy fluxes is negative or close to zero during this period, the annual net mass loss is significantly lower than average (Figure 7c).

To better understand the interannual variability of the surface mass balance, three years with limited net mass loss: 1999/2000, 2000/2001, and 2005/2006 were compared to three years with high mass loss: 2004/2005, 2009/2010, and 2016/2017 (Table 3).

Results (illustrated for two contrasting years in Figure 8) show that during the transition period, years with limited mass loss systematically had a higher glacier-wide albedo (Figure 8a). This trend was sometimes inverted between March and May. At the annual scale, the mean annual albedo of the three years with limited melt was 13% higher than the mean for the three years with significant melt. During the transition period, it was 11% higher, while during the dry season it was 30% higher. However, during the core wet season, it was only 1% higher, this small difference is due to the frequent precipitation events during this period regardless of the year considered.

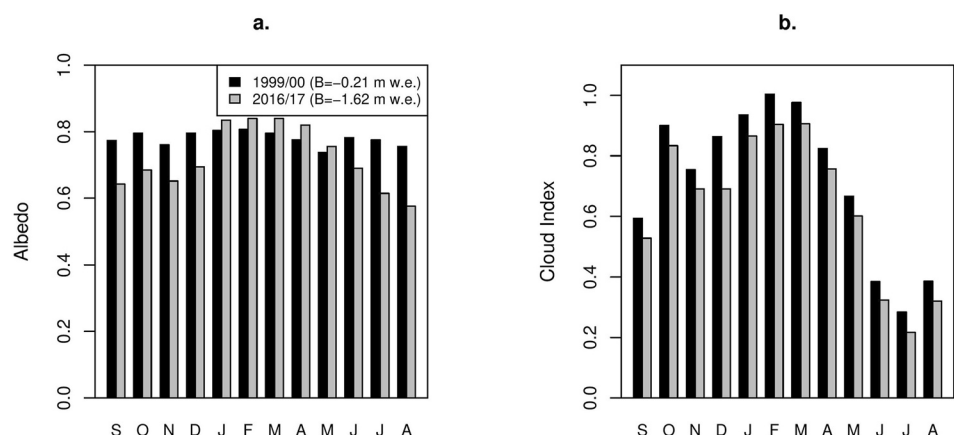


Figure 8. (a) Modeled monthly mean glacier-wide albedo (α), and (b) monthly mean cloud index (CI) for both a year with limited net mass loss (1999/2000; $B = -0.21$ m w.e.) and a year with high net mass loss (2016/2017; $B = -1.62$ m w.e.).

In addition, years with a significant mass loss tended to be less cloudy than years with a limited mass loss (Figure 8b). This is quantified by the mean monthly cloud cover index (CI) defined by Sicart et al. (2016) which is the difference between the cloud longwave emission factor and the bulk cloud shortwave transmissivity factor. The higher the index, the greater the ability of the clouds to reduce incoming solar radiation and increase incoming longwave radiation as. At the annual scale, the mean CI of the three years with limited mass loss was 15% higher than for years with significant mass loss, and at least 6% higher regardless of the season considered.

During the transition period, melt is highest during clear sky days (CI close to 0) as clouds reduce the amount of incoming energy at the surface. This coupled to the gradually increasing top of atmosphere radiation (as the summer solstice approaches) and the limited number of cloud events throughout the period make the albedo a key variable in controlling melt energy (via a feedback effect). Indeed, although the annual mass balance is poorly correlated with the incoming shortwave radiation ($R^2 = 0.28$ when considering the nine years), it is well correlated with net shortwave radiation ($R^2 = 0.84$) which highlights the importance of the albedo in the energy budget. Thus, despite observed similar differences in mean glacier-wide albedo and CI between years with low and high mass loss (Figure 8), it is the albedo that has the highest impact on melt energy.

This analysis shows that the transition period is most important in terms of controlling the interannual variability of the surface mass balance mainly because solar radiation approaches its maximum while cloud events are still sporadic, meaning it has the highest net incoming radiation. Coupled with the fact that during the transition period, the surface temperature in the ablation zone is close to 0°C, which limits the magnitude of the ground heat flux. As a result, most of the excess energy in the energy balance is converted into melt.

Finally, in order to assess if the mass balance deficit occurring during the transition season was persistent across the year, we carried out model runs where the data of the transition season of a year with limited mass loss (e.g., 2005/2006) was replaced by the data from another year with significant mass loss (e.g., 2004/2005) and vice-versa. The simulations show that the mass balance generated by the transition season is repercutated throughout the year. For example, when the year 2004/2005 is run with the transition season of 2005/2006, the annual simulated mass loss is reduced by 1.18 m w.e. Similarly, when 2005/2006 is run with the 2004/2005 transition season, the simulated annual net mass loss is increased by 1.00 m w.e.

4.2. Sensitivity to Precipitation Scenarios

4.2.1. Application to Three Contrasting Years

Figure 9 shows some impacts of the three scenarios over the 2008/2009 transition period. Overall patterns are similar for years with high and limited mass balances (not shown).

Evenly redistributing the precipitation events (S1 and S2) maintained a larger snow-covered area (Figure 9a) throughout most of the transition period, as also indicated by a generally higher albedo (Figure 9b), and hence a lower net shortwave radiation balance (Figure 9c), which in turn, resulted in a lower melt rate (Figure 9d). Averaged over the three years to which the scenarios were applied, scenarios S1 and S2 reduced the melt rate by 7% and 2%, respectively, whilst scenario S3 increased the melt rate by 12% over the transition period. Note that because scenario S1 involved moving more precipitation events than scenario S2, it reduced the melt rate more than the latter (as it maintained a larger glacier fresh snow cover).

In contrast, with scenario S3, grouping all the precipitation events at the beginning of the month yielded a much thicker snow cover at the beginning of the month (except in September 2008, due to a small amount of measured precipitation: 29 mm w.e.). However, due to a lack of precipitation for the rest of the month, this snow cover disappeared, resulting in a lower albedo than in the reference run, and thus, over the whole period, to larger amounts of energy available for melt.

Impacts of each scenario on the surface mass balance are shown in Figure S3 in Supporting Information S1 and Table 4 lists the precipitation amounts, simulated surface mass balances for scenario S1 and the reference run over the transition period.

Scenario S1 resulted in a smaller net mass loss over the transition period than the reference run in all years while scenarios S2 and S3 resulted in higher or lower net mass loss depending on the year. Overall, S3 led to the largest deviations from the reference run in all three years.

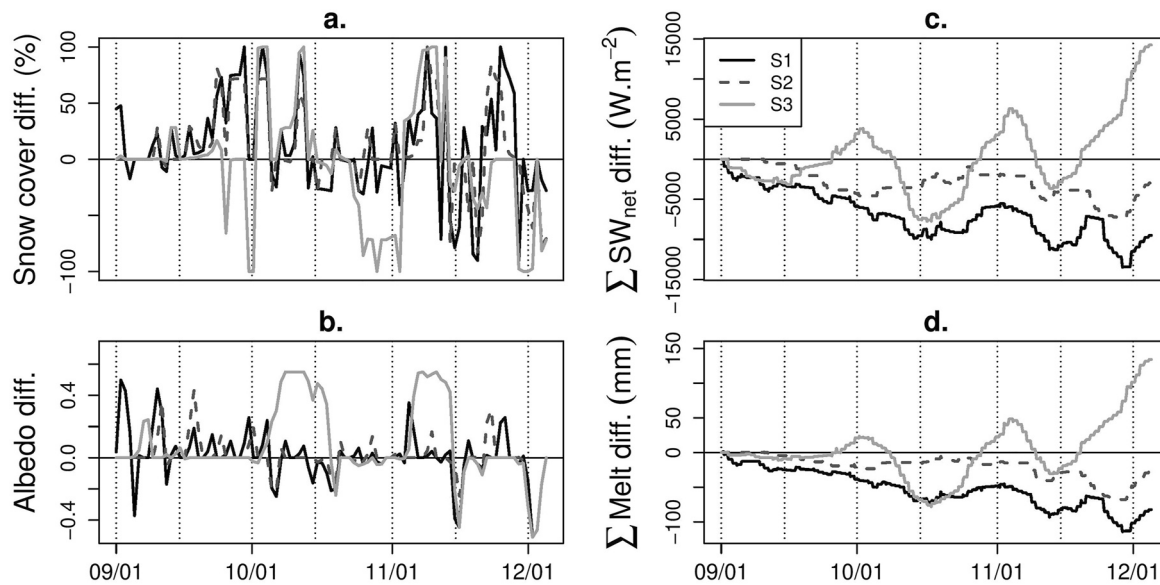


Figure 9. Impact of the three precipitation scenarios S1–S3 on glacier-wide (a) daily fresh snow cover area, (b) albedo, (c) net shortwave radiation and (d) melt compared to the reference run for the period September–November 2008. Results are shown as daily anomalies (a, b) and cumulative anomalies from the reference model run (c, d).

In 2004/2005, scenario S1 led to a smaller reduction in net mass loss than in the other two years because the precipitation events were already rather well distributed over time (data not shown). Compared to the reference run, the melt rate for scenario S1 was lower in September and October (Table S1 in Supporting Information S1) due to increased precipitation events. On the other hand, in November, scenario S1 resulted in six fewer precipitation events, and, combined with the fact that November is the month with the highest potential solar irradiance, there was an overall decrease in the glacier-wide albedo that significantly increased the melt rate. As a result, all the reduction in melt rate obtained between September and October was offset by the increased melt rate in the second half of November.

Table 4

Summary of the Precipitation Amounts and Number of Events Above 2 mm/d Along With Simulated Surface Mass Balance (B) and Melt for Both the Reference Model Runs (Using Measurements Used as Model Inputs) and the Model Run Forced by the S1 Scenario) Over the Transition Period (September–November)

Years	Precipitation		Reference model run		Scenario S1 model run	
	Amounts (m)	#P > 2 mm/d	B (m w.e.)	Melt (m w.e.)	B (m w.e.)	Melt (m w.e.)
<i>1999/2000</i>	0.42	36	−0.12	0.55	−0.05	0.50
<i>2000/2001</i>	0.32	29	−0.39	0.67	−0.16	0.45
2004/2005	0.29	32	−0.99	1.23	−1.00	1.22
<i>2005/2006</i>	0.52	48	0.11	0.45	0.22	0.35
<i>2008/2009</i>	0.25	22	−0.73	0.91	−0.69	0.87
2009/2010	0.37	30	−0.30	0.59	−0.23	0.45
<i>2011/2012</i>	0.39	35	−0.33	0.76	−0.39	0.81
<i>2012/2013</i>	0.32	26	−0.49	0.81	−0.50	0.81
2016/2017	0.13	22	−0.96	1.04	−0.90	0.98
\bar{X}	0.33	31	−0.47	0.78	−0.41	0.72
σ	0.11	8	0.37	0.26	0.40	0.29

Note. The three years in italics are years in which the annual mass loss is significantly less than the average ($B > B_{\text{mean}} + \sigma/2$). The three years in bold are those in which the annual mass loss is significant ($B < B_{\text{mean}} - \sigma/2$).

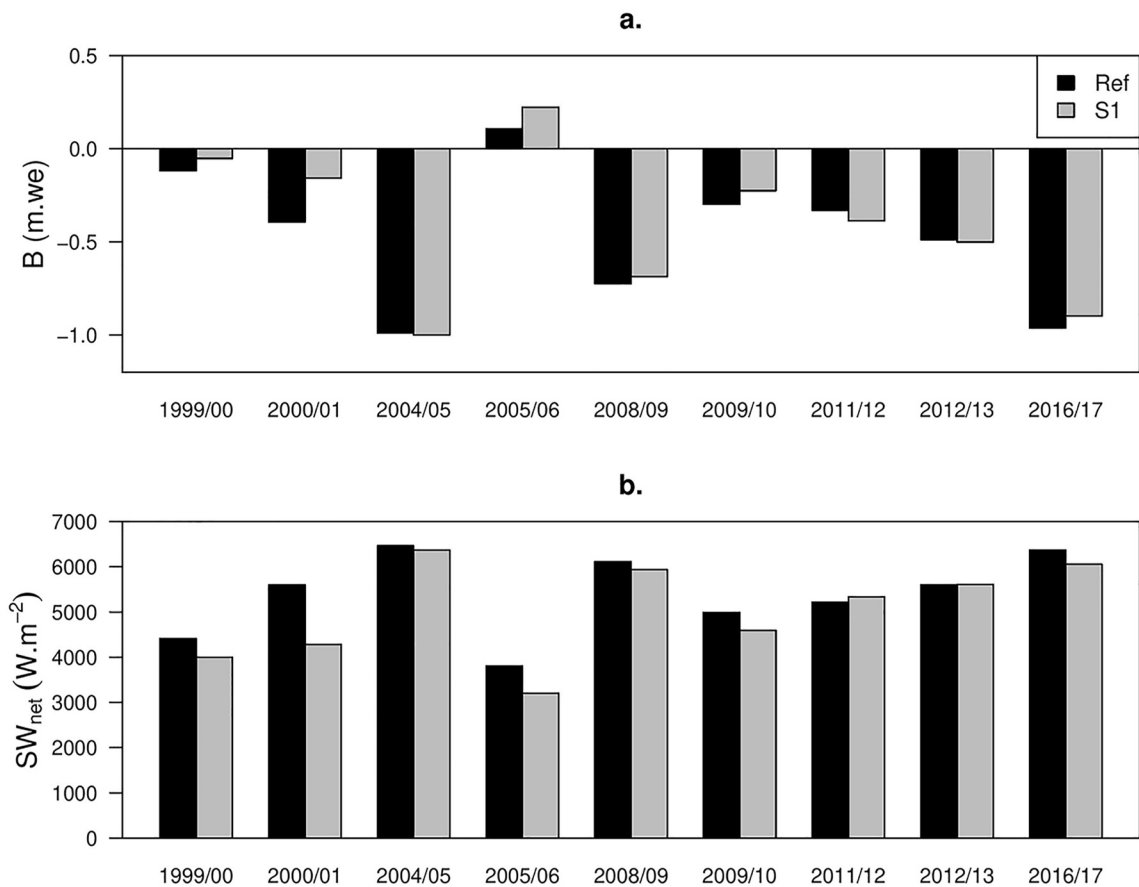


Figure 10. Simulated glacier-wide (a) surface mass balance and (b) net shortwave radiation over the transition period of all nine simulated years for both the reference model run and the precipitation scenario S1.

In contrast, for this year, scenario S3 reduced the net mass loss more than S1 and S2, as it allowed the formation of a thick snow-pack over the glacier. This snow-pack remained throughout the rest of the month due to numerous precipitation events of less than 2 mm/d (hence left untouched in the scenario).

Additionally, precipitation at the weather station during the transition period was lower in 2004/2005 than the nine-year average: 294 mm vs. 334 mm, partly explaining the strongly negative mass balance that year. The impact of the scenarios for the year 2004/2005 highlights the important role of the temporal distribution of precipitation in the surface mass balance variability.

Because scenario S1 was the scenario that generated the largest reduction in melt over the transition period, we applied this scenario to all nine simulated years.

4.2.2. Application of Scenario S1 to All Years

Figure 10 shows the impact of S1 on the surface mass balance and net shortwave energy (plots a, b). As seen, the impact of the scenarios on the net shortwave radiation and surface mass balance are very similar: the more scenario S1 reduces the net shortwave energy balance, the smaller the surface mass loss. Averaged over the nine simulated years, scenario S1 reduced the mass loss by 0.06 m w.e. over the transition season (Figure 10a) and 0.05 m w.e. at the annual scale.

Scenario S1 reduced the net shortwave radiation on average by 9% compared to the reference runs (Figure 10b). This effect is directly linked to the fact that spreading out the precipitation events maintained a greater snow cover extent (Figure 9a) and hence a higher glacier-wide albedo (Figure 9b).

The sensible heat flux was reduced by 25% and the latent heat flux was 9% less negative compared to the reference runs. These differences are linked to the different types of glacier surface: scenario S1 yielded a larger snow

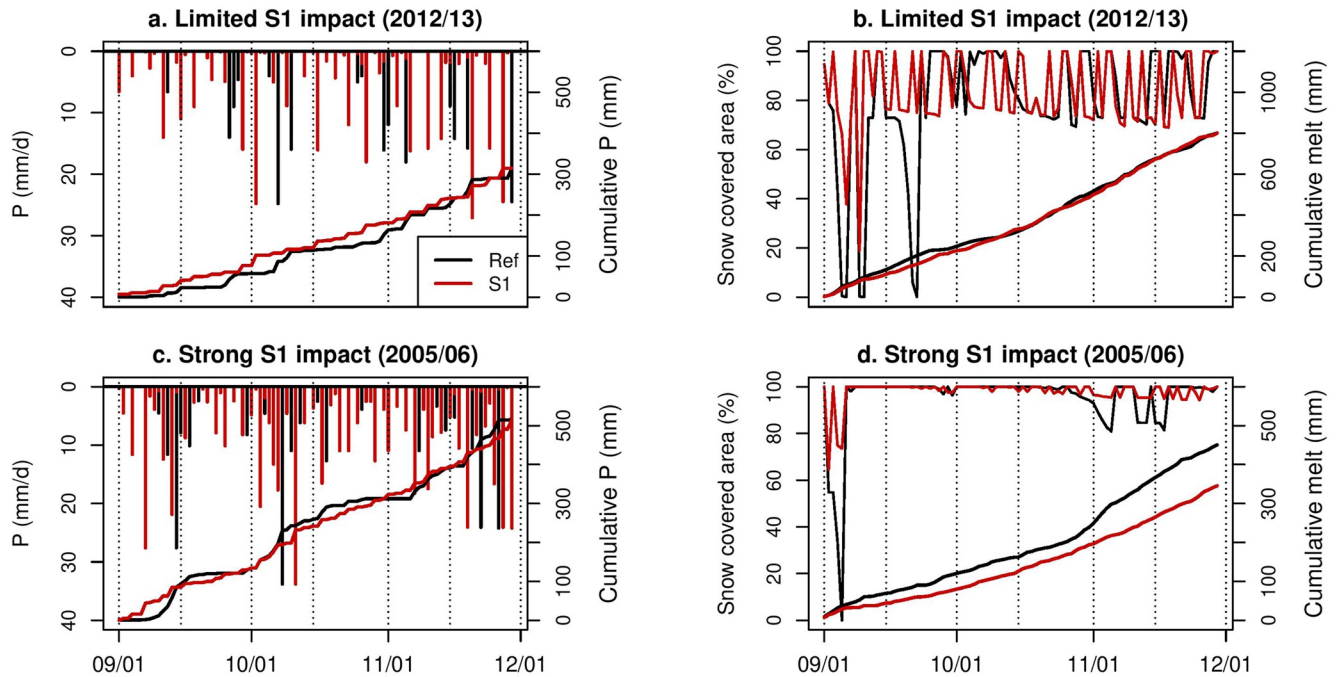


Figure 11. Comparison of precipitation scenario S1 model run with reference run for the transition period (September–November). (a, c) Daily and cumulative precipitation at the weather station used for model forcing. (b, d) Modeled daily glacier area with fresh snow and cumulative melt. Results are shown for a year where S1 has a limited impact (2012/2013, plots a, b) and a year where it has a strong impact (2005/2006, plots c, d).

cover extent than the reference run which reduced the roughness heights of wind on the surface ($z_{0\text{snow}} = z_{0\text{ice}}/10$). Despite these rather large differences, the turbulent fluxes remained small throughout the transition period and had a limited impact on melt rate. Finally, the impact scenario S1 had on the air temperature and relative humidity was negligible on the simulated surface mass balance.

Figure 11 illustrates the impact of scenario S1 in a year when it has a negligible impact on the surface mass balance (2012/2013, Figures 11a and 11b) and in a year when it has a significant impact (2005/2006, see Figures 11c and 11d and Table 4 for the numerical values).

In 2012/2013, because the measured precipitation events were well distributed (Figure 11a), scenario S1 results did not differ much from those of the reference run. In terms of mass loss at the monthly scale, for September and October, the scenario did not reduce the net mass loss much. In November a large precipitation event was missed (moved to October) causing the scenario to generate a higher mass loss than the reference run. Therefore, for this year, scenario S1 did not have much of an impact on the fresh snow cover and hence on the melt rate (Figure 11b). As for 2004/2005, the seasonal precipitation amount (316 mm) was below average (334 mm) partly explaining the large mass loss over the season.

Conversely, in 2005/2006, the observed precipitation events were concentrated (Figure 11c). In this case, spreading out the precipitation events maintained a thicker and larger cover of fresh snow on the glacier compared to the reference run resulting in a higher albedo and hence a lower melt rate (Figure 11d and Table 4). Significantly higher precipitation during the transition period (517 mm) than the long-term average (334 mm), contributed to a positive surface mass balance over this period.

Scenario S1 had contrasting impacts at the annual scale. For 2005/2006, scenario S1 limited mass loss more at the annual scale than over the transition period (see Table S1 in Supporting Information S1), because the snow-pack over the glacier at the end of November was thick enough to guarantee limited melt in December (until the arrival of the core wet season). On the other hand, in years when scenario S1 had a negligible impact over the transition season (e.g., 2012/2013), redistribution of the precipitation event resulted in a thinner snow-pack in December, as a result, the glacier-wide albedo decreased and the melt rate increased, resulting in greater annual mass loss. Overall, when scenario S1 increased the mass loss over the transition period, it increased the annual mass loss

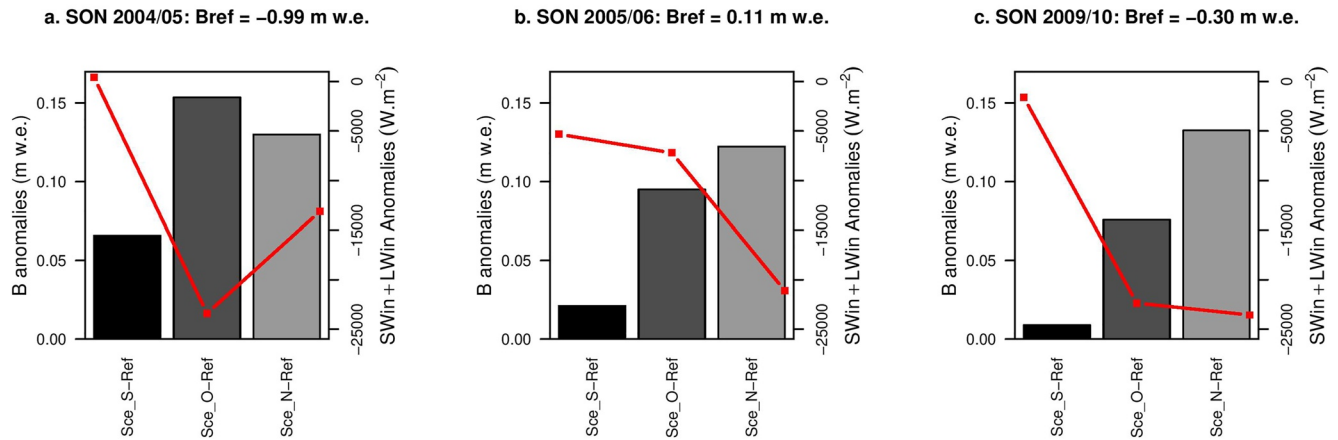


Figure 12. Transition period surface mass balance anomalies of the cloud scenarios (scenario—reference run) for three contrasting years along with their incoming radiation fluxes.

systematically (by 5% on average). This observation highlights the combined importance of the seasonal precipitation amounts and their temporal distribution on the melt rate in the period preceding the arrival of the core wet season.

In years with large annual net mass loss (2004/2005, 2009/2010, and 2016/2017), on average, scenario S1 reduced the mass loss by 0.04 m w.e. at both transition period and annual scales. In years with limited mass loss (1999/2000, 2000/2001, and 2005/2006), net mass loss was reduced by an average of 0.14 m w.e. during the transition period and 0.15 m w.e. at the annual scale. Such marked differences between years with limited mass loss and years with significant mass loss can be explained by both precipitation amounts and by the number of events greater than or equal to 2 mm/d that occurred during the transition period. As can be seen in Table 4, years with a significant mass loss had an average of 264 mm of precipitation during the transition period in 28 events, whereas years with limited mass loss had an average of 419 mm of precipitation in 38 events.

Our investigation of the energy balance components showed that the net short-wave energy budget (via an albedo feedback effect) tends to control melt. Finally, analysis of the nine years showed that the impact of any scenario is limited if the measured precipitation events are already evenly distributed over time.

4.3. Sensitivity to Cloud Scenarios

Cloud scenarios had a strong impact on the surface mass balance compared to the reference runs as they systematically reduced the melt rate (Figure 12 and Figure S4 in Supporting Information S1). Averaged over all nine years, the melt rate over the transition period decreased by 6%, 15%, and 20% in the September, October, and November scenarios respectively. At the annual scale, it decreased by 2%, 5%, and 6%, respectively, thereby underlining the strong impact of clouds on surface mass balance.

As mentioned above, the November scenario limited the mass loss most. This was true for seven out of the nine years. The two exceptions were the years 1999/2000 and 2004/2005, when the October scenario limited the melt rate most. This is because these were the only two years during which there were more clear sky days in October than in November.

Although the cloud scenarios reduced the melt rate, which implied that the albedo in the ablation zone did not decay as fast as in the reference run, they had a limited impact on the glacier-wide albedo as the ablation zone represents less than 30% of the glacier surface area.

The highest observed mean difference (considering the nine-year average) in the simulated turbulent fluxes between the scenarios and the reference runs was -5% in the October scenario. This confirms that the loss of coherence between measured parameters in the cloud scenarios has a small impact on the calculation of the turbulent fluxes.

Figure 12 shows that net mass loss during the transition period decreases as incoming radiation decreases.

Scen_S has the least impact on the surface mass balance although September is the month with the highest average number of clear-sky days: F was largest and Tn lowest (Table 2). The limited impact can be explained by the seasonal changes in incoming radiation at the top of the atmosphere. In September, the daily mean top of atmosphere shortwave radiation (\pm standard deviation of daily values) is $402 \pm 13 \text{ W m}^{-2}$, $435 \pm 6 \text{ W m}^{-2}$ in October, and $446 \pm 1 \text{ W m}^{-2}$ in November. Therefore, Scenario Scen_S reduced less incoming shortwave energy than the October or November scenarios.

Thus, the cloud scenarios had a significant impact on the surface mass balance but these are probably underestimated because adding overcast conditions over the whole month would most certainly add precipitation events that would further limit the mass loss. Basic statistics linking the number of cloudy days and precipitation during the transition period in the nine years showed that there is an average of one precipitation event of 4.5 mm w.e. per 1.7 cloudy days. From this information, adding 10 cloudy days in September would add six precipitation events whereas adding six cloudy days in October and November would add three to four precipitation events.

5. Summary and Conclusions

A nine-year data set at hourly time scale was used as input data for a distributed energy mass balance model on Zongo Glacier. This allowed the evaluation of different processes that impact the melt rate and the mass balance.

In contrast to previous classifications based on surface mass balance variations (e.g., Rabatel et al., 2012, 2013) or precipitation and melt rates (Sicart et al., 2011), we found that three seasons (wet, dry, and transition) can be identified based on the cloud radiative properties. During the transition period, clouds have a moderate impact on the sum of the incoming short and longwave radiation fluxes with a peak distribution centered around -120 W m^{-2} . During the wet season, the clouds have a strong attenuation impact on the incoming radiation fluxes with a peak around -150 W m^{-2} . Such a strong impact is typical of thick (sunlight attenuating) cumulus-type clouds resulting from convective events. Finally, during the dry season, the cloud impact on the incoming radiation fluxes is low (peak around -20 W m^{-2}), which is typical of thin high-altitude clouds. The changes in cloud radiative properties have an impact on the melt rate especially toward the end of the transition season and during the wet season when solar attenuation is at its maximum as these offset the effect of the increased top of atmosphere radiation (as it is the austral summer).

During model calibration, we found that adjusting the DEMs and glacier contours for each year enhanced the simulation precision specifically for years with significant mass loss because, for these years, melt would otherwise be overestimated.

Melt energy and its interannual variations were maximum during October and November which means that it is a key period in controlling the annual variability of the surface mass balance. Although some energy was available during the dry season, most was converted into ground heat flux due to the intense night cooling of the glacier surface thereby shortening the daily melting period, resulting in low melt rates.

The sensitivity analysis of the distribution of the precipitation events over the transition period validated the hypothesis that the frequency of precipitation events is a key driver of the interannual variability of the surface mass balance: evenly distributed precipitation events with no change in the seasonal snow amounts maintained a larger cover of fresh snow on the glacier surface, which increased the glacier-wide albedo. As a result, the net shortwave radiation budget was reduced, in turn reducing the melt rate. The contrasting impacts on the melt rate reduction (very strong impact in years with average or above average seasonal precipitation amounts and smaller impact in years with below average precipitation) highlights the combined importance of the distribution of precipitation events over time and of the seasonal precipitation amounts.

The sensitivity analysis of the cloud cover showed that prolonged cloudy periods in October—and more particularly in November—had the potential to dramatically reduce the melt rate at both the seasonal and annual scales. A sustained cloud cover in November had more impact than in the other months of the transition period as November is the month when potential solar irradiance is close to its annual maximum.

These results emphasize the role of the onset of the wet season on the annual glacier surface mass balance as hypothesized by Sicart et al. (2011) based on the analysis of the seasonal changes of the energy fluxes during one hydrological year.

All in all, the temporal distribution of precipitation is a key driver of the interannual variability of the surface mass balance via an albedo feedback effect that reduces the net shortwave radiation budget (main driver of melt) and hence the melt rate.

The methodology used to generate the precipitation scenarios could be used to assess past and future climate over Zongo Glacier using paleoclimate proxy information or global climate model (GCM) outputs to constrain climate scenarios. Such studies would be of interest as the future of Zongo Glacier and the neighboring glaciers in the Cordillera Real of Bolivia is crucial both in terms of water supply and for hydroelectricity production.

Data Availability Statement

The data used in this study can be found at the following link: <https://glacioclim.osug.fr/335-Energy-balance-on-a-tropical-glacier-in-Bolivia> (Autin et al., 2022).

Acknowledgments

This study has been realized within the framework of the Andean part of the French *Service National d'Observation GLACIOCLIM* (www.glacioclim.osug.fr, UGA-OSUG, CNRS-INSU, IRD, IPEV, INRAE), and the International Joint Laboratory LMI GREAT-ICE (IRD, EPN-Quito). The glaciological program is coordinated in La Paz by Dr. Soruco (IGEMA-UMSA) who organizes, in particular, the follow-up of the glaciological measurements in Bolivia. The authors are grateful to everyone that has been involved in the long-term in situ monitoring program on Zongo Glacier. All authors acknowledge the support of LabEx OSUG@2020 (*Investissements d'Avenir*—ANR10_LABX56).

References

- Abermann, J., Kinnard, C., & MacDONELL, S. (2014). Albedo variations and the impact of clouds on glaciers in the Chilean semi-arid Andes. *Journal of Glaciology*, 60(219), 183–191. <https://doi.org/10.3189/2014jog13j094>
- Autin, P., Sicart, J. E., Rabatel, A., Soruco, A., & Hock, R. (2022). Climate controls on the interseasonal and interannual variability of the surface mass and energy balances of a tropical glacier (Zongo Glacier, Bolivia, 16°S): New insights from the multi-year application of a distributed energy balance model dataset [Data Set]. Retrieved from <https://glacioclim.osug.fr/335-Energy-balance-on-a-tropical-glacier-in-Bolivia>
- Beljaars, A. C. M., & Holtslag, A. A. M. (1991). Flux parameterization over land surfaces for atmospheric models. *Journal of Applied Meteorology and Climatology*, 30(3), 327–341. [https://doi.org/10.1175/1520-0450\(1991\)030<0327:fpolsf>2.0.co;2](https://doi.org/10.1175/1520-0450(1991)030<0327:fpolsf>2.0.co;2)
- Bradley, R. S., Keimig, F. T., Diaz, H. F., & Hardy, D. R. (2009). Recent changes in freezing level heights in the tropics with implications for the deglaciation of high mountain regions. *Geophysical Research Letters*, 36(17), L17701. <https://doi.org/10.1029/2009gl013712>
- Braun, M., & Hock, R. (2004). Spatially distributed surface energy balance and ablation modeling on the ice cap of King George Island (Antarctica). *Global and Planetary Change*, 42(1–4), 45–58. <https://doi.org/10.1016/j.gloplacha.2003.11.010>
- Cuffey, K. M., & Paterson, W. S. B. (2010). *The physics of glaciers* (Vol. 504). Amsterdam: Academic Press. Cambridge University Press (CUP).
- Cusicanqui, D., Soruco, Á., Rabatel, A., & Anthelme, F. (2015). Mass balance of Zongo Glacier between 2006 and 2013 using volumetric method, employing Pléiades high-resolution images acquired over the Cordillera Real, Bolivia (16°S, 68°W). *Revista Boliviana de Geociencias*, 8(7), 5–20.
- Dussailant, I., Berthier, E., Brun, F., Masiokas, M., Hugonnet, R., Favier, V., et al. (2019). Two decades of glacier mass loss along the Andes. *Nature Geoscience*, 12(10), 802–808.
- Espinoza, J. C., Ronchail, J., Lengaigne, M., Quispe, N., Silva, Y., Bettolli, M. L., et al. (2013). Revisiting wintertime cold air intrusions at the east of the Andes: Propagating features from subtropical Argentina to Peruvian Amazon and relationship with large-scale circulation patterns. *Climate Dynamics*, 41(7–8), 1983–2002. <https://doi.org/10.1007/s00382-012-1639-y>
- Franco, B., Ribstein, P., Saravia, R., & Tiriau, E. (1995). Monthly balance and water discharge of an inter-tropical glacier: Zongo Glacier, Cordillera Real, Bolivia, 16°S. *Journal of Glaciology*, 41(137), 61–67. <https://doi.org/10.3189/s0022143000017767>
- Franco, B., Vuille, M., Favier, V., & Cáceres, B. (2004). New evidence for an ENSO impact on low-latitude glaciers: Antizana 15, Andes of Ecuador, 0°28'S. *Journal of Geophysical Research: Atmospheres*, 109(D18).
- Garreaud, R. (2000). Intraseasonal variability of moisture and rainfall over the South American Altiplano. *Monthly Weather Review*, 128(9), 3337–3346. [https://doi.org/10.1175/1520-0493\(2000\)128<3337:ivomar>2.0.co;2](https://doi.org/10.1175/1520-0493(2000)128<3337:ivomar>2.0.co;2)
- Garreaud, R., Vuille, M., & Clement, A. C. (2003). The climate of the Altiplano: Observed current conditions and mechanisms of past changes. *Paleogeography, Paleoclimatology, and Paleoecology*, 194(1–3), 5–22. [https://doi.org/10.1016/s0031-0182\(03\)00269-4](https://doi.org/10.1016/s0031-0182(03)00269-4)
- Garreaud, R., & Wallace, J. M. (1998). Summertime incursions of midlatitude air into subtropical and tropical South America. *Monthly Weather Review*, 126(10), 2713–2733. [https://doi.org/10.1175/1520-0493\(1998\)126<2713:siomai>2.0.co;2](https://doi.org/10.1175/1520-0493(1998)126<2713:siomai>2.0.co;2)
- Gurgiser, W., Marzeion, B., Nicholson, L., Ortner, M., & Kaser, G. (2013). Modeling energy and mass balance of Shallap Glacier, Peru. *The Cryosphere*, 7(6), 1787–1802. <https://doi.org/10.5194/tc-7-1787-2013>
- Gurgiser, W., Mölg, T., Nicholson, L., & Kaser, G. (2013). Mass-balance model parameter transferability on a tropical glacier. *Journal of Glaciology*, 59(217), 845–858. <https://doi.org/10.3189/2013jog12j226>
- Hardy, D. R., Vuille, M., Braun, C., Keimig, F., & Bradley, R. S. (1998). Annual and daily meteorological cycles at high altitude on a tropical mountain. *Bulletin of the American Meteorological Society*, 79(9), 1899–1913. [https://doi.org/10.1175/1520-0477\(1998\)079<1899:aadmca>2.0.co;2](https://doi.org/10.1175/1520-0477(1998)079<1899:aadmca>2.0.co;2)
- Hastenrath, S. (1997). Measurements of diurnal heat exchange on the Quelccaya Ice Cap, Peruvian Andes. *Meteorology and Atmospheric Physics*, 62(1), 71–78. <https://doi.org/10.1007/bf01037480>
- Hock, R. (1998). *Modeling of glacier melt and discharge*. (Doctoral dissertation). Retrieved from <http://www.agu.org/pubs/cross-ref/2009/2009JD011949.shtml>
- Hock, R., & Holmgren, B. (2005). A distributed surface energy-balance model for complex topography and its applications to Storglaciären. *Journal of Glaciology*, 51(172), 25–36.
- Hock, R., & Tijm-Reijmer, C. (2012). *A mass-balance, glacier runoff, and multi-layer snow model DEBAM and DETIM distributed energy balance and distributed enhanced temperature index model users manual [software manual]*. Retrieved from <http://www2.gi.alaska.edu/~regine/modelmanual.pdf>
- Hurley, J. V., Vuille, M., & Hardy, D. R. (2016). Forward modeling of $\delta^{18}\text{O}$ in Andean ice cores. *Geophysical Research Letters*, 43(15), 8178–8188. <https://doi.org/10.1002/2016gl070150>
- Kaser, G. (1999). A review of the modern fluctuations of tropical glaciers. *Global and Planetary Change*, 22(1–4), 93–103. [https://doi.org/10.1016/s0921-8181\(99\)00028-4](https://doi.org/10.1016/s0921-8181(99)00028-4)

4.6 Summary

Climate controls of Zongo Glacier's surface mass balance

Temperature and surface mass balance:

- Temperature and the surface mass balance **in the ablation zone** are significantly correlated at the annual scale and during the wet season. This is because temperature impacts the rain-snow limit, thus, warmer temperature can cause rain over the lower reaches of the glacier
- Temperatures and **glacier-wide** surface mass balance do not share a common variance. This is because they are negative over most of the glacier all year round.

Cloud radiative properties:

- Probability density functions of the cloud radiative properties can be used to identify the main seasons over the glacier.
- Annual mean values of F , T_n and CI yield trustworthy correlations with B_{Abla} .
- Precipitation events mostly occur on days with highly negative CF values.

Precipitation and surface mass balance:

- Precipitation amounts and number of events have a significant percentage of common variance with the glacier-wide annual surface mass balance.
- Monthly precipitation amounts and number of events have a significant percentage of common variance with the monthly surface mass balance in the ablation zone.

Analysis of the wet season:

- The methods used to identify the wet season onset share little common variance, suggesting that they are poorly correlated.
- Local cloud cover index method shares the highest common variance with regional methods ($R^2 = 0.52$). This suggests that clouds over the glacier have a stronger link to synoptic conditions than local precipitation events.
- The variability of the wet season onset shows no link with the annual glacier-wide surface mass balance variability.

Climate controls on the surface mass balance assessed with DEBAM

- The transition season is the season with the highest amount of energy available for melt.
- Most of the melt rate differences between years of contrasted surface mass balance occurs between September and November.
- Precipitation timing and associated amounts are key drivers of melt.
- A sustained cloud cover over November has a strong potential in limiting annual mass losses.

Chapter 5 - Assessment of the climate which allowed the glacier to reach its Little Ice Age maximum extent

Section 5.1 investigates the climate which allowed Zongo Glacier to reach its maximum extent during the Little Ice Age. As mentioned in Chapter 1, since tropical glaciers react rapidly to changes in climate, they are suitable paleoclimate proxies. Applying a surface energy balance model over the glacier's past extents allows the validation of hypothetical past climate scenarios. In this context, we forced DEBAM with climate scenarios over the Little Ice Age glacier maximum extent in order to identify seasonal changes in precipitation which may have occurred then. Besides, reconstructing the LIA climate allows us to validate the finding of the current climate controls on the surface mass balance (precipitation amounts, timing and cloud cover). This study is presented under the form of the article which we submitted to *Comptes Rendus Géoscience* of the French Academy of Sciences. This article is followed by a small complement regarding the findings of Jomelli et al. (2011, presented in Chapter 1).

Section 5.3 presents a sensitivity study of the simulated surface mass balance to the precipitation and surface temperature altitudinal gradients. These two parameters were assessed because, on top of being poorly known, in the LIA simulations, we lowered the position of the meteorological forcing by 200 m (detailed in section 5.1). Hence, applying the precipitation gradient up to 5400 m a.s.l. (current climate parameterization, Chapter 3) resulted in unrealistically high precipitation amounts over the upper reaches of the glacier. Similarly, lowering the position of the meteorological forcing and considering a constant surface temperature resulted in erroneous simulated turbulent heat fluxes.

5.1 Little Ice Age climate reconstruction

Climate reconstruction of the Little Ice Age maximum extent of the tropical Zongo Glacier using a distributed energy balance model

Philémon AUTIN¹, Jean Emmanuel SICART¹, Antoine RABATEL¹, Regine HOCK^{2,3}, Vincent JOMELLI⁴

¹ Univ. Grenoble Alpes, CNRS, IRD, Grenoble-INP, Institut des Géosciences de l'Environnement (IGE, UMR 5001), F-38000 Grenoble, France

² Department of Geoscience, Oslo University, Oslo, Norway

³ Geophysical Institute, University of Alaska, Fairbanks, AK, United States of America

⁴ CNRS Cerege, Technopôle de l'Environnement Arbois-Méditerranée, Aix en Provence, France

To be submitted to: *Comptes Rendus Géosciences de l'Académie des Sciences*

Corresponding author:

Philémon AUTIN

Institut des Géosciences de l'Environnement

Bâtiment Glaciologie

54, rue Molière

38400 Saint Martin d'Hères – France

+33 (0)4 76 82 42 10

philemon.autin@univ-grenoble-alpes.fr

Abstract

This study assessed the climate conditions that caused the tropical Zongo Glacier (16°S, Bolivia) to reach its Little Ice Age (LIA) maximum extent in the late 17th century. For this, we used sensitivity analyses of the annual surface mass balance in different physically coherent climate scenarios constrained by information taken from paleoclimate proxies and sensitivity studies of past glacier advances. The scenarios were constructed using shuffled input hourly data for the model: measurements of air temperature and relative humidity, precipitation, wind speed, incoming short and longwave radiation fluxes, and assessed using a distributed energy balance model. They were considered plausible if close to equilibrium glacier-wide mass balance conditions were obtained. Results suggest that a 1.1 °C cooling and ~ 20% increase in annual precipitation compared to current climate was required. Two different precipitation patterns allow LIA equilibrium: evenly distributed precipitation events across the year and an early wet season onset.

Key words: Tropical glacier, Surface energy balance model, Little Ice Age climate

1 Introduction

The Little Ice Age (LIA) was a multi-secular cold period, lasting roughly from 1350 to 1850 AD, during which glaciers advanced worldwide (e.g., Solomina et al., 2015; 2016). The magnitude and timing of the glacial advances was not synchronous worldwide (Grove, 1988; Rabatel et al., 2008; Neukom et al., 2014; Solomina et al., 2015, 2016). The evolution of glaciers since the Little Ice Age has been most frequently studied in mid-latitudes. In the French Alps, glaciers reached their maximum extent around the first half of the 17th century and their front oscillated in a position slightly up-valley before readvancing close to their maximum extent throughout the first half of the 19th century (e.g., Grove, 1988; Vincent et al., 2004; 2005, Solomina et al., 2015; 2016). Paul & Bolch (2019) reviewed a number of studies of the evolution of Alpine glaciers since the LIA and concluded that it could be summarized by a km scale retreat, a rise in the equilibrium-line altitude (ELA) of 100-200 m, and an up-shift of several hundred meters in glacier terminus positions. In Pyrenean glaciers, Campos et al. (2021) reported ELA rises of 220 m.

On the other hand, the evolution of glaciers in Tropical South America since the LIA has been the subject of few studies. The majority of glaciers reached their maximum extent between 1630 and 1720 and have been retreating ever since; their retreat has been interrupted

several times by minor advances (Rabatel, 2005; Rabatel et al., 2005; 2008; Jomelli et al., 2009; 2011). Based on the dating of 15 Bolivian glaciers using lichenometry, radiocarbon or ^{10}Be techniques, Rabatel et al. (2008) estimated that their ELA rose by 285 ± 50 m since the LIA while, based on the Telata Glacier also in Bolivia, Jomelli et al. (2011) estimated that the ELA rose by 320 m.

Understanding past glacier variations is a key to better insights into future changes. In the case of tropical glaciers, this is of particular interest as they represent an important water resource for Andean populations (e.g., Soruco et al., 2015). Tropical glaciers react rapidly to climate perturbations (by advancing or retreating, e.g., Kaser, 2001; Thompson et al., 2006) making them suitable paleoclimate proxies to evaluate past climate scenarios.

Over tropical South America, paleoclimate proxies such as ice cores, sediments, tree rings or speleothems (e.g., Thompson et al., 2006; Ledru et al., 2013; Apaestegui et al., 2018; Campos et al., 2019) and glacier sensitivity analyses (e.g., Rabatel et al., 2005, 2008; Malone et al., 2015) provide valuable temperature and precipitation data on the LIA. The main drawback of these methods is the temporal scale (annual to decadal). For example, glacier studies usually use simple approaches (e.g. simplified energy balance methods, Hastenrath and Ames, 1996) which only allow comparison of glacier steady state conditions at two different periods, but do not provide detailed insights into seasonal changes in climatic forcing on the glacier mass balance.

The annual mass balance of South American tropical glaciers depends on the timing and length of the wet season during the austral summer (Sicart et al., 2011) and they are highly sensitive to the temporal distribution of precipitation between September and the onset of the wet season (Autin et al., 2022). Several studies suggest that the onset and length of the wet season may have changed during the Little Ice Age (e.g. Diaz and Vera, 2018), a feature that cannot be captured by models using annual temperature and precipitation amounts. Hence, such models may largely underestimate past mass balance variability (Sicart et al., 2011). In addition, sub-annual precipitation records are rare over low latitude mountains and precipitation predictions are unreliable, making reconstructing past glacier advances and estimating future retreat challenging in these regions.

In this study, we used the distributed energy balance model (DEBAM, Hock and Holmgren 2005) that had been adapted to tropical glaciers by Sicart et al. (2011). This model is based on equations of mass and energy conservation and, in theory, the physical

interpretation of the parameters can be linked to measurable quantities (Beven, 1989). However, because natural sub-grid heterogeneities can lead to a mismatch of scales between measured and modeled variables, the calibration process is often complicated (Klemes, 1983; Seibert, 1999). Thus, to limit the risk of using a model calibration that makes the model subject to the three rules of classical tragedy: unity of place, unity of action and unity of time (De Marsily, 1994), a parsimonious approach was chosen to minimize the number of parameters with the aim of matching model complexity to the availability of field observations. In this way, we expect that even if the models represent more fiction than reality, the fiction nevertheless helps understand reality (Seibert, 1999).

We chose to apply the model to the tropical Zongo Glacier (16°S, Bolivia) because this glacier's present-day climate controls have already been well studied (e.g., Rabatel et al., 2013; Autin et al., 2022) and its LIA maximum reconstructed (Rabatel, 2005). Run at an hourly time step, this model makes it possible to investigate the effect of changes in seasonal precipitation patterns on the surface mass balance at the LIA maximum extent of the glacier.

For this purpose, we created scenarios that differ in precipitation amounts and seasonality but where the physical consistency between measured meteorological variables is retained (i.e. physically-coherent scenarios). The scenarios that resulted in an equilibrium state (surface mass balance close to zero) were considered plausible LIA scenarios.

2. Study site and background on the LIA in the tropical Andes

2.1 Study site and present climate

Zongo Glacier (16°15'S, 68°10'W, Cordillera Real, Bolivia) is a valley-type glacier extending from ~6,000 m a.s.l. down to ~4,950 m a.s.l. A glacier monitoring program began in 1991 through collaboration between a Bolivian university (*Universidad Mayor de San Andrés*) and IRD (French Research Institute for Development, Francou et al., 1995; Ribstein et al., 1995). Rabatel et al. (2013) and Sicart et al. (2015) provide a detailed overview of the monitoring network, which includes three automatic weather stations (AWS), one on the glacier, and two off-glacier, along with a discharge gauging station, and several ablation stakes and snow pits (Figure 1).

Being in the outer tropics, the climate over the glacier is characterized by marked precipitation and cloud cover seasonality, with a single wet season in austral summer and a pronounced dry season in austral winter (Troll, 1941). A number of authors have identified

and described three seasons with distinct melt mechanisms over this tropical glacier where the hydrological year starts on the first of September (e.g., Sicart et al., 2011, Rabatel et al., 2012, Autin et al., 2022).

The transition season (September to November) is characterized by increasing melt rates due to limited precipitation (around 20% of the annual amount, Ramallo, 2013) and increasing solar radiation as the top of atmosphere radiation approaches its maximum annual value reached at the austral summer solstice (Sicart et al., 2011). Autin et al. (2022) simulated nine years of distributed surface energy balance over Zongo Glacier using DEBAM and showed that this period plays a key role in controlling annual mass losses and that the timing of precipitation events in the season is a key driver of melt.

The wet season (December to March) is linked to the mature phase of the South American monsoon system (SAMS). During the SAMS, a strong anticyclonic system in the upper troposphere (the Bolivian High, Lenters and Cook, 1997) coupled with the southward displacement of the South American low-level jet (SALLJ) result in strong easterly winds on the eastern slopes of the Cordillera Real. This leads to moisture transport over the Cordillera Real, which, coupled with solar heating of the surface, results in frequent afternoon/early evening convection events over Zongo (e.g., Garreaud et al., 2003). This season is characterized by decreasing melt rates due to the strong cloud cover and albedo feedback effect. Over this period, little mass loss is observed as most of the melt comes from large snowfall events (70% of the annual amounts, Ramallo, 2013). In addition, it is the glacier accumulation season.

April - May is a second transition period from the end of the wet season to the onset of the dry season (June to August). During this period, the precipitation amounts and distribution are highly variable due to the interannual variability of the demise of the wet season (based on 18 years of measurements, the amount of precipitation received over this period is 50 ± 27 mm w.e.).

The dry season is characterized by low melt rates and rare precipitation events. The absence of clouds in the dry season creates an incoming longwave radiation deficit leaving little energy available for melt (Sicart et al., 2011). In addition, the dry and cold air coupled with high wind speeds favors sublimation over melt (Wagnon et al., 1999, Sicart et al., 2005) resulting in limited mass loss over this period.

A number of studies (e.g., Sicart et al., 2005; Wagnon et al., 1999) identified the net all-wave radiation flux as the main driver of melt at seasonal and interannual time scales, more specifically, the incoming shortwave radiation flux. Autin et al. (2022) showed that melt energy is highest during the transition season and that the interannual variability of the surface mass balance is mostly driven by the temporal distribution of precipitation events and their amounts and, to a lesser extent, by the cloud cover throughout this season. Similarly, Sicart et al. (2005; 2016) showed that the marked cloud and precipitation seasonality is an important factor in controlling seasonal mass balance variability.

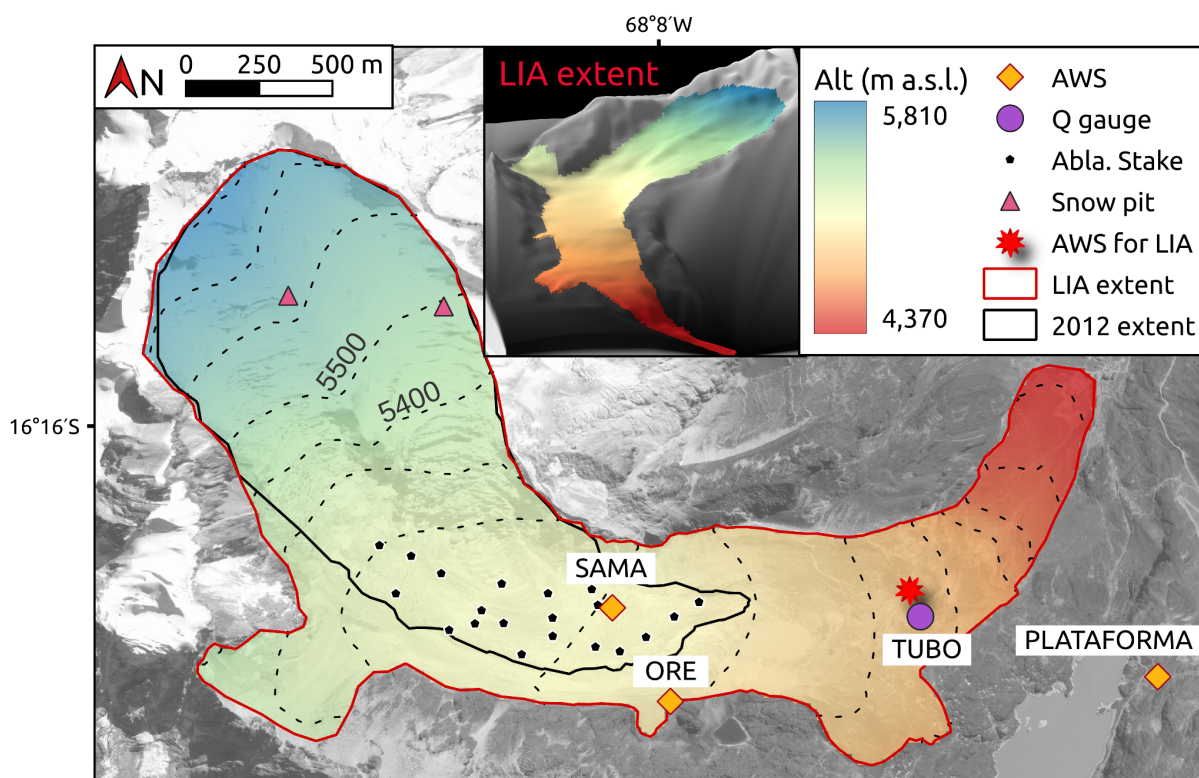


Figure 1. Zongo Glacier ($16^{\circ}15'S$, $68^{\circ}10'W$) showing its monitoring network. The red line represents the maximum extent of the LIA and the corresponding digital elevation model, the black line shows the extent of the glacier in 2012. The map in the top inset is a 3D view of the extent of the glacier at its LIA maximum extent. SAMA (5050 m a.s.l.), ORE (5050 m a.s.l.) and PLATAFORMA (4750 m a.s.l.) are the three automatic weather stations (AWS) installed on and around the glacier, TUBO is a discharge gauging station located at 4,830 m a.s.l. The red star shows the position at which the measurements are used to force the model in LIA simulations. Source of the background image: Pleiades satellite in 2013, © CNES - Airbus D&S. Digital Elevation Model: Rabatel (2005).

2.2 LIA climate reconstructions in the tropical Andes

Ice cores are paleoclimate proxies that provide valuable information at seasonal and annual scales over the last 1,000 years as well as information at a coarser temporal scale over the last 20,000 years (Vimeux et al., 2009; Hurley et al., 2019). Using an ice core drilled in the Quelccaya ice cap (QIC, southern Peru), Thompson et al. (1986, 2006) showed a significant decrease in both $\delta^{18}\text{O}$ and dust concentration during the LIA (1500-1800 AD) that they associated with a decrease in temperatures. More recently, Hurley et al. (2019) showed that changes in $\delta^{18}\text{O}$ are primarily linked with ENSO activity which, in turn, is related to changes in the activity of the South American monsoon system (SAMS) rather than temperature changes. Thus, in agreement with Hurley et al., (2019), we consider that the lower $\delta^{18}\text{O}$ observed during the LIA is associated with increased precipitation rather than with colder temperatures.

Morales et al. (2012) analyzed *Polylepis Tarapacana* tree rings across the Altiplano to reconstruct the climate between 1300 and 2000 AD and found that sustained wet conditions prevailed between 1600 and 1750 AD leading to precipitation positive anomalies (up to 40% at its highest with respect to the average measurement for the period 1982–2000).

Speleothems (Campos et al., 2019; Apaestegui et al., 2018; Vuille et al., 2012) and sediments of diverse origin (Ledru et al., 2013; Bird et al., 2012; Sachs et al., 2009; Haug et al., 2001) provide information on changes in temperature and precipitation patterns over the past 2000 years. Their wide spatial availability across tropical South America enables a 2000-year reconstruction of the SAMS. These studies suggest that a southern shift of the Inter Tropical Convergence Zone (ITCZ) linked to decreased radiative forcing (Maunder minimum, 1645–1715 AD, Lean, 2000) caused colder North Atlantic Sea Surface Temperatures during the LIA, resulting in an intensification of SAMS that led to unprecedented moisture levels over the Eastern Cordillera.

Díaz and Vera (2018) assessed four Paleoclimate Model Intercomparison Project 3 / Climate Model Intercomparison Project 5 (PMIP3/CMIP5, Braconnot et al., 2011) model ensemble runs between 850 and 2005 AD over South America. These authors found that the models can correctly reproduce temperature variations over the past millennium (with respect to paleoclimate proxy information) but cannot represent the associated changes in precipitation. Similarly, we considered temperature and precipitation time series of two

ensemble runs with paleoclimate proxy information from Michel (2020) and Tardiff et al. (2019) thereby corroborating the findings of Diaz and Vera (2018).

Diaz and Vera (2018) also analyzed large-scale atmospheric conditions (250 hPa and 800 hPa zonal winds) of PMIP3/CMIP5 ensemble runs and showed an equatorial shift of the southern branch of the Hadley cell during the LIA that resulted in a wetter tropical South America (Lu & Vecchi, 2014). However, because the simulated precipitation amounts do not match proxy information, these models cannot be used to compare past precipitation amounts and present conditions.

Glacier modeling can be used to assess climate conditions which lead to a known past glacier extent. Based on a synthesis of sensitivity studies of tropical South American glaciers, Kaser (1999) attributed two thirds of the glacier retreat in the Cordillera Blanca since the LIA to a decrease in vapor pressure, and the remaining third to an increase in air temperature. Malone et al. (2015) applied a coupled ice-flow mass balance model on the Quelccaya Ice Cap to reconstruct annual climate conditions during the LIA and concluded that the glacier is more sensitive to temperature than to precipitation. Finally, Rabatel et al. (2005, 2008) applied the Kaser (2001) model and Hastenrath (1984) approach to Bolivian tropical glaciers and found that for the glaciers to have reached their maximum extent during the LIA, a 20-30% increase in precipitation (that goes hand-to-hand with an increase in cloudiness) and cooler temperatures (~ 1 to 1.2 °C) with respect to today's climate conditions would have been required.

These different studies converge on the LIA climate: there was an increase of between 20% and 40% in annual precipitation and it was about 1 °C cooler. However, uncertainties on how this extra precipitation was distributed within the year remain, which is just what our study aims to clarify, as using an energy balance model is the only way to investigate the effect of seasonal precipitation patterns on the annual surface mass balance.

3. Method

We used the distributed surface energy balance model (DEBAM, Hock and Holmgren, 2005) to simulate the glacier surface mass balance of Zongo Glacier over the reconstructed surface area of the glacier during the LIA. The model is forced by hourly time series of meteorological data based on measurements recorded by an automatic weather station in nine years distributed between 1999 and 2017. The observations are used to

construct four climate scenarios that are then assessed based on their ability to yield a near-balanced mass budget. Further details are given below.

3.1 Mass balance model

3.1.1 Model description

DEBAM simulates the glacier surface mass balance and melt discharge at hourly intervals over the grid cells of a digital elevation model (20×20 m cells) using an energy-balance approach (Hock and Holmgren, 2005). In this study, we use the multi-year calibration of Zongo by Autin et al. (2022). The model requires seven input meteorological variables (air temperature and relative humidity, wind speed, precipitation, incoming short and longwave radiation and outgoing longwave radiation) and solves the following surface energy balance equation:

$$Q_M = SW_{in}(1 - \alpha) + LW_{net} + H + LE + Q_G + R \quad (1)$$

where Q_M is the melt energy, SW_{in} is the incoming shortwave radiation, α the albedo, LW_{net} the net longwave radiation balance, H and LE are the turbulent sensible and latent heat fluxes, respectively, Q_G is the subsurface heat flux and R the sensible heat supplied by rain (negligible over Zongo Glacier, Sicart et al., 2011). The model convention is such that energy fluxes directed towards the surface are positive and those away from the surface are negative.

Incoming shortwave radiation was extrapolated across the glacier by splitting it into its direct and diffuse components. The albedo was modeled using a version of Oerlemans and Knap (1998)'s albedo parameterization adapted to tropical glaciers. This parametrization accounts for the rapid alternation (a few days) of accumulation and melt in the wet season, and the impact of ice on the albedo over shallow snow depths (Sicart, 2002). The incoming longwave radiation flux was assumed to be spatially constant.

Surface temperature was calculated at the AWS from the outgoing longwave radiation measurements and an altitudinal gradient of -0.1 °C/100 m was applied to extrapolate surface temperatures across the glacier (with an upper limit of 0 °C). The subsurface snow module (Hock and Tijm-Reijmer, 2012) was not used to evaluate spatial changes in the surface temperature due to lack of data to constrain the model (i.e. subsurface temperature and density profiles). This implies that we neglected the sub-surface heat flux in our simulations.

The sensible and latent turbulent heat fluxes were calculated according to the aerodynamic profile method between the glacier surface and the measurement height (wind speed, air temperature and relative humidity) based on the Monin-Obukhov similarity theory (see Hock and Holmgren, 2005 for more details). The stability functions were based on Beljaars and Holtslag (1991) for stable conditions and on the Businger-Dyer expressions from Paulson (1970) for unstable conditions. Relative humidity and wind speed were considered spatially constant across the glacier.

Discharge at the glacier terminus was simulated using a runoff module that routes glacier melt and rain water through the glacier using three linear reservoirs representing firn, snow and ice (storage constants of 350, 30 and 16 h, respectively, taken from Sicart et al., 2011) In addition, for non-glacierized surfaces (30% of the catchment in the recent climate), a runoff coefficient of 0.8 was considered (based on Ribstein et al., 1995).

3.1.2 Model calibration and validation

We used the model parameter values from Autin et al. (2022), who calibrated and validated the model over Zongo Glacier over nine years, distributed between 1999 and 2017. This calibration was a trade-off between years with high and low mass losses where particular emphasis was placed on accurately representing the transition and the wet season, as they play a key role both in the annual surface mass balance and in year-to-year variability. The transition season is the period when the glacier loses on average half its annual mass loss in the ablation zone, while the wet season is the accumulation period. Because their calibration did not include the multi-layer snow model, melt is overestimated during the dry season (JJA) which contributes to most of the average annual net mass loss overestimation (based on the 9 simulated years, the mass loss overestimation is 0.18 m w.e., when the average mass loss is -0.88 m w.e., Autin et al., 2022).

Analysis of 19 years of daily discharge and precipitation data provided by Ramallo (2013) showed that only 9% of the annual volume passes through the weir at TUBO (Fig. 1) during the dry season, given that not all the discharge is a result of glacier mass loss, as an average of 4.3% of the annual precipitation occurred over the same period. Nonetheless, most of the discharge observed at TUBO comes from the glacier meltwater as its catchment is 70% glacierized and the snow on the moraines melts completely in a few days (e.g. Lejeune, 2009). Hence, this low discharge highlights the limited mass loss that occurs during this season (see also Autin et al., 2022; Sicart et al., 2011).

Therefore, the dry season is generally a period of low ablation whereas the high variability of the mass balance in the transition and wet seasons mostly controls the interannual ablation and accumulation variability. As model uncertainties are high during the dry season (importance of poorly known turbulent fluxes plus we disregard the subsurface heat flux), we end the simulations on May 31.

To achieve a 1 °C cooling representative of the climate in the late 17th century, the AWS measurements were applied to a grid cell at 4,850 m a.s.l. instead of at 5,050 m a.s.l. (the method is detailed in section 3.2.1). To avoid unrealistically high precipitation amounts at the top of the glacier caused by lowering the elevation of the forcing data, we applied the precipitation gradient of +10% / 100 m used by Autin et al. (2022) from the glacier front up to 5,200 m a.s.l. (instead of up to 5,400 m a.s.l. in Autin et al., 2022).

Table 1. Summary of the main parameter values used for the DEBAM simulations.

Parameter	Value
Fresh snow albedo	$\alpha_{\text{fresh-snow}} = 0.85$
Firn albedo	$\alpha_{\text{firn}} = 0.6$
Ice albedo	$\alpha_{\text{ice}} = 0.3$
Clear sky transmissivity for solar radiation	$\tau_{\text{clear-sky}} = 0.8$
Roughness height of momentum over ice	$z_{0\text{ice}} = 0.026 \text{ m}$
Roughness heights of temperature, humidity and momentum over snow	$z_{0\text{snow}} = z_{0\text{T}} = z_{0\text{q}} = 0.0026 \text{ m}$
Precipitation gradient from 4370 to 5200 m asl	$\frac{\partial P}{\partial z} = + 10\%/100\text{m}$
Glacier surface temperature gradient	$\frac{\partial T_s}{\partial z} = - 0.1 \text{ }^\circ\text{C}/100 \text{ m}$

3.2 Input datasets

3.2.1 Glacier extent at the LIA maximum extent and model initialization

Using lichenometry techniques, the LIA maximum extent of the glacier was dated to 1680 ± 28 AD (Rabatel et al., 2008). A digital elevation model (DEM) of Zongo Glacier was reconstructed by redrawing contour lines so that the glacier fills the moraines (Rabatel,

2005). Between the LIA maximum extent and 2012, the glacier retreated 1.5 km, the terminus elevation rose by 550 m and the glacier lost 43% of its surface area (see the red and black lines outlining the glacier in Fig. 1).

We hypothesize that since tropical glaciers react rapidly to climate perturbations (Kaser, 1999, Rabatel, 2005), a hydrological year for which the glacier is close to equilibrium ($B \approx 0$ m w.e.) in the current climate or during the LIA is representative of their respective steady state climate.

To obtain information on potential LIA glacier equilibrium characteristics (to serve as comparison for the simulation results), we evaluated the LIA steady state equilibrium-line altitude (ELA_0) considering the frequently used constant area accumulation ratio (AAR) method (e.g. Rabatel, 2005; Jomelli et al., 2009). We evaluated the current climate ELA_0 (5,233 m a.s.l.) by linearly interpolating 25 observed annual ELAs as a function of surface mass balance. We then defined the corresponding AAR (0.68) based on the mean AAR value obtained from the existing glacier digital elevation models (DEM, Autin et al., 2022). Considering a constant AAR, we derived the LIA ELA_0 ($ELA_{0, LIA} = 5,078$ m a.s.l., i.e. 155 m lower).

The equilibrium snow line altitude (SLA_0) for the LIA maximum extent was considered to have shifted by the same elevation as the ELA_0 putting it at an altitude of 4,883 m a.s.l considering the recent climate $SLA_0 = 5,037$ m a.s.l. (based on data from Rabatel et al., 2012). The SLA_0 defined this way was considered as the limit of the firn for model initialization.

3.2.2 LIA climate scenarios

We created four LIA climate scenarios based on nine years of available meteorological data between 1999 and 2017 (Autin et al., 2022). All four scenarios assume a 1.1 °C reduction in air temperature compared to the current climate. Three scenarios assume a 19-22% increase in annual precipitation based on paleoclimate proxy information and glacier climate studies of the past (section 2.2), but differ in the way the additional precipitation is distributed across the year:

- Reference scenario: no difference in precipitation compared to the current climate
- Scenario 1: an earlier onset and longer wet season

- Scenario 2: a wetter wet season (December to March)
- Scenario 3: a wetter transition season (September-November) and April-May (the second transition period).

The reference scenario (hydrological year 2011/2012) was selected from the nine years of glacier observations so that the precipitation seasonality most closely matched the average monthly variations observed in the 23 years of precipitation from PLATAFORMA, which we assumed to represent current climate precipitation seasonality (Fig. 2a, 3a). We use this AWS rather than the on-glacier SAMA AWS to define average seasonality due to the much longer record (the annual amounts are well correlated: $R^2 = 0.74$). In addition, when the model is applied to the 2012 geometry, the surface mass balance up to June for 2011/12 is close to 0 m w.e. making it an ideal candidate to assess the impact of cooling on the glacier LIA extent mass balance (Fig. 2b).

Scenarios 1 to 3 were obtained by replacing some months in the meteorological SAMA time series (including all meteorological variables used to force the model) in 2011/12 by the same month's data from other years in the 9-year data set, chosen to yield an increase of ~20% in annual precipitation compared to the long term average. We chose this procedure in preference to artificially adjusting precipitation amounts to preserve consistency between all meteorological variables for each month. In detail, we constructed the three precipitation scenarios as follows:

Scenario 1 (an earlier and longer wet season) was obtained by replacing the 2011/12 October and November data by the data from the same month of another year chosen among the two wettest months in the dataset (Fig. 3b). Scenario 2 (a more intense wet season) was obtained by replacing the months of December to March by those in the dataset that had the highest number of events ≥ 2 mm/d (Fig. 3c). Finally, scenario 3 (wetter September, October, November, April and May), was obtained by selecting the months in the transition seasons that had above average precipitation compared to the long term on-glacier average (Fig. 3d). For all the scenarios, we used a trial-and-error procedure to determine which year's monthly data to use to replace corresponding data in the 2011/2012 dataset, to achieve the targeted ~20% increase in annual precipitation amounts.

The reference scenario has 1.70 m w.e. of annual precipitation while scenarios 1 to 3 have 1.92, 1.92 and 1.97 m w.e., respectively, which represents a 6% increase in precipitation

for the reference scenario, of 19% for scenarios 1 and 2, and a 22% increase for scenario 3, compared to the average of the nine years of the current climate (1.61 m w.e.).

Comparing the scenarios with the 9-year average (up to May 31) revealed that all the scenarios have less incoming shortwave radiation (Fig. 4a) and increased longwave radiation (Fig. 4b). The latter is due to increased cloud radiative forcing that summarizes the impact of the clouds on the incoming radiation fluxes (Fig. 4c). This is a direct result of selecting / creating years with above-average precipitation (Fig. 4d). By construction, all the scenarios are colder than the measured 9-year average (Fig. 4e), a result of the increased cloudiness and associated reduced incoming radiation. Finally, all the scenarios have annual scale glacier surface temperatures close to the nine-year average (illustrated by the mean outgoing longwave radiation in Fig. 4f).

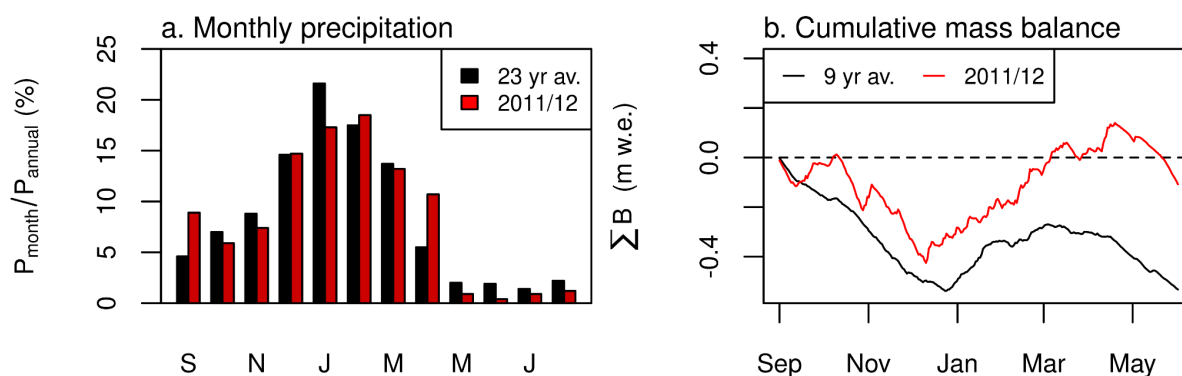


Figure 2. a) Proportion of annual precipitation for each month at the on-glacier AWS SAMA (2011/12) and off-glacier AWS PLATAFORMA (average of 23 years between 1991 and 2017). b) Simulated cumulative surface mass balance for the 9-year average (1999-2017) and 2011/2012 (reference scenario) over the current glacier geometry.

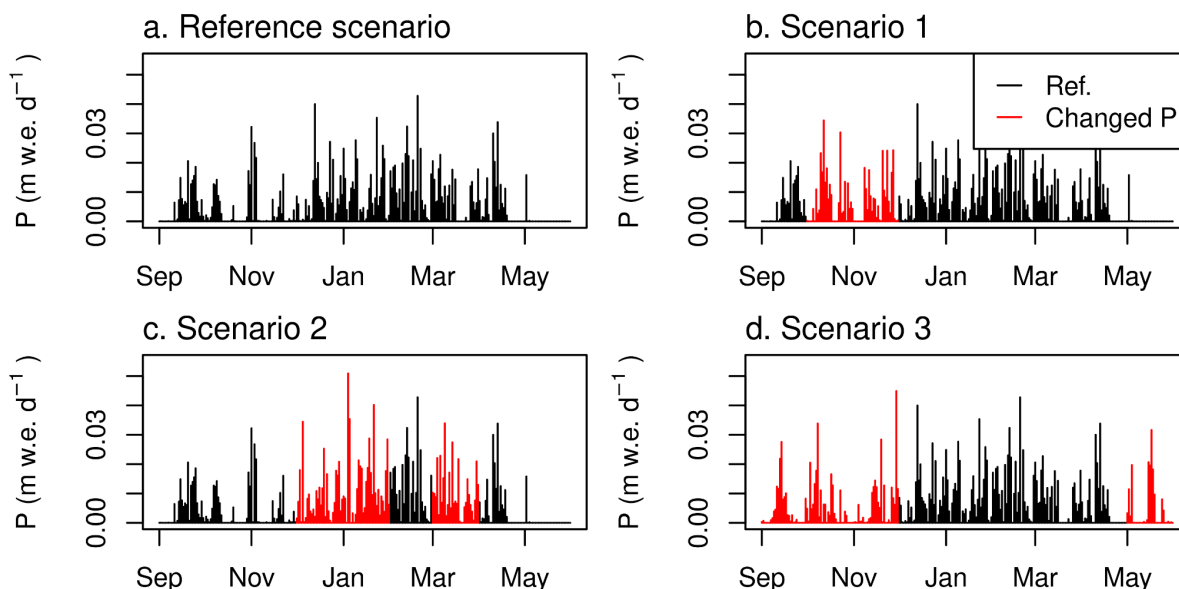


Figure 3. Daily precipitation in the four LIA climate scenarios analyzed in this study. The modifications applied to the reference scenario (2011/2012) are in red.

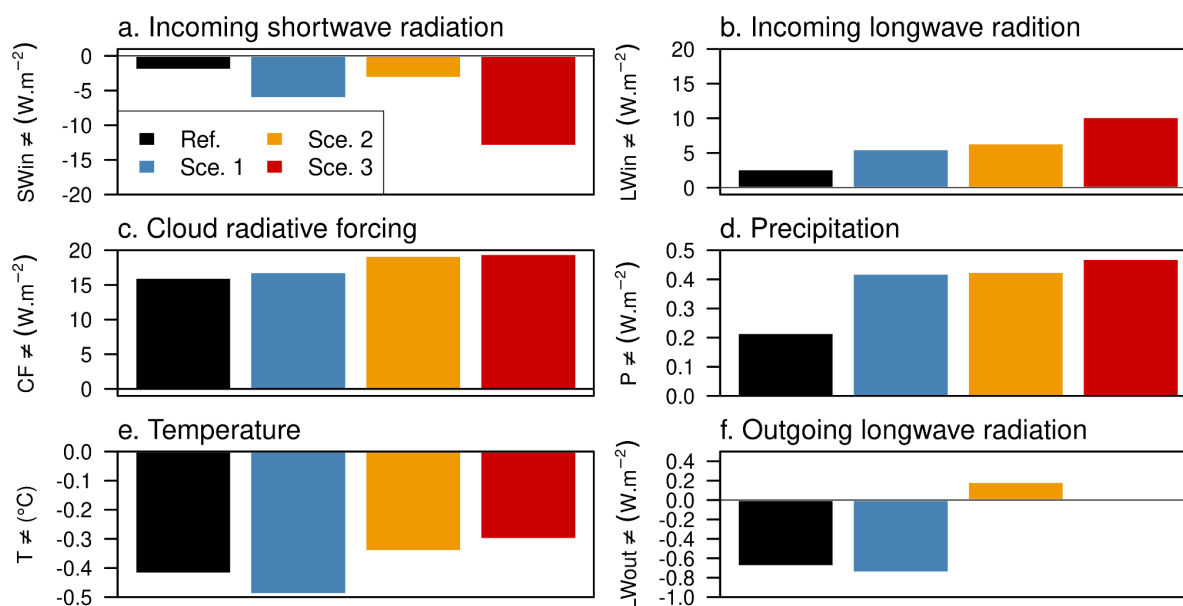


Figure 4. Annual scale differences between the scenarios and the 9-year average ($X_{\text{Sce}} - X_{\text{RT}}$) of (a) incoming shortwave and (b) longwave radiation, (c) cloud radiative forcing, (d) precipitation, (e) air temperature and (f) outgoing longwave radiation used to derive the glacier surface temperature.

4. Results and discussion

4.1. Surface mass balance for the LIA glacier geometry

Figure 5 shows the impact of the scenarios on the cumulative surface mass balance between September 1 and May 31. At the glacier scale, the reference scenario yields a highly negative surface mass balance (Fig. 5a, $B = -0.52$ m w.e.), scenario 1 results in close to equilibrium conditions (Fig. 5b, $B = -0.15$ m w.e.). Scenario 2 results in a slightly more negative mass balance (Fig. 5c, $B = -0.26$ m w.e.). Finally, scenario 3 results in a slightly positive surface mass balance (Fig 5d, $B = 0.08$ m w.e.).

In scenario 3, the surface mass balance reaches 1.62 m w.e. in the upper reaches of the glacier (Fig. 5d). Considering that melt can be disregarded over this part of the glacier (at about 5,800 m a.s.l.), it is a reasonable value because the annual precipitation amounts received at the AWS (close to 2 m w.e. for all scenarios) which, via the precipitation gradient applied in the simulations (+10%/100 m up to 5,200 m a.s.l.), implies that over 2.56 m w.e. reaches the upper part of the glacier.

At the glacier terminus, the cumulative mass loss, which ranges between 9.0 and 10.1 m w.e. depending on the scenario (Fig. 5), is significantly higher than that observed in recent times, when the glacier-wide mass balance has been close to zero (for example, measurements over the year 2000/2001 show $B_{\text{Glacier-wide}} = 0.49$ m w.e. and $B_{\text{Glacier terminus}} = -6.24$ m w.e.). This difference can be explained by the larger accumulation zone in the LIA configuration (2.50 km² versus 1.55 km² in 2000/2001) and similar annual precipitation amounts (2000/2001 is one of the wettest year in the current climate dataset) leading to a larger accumulation volume (an extra $1.8 \cdot 10^6$ m³). As a result, the downward ice flux is strengthened during the LIA, allowing the glacier front to reach low altitudes where melt rates are high (especially since in the lower reaches of the LIA glacier extent, the slope of the bedrock is steep and the width of the tongue is constrained by the topography, top inset in Fig. 1).

The ablation area of tropical glaciers is characterized by steep altitudinal mass balance gradients due to marked variations in albedo (Sicart et al., 2011). The simulations give similar mass balance gradients during the LIA as under the current climate (around 2 m w.e. /100 m, fig. 6a) probably because this gradient is mostly controlled by atmospheric variables and the LIA scenarios were built using shuffled present-day meteorological forcing data.

For the LIA scenarios, the specific mass turnover τ (Eq. 2, e.g., Ohmura et al., 1992) was larger than for recent climatic conditions ($\tau_{\text{LIA, all scenarios}} > 2$ m w.e. whereas $\tau_{2000/01} = 0.98$

m w.e., Table 2) emphasizing the role of the ice flux in compensating for the melt rates in the ablation zone.

$$\tau = \frac{c+|a|}{2} \quad (2)$$

where τ is the specific mass turnover, c the specific mass gain (in the accumulation zone) and a is the specific mass loss (in the ablation zone).

Considering a constant AAR method to define the ELA_0 is not valid here as this method yields a value that is much higher than our simulations show ($ELA_{0, LIA} = 5,078$ m a.s.l. with the AAR method versus 4,908 to 5,000 m a.s.l. depending on the scenario). Indeed, the AAR obtained with the LIA simulations is ~ 0.8 , whereas the AAR_0 for the current climate is 0.68. Based on the analysis of the specific mass turnover and altitudinal mass balance gradients, this method is not valid primarily because of the topographic conditions (narrow and steep but because of the long ablation zone with a small surface area). This topographical setting coupled with the strong downward ice flux enabled the glacier terminus to reach ~ 500 m below the ELA_0 during the LIA, as opposed to ~ 250 m in current climate conditions.

Other methods exist to reconstruct past ELA_0 , for example, based on the altitude of lateral moraines, Rabatel (2005) estimated the ELA_0 during the LIA to be at 5,090 m a.s.l. Based on our results, this altitude is overestimated by ~ 150 m, suggesting that the lateral moraine method can only give a maximum ELA due to uncertainties linked to moraine accretion from the glacier fluctuations between the LIA maximum extent and now, or by moraine erosion since the glacier retreat.

Mass balance (Fig. 6a) and changes in volume (Fig. 6b) by altitude make it possible to assess the variability of the spatial mass balance induced by the LIA scenarios. The mass balance profiles show high variability in the ablation zone. Analysis of changes in simulated snow heights, albedo and mass balance in the ablation zone (4,400 – 4,850 m a.s.l.) showed that this variability is driven by albedo feedback effects (not shown). At the annual scale, the increased variation in albedo with altitude is due to the increased influence of snow temporarily covering the ice (from ± 0.002 at 4,400 m a.s.l. to ± 0.04 at 4,850 m a.s.l.). Hence, via an albedo feedback effect, the timing and intensity of the precipitation play an important role in controlling melt rates in the upper reaches of the ablation zone.

Above ~4,600 m a.s.l., scenarios 1 and 3 (Fig. 6a, blue and red lines, respectively) diverge, with a less negative mass balance gradient in scenario 1 because in scenario 3, the precipitation events are more evenly distributed, resulting in higher albedo values. Similarly, above ~4,700 m a.s.l., scenario 2 shows a shallower mass balance profile than the reference scenario (orange and black lines, respectively), because intense precipitation events throughout the wet season enable a thicker snowpack, thereby increasing the albedo and reducing annual mass loss.

Table 2 shows that the more positive the glacier-wide surface mass balance, the more negative the specific ablation and, in some cases, the lower the specific accumulation (observed in scenarios 1 and 2). Considering the mean differences between the reference scenario and in the three scenarios with changes in precipitation patterns, the variability of the specific ablation rate is higher than that of the accumulation rate (whereas, Table 2) because of the effect of albedo feedback on the melt rate.

Considering the two most extreme scenarios in terms of surface mass balance value (the reference scenario and scenario 3), despite higher variability of the surface mass balance profile in the lower reaches of the glacier (below the ELA, Fig. 6a.), the biggest differences in volume occur in the upper reaches (above the ELA, Fig. 6b), suggesting that accumulation processes play an important role in the glacier-wide surface mass balance. Compared to the reference scenario, scenario 3 generates an excess in volume of $0.55 \cdot 10^6 \text{ m}^3$ ($1.1 \cdot 10^6 \text{ m}^3$) in the lower (upper) reaches of the glacier.

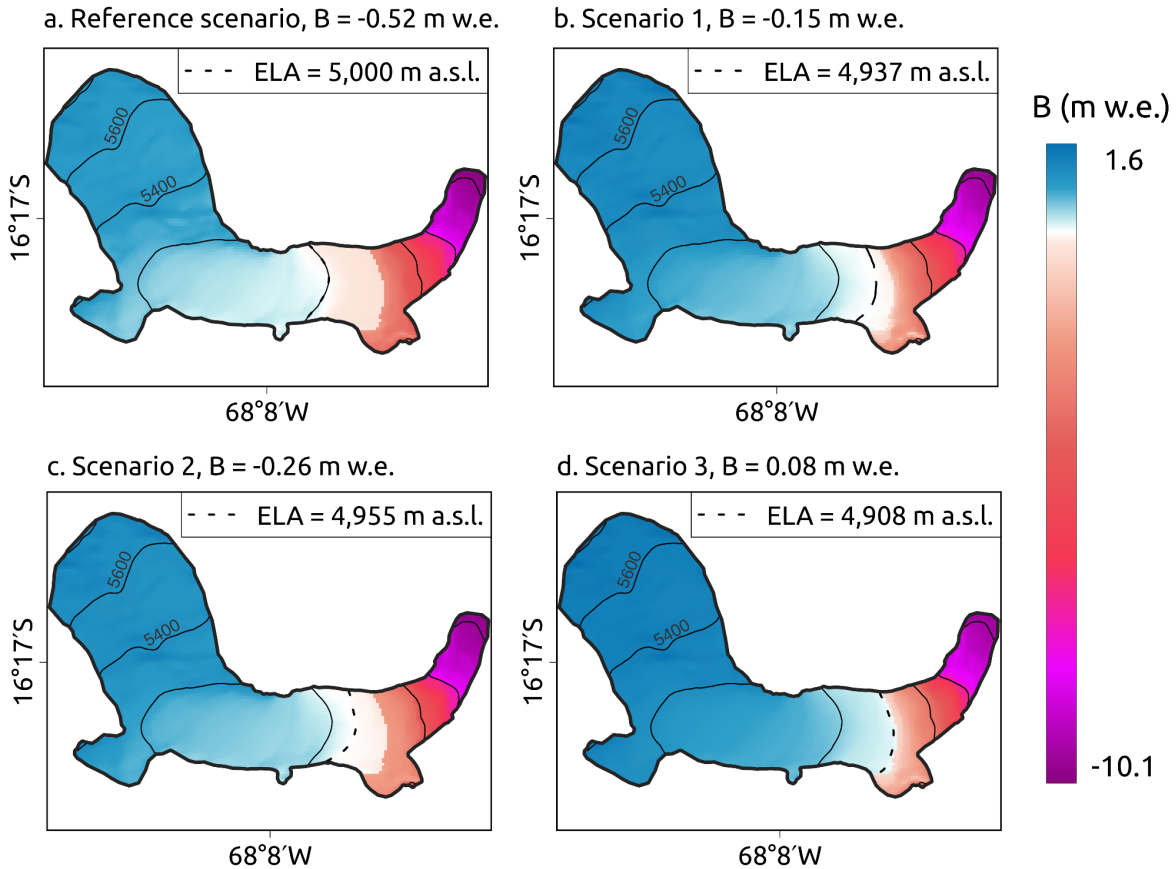


Figure 5. Annual surface mass balance maps for the four LIA scenarios. The dashed lines represent the simulated ELA.

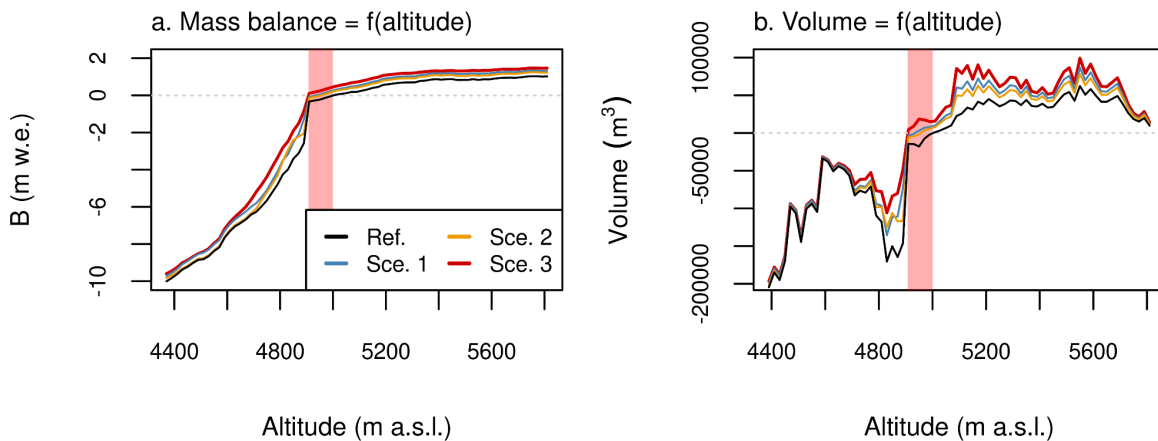


Figure 6. Surface mass balance as a function of altitude (a) and corresponding changes in mass (b) in the four scenarios. The shaded area highlights the altitudinal range for the simulated equilibrium-line altitudes (4,908-5,000 m a.s.l.).

Table 2. Summary of simulated glacier-wide surface mass balance B , specific ablation a , accumulation c , and mass turnover τ for the four LIA scenarios along with the differences in a and c between the reference scenario and scenarios 1-3.

Scenarios	B (m w.e.)	a (m w.e.)	c (m w.e.)	τ (m w.e.)	Δa (m w.e.)	Δc (m w.e.)
Reference	-0.52	-3.31	0.96	2.13	0	0
1	-0.15	-4.28	0.90	2.59	0.97	0.06
2	-0.26	-3.78	0.93	2.35	0.47	0.03
3	0.08	-4.69	1.04	2.86	1.38	-0.07

4.2. Impact of the climate scenarios on the surface energy fluxes

Scenarios 1 and 3 yield close to equilibrium annual glacier-wide surface mass balances whereas the reference scenario and scenario 2 result in negative mass balance conditions. The main differences in melt rates between these two groups occur between September and November (Fig. 7a). As mentioned in section 2.1, the transition season is characterized by increased solar radiation at the top of atmosphere and a low surface albedo, leading to large net shortwave energy fluxes that are responsible for the highest melt rates of the year, meaning this period plays a key role in controlling the annual surface mass balance (Sicart et al., 2011). As a result, the two scenarios that are the most efficient at limiting mass loss are those with increased precipitation amounts and frequencies during the transition season (scenarios 1 and 3). Indeed, clouds reduce the incoming shortwave radiation fluxes and snowfall increases the glacier albedo, thereby reducing melt energy compared to the other two scenarios (Fig. 7b).

During the wet season, scenario 2 differs from scenarios 1 and 3 because it was constructed to maximize the number of large-scale precipitation events (section 3.2.2). It reduces the amount of melt energy because the combined effect of clouds and precipitation reduces the net shortwave energy fluxes more than the clouds increase the net longwave energy budget (Fig. 7b and c, respectively). This reduction, combined with the large precipitation amounts in this scenario explain the rapid mass gains observed in Fig. 7a.

An early and longer wet season (scenario 1) is more efficient at reducing mass loss than a more intense wet season (scenario 2) because it reduces the incoming shortwave

radiation (cloud cover) and increases the albedo (snowfall events) during the period of maximum potential solar radiation (summer solstice), which limits the mass loss over the transition season. During the core wet season, increased precipitation intensity and frequency (scenario 2) increases the mass gain but does not compensate for the losses during the transition season (Fig. 7a).

During the core wet season, the glacier-wide averaged cumulative sensible heat flux is negative in all the scenarios, showing that the temperature of the glacier surface remains higher than the temperature of the air (Fig. 7d). The higher temperature in the simulations is probably because in the model, the air temperature is extrapolated using a stronger altitudinal gradient than the surface temperatures ($-0.55\text{ }^{\circ}\text{C}/100\text{ m}$ versus $-0.1\text{ }^{\circ}\text{C}/100\text{ m}$), resulting in a large part of the glacier where the simulated surface temperature is warmer than the air. However, considering the small cumulative sums of these fluxes over the year (-200 and 200 W m^{-2}), the impact on the melt rate is limited. Finally, in all the scenarios, the latent heat fluxes act as an energy sink (sublimation) whose annual amount is about half the sum of the net longwave energy flux (Fig. 7e). Because more energy is lost *via* the latent heat flux than the energy provided by the sensible heat flux, the sum of the turbulent fluxes is negative (energy sink), a feature observed under the current climate (e.g., Sicart et al., 2011).

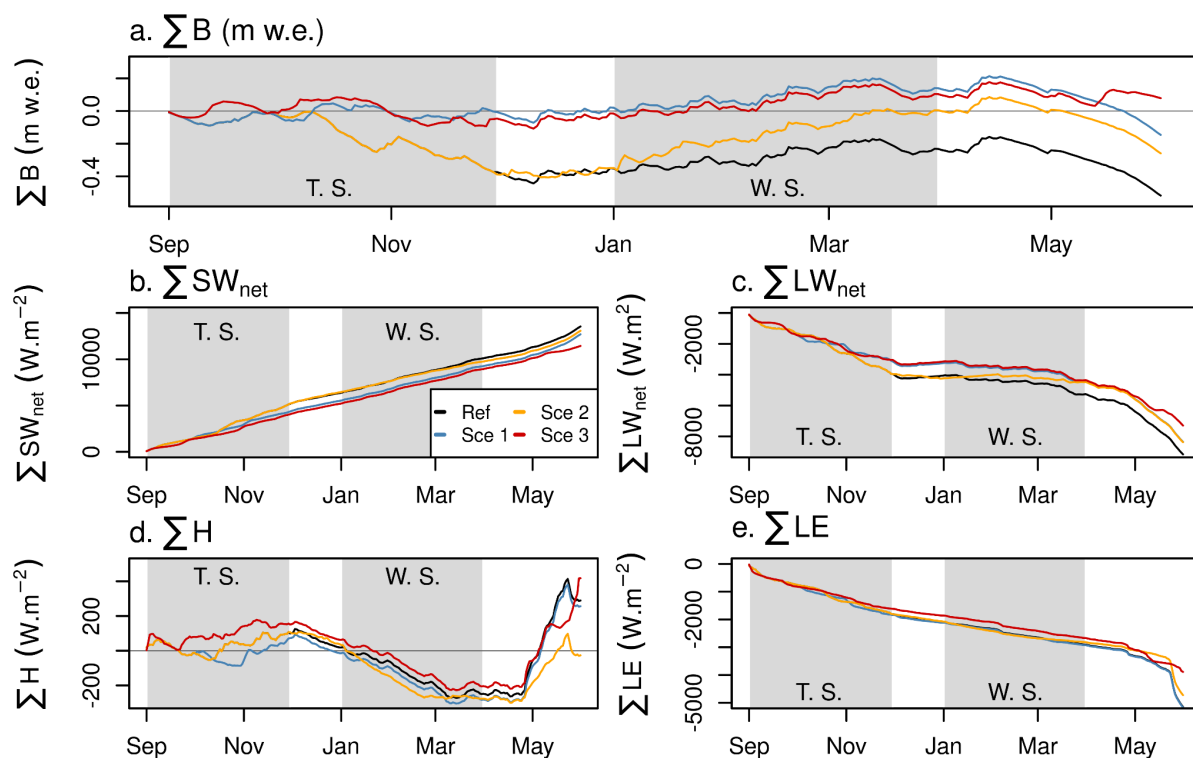


Figure 7. Cumulative glacier-wide surface mass balance (a), net shortwave (b) and longwave (c) energy budgets along with the sensible (d) and latent (e) heat fluxes in the four LIA scenarios. The gray areas represent the transition (T.S.) and wet (W.S.) seasons.

4.3 Sources of modeling errors

An important source of error is that we neglect the subsurface heat flux in the simulations, implying errors in the surface temperature. Although under the current climate, the subsurface heat flux only plays a significant role in reducing melt rates via nighttime cooling over the glacier's accumulation zone and over the whole surface of the glacier in the dry season (e.g., Sicart et al., 2011), this heat flux may be significant during a large part of the year in the cooler LIA climate, particularly over the upper reaches of the glacier. Errors in the simulated surface temperature are partly offset by the surface temperature altitudinal gradient applied in the simulations. As the accumulation area is larger during the LIA than under the current climate (AAR = 0.8 versus 0.68), the model may overestimate the glacier-wide melt rates.

The model may also underestimate the turbulent fluxes. This is due to a number of reasons including the fact that a uniform wind speed is considered across the glacier, or the fact that errors in the simulated albedo impact the type of surface simulated (snow/firn/ice) via imprecise melt rates. Overestimation of the simulated surface temperatures in the

accumulation zone also influences the turbulent fluxes via a reduced surface-air temperature gradient. Another source of error is that the model considers constant stability functions throughout the year whereas in reality, these vary with the meteorological conditions (Sicart et al., 2011). As a result, the glacier-wide latent heat flux is underestimated making the turbulent fluxes a smaller energy sink than they should be, thereby contributing to overestimating the melt rates.

Other sources of errors that impact the simulations are the air temperature and precipitation gradients which are poorly known under current climate conditions (and may have been different in the LIA climate). Considering these sources of errors in the modeling, it is likely that the model overestimates the melt rates and hence, the annual mass losses.

5 Concluding remarks

This study assessed the seasonal climate changes that occurred in tropical South America during the Little Ice Age (late 17th century) using a distributed surface energy balance applied to the tropical Zongo glacier (16°S, Bolivia) and scenarios that maintain physical coherence between the measured meteorological variables.

Using information provided by paleoclimate proxies, global climate model simulations and glacier-climate sensitivity studies of past glacier extents over tropical South America, we constructed three scenarios that focus on the distribution of precipitation over time. One scenario considered a wetter year (above average precipitation in September, October, November, April and May) and the other two others tested different wet season configurations: one considered an early onset of the wet season and the other a more intensive wet season. To ensure physical coherence between the measured variables, the scenarios were obtained by shuffling months of measurements of the current climate based on 9 years of continuous hourly measurements. The three scenarios were compared to a reference scenario in which the monthly precipitation is representative of the current climate and a 1.1 °C decrease in temperature. The climate scenarios were assessed based on the resulting surface mass balance of the glacier's LIA maximum extent. They were considered plausible if close to equilibrium conditions were obtained ($B \approx 0$ m w.e.).

The reference scenario was the one that resulted in the highest mass loss ($B = -0.52$ m w.e.) suggesting that, by itself, 1.1 °C cooling cannot explain the glacier's maximum extent during the LIA. Spreading precipitation out over the year, and more specifically, including

more frequent precipitation events during the transition periods, via an albedo feedback effect, is key to reproducing a glacier that is close to equilibrium at its maximum extent during the LIA. In addition, a longer wet season (scenario 1, $B = -0.15$ m w.e.) is more efficient in reducing mass loss than a more intense one (scenario 2, -0.26 m w.e.), as the former shortens the transition period and hence limits the otherwise large mass losses that occur in the wet season. This confirms recent findings concerning the important role of the distribution of precipitation over the transition season in controlling the annual mass loss (e.g., Autin et al., 2022).

Thus, the simulations indicate that the LIA climate was likely 1.1 °C cooler with ~20% extra precipitation at the annual scale, in rough agreement with Rabatel et al. (2008). However, our method also allowed us to investigate the effects of changes in the seasonal distribution of precipitation on the mass balance. Our results suggest that the 20% annual increase in precipitation is in agreement with the LIA glacier extent only if increased precipitation occurs in the transition season (period of highest melt rates) that precede the core wet season (December-March).

The simulations also reveal a significant change in the AAR of the glacier from around 0.68 for the current climate versus 0.80 for the LIA climate, mostly due to topographic conditions (the ablation area was steep and narrow during the LIA). This suggests that methods based on constant AAR to reconstruct the LIA climate result in overestimation of the past ELA0 of about 120 m. Indeed, we hypothesize that this topographic setting coupled with the large accumulation volumes favored a strong downward ice flux that allowed the glacier to extend farther below the ELA during the LIA than what is observed under the current climate.

Applying the model to other glaciers in the tropical Andes with different morpho-topographic variables would provide further insights into which LIA scenarios are most plausible and an in-depth understanding of the limits of the AAR method. Another possible further study includes coupling DEBAM to a model of glacier dynamics to better quantify the role of the ice flux and mass turnover in reaching glacier steady-state conditions.

Acknowledgements

This study was conducted in the framework of the International Joint Laboratory LMI GREAT-ICE, the International Research Network Andes-C2H (IRD and Andean partners)

and the French *Service National d'Observation* GLACIOCLIM (www.glacioclim.osug.fr, UGA-OSUG, CNRS-INSU, IRD, IPEV, INRAE). GLACIOCLIM is coordinated in La Paz by Dr. Alvaro Soruco (UMSA/IGEMA) who organizes the follow-up of the glaciological measurements on Zongo Glacier. The authors are grateful to everyone involved in the long-term *in-situ* monitoring of Zongo Glacier and acknowledge the support of LabEx OSUG@2020 (*Investissements d'Avenir* – ANR-10-LABX-0056).

5.2 Comment on the results of Jomelli et al. (2011) on the LIA climate

As mentioned in Chapter 1, Jomelli et al. (2011) assessed the LIA climate condition over the Telata Glacier (closeby Zongo Glacier). In order to assess the temperature and precipitation changes which occurred during the LIA, they applied an improved positive degree-day model coupled to a dynamic ice flow model (Blard et al., 2007) over the Telata Glacier LIA maximum extent. Their study suggests that, compared to current climate conditions, the LIA was likely 2.1 ± 0.8 °C cooler and that there was a 15% decrease in precipitation amounts.

To assess these findings, we carried out a simulation with the year 2004/05 which had ~15% less precipitation than the 9 year average. In the model, to achieve a 2.2 °C cooling, the meteorological forcing was applied at 4660 m a.s.l. Besides, to be consistent with the other simulations, the precipitation gradient was applied up to 5000 m a.s.l. Results show that such a climate setting does not allow the glacier to reach its maximum extent as the simulated glacier-wide surface mass balance up to the 31st of May is -0.41 m w.e. In addition to our simulation results, multiple paleoclimate proxies suggest an intensification of the precipitation during the LIA. Thus, the findings of Jomelli et al. (2011) are not confirmed by our study.

5.3 Sensitivity analyses carried out for the model initialization of LIA simulations

This section presents the sensitivity analyses on the impact of precipitation surface temperature gradients on the simulated surface mass balance. These were carried out because, to obtain a 1.1 °C cooling in the LIA simulations, the position of the meteorological forcing in DEBAM was lowered by 200 m.

Regarding the precipitation gradient, this impacted the amount of precipitation falling on the upper reaches of the glacier. In addition, considering a constant surface temperature (as was done for the current climate) resulted in unrealistically large portions of the glacier being warmer than the air.

5.3.1 Sensitivity of the simulated surface mass balance to the altitude up to which the precipitation gradient is applied

In the LIA simulations the meteorological forcing position in DEBAM was lowered by 200 m below its present day altitude to simulate a cooling of 1.1°C (see section 5.1). To avoid unrealistic precipitation amounts in the upper reaches of the glacier, we investigated the impact of changing the altitude up to which the precipitation gradient is applied. The sensitivity analysis presented here is considering simulations with constant surface temperature across the glacier. We tested the following:

- No precipitation gradient (dP_0)
- +10%/100m up to 5200 m a.s.l. (dP_{5200})
- +10%/100m up to 5400 m a.s.l. which is the altitude up to which the gradient was applied for current climate simulations (dP_{5400})
- +10%/100m up to 5800 m a.s.l. (dP_{5800})

The impact of the precipitation gradients on annual precipitation amounts by altitude is shown on Figure 5.1. Compared to the precipitation amounts applied at the forcings' altitude (4850 m a.s.l.), applying the gradient up to 5800 m a.s.l. almost triples the amount of annual precipitation received in the upper reaches of the glacier (blue curve). Because this is highly unlikely, only the results obtained with dP_0 , dP_{5200} and dP_{5400} are presented.

When the gradients are applied, annual precipitation amounts are lowered below the AWS. In the case of dP_{5200} , the total precipitation volumes reaching the glacier are 27 % higher than with dP_0 as only 13% of the glacier's surface area is below 4850 m a.s.l. This explains the changes in simulated snow heights and cumulated surface mass balance observed in the ablation and accumulation areas

(Fig. 5.2a, b, respectively). In the accumulation zone (Fig. 5.2b), snow height and cumulative mass balance are almost identical suggesting limited melt rates. Applying the precipitation gradients increases the amount of precipitation received over the glacier which, despite increased melt rates in the ablation area, limits the glacier-wide mass loss (Fig 5.2c).

Comparison of annual surface mass balance maps obtained with dP_0 and the other two gradients revealed that the gradients significantly limit the mass loss above the AWS and lower it beneath (Fig. 5.3). For example, dP_{5200} results in an increased mean specific mass loss of 0.71 m w.e. below 4850 m a.s.l. (13 % of the glacier surface). Conversely, it causes a mean specific mass gain of 0.55 m w.e. above 4850 m a.s.l. Since 87% of the glacier's surface area is above 4850 m a.s.l., applying the gradients significantly lowers the annual glacier-wide mass losses.

In order to be coherent with the way DEBAM was calibrated (over the 1999-2017 period), we chose to apply the gradient up to 5200 m a.s.l. so that it is applied over the same elevation range as for current climate simulations.

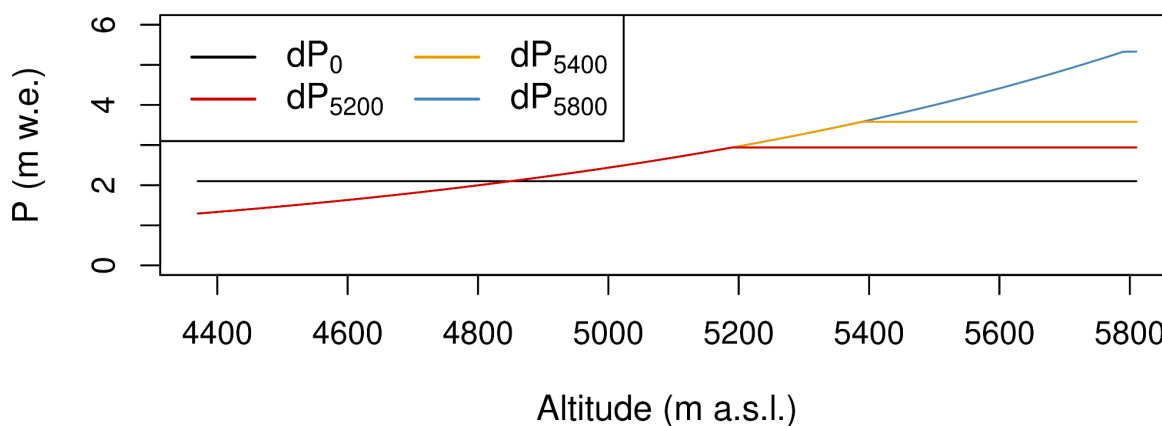


Figure 5.1. Impact of the altitude up to which the precipitation gradient is applied on the annual precipitation amounts.

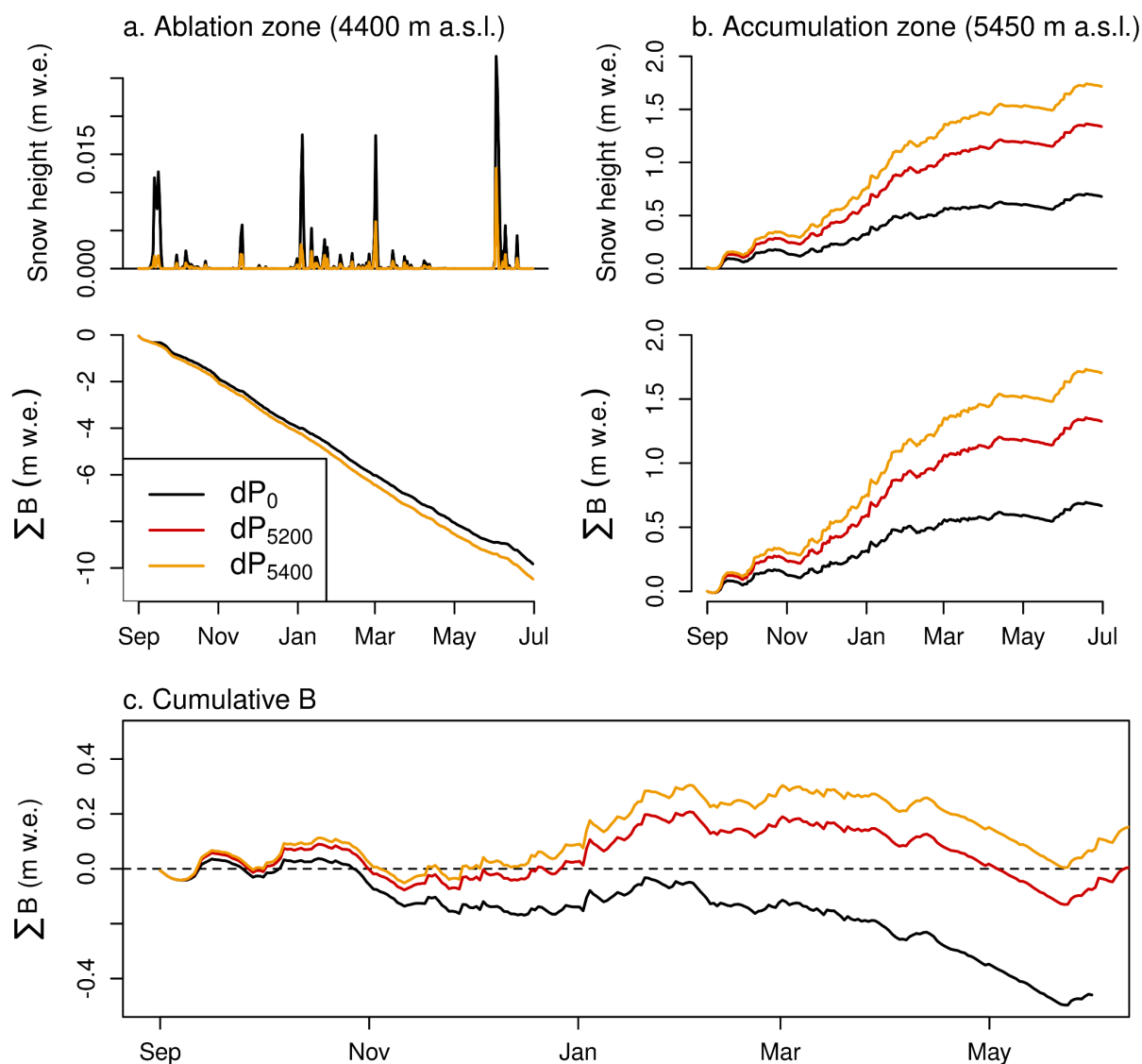


Figure 5.2. Snow heights and cumulative surface mass balance at 4400 and 5450 m a.s.l. (plots a and b, respectively), and the cumulative glacier-wide surface mass balance (c). Below 4850 m a.s.l. (plot a), dP_{5200} and dP_{5400} yield the same results as the same reduction in precipitation amounts is applied.

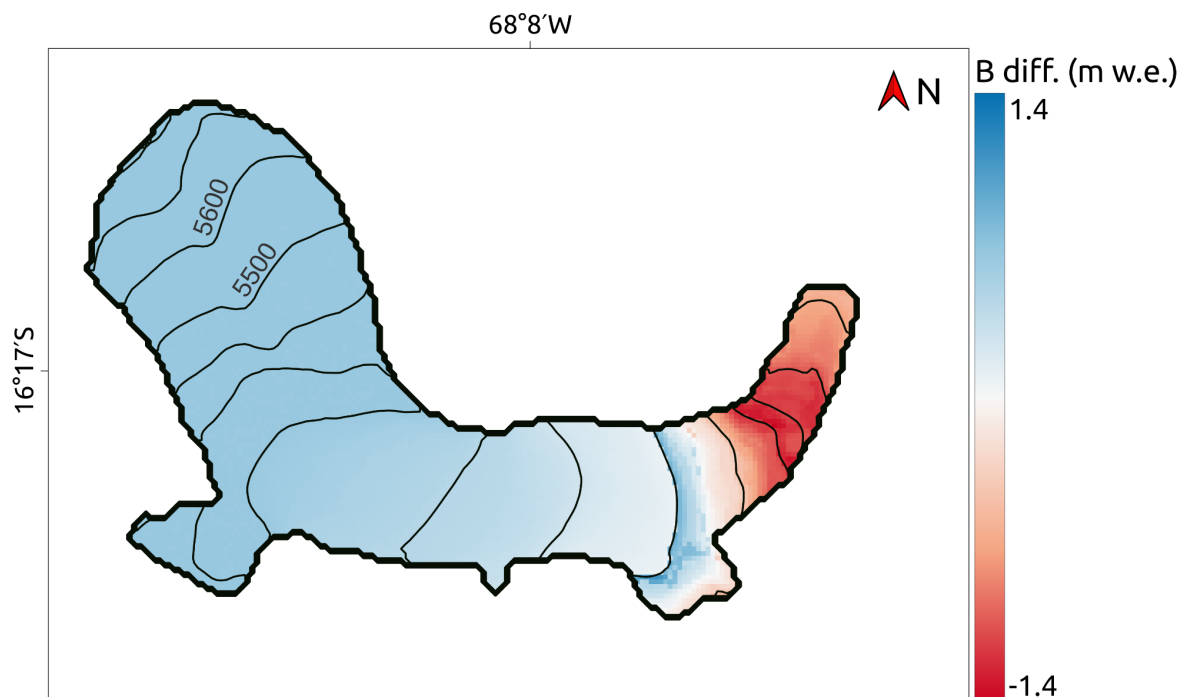


Figure 5.3. Map showing the difference in annual surface mass balance obtained with dP_{5200} and dP_0 ($dP_{5200} - dP_0$). The color scale is centered around 0 (white) thus, parts in red show higher mass losses obtained with dP_{5200} than with dP_0 .

5.3.2 Impact of the surface temperature gradient on the simulated surface mass balance

We tested four surface temperature gradients ranging from 0 °C / 100 m to -0.3 °C / 100 m by 0.1 °C increments named dTs_0 to dTs_3 . All runs were carried out considering a +10 % / 100 m precipitation gradient up to 5200 m a.s.l.

Simulations show that the more negative the surface temperature gradient the higher the melt (Fig. 5.4 a-d and i) and hence, the more negative the surface mass balance (Fig. 5.4e-h and j). This is counterintuitive as we would expect that the mass loss would be reduced when cooling the surface above 4,850 m a.s.l. *via* delayed diurnal melt. As seen on the surface mass balance maps, dTs_3 yields a higher equilibrium-line altitude than dTs_0 (white bands on Fig 5.4 e & h).

To provide an insight into the mechanisms that increase melt, maps of annual mean values of the simulated turbulent fluxes are presented on Figure 5.5 (Row 1 is the sensible heat flux, row 2 the latent heat fluxes and row 3 their sum). A strong surface cooling above 4850 m a.s.l. reduces the glacier surface to air temperature

gradient, as a result, both the sensible and latent heat fluxes become less negative with altitude (Fig. 5.5 a-d & e-h, respectively). As a result, the turbulent fluxes are less an energy sink to eventually become a source of melt energy (with dTs_3 , Fig. 5.5 i-l). A less negative latent heat flux lowers sublimation which coupled with more energy available for melt results in increasing melt rates as the surface temperature gradient becomes more negative.

In terms of energy, at the annual scale (considering glacier-wide averaged fluxes), the surface temperature gradients increase the latent heat flux more than the sensible heat flux (table 5.1): at the annual scale, the differences between dTs_3 and dTs_0 range from -4 to 12 W m⁻² for H and between -4 and 15 W m⁻² for LE.

In order to avoid a small negative cumulative latent heat flux coupled to a large negative sensible heat flux over high elevations (where, at the annual scale, the glacier surface should be colder than the air temperature), we decided to keep $dTs_1 = -0.1$ °C / 100 m.

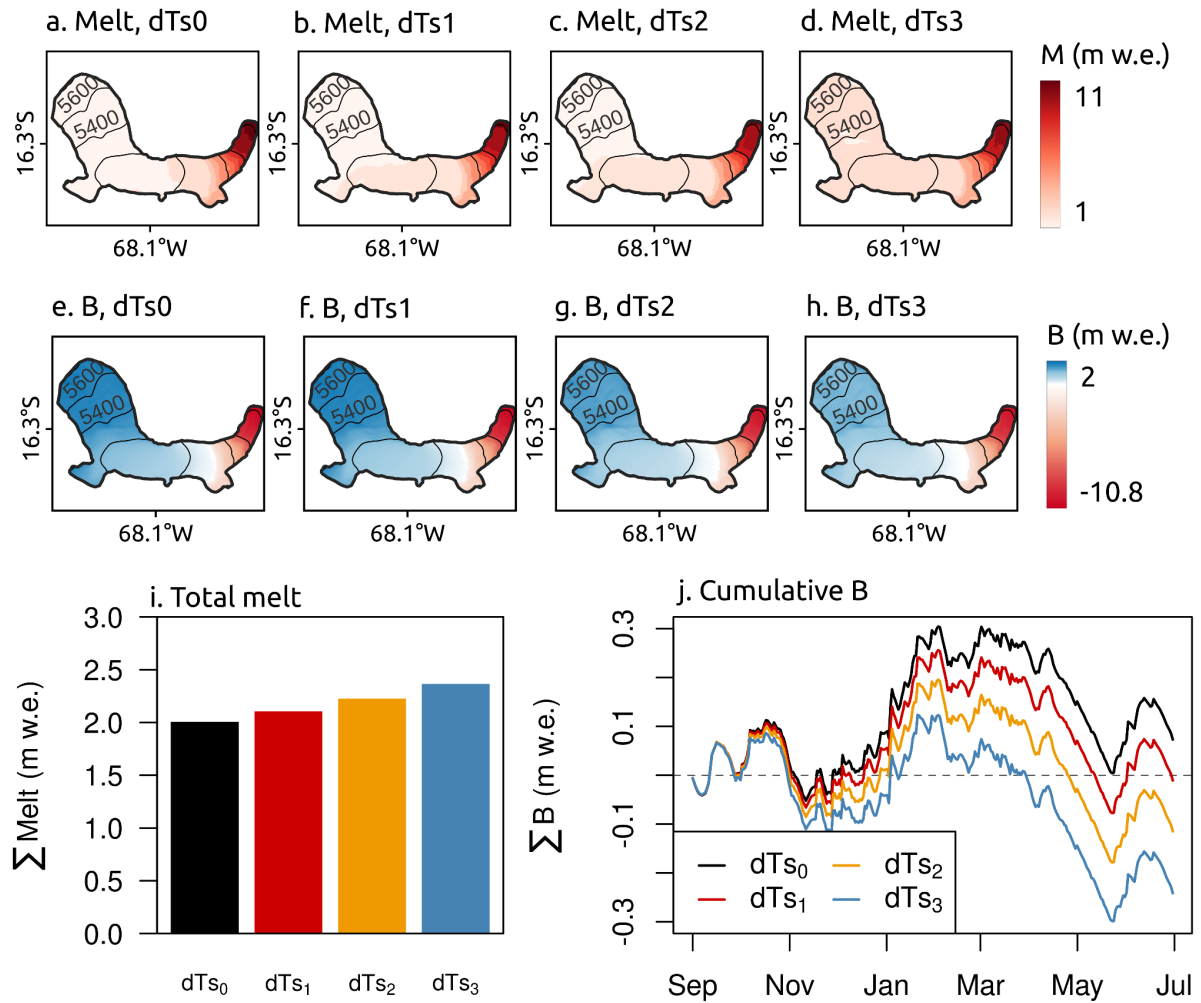


Figure 5.4. Annual melt (a-d) and surface mass balance maps (e-h) along with the total melt (i) and cumulative glacier-wide surface mass balance (j) for the four configurations tested.

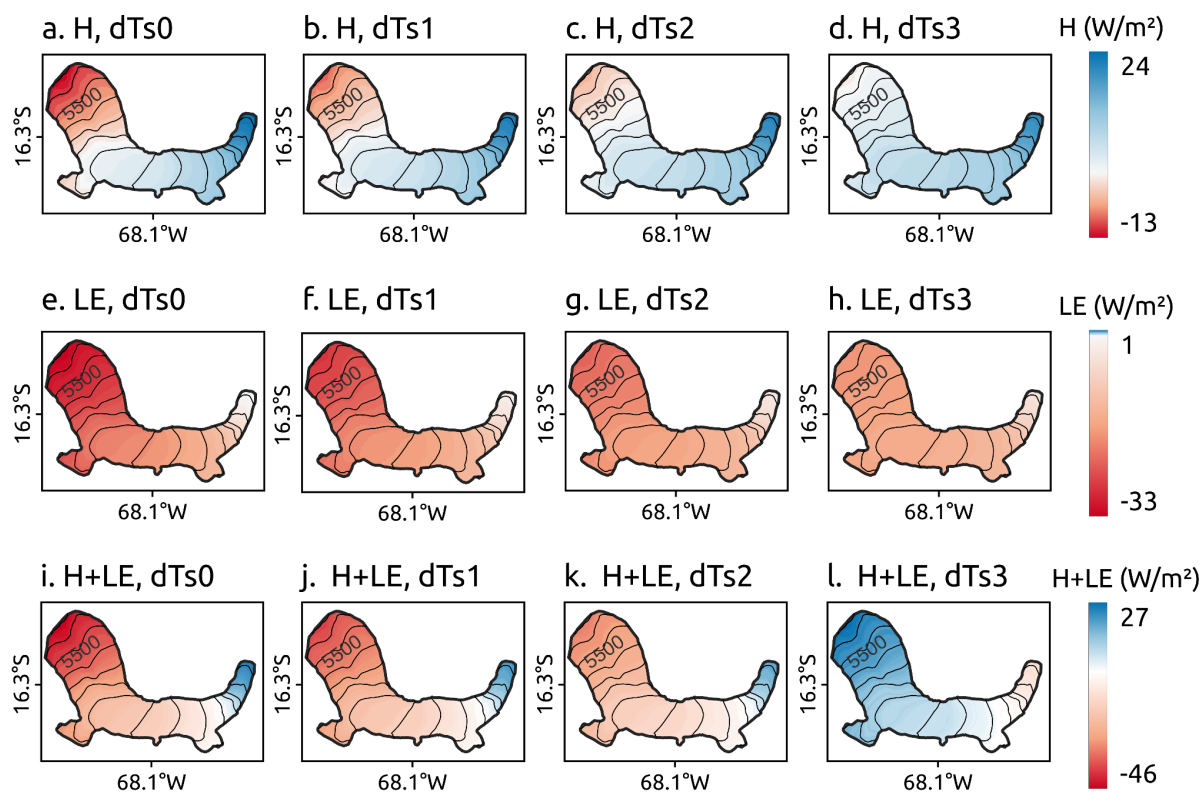


Figure 5.5. Impact of different surface temperature gradients on simulated latent (top row) and sensible (bottom row) heat fluxes

Table 5.1. Annual glacier-wide sensible and latent heat fluxes for the four model initializations considered and their differences to dTs_0 .

$\frac{\partial Ts}{\partial z}$	$\Sigma H \text{ (W m}^{-2}\text{)}$	$\Sigma \left(H_{dTs_x} - H_{dTs_0} \right) \text{ (W m}^{-2}\text{)}$	$\Sigma LE \text{ (W m}^{-2}\text{)}$	$\Sigma \left(LE_{dTs_x} - LE_{dTs_0} \right) \text{ (W m}^{-2}\text{)}$
0	387	0	-6250	0
dTs_1	877	490	-5643	607
dTs_2	1370	983	-5049	1201
dTs_3	1864	1477	-4477	1773

5.4 Summary

Assessment of the climate which allowed Zongo Glacier to reach its LIA Maximum extent

LIA climate compared to the current climate

- A 1.1 °C cooling and an increase of ~ 20% of the annual precipitation amounts is required to obtain glacier equilibrium conditions during the LIA
- Extra precipitation was either during the transition season or the wet season started about a month earlier than now.

Glacier-climate relationship during the LIA

- Simulations show that for an equilibrium state position, compared to observations under the current climate, higher mass losses in the lower reaches of the glacier occurred during the LIA.
- We hypothesize that these mass losses are compensated by a strong downward ice flux linked to the large accumulation volumes which occurred during the LIA.

General conclusion and perspectives

This Phd thesis is a case study of the tropical Zongo Glacier. Being in the outer tropics, its climate is characterized by a strong cloud cover and precipitation seasonality (e.g., Hastenrath, 1991). Hence over the glacier, three seasons are considered (e.g., Sicart et al., 2011): a wet season (austral summer) which is the main accumulation period, a dry season (austral winter) where limited melt is observed and a transition season (September-November) characterized by increasing melt rates. In addition, because the glacier is at a low latitude (16°S), the solar insolation is high all year round and has a limited seasonality. Previous studies showed that solar radiation was often the main source of fusion and that incoming longwave radiation played an important role on the melt rate seasonality (e.g., Sicart et al., 2005).

The first part of this PhD thesis aimed at providing insights at the current climate - glacier relationship *via* the application of a distributed surface energy balance model over nine years (DEBAM, Hock and Holmgren, 2005). The second part of this PhD consisted in using the glacier's maximum extent during the Little Ice Age (late 17th century) to assess the climate which caused this glacier extent. This part allowed us to test hypotheses on the climate controls of the surface mass balance found in the first part of this PhD. Besides, it allowed us to investigate the seasonal precipitation changes which may have occurred during the Little Ice Age.

Current climate (1991-2017)

To examine the climate controls on the surface mass balance seasonal and interannual variability, three datasets were considered:

- Daily precipitation measurements from the MEVIS/PLATAFORMA AWS, below the glacier at 4750 m a.s.l between 1991 and 2011. This was used to assess the long term links between precipitation and glacier surface mass balance.
- 9 years of gap-filled hourly precipitation, relative humidity, temperature, incoming shortwave radiation, incoming and outgoing longwave radiation

measured on the glacier between 1999 and 2017. We used this dataset to assess the climate controls on the surface mass balance using DEBAM.

- 14 years of cloud radiative indexes derived from incoming short and longwave radiation measurements between 1999 and 2017. Following Sicart et al. (2016), we considered the cloud shortwave attenuation and longwave emission factors, the cloud cover index (which has high values for warm/thick clouds and low ones for cold/thin clouds). The last aspect we considered was the cloud radiative forcing which is the impact of the clouds on the downwelling fluxes. These radiative indexes were used to investigate the relationships between clouds, precipitation and surface mass balance.

Analysis of the cloud radiative properties showed that their probability density functions could be used to define the three seasons in the year. This adds a new tool to previous definitions of the seasons based on interannual variability of the monthly surface mass balance in the ablation zone (Rabatel et al., 2013) or on melt, surface temperature and precipitation (e.g., Sicart et al., 2011).

The links between cloud radiative properties and precipitation events at the monthly, seasonal and annual scales are not clear and would require further investigations. Our study showed a clear link between the annual mean precipitation intensity (of days with precipitation) and the cloud cover index ($R^2 = 0.78$). Besides, days with precipitation tend to have cloud index values which are, on average, 57 % higher than on cloudy days without precipitation. Similarly, the cloud radiative forcing decreases by 49 % suggesting that precipitation events are mainly due to warm and/or thick clouds.

At the annual scale, cloud radiative indexes (except the cloud radiative forcing) share significant proportions of common variance with the surface mass balance in the ablation zone and, to a lesser extent, with the glacier-wide one ($R^2 = 0.75$ and 0.44 , respectively when considering the cloud cover index). This suggests that, *via* attenuation of incoming shortwave and emission of longwave radiation fluxes, clouds play an important role in the variability of the surface mass balance.

The analysis of the interannual variability of precipitation and the surface mass balance showed that three annual precipitation characteristics explain large portions of the annual glacier-wide surface mass balance variability ($R^2 = 0.51$, 0.72 and 0.46 , for precipitation amounts, number of precipitation events and mean

precipitation intensity during days with precipitation, respectively). This shows the strong control precipitation exerts on the annual surface mass balance *via* an albedo feedback effect and accumulation.

Analysis of different methods to define the wet season onset and duration, considering either local or regional precipitation measurements or local radiation measurements, showed that the local cloud cover index is more related to synoptic conditions than local precipitations. This result may suggest that the cloud cover, derived from local radiative measurements, is a better index to define the wet season than the local precipitation measurements. We also found that, as opposed to what some authors suggest (e.g., Francou et al., 1995; Sicart et al., 2011), the wet season onset does not impact the interannual variability of the surface mass balance. These results led us to define a transition season between September and November, a core wet season between January and March and a dry season between June and August.

The distributed energy balance model (DEBAM) used in this study has been adapted and calibrated to simulate the Zongo Glacier's surface energy balance over one year by Sicart et al. (2011). To account for the long observation dataset used in our study, the model was partly recalibrated considering two contrasting years (with limited and significant mass losses, respectively). As a result, we changed the fresh snow albedo value from 0.9 in Sicart et al. (2011) to 0.85, to be in better agreement with both observations and broadband albedo calculations (e.g., Gardner and Sharp, 2010). We also changed the roughness lengths of momentum over ice from 10 mm to 26 mm taking into consideration Eddy-Covariance measurements that have been carried out on Zongo glacier in 2007 (Litt et al., 2014). However, because the model does not account for the subsurface heat flux, it cannot reproduce the night cooling of the surface which delays diurnal melt during the dry season (austral winter).

Analysis of the simulated energy fluxes over nine years showed that the transition period is the period during which there is the most energy available for melt. This corroborates previous findings which highlight that it is a key period in controlling annual melt rates (e.g., Sicart et al., 2011).

The study of the links between meteorological variables and surface mass balance showed that precipitation (*via* an albedo feedback effect) and cloud cover (*via* its impact on the downwelling radiation fluxes) are the main drivers of the

seasonal and annual mass balance variabilities. To have a better understanding on how they control the surface mass balance, we carried out sensitivity analyses of the timing of precipitation events and of the cloud cover over the transition season on the surface mass balance.

To assess the impact of the timing of precipitation on the surface mass balance, we generated scenarios by shuffling days of meteorological measurements during the transition season without changing the seasonal amounts. This maintained physical consistency between the measurements at the daily scale. Results showed that precipitation timing and associated amounts are key controls of the surface mass balance. *Via* an albedo feedback effect, evenly spreading out the snowfall events in time strongly reduces the melt rate.

The impact of cloud cover on surface mass balance was assessed by lowering the incoming shortwave radiation and increasing the incoming longwave radiation to reproduce cloud radiative effects. For each of the nine years, we tested three scenarios considering a continuous cloud cover over each month of the transition season (September, October and November). Results showed that a sustained cloud cover in November (and, to a lesser extent, in October) had a strong ability in lowering both seasonal and annual mass losses.

This multi-year analysis of the climate controls on the surface mass balance confirmed that the transition season is a key period in controlling annual mass loss. The sensitivity analyzes put forward the strong role of the timing of large precipitation events in controlling the annual melt rates.

Seventeenth century climate

To investigate the climate which allowed Zongo Glacier to reach its Little Ice Age maximum extent (1680 ± 28 AD, Rabatel, 2005), we considered a digital elevation model of the glacier at this extent and forced DEBAM with four different climate scenarios. These were considered representative of the Little Ice Age climate if close to equilibrium conditions were obtained (i.e., a glacier-wide surface mass balance close to 0 m w.e.).

To obtain information on the LIA climate, we considered studies based on paleoclimate proxies, last millennium ensemble runs using Global Climate Models (GCMs) and glacier sensitivity studies of past glacier extents in the Andes. Although

none of these studies provide insights at the seasonal changes which may have occurred during the LIA, we retained the following annual-scale information to constrain our scenarios: the Andes were about 1.1 °C cooler than today, with a 20-40% increase in annual precipitation amounts (e.g., Rabatel, 2005, Morales et al., 2012).

Based on the modeling study of the meteorological forcing on the surface mass balance in the current climate (part 1), we investigated the seasonal changes in precipitation and cloud cover during the transition and wet seasons. In addition, we considered a uniform 1.1°C cooling for all the scenarios. This cooling was obtained by lowering the position of the meteorological forcing in the model by 200 m (a -0.55 °C / 100 m is applied in the simulations).

The measurements of the year 2011/12 were selected to be the reference scenario as the monthly precipitation distribution of this year is considered to be representative of the long term one. This scenario was used to assess the impact of cooling without any precipitation changes. The other three scenarios looked at the changes in seasonal precipitation distribution (in addition to the 1.1 °C cooling of the air temperature). One scenario had a wetter transition season and wetter April-May. The other two scenarios assessed changes in wet season characteristics: the first had a longer wet season whereas the second one a wet season with increased precipitation amounts.

In order to maintain physical consistency between the meteorological forcing, we built the last three scenarios by swapping months of measurements from the reference scenario with corresponding months of other years to obtain the required precipitation changes. As a result, each scenario had about 20% extra precipitation compared to the current climate average.

Simulation results showed that close to equilibrium conditions could only be obtained with either a year with more frequent precipitation events between September and May or with an earlier wet season onset. Such results comfort findings for the current climate: the transition period (September-November) plays a key role in controlling the annual mass loss.

Besides, results showed that for the LIA scenarios which resulted in equilibrium conditions, significantly higher mass losses were observed in the lower reaches of the glacier (with respect to those observed over years with glacier-wide

surface mass balance at equilibrium in the current climate). During the LIA, the accumulation zone was much larger than now, resulting in significantly more accumulation. These large volumes, favored by the topographic conditions (narrow and steep ablation zone), created a strong downward ice flux which compensated for the high mass losses in the lowermost part of the glacier.

Perspectives

The nine year hourly dataset provides a unique opportunity to carry out physically-consistent climate sensitivity analyses (by shuffling hours/days/months of measurements). Whilst, for the current climate our focus was on the transition season, sensitivity analyses over other seasons could be tested.

Including the subsurface heat flux in the simulations would allow a more comprehensive modeling of the glacier surface mass balance and associated controls on melt and sublimation during the dry season. To do this, and to avoid error compensation, accurate snow and firn density subsurface temperature profiles measurements should be carried out.

In this PhD, a preliminary analysis between local and regional climates was carried out and revealed that the cloud cover index over Zongo Glacier could be better linked to larger scale climate features than precipitation measurements. However, we found no clear links between precipitation events and cloud radiative properties. These findings would require further investigation as they could potentially provide an understanding of the links between local and regional climate features.

Regarding the model application over the current climate, it would be worth applying the model to other glaciers of the outer tropics. For example, Fyffe et al. (2022) applied a surface energy balance model over five glaciers of the Peruvian Cordillera Blanca and found that the controls of the surface mass balance were similar to those found over Zongo Glacier: energy balance is dominated by the net shortwave radiation and the low melt rates observed during the dry season are due to a combination of sublimation and net longwave radiation deficit. However, their study does not provide detailed insights on the controls of the seasonal and annual surface mass balance variabilities. In this context, applying similar sensitivity

analyses to the ones carried out in this PhD would provide insights on the climate controls on the annual surface mass balance across the outer tropics.

Similarly, a possible continuation to this study could be to compare the melt mechanisms which occur in the inner and outer tropics. Indeed, previous studies carried out in the inner tropics have put forward climate controls on the surface mass balance which differ slightly from those of the outer tropics. For example Maisincho (2015) applied a surface energy balance model over Antizana Glacier 15a and found that there was a clear relationship between temperature and ablation. He also found that, as for Zongo Glacier, incoming longwave radiation and albedo were key controls of melt. Thus, similar sensitivity analyzes as the ones we used could be applied here and would provide detailed understanding of both seasonal and annual surface mass balance climate controls. Besides, since the inner tropics are characterized by sustained cloud cover all year round, a study of the links between the surface mass balance and the cloud index would provide information on how different types of clouds impact melt rates.

For the LIA climate reconstruction, applying similar scenarios to other tropical glaciers with known LIA maximum extent would allow an assessment of the coherence of our findings over the Zongo Glacier. In addition, doing so would provide insights on whether or not considering a constant accumulation-area ratio systematically overestimates past steady state equilibrium-line altitudes.

Indeed, our findings suggest that an AAR value estimated from today's conditions applied to the LIA glacier extension results in an overestimation of the LIA ELA. Applying the same methodology to other glaciers in the area would provide insights on whether or not the overestimation is linked to the glacier topography (steep and narrow glacier tongue in the case of Zongo Glacier) or if it is a general trend in the tropics.

Besides, as we hypothesized that there was a strong downward ice flux (i.e. an increased mass turnover compared to current climate), coupling DEBAM to a glacier dynamic model would allow us to test this hypothesis. This model setting could then be applied to other glaciers in the area to provide information on the glacier dynamics trend in tropical South America during the LIA.

The methodology we applied to generate scenarios (by shuffling months of measurements) proved to be efficient to assess the climate of the Little Ice Age. It

provided insights on the seasonal precipitation mechanisms despite the fact that it was constrained by information with coarse temporal resolution (annual to decadal - paleoclimate proxies, GCMs and sensitivity studies). Because paleoclimate proxies provide information over the past 20,000 years, similar methodologies could probably be used to assess climate variations which occurred in the Andes during the Holocene.

Similarly, considering that GCM predictions of synoptic conditions can be used to evaluate potential evolutions of the South American Monsoon System, the method used to assess the LIA climate could be used to assess future glacier evolutions. Indeed, accurate predictions of the evolution of tropical glaciers is of key importance as these play an important role in regulating water availability throughout the year (e.g., Buytaert et al., 2017). Thus, to avoid droughts or energy shortages, predicting their evolution as early as possible is required to adapt water management and energy production policies.

References

- Abermann, J., Kinnard, C., & MacDonell, S. (2014). Albedo variations and the impact of clouds on glaciers in the Chilean semi-arid Andes. *Journal of Glaciology*, *60*(219), 183-191.
- Ames, A., & Francou, B. (1995). Cordillera Blanca, glaciares en la Historia, *Bulletin de l'institut français d'études andines*, *24*(1), 37-64.
- Apaéstegui, J., Cruz, F. W., Vuille, M., Fohlmeister, J., Espinoza, J. C., Sifeddine, A., Strikis, N., Guyot, J. L., Ventura, R., Cheng, H., & Edwards, R. L., (2018). Precipitation changes over the eastern Bolivian Andes inferred from speleothem ($\delta^{18}O$) records for the last 1400 years. *Earth and Planetary Science Letters*, *494*, 124-134.
- Arias, P. A., Fu, R., Vera, C., & Rojas, M. (2015). A correlated shortening of the North and South American monsoon seasons in the past few decades. *Climate dynamics*, *45*(11), 3183-3203.
- Autin, P., Sicart, J. E., Rabatel, A., Soruco, A., & Hock, R. (2022, under review). Climate controls on the interseasonal and interannual variability of the surface mass and energy balances of a tropical glacier (Zongo Glacier, Bolivia, 16°S): new insights from the multi-year application of a distributed energy balance. *Journal of Geophysical Research Atmospheres*.
- Beeman, J. (2015). Modeling glacier surface response to monsoon-regime changes: Glaciar Zongo , Bolivia. *MSc dissertation*, Université Grenoble Alpes.
- Beljaars, A., & Holtslag, A. (1991). Flux parameterization over land surface for atmospheric models. *Journal of Applied Meteorology*, *30*(3), 327–341.
- Beven, K. J. (1989). Changing ideas in hydrology: The case of physically based models. *Journal of Hydrology*, *105*, 157–172.
- Bird, B. W., Abbott, M. B., Vuille, M., Rodbell, D. T., Stansell, N. D., & Rosenmeier, M. F. (2011). A 2,300-year-long annually resolved record of the South American summer monsoon from the Peruvian Andes. *Proceedings of the National Academy of Sciences of the United States of America*, *108*(21), 8583–8588.
- Blard, P. H., Lavé, J., Pik, R., Wagnon, P., & Bourlès, D. (2007). Persistence of full glacial conditions in the central Pacific until 15,000 years ago. *Nature*, *449*(7162), 591-594.
- Braconnot, P., Harrison, S. P., Otto-Bliesner, B. L., Abe-Ouchi, A., Jungclaus, J., & Peterschmitt, J.-Y. (2011). The Paleoclimate Modeling Intercomparison Project contribution to CMIP5. *CLIVAR Exchanges*, *16*(56), 15–19.

-
- Bradley, R. S., Keimig, F. T., Diaz, H. F., & Hardy, D. R. (2009). Recent changes in freezing level heights in the Tropics with implications for the deglaciation of high mountain regions. *Geophysical Research Letters*, 36(17).
- Braun, M., & Hock, R. (2004). Spatially distributed surface energy balance and ablation modelling on the ice cap of King George Island (Antarctica), *Global Planetary Change*, 42(1–4), 45–58.
- Brutsaert W. (1975). On a derivable formula for long-wave radiation from clear skies. *Water Resources Research*, 11(5), 742–744.
- Buytaert, W., Moulds, S., Acosta, L., De Bievre, B., Olmos, C., Villacis, M., ... & Verbist, K. M. (2017). Glacial melt content of water use in the tropical Andes. *Environmental Research Letters*, 12(11), 114014.
- Caballero, Y. (2001), Modélisation des écoulements d'origine pluvio-nivo-glaciaire en contexte de haute montagne tropicale: Application à la haute-vallée du Zongo (Bolivie), *Doctoral dissertation*, Université Montpellier II - Sciences et Techniques du Languedoc (USTL),
- Caballero, Y., Chevallier, P., Gallaire, R., & Pillco, R. (2004). Flow modelling in a high mountain valley equipped with hydropower plants: Rio Zongo Valley, Cordillera Real, Bolivia. *Hydrological Processes*, 18(5), 939-957.
- Campos, J. L., Cruz, F. W., Ambrizzi, T., Deininger, M., Vuille, M., Novello, V. F., & Strikis, N. M. (2019). Coherent South American Monsoon Variability During the Last Millennium Revealed Through High-Resolution Proxy Records. *Geophysical Research Letters*, 46(14), 8261–8270.
- Campos N, Alcalá-Reygosa J, Watson S, Kougkoulos I, Quesada Román A, & Grima N. (2021). Modeling the retreat of the Aneto Glacier (Spanish Pyrenees) since the Little Ice Age, and its accelerated shrinkage over recent decades. *Holocene*, 31, 1315–1326.
- Cook, S. J., Kougkoulos, I., Edwards, L. A., Dortch, J., & Hoffmann, D. (2016). Glacier change and glacial lake outburst flood risk in the Bolivian Andes. *The Cryosphere*, 10(5), 2399-2413.
- Corripio, J. G. (2004). Snow surface albedo estimation using terrestrial photography. *International journal of remote sensing*, 25(24), 5705-5729.
- Cuffey, K. M., & Paterson, W. S. B. (2010). *The physics of glaciers*. Academic Press.
- Cullen, N. J., Mölg, T., Kaser, G., Steffen, K., & Hardy, D. R. (2007). Energy-balance model validation on the top of Kilimanjaro, Tanzania, using eddy covariance data. *Annals of Glaciology*, 46, 227-233.
-

-
- Cusicanqui, D., Soruco, Á., Rabatel, A., & Anthelme, F. (2015). Mass balance of Zongo Glacier between 2006 and 2013 using volumetric method, employing Pléiades high resolution images acquired over the Cordillera Real, Bolivia (16°S, 68°W). *Revista Boliviana de Geociencias*, 8(7), 5–20.
- De Marsily, G. (1994). Quelques réflexions sur l'utilisation des modèles en hydrologie.[Tribune libre]. *Revue des sciences de l'eau/Journal of Water Science*, 7(3), 219-234.
- Díaz, L. B., & Vera, C. S. (2018). South American precipitation changes simulated by PMIP3/CMIP5 models during the Little Ice Age and the recent global warming period. *International Journal of Climatology*, 38(6), 2638–2650.
- Douville, H., Royer, J. F., & Mahfouf, J. F. (1995). A new snow parameterization for the Meteo-France climate model. *Climate Dynamics*, 12(1), 21-35.
- Dussailant, I., Berthier, E., Brun, F., Masiokas, M., Hugonnet, R., Favier, V., Rabatel, A., Pitte, P., & Ruiz, L. (2019). Two decades of glacier mass loss along the Andes. *Nature Geoscience*, 12(10), 802-808.
- Dumont, M., Sirguey, P., Arnaud, Y., & Six, D. (2011). Monitoring spatial and temporal variations of surface albedo on Saint Sorlin Glacier (French Alps) using terrestrial photography. *The Cryosphere*, 5(3), 759-771.
- Espinoza J. C., Ronchail J., Lengaigne M., Quispe N., Silva Y., Bettolli M.L., Avalos G., & Llacza A. (2013). Revisiting wintertime cold air intrusions at the east of the Andes: propagating features from subtropical Argentina to Peruvian Amazon and relationship with large-scale circulation patterns. *Climate Dynamics*, 41(7–8), 1983–2002.
- Espinoza, J. C., Chavez, S., Ronchail, J., Junquas, C., Takahashi, K., & Lavado, W. (2015). Rainfall hotspots over the southern tropical Andes: Spatial distribution, rainfall intensity, and relations with large-scale atmospheric circulation. *Water Resources Research*, 51(5), 3459-3475
- Francou, B., Ribstein, P., Saravia, R., & Tiriau, E. (1995). Monthly Balance and Water Discharge of an Inter-Tropical Glacier: Zongo Glacier, Cordillera Real, Bolivia, 16°S. *Journal of Glaciology*, 41(137), 61–67.
- Francou, B., Ribstein, P., & Pouyaud, B. (1997). La fonte des glaciers tropicaux - Ils comptent parmi les indicateurs les plus fiables d'un réchauffement global. *Recherche*, 28(302), 34-37.
- Fu, R., Yin, L., Li, W., Arias, P. A., Dickinson, R. E., Huang, L., Chakraborty, S., Fernandes, K., Liebmann, B., Fisher, R., & Myneni, B. (2013). Increased Dry-Season Length over Southern Amazonia in Recent Decades and Its Implication for Future

Climate Projection. *Proceedings of the National Academy of Sciences of the United States of America*, 110(45), 18110 – 15.

Funk, C., Peterson, P., Landsfeld, M., Pedreros, D., Verdin, J., Shukla, S., Husak, G., Rowland, J., Harrison, L., Hoell, A., & Michaelsen, J. (2015). The climate hazards infrared precipitation with stations—a new environmental record for monitoring extremes. *Scientific data*, 2(1), 1-21.

Fyffe, C. L., Potter, E., Fugger, S., Orr, A., Fatichi, S., Loarte, E., Medina, K., Hellström, R. A., Bernad, M., Aubry-Wake, C. Gurgiser, W., Perry, L. B., Suarez, W., Quincey, D. J. and Pellicciotti, F (2021). The energy and mass balance of Peruvian glaciers. *Journal of Geophysical Research: Atmospheres*, 126, e2021JD034911.

Gardner, A. S., & Sharp, M. J. (2010). A review of snow and ice albedo and the development of a new physically based broadband albedo parameterization. *Journal of Geophysical Research: Earth Surface*, 115(1), 1–15.

Garreaud, R. D., & Wallace, J. (1998). Summertime incursions of midlatitude air into subtropical and tropical South America. *Monthly Weather Review*, 126(10), 2713–2733.

Garreaud, R. D. (2000). Cold air incursions over subtropical South America: Mean structure and dynamics, *Monthly Weather Review*, 128(7), 2544-2559

Garreaud, R., Vuille, M., & Clement, A. C. (2003). The climate of the Altiplano: Observed current conditions and mechanisms of past changes. *Palaeogeography, Palaeoclimatology, Palaeoecology*, 194(1-3), 5–22.

Garreaud, R. D., Vuille, M., Compagnucci, R., & Marengo, J. (2009). Present-day South American climate, *Paleogeography, Paleoclimatology, Paleoecology*, 281(3-4), 180-195.

Gärtner-Roer, I., Nussbaumer, S. U., Hüsler, F., & Zemp, M. (2019). Worldwide assessment of national glacier monitoring and future perspectives. *Mountain Research and Development*, 39(2), A1-A11.

Gautier, E. (2012). Influence d'El Niño sur le régime thermique du glacier Zongo, Bolivie, 16°S. *Msc dissertation*, Université Joseph Fourier.

Greuell, W., & Konzelmann, T. (1994). Numerical modelling of the energy balance and the englacial temperature of the Greenland Ice Sheet. Calculations for the ETH-Camp location (West Greenland, 1155 m a.s.l.), *Global and Planetary Change*, 9(1-2), 91–114.

Greuell, W., Knap, W. H., & Smeets, P. C. (1997). Elevational changes in meteorological variables along a midlatitude glacier during summer. *Journal of Geophysical Research: Atmospheres*, 102(D22), 25941-25954.

-
- Grove, JM (1988). The Little Ice Age. London: Routledge, xxii+ 498 pp. *Progress in Physical Geography*, 32(1), 103-106.
- Guillaumin, D. (2014). Étude de sensibilité du bilan de masse d'un glacier bolivien aux forçages climatiques par application d'un modèle distribué de bilan d'énergie. *Msc dissertation*, Ecole Polytechnique.
- Gurgiser, W., Marzeion, B., Nicholson, L., Ortner, M., & Kaser, G. (2013). Modeling energy and mass balance of Shallap Glacier, Peru. *Cryosphere*, 7(6), 1787–1802.
- Gurgiser, W., Mölg, T., Nicholson, L., & Kaser, G. (2013a). Mass-balance model parameter transferability on a tropical glacier. *Journal of Glaciology*, 59(217), 845-858.
- Gutierrez-Cori, O., Espinoza, J. C., Li, L., Wongchuig, S., Arias, P., Ronchail, J., & Segura, H. (2021). On the hydroclimate-vegetation relationship in the southwestern Amazon during the 2000–2019 period. *Frontiers in Water*, 3, 648499.
- Hardy, D. R., Vuille, M., Braun, C., Keimig, F., & Bradley, R. S. (1998). Annual and daily meteorological cycles at high altitude on a tropical mountain. *Bulletin of the American Meteorological Society*, 79(9), 1899-1914.
- Hastenrath, S. (1981). *The glaciation of the Ecuadorian Andes*. Balkema.
- Hastenrath, S. (1984). *The glaciers of equatorial East Africa* (Vol. 2). Springer Science & Business Media.
- Hastenrath, S. (1991). *Glaciological Studies on Mount Kenya 1971-83-91*. Department of Meteorology, University of Wisconsin-Madison.
- Hastenrath, S., & Ames, A. (1995). Diagnosing the imbalance of Yanamarey Glacier in the Cordillera Blanca of Peru. *Journal of Geophysical Research*, 100(D3), 5105–5112.
- Hastenrath, S. (1997). Measurements of diurnal heat exchange on the Quelccaya Ice Cap, Peruvian Andes. *Meteorology and Atmospheric Physics*, 62(1), 71-78.
- Haug, G. H., Hughen, K. A., Sigman, D. M., Peterson, L. C., & Röhl, U. (2001). Southward migration of the intertropical convergence zone through the holocene. *Science*, 293(5533), 1304–1308.
- Hock, R. (1998). Modelling of Glacier Melt and Discharge. *Doctoral dissertation*, Federal Institute of Technology, Switzerland.
- Hock, R., & Holmgren, B. (2005). A Distributed Surface Energy-Balance Model for Complex Topography and Its Applications to Storglaciaren. *Journal of Glaciology*, 51(172), 25–36.

-
- Hock, R., & Tijm-Reijmer, C. (2012). A Mass-Balance, Glacier Runoff and Multi-Layer Snow Model DEBAM and DETIM Distributed Energy Balance and Distributed Enhanced Temperature Index Model Users Manual.
- Hugonnet, R., McNabb, R., Berthier, E., Menounos, B., Nuth, C., Girod, L., & Kääb, A. (2021). Accelerated global glacier mass loss in the early twenty-first century. *Nature*, *592*(7856), 726-731.
- Hurley, J. V., Vuille, M., Hardy, D. R., Burns, S. J., & Thompson, L. G. (2015). Cold air incursions, $\delta^{18}\text{O}$ variability, and monsoon dynamics associated with snow days at Quelccaya Ice Cap, Peru. *Journal of Geophysical Research: Atmospheres*, *120*(15), 7467-7487.
- Hurley, J. V., Vuille, M., & Hardy, D. R. (2016). Forward modeling of $\delta^{18}\text{O}$ in Andean ice cores. *Geophysical Research Letters*, *43*(15), 8178-8188.
- Hurley, J. V., Vuille, M., & Hardy, D. R. (2019). On the Interpretation of the ENSO Signal Embedded in the Stable Isotopic Composition of Quelccaya Ice Cap, Peru. *Journal of Geophysical Research : Atmospheres*, *124*(1), 131–145.
- IPCC 5th Assessment Report, WG 1 Glossary: IPCC, (2014), Annex II: Glossary [Mach, K.J., S. Planton and C. von Stechow (eds.)]. In: Climate Change 2014: Synthesis Report. Contribution of Working Groups I, II and III to the Fifth Assessment Report of the Intergovernmental Panel on Climate Change [Core Writing Team, R.K. Pachauri and L.A. Meyer (eds.)]. IPCC, Geneva, Switzerland, pp. 117-130.
- Jomelli, V., Favier, V., Rabatel, A., Brunstein, D., Hoffmann, G., & Francou, B. (2009). Fluctuations of glaciers in the tropical Andes over the last millennium and palaeoclimatic implications: A review. *Palaeogeography, Palaeoclimatology, Palaeoecology*, *281*(3-4), 269-282.
- Jomelli, V., Khodri, M., Favier, V., Brunstein, D., Ledru, M. P., Wagnon, P., Blard, P. H., Sicart, J. E., Braucher, R., Grancher, D., Bourlès, D. LO., Braconnot, P., & Vuille, M. (2011). Irregular tropical glacier retreat over the Holocene epoch driven by progressive warming. *Nature*, *474*(7350), 196-199.
- Junquas, C., Takahashi, K., Condom, T., Espinoza, J. C., Chávez, S., Sicart, J. E., & Lebel, T. (2018). Understanding the influence of orography on the precipitation diurnal cycle and the associated atmospheric processes in the central Andes. *Climate dynamics*, *50*(11), 3995-4017.
- Kaser, G., Ames, A., & Zamora, M. (1990). Glacier Fluctuations and Climate in the Cordillera Blanca, Peru." *Annals of Glaciology*, *14*(May), 136–40.
- Kaser, G. (1999). A review of the modern fluctuations of tropical glaciers. *Global and Planetary Change*, *22*(1-4).
-

-
- Kaser, G. (2001). Glacier-climate interaction at low latitudes. *Journal of Glaciology*, 47(157), 195–204.
- Klemes, V. (1983). Conceptualization and scale in hydrology. *Journal of Hydrology*, 65, 1–23.
- Kougkoulos, I., Cook, S. J., Edwards, L. A., Clarke, L. J., Symeonakis, E., Dortch, J. M., & Nesbitt, K. (2018). Modelling glacial lake outburst flood impacts in the Bolivian Andes. *Natural Hazards*, 94(3), 1415-1438.
- Lean, J. (2000). Evolution of the Sun's spectral irradiance since the Maunder Minimum. *Geophysical Research Letters*, 27, 2425–2428.
- Ledru, M.-P., Jomelli, V., Samaniego, P., Vuille, M., Hidalgo, S., Herrera, M., & Ceron, C. (2013). The Medieval Climate Anomaly and the Little Ice Age in the eastern Ecuadorian Andes. *Climate of the Past*, 9(1), 307–321.
- Lehmann, B., Soruco A., Sicart, J. E., Francou, B., Rabatel, A., & Vincent, P. (2013). Cuencas Glaciares, Zongo-Charquini Sur, Bolivia, 16°S, Mediciones Glaciológicas, Hidrológicas y Meteorológicas. Año Hidrológico 2011-2012. *Informe 2011-2012, IRD, IHH*, 111p.
- Lejeune, Y., Wagnon, P., Bouilloud, L., Chevallier, P., Etchevers, P., Martin, E., Sicart, J. E., & Habets, F. (2007). Melting of snow cover in a tropical mountain environment in Bolivia: Processes and modeling. *Journal of Hydrometeorology*, 8(4), 922–937.
- Lejeune, Y. (2009). Apports des modèles de neige CROCUS et de sol ISBA à l' étude du bilan glaciologique d' un glacier tropical et du bilan hydrologique de son bassin versant. *Doctoral dissertation*, Université Joseph Fourier - Grenoble.
- Lenters, J. D., & Cook, K. H. (1997). On the origin of the Bolivian high and related circulation features of the South American climate. *Journal of the Atmospheric Sciences*, 54(5), 656–677.
- Li, Y. J., Ding, Y. J., Shangguan, D. H., & Wang, R. J. (2019). Regional differences in global glacier retreat from 1980 to 2015. *Advances in Climate Change Research*, 10(4), 203–213.
- Litt, M., Sicart, J. E., Helgason, W. D., & Wagnon, P. (2014). Turbulence Characteristics in the Atmospheric Surface Layer for Different Wind Regimes over the Tropical Zongo Glacier (Bolivia, 16S), *Boundary-Layer Meteorology*, 154(3),471–495.
- Litt, M., Sicart, J. E., & Helgason, W. (2015). A study of turbulent fluxes and their measurement errors for different wind regimes over the tropical Zongo Glacier (16 S) during the dry season. *Atmospheric Measurement Techniques*, 8(8), 3229-3250.

-
- Lliboutry, L., Morales, B., & Schneider, B. (1977). Glaciological problems set by the control of dangerous lakes in Cordillera Blanca, Peru. III. Study of moraines and mass balance at Safuna. *Journal of Glaciology*, 18(79), 275-290.
- Maisincho, L. (2015). Analyse de la fonte glaciaire et nivale dans les Andes tropicales à partir d'un bilan d'énergie : Glacier de l'Antisana, Equateur (0°28'S). Sciences de la Terre. *PhD dissertation*, Université Grenoble Alpes; Escuela politécnica nacional (Quito).
- Male, D. H., & Granger, R. J. (1981). Snow surface energy exchange. *Water Resources Research*, 17(3), 609-627.
- Malone, A. G. O., Pierrehumbert, R. T., Lowell, T. V., Kelly, M. A., & Stroup, J. S. (2015). Constraints on southern hemisphere tropical climate change during the Little Ice Age and Younger Dryas based on glacier modeling of the Quelccaya Ice Cap, Peru. *Quaternary Science Reviews*, 125, 106–116.
- Masiokas, M. H., Rabatel, A., Rivera, A., Ruiz, L., Pitte, P., Ceballos, J. L., Barcaza, G., Soruco, A., Brown, F., Dussailant, I., & MacDonell, S. (2020). A Review of the Current State and Recent Changes of the Andean Cryosphere. *Frontiers in Earth Science*, 8(June), 1–27.
- Maussion, F., Gurgiser, W., Großhauser, M., Kaser, G., & Marzeion, B. (2015). ENSO influence on surface energy and mass balance at Shallap Glacier, Cordillera Blanca, Peru, *The Cryosphere*, 9(4), 1663–1683.
- Marengo, J. A., Tomasella, J., Alves, L. M., Soares, W. R., & Rodriguez, D.A. (2011). The drought of 2010 in the context of historical droughts in the Amazon region. *Geophysical Research Letters*, 38(12), 1-5.
- Marengo, J. A., Liebmann, B., Grimm, A. M., Misra, V., Silva Dias, P. D., Cavalcanti, I. F. A., Carvalho, L. M. V., Berbery, E. H., Ambrizzi, T., Vera, C. S., Saulo, A.C., Nogues-Paegle, J., Zipser, E., Seth, A. & Alves, L. M. (2012). Recent developments on the South American monsoon system. *International Journal of Climatology*, 32(1), 1-21.
- Marks, D., & Dozier, J. (1979). A clear-sky longwave radiation model for remote alpine areas. *Archiv für Meteorologie, Geophysik und Bioklimatologie, Serie B*, 27(2), 159-187.
- Michel, S. (2020). Caractérisation des variations climatiques du dernier millénaire à l'aide de nouvelles méthodes statistiques: reconstruction paléoclimatiques et intégration dans un modèle de circulation globale du climat. *Doctoral dissertation*, Université de Bordeaux.

-
- Mölg, T., & Hardy, D. R. (2004). Ablation and associated energy balance of a horizontal glacier surface on Kilimanjaro. *Journal of Geophysical Research: Atmospheres*, 109(16), 1–13.
- Mölg, T., Hardy, D. R., Cullen, N. J., & Kaser, G. (2008). Tropical Glaciers , Climate Change, and Society. *Trends in natural landscapes*, pp. 168–182.
- Mölg, T., Cullen, N. J., Hardy, D. R., Kaser, G., & Klok, L. (2008). Mass Balance of a Slope Glacier on Kilimanjaro and Its Sensitivity to Climate Thomas. *International Journal of Climatology*, 28(6), 881–92.
- Mölg, T., Cullen, N. J., & Kaser, G. (2009). Solar radiation , cloudiness and longwave radiation over low-latitude glaciers: implications for mass-balance modelling. *Journal of Glaciology*, 55(190), 292–302.
- Morales, M. S., Christie, D. A., Villalba, R., Argollo, J., Pacajes, J., Silva, J. S., Alvarez, C. A., Llancabure, J. C., & Gamboa, C. C. (2012). Precipitation changes in the South American Altiplano since 1300 AD reconstructed by tree-rings. *Climate of the Past*, 8(2), 653–666.
- Morato, T., Vaezi, M., & Kumar, A. (2019). Assessment of energy production potential from agricultural residues in Bolivia. *Renewable and Sustainable Energy Reviews*, 102(2019), 14-23.
- Neukom, R., Gergis, J., Karoly, D. J., Wanner, H., Curran, M., Elbert, J., González-Rouco, F., Linsley, B. K., Moy, A. D., Mundo, I., Raible, C. C., Steig, E. J., Van Ommen, T., Vance, T., Villalba, R., Zinke, J., & Frank, D. (2014). Inter-hemispheric temperature variability over the past millennium. *Nature Climate Change*, 4(5), 362–367.
- Nicholson, L. I., Prinz, R., Mölg, T., & G. Kaser, G. (2013). Micrometeorological Conditions and Surface Mass and Energy Fluxes on Lewis Glacier, Mt Kenya, in Relation to Other Tropical Glaciers. *Cryosphere*, 7(4), 1205–25.
- Oerlemans, J., & Knap, W. H. (1998). A 1 Year Record of Global Radiation and Albedo in the Ablation Zone of Morteratschgletscher, Switzerland. *Journal of Glaciology*, 44(147), 231–38.
- Ohmura, A., Kasser, P., & Funk, M. (1992). Climate at the equilibrium line of glaciers. *Journal of Glaciology*, 38(130), 397–411.
- Østby, T. I., Schuler, T. V., Hagen, J. O., Hock, R., Kohler, J., & Reijmer C.H. (2017). Diagnosing the Decline in Climatic Mass Balance of Glaciers in Svalbard over 1957-2014. *Cryosphere*, 11(1), 191–215.
- Paul, F., & Bolch, T. (2019). Glacier Changes Since the Little Ice Age. University of Zurich, pp. 23–42.

-
- Paulson, C.A. (1970). The mathematical representation of wind speed and temperature profiles in the unstable atmospheric surface layer. *Journal of Applied Meteorology*, 9, 857-861.
- Permana, D. S., Thompson, L. G., Mosley-Thompson, E., Davis, M. E., Lin, P. N., Nicolas, J. P., Bolzan, J. F., Bird, B. W., Mikhalenko, V. N., Gabrielli, P., Zagorodnov, V., Mountain, K. R., Schotterer, U., Hanggoro, W., Habibie, M. N., Kaize, Y., Gunawan, D., Setyadi, G., Susanto, R. D., Fernández, A., & Mark, B. G. (2019). Disappearance of the last tropical glaciers in the western pacific warm pool (Papua, Indonesia) appears imminent. *Proceedings of the National Academy of Sciences of the United States of America*, 116(52), 26382–26388.
- Perry, L. B., Seimon, A., Andrade-Flores, M. F., Endries, J. L., Yuter, S. E., Velarde, F., Arias, S., Bonshoms, M., Burton, E. J., Winkelmann, I. R., Cooper, C. M., Mamani, G., Rado, M., Montoya, N., & Quispe, N. (2017). Characteristics of Precipitating Storms in Glacierized Tropical Andean Cordilleras of Peru and Bolivia. *Annals of the American Association of Geographers*, 107(2), 309–322.
- Prinz, R., Nicholson, L. I., Mölg, T., Gurgiser, W., & Kaser, G. (2016). Climatic controls and climate proxy potential of Lewis Glacier, Mt. Kenya. *Cryosphere*, 10(1), 133–148.
- Rabatel, A. (2005). Chronologie et interprétation paléoclimatique des fluctuations des glaciers dans les Andes de Bolivie (16°S) depuis le maximum du Petit Âge Glaciaire (17ème siècle), *Doctoral dissertation*, Université Joseph Fourier, Grenoble 1.
- Rabatel, A., Jomelli, V., Naveau, P., Francou, B., & Grancher, D. (2005). Dating of Little Ice Age glacier fluctuations in the tropical Andes: Charquini glaciers, Bolivia, 16 S. *Comptes Rendus Géoscience*, 337(15), 1311-1322.
- Rabatel, A., Francou, B., Jomelli, V., Naveau, P., & Grancher, D. (2008). A chronology of the Little Ice Age in the tropical Andes of Bolivia (16°S) and its implications for climate reconstruction. *Quaternary Research*, 70(2), 198–212.
- Rabatel, A., Bermejo, A., Loarte, E., Soruco, A., Gomez, J., Leonardini, G., Vincent, C., & Sicart, J. E. (2012). Can the snowline be used as an indicator of the equilibrium line and mass balance for glaciers in the outer tropics? *Journal of Glaciology*, 58(212), 1027–1036.
- Rabatel, A., Francou, B., Soruco, A., Gomez, J., Cáceres, B., Ceballos, J. L., Basantes, R., Vuille, M., Sicart, J. E., Huggel, C., Scheel, M., Lejeune, Y., Arnaud, Y., Collet, M., Condom, T., Consoli, G., Favier, V., Jomelli, V., Galarraga, R., Ginot, P., Maisincho, L., Mendoza, J., Ménégos, M., Ramirez, E., Ribstein, P., Suarez, W., Villacis, M., & Wagnon, P. (2013). Current state of glaciers in the tropical Andes: A multi-century perspective on glacier evolution and climate change. *The Cryosphere*, 7(1), 81–102.
-

-
- Rabatel, A. (2015). Apports d'une approche combinant mesures in situ et télédétection optique pour le suivi des glaciers de montagne : cas des Andes tropicales et des Alpes occidentales. *HDR thesis*, Université Grenoble Alpes.
- Ramallo, C (2013). Caractérisation du régime pluviométrique et sa relation à la fonte du Glacier Zongo (Cordillère Royale). *Doctoral dissertation*, Université Grenoble Alpes.
- Reijmer, C. H., & Hock, R. (2008). Internal Accumulation on Storglaciären, Sweden, in a Multi-Layer Snow Model Coupled to a Distributed Energy- and Mass-Balance Model. *Journal of Glaciology*, 54(184), 61–72.
- Réveillet, M., Rabatel, A., Gillet-Chaulet, F., & Soruco, A. (2015). Simulations of Changes to Glacier Zongo, Bolivia (16°S), over the 21st Century Using a 3-D Full-Stokes Model and CMIP5 Climate Projections. *Annals of Glaciology*, 56(70), 89–97.
- Ribstein, P., Tiriau, E., Francou, B., & Saravia, R. (1995). Tropical Climate and Glacier Hydrology: A Case Study in Bolivia. *Journal of Hydrology*, 165(1–4), 221–34.
- Ronchail, J. (1989). Advections polaires en Bolivie : mise en évidence et caractérisation des effets climatiques. *Hydrologie Continentale*, 4(1), 49–56.
- Sachs, J. P., Sachse, D., Smittenberg, R. H., Zhang, Z., Battisti, D. S., & Golubic, S. (2009). Southward movement of the Pacific intertropical convergence zone AD 1400-1850. *Nature Geoscience*, 2(7), 519–525.
- Schneider, T., & Jansson, P. (2004). Internal accumulation in firn and its significance for the mass balance of Storglaciären, Sweden. *Journal of Glaciology*, 50(168):25–34.
- Schulla, J. (1997). Hydrologische Modellierung von Flussgebieten zur Abschätzung der Folgen von Klimaänderungen Abhandlung. *Doctoral dissertation*, Technische Universität Dresden.
- Seehaus, T., Malz, P., Sommer, C., Soruco, A., Rabatel, A., & Braun, M. (2019). Mass balance and area changes of glaciers in the Cordillera Real and Tres Cruces, Bolivia, between 2000 and 2016. *Journal of Glaciology*, 66(255), 124–136.
- Segura, H., Junquas, C., Espinoza, J.C., Vuille, M., Jauregui, Y.R., Rabatel, A., Condom, T., & Lebel, T. (2019). New insights into the rainfall variability in the tropical Andes on seasonal and interannual time scales, *Climate Dynamics*, 53(1-2), 405-426.
- Seibert, J. (1999). Conceptual Runoff Models: Fiction or Representation of Reality? 52 pp., *Uppsala University Press*, Uppsala, Sweden
-

-
- Sicart, J.E., Ribstein, P., Wagnon, P., & Brunstein, D. (2001). Clear-sky albedo measurements on a sloping glacier surface: A case study in the Bolivian Andes. *Journal of Geophysical Research: Atmospheres*, 106(D23), 31729-31737.
- Sicart, J. E. (2002). Contribution à l'étude Des Flux d'énergie, Du Bilan de Masse et Du Débit de Fonte d'un Glacier Tropical: Le Zongo, Bolivie. *Doctoral dissertation*, Université Paris IV Pierre et Marie Curie.
- Sicart, J. E., Ribstein, P., Chazarin, J. P., & Berthier, E. (2002). Solid precipitation on a tropical glacier in Bolivia measured with an ultrasonic depth gauge." *Water Resources Research*, 38(10), 7-1-7-7.
- Sicart, J. E., Wagnon, P., & Ribstein, P. (2005). Atmospheric controls of the heat balance of Zongo Glacier (16°S, Bolivia), *Journal of Geophysical Research: Atmospheres*, 110(12), 1-17.
- Sicart, J.E., Ribstein, P., Francou, B., Pouyaud, B., & Condom, T. (2007). Glacier mass balance of tropical Zongo glacier, Bolivia, comparing hydrological and glaciological methods. *Global and Planetary Change*, 59(1-4), 27-36.
- Sicart, J. E., Hock, R., & Six, D. (2008). Glacier Melt, Air Temperature, and Energy Balance in Different Climates: The Bolivian Tropics, the French Alps, and Northern Sweden. *Journal of Geophysical Research Atmospheres*, 113(24), 1-11.
- Sicart, J. E., Hock, R., Ribstein, P., & Chazarin, J. P. (2010). Sky Longwave Radiation on Tropical Andean Glaciers: Parameterization and Sensitivity to Atmospheric Variables. *Journal of Glaciology*, 56(199), 854-60.
- Sicart, J. E., Hock, R., Ribstein, P., Litt, M., & Ramirez, E. (2011). Analysis of Seasonal Variations in Mass Balance and Meltwater Discharge of the Tropical Zongo Glacier by Application of a Distributed Energy Balance Model. *Journal of Geophysical Research*, 119(D13), 1-18.
- Sicart, J. E., Litt, M., Helgason, W., Ben Tahar, V., & Chaperon, T. (2014). A study of the atmospheric surface layer and roughness lengths on the high-altitude tropical Zongo glacier, Bolivia. *Journal of Geophysical Research: Atmospheres*, 119(3), 3793-3808.
- Sicart, J. E., Villacís, M., Condom, T., & Rabatel, A. (2015). GREATICE monitors glaciers in the tropical Andes. *Eos*.
- Sicart, J. E., Espinoza, J. C., Quéno, L., & Medina, M. (2016). Radiative properties of clouds over a tropical Bolivian glacier: seasonal variations and relationship with regional atmospheric circulation. *International Journal of Climatology*, 36(8), 3116-3128.
-

-
- Sicart, J.E. (2021), Contribution à l'étude des flux d'énergie en surface de glaciers de montagne dans les Andes tropicales et dans les Alpes. *HDR dissertation*, Université Grenoble Alpes.
- Solomina, O., Bradley, R. S., Hodgson, D. A., Ivy-Ochs, S., Jomelli, V., Mackintosh A. N., Nesje, A., Owen, L. A., Wanner, H., Wiles, G.C., & Young N.E. (2015). Holocene glacier fluctuations. *Quaternary Science Reviews*, 111, 9–34.
- Solomina, O., Bradley, R. S., Jomelli, V., Geirsdottir, A., Kaufman, D., Koch, J., Masiokas, M., Miller, G., Nesje, A., Nicolussi, K., Owen, L., Wanner, H., Wiles, G., & Yang, B. (2016). Glacier fluctuations in the last 2000 years. *Quaternary Science Reviews*, 149, 61–90.
- Soruco, A., Vincent, C., Francou, B., Ribstein, P., Berger, T., Sicart, J. E., Wagnon, P., Arnaud, Y., Favier, V., & Lejeune, I. (2009). Mass Balance of Glacier Zongo, Bolivia, between 1956 and 2006, Using Glaciological, Hydrological and Geodetic Methods. *Annals of Glaciology*, 50(50), 1–8.
- Soruco, A., Vincent, C., Rabatel, A., Francou, B., Thibert, E., Sicart, J. E., & Condom, T. (2015). Contribution of Glacier Runoff to Water Resources of La Paz City, Bolivia (16° S). *Annals of Glaciology*, 56(70), 147–54.
- Sturm, M., Holmgren, J., König, M., & Morris, K. (1997). The thermal conductivity of seasonal snow. *Journal of Glaciology*, 43(143):26–41.
- Tardif, R., Hakim, G. J., Perkins, W. A., Horlick, K. A., Erb, M. P., Emile-Geay, J., Anderson, D., Steig, E., & Noone, D. (2019). Last Millennium Reanalysis with an expanded proxy database and seasonal proxy modeling. *Climate of the Past*, 15(4), 1251-1273.
- Thompson, L. G., Mosley-Thompson, E., Dansgaard, W., & Grootes, P. M. (1986). The Little Ice Age as recorded in the stratigraphy of the tropical Quelccaya ice cap. *Science*, 234(4774), 361-364.
- Thompson, L. G., Mosley-Thompson, E., Brecher, H., Davis, M., León, B., Les, D., Lin, P. N., Mashiotta, T., & Mountain, K. (2006). Abrupt tropical climate change: Past and present. *Proceedings of the National Academy of Sciences of the United States of America*, 103(28), 10536–10543.
- Troll, C. (1941). Studien zur vergleichenden Geographie der Hochgebirge der Erde. Bonner Mitt. 21, Universität Bonn, Bonn, Germany.
- Vera, C., Higgins, W., Amador, J., Ambrizzi, T., Garreaud, R., Gochis, D., Gutzler, D., Lettenmaier, D., Marengo, J., Mechoso, C. R., Noguez-Paegle, J., Silva Dias, P. L., & Zhang, C. (2006). Toward a unified view of the American monsoon systems. *Journal of climate*, 19(20), 4977-5000.

-
- Vimeux, F., Ginot, P., Schwikowski, M., Vuille, M., Hoffmann, G., Thompson, L. G., & Schotterer, U. (2009). Climate variability during the last 1000 years inferred from Andean ice cores: A review of methodology and recent results. *Palaeogeography, Palaeoclimatology, Palaeoecology*, 281(3-4), 229-241.
- Vincent, C., Kappenberger, G., Valla, F., Bauder, A., Funk, M., & Le Meur, E. (2004). Ice ablation as evidence of climate change in the Alps over the 20th century. *Journal of Geophysical Research: Atmospheres*, 109(D10).
- Vincent, C., Le Meur, E., Six, D., & Funk, M. (2005). Solving the paradox of the end of the Little Ice Age in the Alps. *Geophysical Research Letters*, 32(9).
- Vincent, C., Soruco, A., Azam, M. F., Basantes-Serrano, R., Jackson, M., Kjølmoen, B., Thibert, E., Wagnon, P., Six, D., Rabatel, A., Ramanathan, A., Berthier, E., Cusiquanci, D., Vincent, P., & Mandla, A. (2018). A Nonlinear Statistical Model for Extracting a Climatic Signal From Glacier Mass Balance Measurements. *Journal of Geophysical Research: Earth Surface*, 123(9), 2228–42.
- Vuille, M., Hardy, D. R., Braun, C., Keimig, F., & Bradley, R. S. (1998). Atmospheric Circulation Anomalies Associated with 1996/1997 Summer Precipitation Events on Sajama Ice Cap, Bolivia. *Journal of Geophysical Research*, 103(D10), 191–204.
- Vuille, M., & Werner, M. (2005). Stable isotopes in precipitation recording South American summer monsoon and ENSO variability: Observations and model results. *Climate Dynamics*, 25(4), 401-413.
- Vuille, M., Francou, B., Wagnon, P., Juen, I., Kaser, G., Mark, B., & Bradley, R. S. (2008). Climate change and tropical Andean glaciers: Past, present and future. *Earth-Science Reviews*, 89(3-4), 79-96.
- Vuille, M., Burns, S. J., Taylor, B. L., Cruz, F. W., Bird, B. W., Abbott, M. B., Kanner, L. C., Cheng, H., & Novello, V. F. (2012). A review of the South American monsoon history as recorded in stable isotopic proxies over the past two millennia. *Climate of the Past*, 8(4), 1309-1321.
- Wagnon, P., Ribstein, P., Francou, B., & Pouyaud, B. (1999). Annual cycle of energy balance of Zongo Glacier. *Journal of Geophysical Research*, 104(1998), 3907–3923.
- Zemp, M., Huss, M., Thibert, E., Eckert, N., McNabb, R., Huber, J., & Cogley, J. G. (2019). Global glacier mass changes and their contributions to sea-level rise from 1961 to 2016. *Nature*, 568(7752), 382-386.

List of figures

- 1.1 Worldwide tropical glacier distribution, adapted from Kaser & Osmaston (2002) 5
- 1.2 The three phases of ENSO: normal conditions (a), warm El Niño phase (b) and cold La Niña phase (c). The left side of the diagram is the western Pacific ocean (Asian side) and the right side shows eastern Pacific ocean towards South America. Red and orange colors show warm sea surface temperatures (SSTs) and the yellow and green ones show cooler SSTs. The blue band shows the approximate location of the thermocline (water at about 20°C). Rain clouds form over the warmest SSTs. Source: Pacific Marine Environmental Laboratory: <https://www.pmel.noaa.gov/elnino/schematic-diagrams> 6
- 1.3 Average CHIRPS precipitation (shaded) and vertically integrated water vapor flux (vectors) between December and February (DJF, plot a) and between June and August (JJA, plot b). The red triangle with a yellow outline shows the approximate position of Zongo Glacier. Source: Segura et al. (2019). 7
- 1.4 Panoramic view of Zongo Glacier on the 15th of July 2015. Photo courtesy: Maxime Harter 7
- 1.5 Daily precipitation and discharge (a) and temperatures (b) over the year 2016/17. The gray rectangles show the seasons following the definition provided in Sicart et al. (2011). On plot b, the 14 days moving average temperature highlights the low seasonal temperature variability. Daily precipitation and temperature measurements were carried out on the glacier (SAMA Automatic Weather Station, 5050 m a.s.l.), discharge measurements were carried out at the glacier outlet (TUBO gauging station, 4850 m a.s.l.). 8
- 1.6 Schematics of the synoptic conditions of Surazo events. Thick dark arrows represent low-level wind advecting cold air whilst the light gray ones represent the low level advection of warm air. Thin contour lines represent surface isobars. Source: Garreaud (2000) 10
- 2.1 Monitoring network on and around the Zongo Glacier. The diamonds show the three automatic weather stations, the purple dot shows the position of the discharge gauge, the red dots and triangles show the ablation stakes and snow pit positions respectively. The blue triangles show the positions of the storage rain gauges. The glacier contour shown is the 2012 glacier extent and the top right inset is a 3D representation of this extent. Background image acquired by the Pléiades satellite in 2016, © CNES - Airbus D&S. 23
- 2.2 TUBO gauging station in 2019, photo courtesy: Victor Ramseyer 24
- 2.3 Photos of the three AWS on and around the glacier. Photographs a and b were taken in 2019 by Victor Ramsayer, photograph c. was taken in 2014 by Maxime Harter. 24
- 2.4 Operating periods of the three automatic weather stations located on and around the glacier (SAMA measurements are in gray, ORE measurements in 27

	red and MEVIS & PLATAFORMA measurements in yellow). Note that the displayed operating periods correspond to periods with at least one variable measured for over 15 days in the corresponding month. The years in bold are those for which hourly data was available for the whole hydrological year after filling the measurement gaps.	
2.5	Correlations between hourly incoming shortwave radiation measured at SAMA and ORE (a), incoming longwave radiation at SAMA and both ORE (black) and PLATAFORMA (yellow, plot b), outgoing longwave radiation at SAMA and ORE (c) and (d) shows the 30 minutes relative humidity measurements at SAMA and ORE. The measurements were carried out during 2012/13.	31
2.6	Annual glacier-wide surface mass balance (B_{GW} , plot a), precipitation amounts (b), mean temperature (c), relative humidity (d), wind speed (e), annual mean incoming shortwave (f), and longwave (g) radiation and outgoing longwave radiation (h), for the nine years with on-glacier hourly data.	33
2.7	Methodology used to estimate snow lines from photographs illustrated over the 25 th of August 2009. Photo courtesy: Maxime Litt	36
2.8	Illustration of the calibration of C on atmospheric emissivity (a) and L_{clear} (b) over Plataforma measurements for the year 2013/14. (c) shows the cloud radiative forcing (CF) and its components (CF_{SW} & CF_{LW}).	40
3.1	Illustration of the different energy fluxes considered in the energy balance.	43
3.2	Observed and simulated albedo between September and October 1999. A time constant, $n^* = 10$ days, is selected in the simulation.	48
3.3	Changes in Zongo Glacier surface area between 1999 and 2016. Data comes from in situ topographical measurements performed within the framework of the GLACIOCLIM observatory.	54
3.4	Observed (black) and simulated (orange) albedo at the AWS (first column) and discharge at the outlet (second column) for the whole simulation dataset.	59
3.5	Nine year averaged simulated discharge and its components and mean contribution of each reservoir to the simulated discharge over the transition season (a and b, respectively), c and d show the same for the wet season.	60
3.6	Annual measured (in black) and simulated (in orange) glacier-wide surface mass balance (B_{GW}) for the nine years studied.	60
3.7	Measured (crosses) and simulated surface mass balance by altitude for the nine years studied.	61
3.8	Observed and simulated glacier surface for two days in 2004/05.	63
3.9	Comparison of the simulation results with or without the snow module when the model is run only at the AWS between 06/08/2012 and 06/12/2012. The results shown are surface temperature derived from LW_{out} measurements and calculated by the snow model (a), direct and diffuse shortwave radiation (b and 66	

	c), energy balance without and with the snow module (d and e) and simulated snow heights at the AWS (f).	
4.1	Methodology used to assess the links between measured meteorological variables and surface mass balance.	70
4.2	Boxplots of monthly precipitation amounts (a), mean cloud radiative forcing (b) and cloud index (c) when considering only days with precipitation.	72
4.3	Glacier-wide annual surface mass balance as a function of annual precipitation amounts (a), #events ≥ 1 mm/h (b) and mean annual intensity (c) along with their corresponding determination coefficients (R^2).	77
4.4	Correlation between monthly precipitation amounts and measured surface mass balance in the 5000-5200 m a.s.l. elevation range considering 19 years of data (1991/92 - 2009/10).	79
4.5	Linear regression between the annual surface mass balance in the ablation zone (B_{Abla}) and annual number of events ≥ 3 mm d^{-1} (a), precipitation amounts (b) and mean precipitation intensity (c).	80
4.6	Geographical extents over which the two regional methods are applied.	82
4.7	Wet season onset and demise dates considering the 19 year measured cycle (1992-2010) at PLATAFORMA with the pentad (a), number of rainy days (b). The dashed lines represent the onset and demise dates of the mean cycles. Source: Ramallo (2013).	83
4.8	Daily Cloud cover index (CI) for the year 2016/17 (in black) along with the 14 days centered moving average (red line). The dashed orange line shows the threshold value and the gray rectangle shows the wet season defined according to the CI method. The light gray rectangles on each side show the 7 days error bars linked to the method.	83
4.9	Wet season onset (a.) and duration (b.) for the two regional methods assessed. On plot a, the axis ranges between August 8 and December 6. The onset date and duration obtained with the local methods are shown on plots (c) and (d), respectively.	85
4.10	Illustration of the wet season's demise for three contrasting years. In red at the April-May precipitation events. The gray boxes show the monsoon onset and duration for each year defined using the cloud cover index method.	89
1 _{JGR} *	Location of Zongo Glacier and its monitoring network. SAMA is the on-glacier AWS, ORE is the AWS on the moraine and PLATAFORMA is the one at the pass. TUBO is a discharge gauging station. The bottom left inset map shows the location of the glacier in South America. The thick black line is the glacier outline in 1999. Thin black lines are elevation contours every 100 m from the 1999 digital elevation model (the first elevation contour being 5,000 m a.s.l.). The image in the background was acquired by the Pléiades satellite in 2013, © CNES - Airbus D&S.	93

2 _{JGR}	Box plot showing the monthly surface mass balances of the ablation zone of Zongo Glacier calculated from 20 ablation stakes (between 5,000 and 5,200 m a.s.l.) for the 27 mass balance years 1990/1991 - 2016/17.	94
3 _{JGR}	Annual cycle of (a) incoming shortwave radiation (SWin) and top of the atmosphere shortwave radiation (Stop) and (b) incoming longwave radiation (LWin) at the on-glacier weather station (SAMA) and theoretical clear-sky incoming longwave radiation (Lclear). Lclear was derived by dividing LWin by the cloud longwave emission factor (F). Daily mean station data are averaged over the nine simulated years between 1999 and 2017. (c) Boxplot showing the interannual variability of the monthly mean near-surface air temperature at the PLATAFORMA weather station (Fig. 1).	95
4 _{JGR}	Probability distribution functions of cloud radiative forcing for the transition period (a.), the core wet season (b.) and the dry season (c.) based on 13 years of data (between 1999 and 2017) at both the on-glacier and PLATAFORMA weather stations.	96
5 _{JGR}	(a) Zongo glacier front positions between the first (1999) and the last modeled year (2016). (b) Simulated glacier-wide annual surface mass balance (B_{sim}) versus balances derived from stake observations and geodetic balances (B_{meas} , Vincent et al., 2018), including the 1:1 line. Simulations using annually adjusted DEMs are compared to those keeping the 1997 DEM and outline constant.	97
6 _{JGR}	Validation of the model results exemplified for the hydrological year 2008/09. Modeled and measured (a) daily mean albedo (α), (b) daily discharge (Q) and (c) annual specific surface mass balance (B) profiles.	99
7 _{JGR}	Monthly mean energy fluxes (a) averaged over the nine simulated years, (b) for a year with a highly negative surface mass balance (2016/17, -1.62 m w.e.) and (c) for a year with limited net mass loss (1999/00, -0.21 m w.e.). The cumulative energy fluxes shown are the simulated fluxes at the automatic weather station (SAMA). Note, a positive sum implies that energy is available for melt, whereas a negative one implies surface cooling via the ground heat flux.	103
8 _{JGR}	(a) Modeled monthly mean glacier-wide albedo (α), and (b) monthly mean cloud index (CI) for both a year with limited net mass loss (1999/00; B = -0.21 m w.e.) and a year with high net mass loss (2016/17; B = -1.62 m w.e.).	103
9 _{JGR}	Impact of the three precipitation scenarios S1-S3 on glacier-wide (a) daily fresh snow cover area, (b) albedo, (c) net shortwave radiation and (d) melt compared to the reference run for the period September to November 2008. Results are shown as daily anomalies (a, b) and cumulative anomalies from the reference model run (c, d).	105
10 _{JGR}	Simulated glacier-wide (a) surface mass balance and (b) net shortwave radiation over the transition period of all nine simulated years for both the reference model run and the precipitation scenario S1.	106

11 _{JGR}	Comparison of precipitation scenario S1 model run with reference run for the transition period (September to November). (a, c) Daily and cumulative precipitation at the weather station used for model forcing. (b, d) Modeled daily glacier area with fresh snow and cumulative melt. Results are shown for a year where S1 has a limited impact (2012/13, plots a, b) and a year where it has a strong impact (2005/06, plots c, d).	107
12 _{JGR}	Transition period surface mass balance anomalies of the cloud scenarios (scenario - reference run) for three contrasting years along with their incoming radiation fluxes.	108
1 _{CRAS} **	Zongo Glacier (16°15'S, 68°10'W) showing its monitoring network. The red line represents the maximum extent of the LIA and the corresponding digital elevation model, the black line shows the extent of the glacier in 2012. The map in the top inset is a 3D view of the extent of the glacier at its LIA maximum extent. SAMA (5050 m a.s.l.), ORE (5050 m a.s.l.) and PLATAFORMA (4750 m a.s.l.) are the three automatic weather stations (AWS) installed on and around the glacier, TUBO is a discharge gauging station located at 4,830 m a.s.l. The red star shows the position at which the measurements are used to force the model in LIA simulations. Source of the background image: Pleiades satellite in 2013, © CNES - Airbus D&S. Digital Elevation Model: Rabatel (2005).	119
2 _{CRAS}	a) Proportion of annual precipitation for each month at the on-glacier AWS SAMA (2011/12) and off-glacier AWS PLATAFORMA (average of 23 years between 1991 and 2017). b) Simulated cumulative surface mass balance for the 9-year average (1999-2017) and 2011/2012 (reference scenario) over the current glacier geometry.	127
3 _{CRAS}	Daily precipitation in the four LIA climate scenarios analyzed in this study. The modifications applied to the reference scenario (2011/2012) are in red.	128
4 _{CRAS}	Annual scale differences between the scenarios and the 9-year average ($X_{Sce} - X_{RT}$) of (a) incoming shortwave and (b) longwave radiation, (c) cloud radiative forcing, (d) precipitation, (e) air temperature and (f) outgoing longwave radiation used to derive the glacier surface temperature.	128
5 _{CRAS}	Annual surface mass balance maps for the four LIA scenarios. The dashed lines represent the simulated ELA.	132
6 _{CRAS}	Surface mass balance as a function of altitude (a) and corresponding changes in mass (b) in the four scenarios. The shaded area highlights the altitudinal range for the simulated equilibrium-line altitudes (4,908-5,000 m a.s.l.).	132
7 _{CRAS}	Cumulative glacier-wide surface mass balance (a), net shortwave (b) and longwave (c) energy budgets along with the sensible (d) and latent (e) heat fluxes in the four LIA scenarios. The gray areas represent the transition (T.S.) and wet (W.S.) seasons.	135
5.1	Impact of the altitude up to which the precipitation gradient is applied on the annual precipitation amounts.	140

5.2	Snow heights and cumulative surface mass balance at 4400 and 5450 m a.s.l. (plots a and b, respectively), and the cumulative glacier-wide surface mass balance (c). Below 4850 m a.s.l. (plot a), dP_{5200} and dP_{5400} yield the same results as the same reduction in precipitation amounts is applied.	141
5.3	Map showing the difference in annual surface mass balance obtained with dP_{5200} and dP_0 ($dP_{5200} - dP_0$). The color scale is centered around 0 (white) thus, parts in red show higher mass losses obtained with dP_{5200} than with dP_0 .	142
5.4	Annual melt (a-d) and surface mass balance maps (e-h) along with the total melt (i) and cumulative glacier-wide surface mass balance (j) for the four configurations tested.	144
5.5	Impact of different surface temperature gradients on simulated latent (top row) and sensible (bottom row) heat fluxes	145
S1.1	Daily seasonal cycles of incoming radiation fluxes, air temperature, specific humidity (derived from relative humidity and temperature) and precipitation at SAMA (black lines), ORE (red lines) and PLATAFORMA (orange lines) over the year 2012/13. SON is the transition season, JFM the core wet season and JJA the dry season.	184
S1.2	Boxplots of seasonal daily precipitation cycles at SAMA, considering 8 years of measurements for the transition (a), wet (b) and dry (c) seasons.	185
S2.1	14 year average daily values of cloud lowwave emission and bulk transmissivity factors along with the cloud index ($CI \pm \sigma$, plot a) and long term average daily cloud radiative forcing ($CF \pm \sigma$, plot b).	187
S2.2	Probability density functions of T_n and F (a & b), linking F and T_n for the dry and wet seasons (c) and the transition season (d) along with the cloud index (e) and cloud radiative forcing (f) pdfs. The black lines are for the wet season (DJF), the red ones for the dry one (JJA) and the yellow ones for the transition period (SON). 14 years of cloud radiative properties between 1999/00 and 2016/17 were used for the plots.	188
S1 _{JGR}	Operating periods of the three automatic weather stations on and around Zongo glacier (Fig. 1) for each of nine simulated mass-balance years. The white boxes represent months with data gaps > 10 days. Note that numerous shorter periods ranging from a few hours to a few days with missing data also occurred (not shown).	191
S2 _{JGR}	Surface mass balance as a function of altitude. The black crosses are the reference measurements. The gray lines represent the mean simulated B (20 m elevation bands). This figure highlights one of the main drawbacks of considering a single calibration for all the years: it is globally robust but, the melt in the ablation zone for some years was underestimated (e.g. 2005/06) while for others, it was overestimated (e.g. 2004/05).	192

S3_{JGR} Impact of scenarios S1-S3 on the glacier-wide surface mass balance over the transition period of mass-balance years 1999/00 (a), 2004/05 (b) and 2008/09 (c). The dashed line shows the surface mass balance in the reference season. 192

S4_{JGR} Impact of the cloud scenario on the surface mass balance during the transition period for the nine years considered.

193

* JGR refers to the figures found in the article published in the Journal of Geophysical Research: Atmospheres (Section 4.5).

**CRAS to the figures found in the article submitted to *Compte Rendus de l'Académie des Sciences: Géoscience* (Section 5.1).

List of tables

2.1	SAMA AWS equipment (on the glacier at 5050 m a.s.l., 1991 - Now)	25
2.2	ORE AWS equipment (on the moraine at 5050 m a.s.l., 25 th August 2003 - 12 th March 2015)	25
2.3	MEVIS AWS equipment (at the pass, 4750 m a.s.l., 1991 up to the 31 st of January 2012)	26
2.4	PLATAFORMA AWS equipment (at the pass, 4750 m a.s.l., 7 th October 2011 - Now)	26
2.5	Detailed summary of the data gaps which were filled considering measurements carried out on the moraine (ORE). Note 2004/05 is in bold and italic as for this year we identified a problem with the measured incoming longwave measurements. We corrected them following the methodology described in the next section.	30
2.6	Example of the site visit information used to validate modeling over the year 2000/01.	35
3.1	Simulation period and firn-line altitude for each modeled year.	55
3.2	Summary of the retained parameter values.	56
4.1	Determination coefficient (R^2) values obtained between the monthly mean cloud radiative properties and the monthly mass balance in the ablation zone, $B_{ab/a}$, and annual glacier-wide surface mass balance B_{GW} . The values in bold are those which are trustworthy as they pass the Student test with an error risk lower than 5% (i.e. $R^2 \geq 0.29$).	74
4.2	Determination coefficient (R^2) values obtained between the monthly mean cloud radiative properties and the seasonal to annual mass balance in the ablation zone, $B_{ab/a}$, and annual glacier-wide surface mass balance B_{GW} . The values in bold are those which are trustworthy as they pass the Student test with an error risk lower than 5 % (i.e. $R^2 \geq 0.29$).	74
4.3	Summary of the determination coefficients (R^2) obtained between the annual glacier-wide surface mass balance and seasonal precipitation characteristics.	76
4.4	Summary of the determination coefficients obtained for three precipitation characteristics over the wet seasons whose onset and demise dates are	88

	defined according to different methods (both local and regional). For the regional methods, only the results obtained with method 1 are presented as it is with this method that the highest R^2 values were found.	
4.5	Summary of the determination coefficients obtained for seasonal precipitation amounts, number of events $\geq 3 \text{ mm d}^{-1}$ and mean seasonal intensity (\bar{I}) over the transition seasons whose demise date is defined as the day before wet season onset derived from different methods (local methods only).	88
1 _{JGR} *	List of the equipment at SAMA along with the sensor heights and precision according to the manufacturer	96
2 _{JGR}	Summary of the 66 th percentile value of the cloud radiative forcing per month and the corresponding cloud longwave emission factor (F^{cloud}) and bulk cloud shortwave transmissivity ($T\tau^{\text{cloud}}$) values retained for the scenario.	101
3 _{JGR}	Simulated annual glacier-wide surface mass balance, melt and precipitation in the nine simulated years, along with the differences from their respective mean values. The three years in italics are years in which the mass loss is considerably less than the average ($B > B_{\text{mean}} + \sigma/2$). The three years in bold are years with considerable mass loss ($B < B_{\text{mean}} - \sigma/2$).	102
4 _{JGR}	Summary of the precipitation amounts and number of events above 2 mm/d along with simulated surface mass balance (B) and melt for both the reference model runs (using measurements used as model inputs) and the model run forced by the S1 scenario) over the transition period (September to November). The three years in italics are years in which the annual mass loss is significantly less than the average ($B > B_{\text{mean}} + \sigma/2$). The three years in bold are those in which the annual mass loss is significant ($B < B_{\text{mean}} - \sigma/2$).	105
1 _{CRAS} **	Summary of the main parameter values used for the DEBAM simulations.	124
2 _{CRAS}	Summary of simulated glacier-wide surface mass balance B , specific ablation a , accumulation c , and mass turnover τ for the four LIA scenarios along with the differences in a and c between the reference scenario and scenarios 1-3.	133
5.1	Annual glacier-wide sensible and latent heat fluxes for the four model initializations considered and their differences to dTs_0 .	145
S1	Impact of precipitation scenario S1 on the surface mass balance of September, October, November, the three-month period and the annual scale. The years in bold are those in which S1 increases the drop in	194

surface mass-balance. The bold and italic font on the bottom right shows the mean impact on the melt at both the seasonal and annual scale.

* JGR refers to the tables found in the article published in the Journal of Geophysical Research: Atmospheres (Section 4.5).

**CRAS to the tables found in the article submitted to *Compte Rendus de l'Académie des Sciences: Géoscience* (Section 5.1).

Glossary and acronyms

AWS	Automatic weather station - 3 on and around the glacier: SAMA, ORE, MEVIS/PLATAFORMA
B_{Abla}	Ablation zone surface mass balance, depending on the context it can be at the monthly, seasonal or annual scale (m w.e.)
B_{GW}	Annual glacier-wide surface mass balance (m w.e.)
B_{Meas}	Measured surface mass balance (m w.e.), for this study it is considered to be the dataset from Vincent et al. (2018)
CF	Cloud radiative forcing ($W m^{-2}$) - cloud impact on the incoming radiation (Sicart et al., 2016)
CI	Cloud cover index - allows to identify the type of cloud (warm/thick and cold/thin clouds for example, Sicart et al., 2016)
DEM	Digital elevation model
Dry Season	Period of limited melt over the glacier (June-August)
ELA	Equilibrium Line Altitude, altitude for which the surface mass balance = 0 m w.e.
ELA₀	Steady state ELA which corresponds to the ELA for a glacier at equilibrium with the climate
ENSO	El Niño Southern Oscillation - According to the IPCC 5 th Assessment Report glossary WG1, the term El Niño was initially used to describe a warm-water current that periodically flows along the coast of Ecuador and Peru, disrupting the local fishery. It has since become identified with a basin-wide warming of the

tropical Pacific Ocean east of the dateline. This oceanic event is associated with a fluctuation of a global-scale tropical and subtropical surface pressure pattern called the Southern Oscillation. This coupled atmosphere–ocean phenomenon, with preferred time scales of two to about seven years, is known as the El Niño–Southern Oscillation (ENSO). It is often measured by the surface pressure anomaly difference between Tahiti and Darwin or the sea surface temperatures in the central and eastern equatorial Pacific. During an ENSO event, the prevailing trade winds weaken, reducing upwelling and altering ocean currents such that the sea surface temperatures warm, further weakening the trade winds. This event has a great impact on the wind, sea surface temperature and precipitation patterns in the tropical Pacific. It has climatic effects throughout the Pacific region and in many other parts of the world, through global teleconnections. The cold phase of ENSO is called La Niña

- F** Cloud longwave emission factor - incoming longwave radiation amplification factor linked to the presence of clouds (Sicart et al., 2016)
- H** Sensible heat flux (W m^{-2})
- ITCZ** Intertropical Convergence Zone, it is an equatorial zonal belt of low pressure, strong convection and heavy precipitation near the equator where the northeast trade winds meet the southeast trade winds. This band moves seasonally. (IPCC 5th Assessment Report, WG 1 Glossary)
- LE** Latent heat flux (W m^{-2})
- LIA** Little Ice Age - a multi secular period (1350-1850 AD) during which glaciers across the world advanced (Solomina et al., 2015; 2016)
- LW_{in}** Incoming longwave radiation (W m^{-2})

LW_{out}	Outgoing longwave radiation ($W\ m^{-2}$)
m w.e.	Meters in water equivalent
Q_M	Melt energy ($W\ m^{-2}$)
SALLJ	South American Low Level Jet - transports moisture from the Amazon Basin to the subtropics (Marengo et al., 2012)
SAMS	South American Monsoon System - its mature phase corresponds to the core wet season over Zongo (January to March)
SEB	Surface energy balance
SLA	Snow Line Altitude
SW_{in}	Incoming shortwave radiation ($W\ m^{-2}$)
SW_{out}	Outgoing shortwave radiation ($W\ m^{-2}$)
T_n	Bulk cloud shortwave transmissivity factor - incoming shortwave radiation reduction factor due to the presence of clouds (Sicart et al., 2016)
Transition season	Period of increasing melt rates over Zongo Glacier (September-November)
Wet season	Main accumulation period over Zongo Glacier (January-March)

Supporting Information

S1. Seasonal patterns of meteorological measurements

To get a better insight at the measurements carried out at the three AWS, we compared seasonal diurnal radiation, temperature, specific humidity and precipitation radiation. The results are illustrated over the year 2012/13 (Fig. S1.1) year with enough data to compare all three AWS.

Seasonal incoming shortwave radiation diurnal patterns (SW_{in} , Fig. S1.1a-c) are almost identical for all three AWS, with a higher daily maximum measured at the ORE for the transition and dry seasons and a higher one at PLATAFORMA during the dry season. These differences are linked to the sky view factor (V_f) at each AWS ($V_f = 0.95, 0.91$ and 0.85 for PLATAFORMA, ORE and SAMA, respectively).

Likewise, the measured incoming longwave radiation (LW_{in} , Fig. S1.1d-f) at all three AWS displays similar seasonal diurnal patterns, with almost identical ones between glacier and moraine measurements (SAMA and ORE, respectively). The higher values observed at PLATAFORMA are partly linked to a combination of higher air temperature and specific humidity as the PLATAFORMA is 300 m lower in elevation than the other two (Fig. S1.1g-i). Another part of the discrepancies observed between the LW_{in} measurements at the different AWS is linked to their respective surroundings and sky view factors. Indeed, measured incoming longwave radiation can be separated between atmospheric emissivity and emission from the surrounding terrain (Eq. S1, e.g., Marks & Dozier, 1979 ; Male & Granger, 1981). Thus, higher measured LW_{in} values at PLATAFORMA are also partly due to the increased emissivity of the surrounding terrain as it is the AWS as it is surrounded by the warmest terrain (lower elevation).

Similarly, compared to the ORE, during the wet season, the lower measured incoming longwave radiation during the night at SAMA during the wet season (compared to ORE measurements are explained by the lower sky view factor and colder surrounding terrain at SAMA (snow/ice) than at the ORE (snow/rocks).

$$LW_{in} = V_f L_0 + (1 - V_f) \epsilon_T \sigma T_T^4 \quad (S1)$$

LW_{in} is the measured incoming longwave radiation, L_0 the clear sky atmospheric emissivity, V_f the sky view factor, σ the Stefan Boltzmann constant ($5.67 \cdot 10^{-8} \text{ W m}^{-2} \text{ K}^{-4}$), ε_T and T_T the adjacent terrain's emissivity and temperature respectively. According to Sicart (2002), $\varepsilon_T=1$ and T_T can be calculated using the empirical relationship presented in Greuell et al. (1997): $T_T = T_{air} + cSW_{in}$ with $c = 0.01 \text{ K W}^{-1} \text{ m}^2$

Temperature and specific humidity patterns follow similar seasonal daily cycles (Fig. S1.1g-k) with higher maximums observed at PLATAFORMA, followed by the ORE and SAMA due to the elevation difference between the stations ($\partial T/\partial z \approx -0.55 \text{ K}/100\text{m}$). On-glacier values are slightly lower than those on the moraine because of its influence on near-surface temperature.

Precipitation patterns (Fig S1.1m-o) show large discrepancies in mean seasonal intensities. These are due to both precipitation elevation gradient in mountainous areas ($+10\%/100 \text{ m}$ in our case, Beeman, 2015) and because the measurements shown come from the tipping bucket rain gauge at PLATAFORMA and ORE whereas it comes from conversion of snow height measurements using the ultrasonic sensor at SAMA. The large differences in precipitation amounts at SAMA and ORE are because the precipitation is measured using the Geonor rain gauge at the ORE (Table 2.2) and, according to Sicart et al. (2002) the undercatch at this AWS is large as solid precipitation is observed most of the time. Thus, if the fresh snow density is known, precipitation measurements using the ultrasonic gauge are the most reliable ones (Chapter 2.2).

Figure S1.2 shows the seasonal daily cycles box plots obtained considering 8 years of ultrasonic measurements at SAMA (between 1999 and 2013). During the transition and wet seasons (Fig. S1.2a, b), the precipitation cycles show little dispersion with a strong precipitation peak between 12h and 15h probably linked to orographic effects (convective precipitation events) and a smaller one at night (linked to regional atmospheric circulation), a feature identified by Sicart et al. (2002) over the glacier and lower in the Zongo Valley (at 3900 m a.s.l.) considering two years of data (1998-2000). This pattern has also been identified over Southern Peru by Perry et al. (2017) who analyzed 6 years of precipitation measurements near The Cuzco international airport between 2004-2010. During the dry season (Fig. S1.2c)

the precipitation maximum occurs in the afternoon; however, measurements have a large spread (large interquartile values).

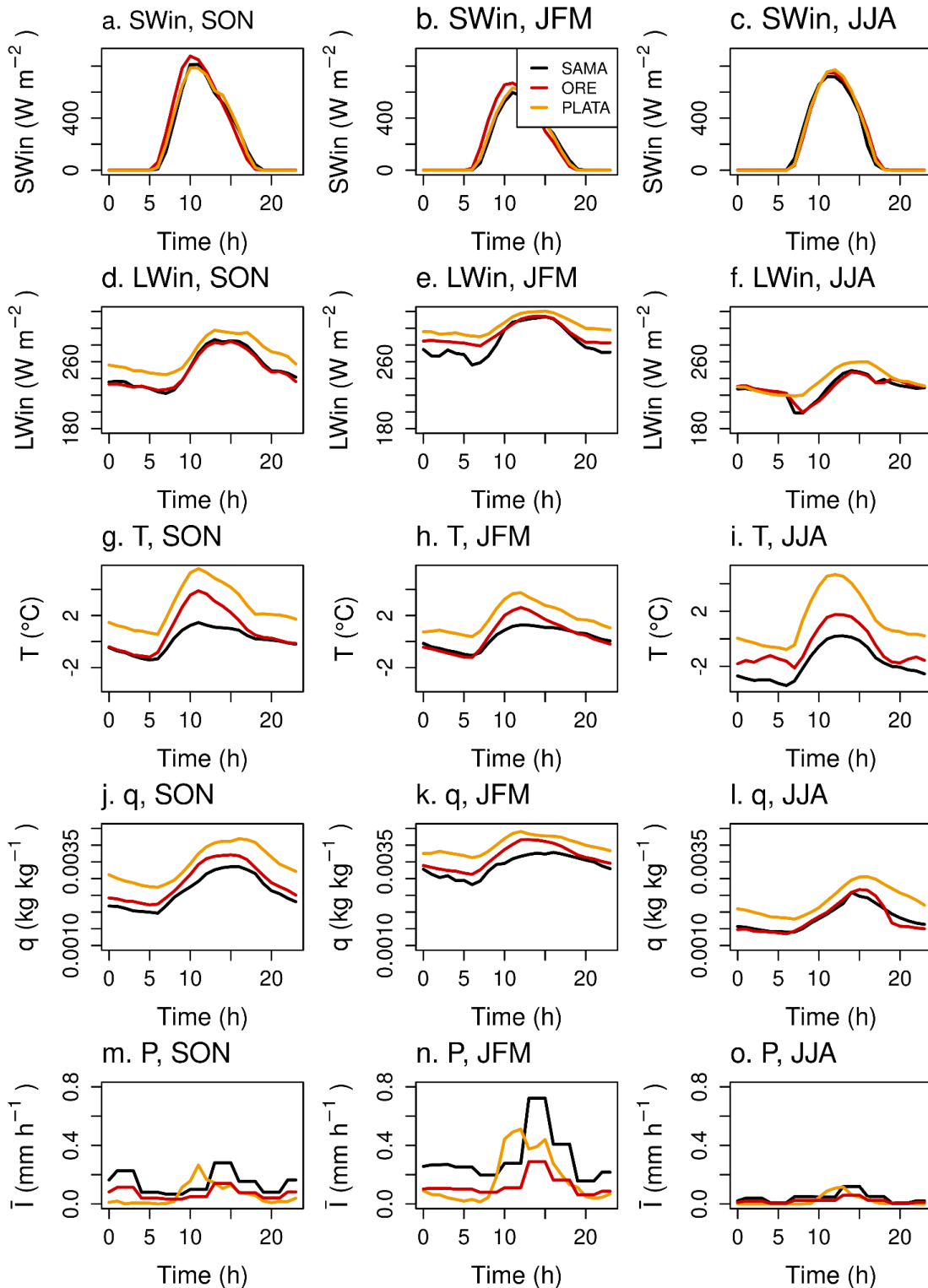


Figure S1.1. Daily seasonal cycles of incoming radiation fluxes, air temperature, specific humidity (derived from relative humidity and temperature) and precipitation at SAMA (black

lines), ORE (red lines) and PLATAFORMA (orange lines) over the year 2012/13. SON is the transition season, JFM the core wet season and JJA the dry season.

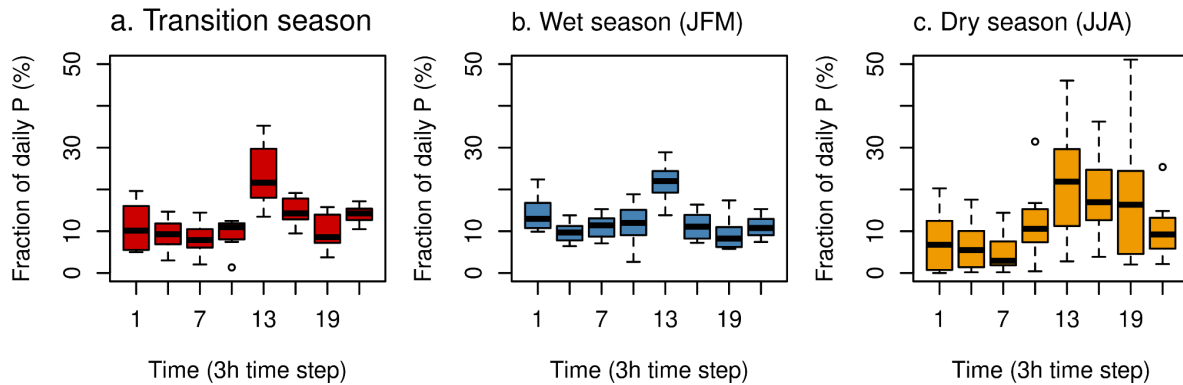


Figure S1.2. Boxplots of seasonal daily precipitation cycles at SAMA, considering 8 years of measurements for the transition (a), wet (b) and dry (c) seasons.

S2. Seasonal cloud radiative properties

The 14 year averaged annual cycle of cloud radiative properties shows that the cloud longwave emission factor F is maximal during the wet season (Fig. S2.1a) and minimal during the dry season whilst the opposite is observed for the cloud bulk shortwave transmissivity factor T_n . This highlights the different cloud types between the wet and dry seasons (warm-thick and cold-thin clouds, respectively). The cloud cover index ($CI = F - T_n$) is maximal during the wet season and minimal during the dry one (black line). Conversely, the mean cloud radiative forcing CF (Fig. S2.1b) is most negative during the wet season (thick clouds with small T_n values) and close to zero during the dry season (predominant clear sky conditions).

We analyzed cloud radiative properties of cloudy days (*i.e.* $F > 1.15$) to build up on the analysis carried out by Sicart et al. (2016) as a longer dataset is now available. To compare the same seasons as in Sicart et al. (2016), the wet season here is considered to be between December and February (comparison with a wet season ranging between January and March showed very similar results).

Figure S2.2a and b shows the probability density functions (pdf) of T_n and F for the three seasons considered. During the wet season, cloudy days are distributed around a high T_n and low F values (0.6 and 1.22, respectively) whilst for the wet season, the opposite is observed with a peak in T_n around 0.45 (and 1.55 for F). This shows that there are two distinct types of clouds between the two seasons:

clouds with a high solar energy blocking potential (low T_n) and high longwave emissivity factor during the wet season (warm and thick cumulus-type clouds) as opposed to high altitude cold and thin clouds during the dry season. The transition season is a mixture of both seasons with a similar peak in T_n as the one observed during the wet season but with a broader distribution, F shows a similar pdf with a peak centered around 1.3.

A link between seasonal values of F and T_n exists for all seasons with higher correlations observed between June and November ($R_{JJA}^2 = R_{SON}^2 = 0.3$ & $R_{DJF}^2 = 0.18$, Fig. S2.2c, d). In Sicart et al. (2016), the correlations obtained for JJA and JFM were significantly higher than what we found ($R_{JJA}^2 = 0.59$ & $R_{DJF}^2 = 0.34$) due to the different sample sizes: 14 years *versus* 9 years. Our results corroborate those of Sicart et al. (2016): during the wet season, clouds which attenuate the incoming solar radiation increase the sky longwave emissivity much more than during the dry season (Fig. S2.2c).

During the transition season, F and T_n density functions confirm the presence of a wider variety of clouds (steeper regression line gradient, Fig. S2.2d). This is even more visible when considering the cloud index density functions (Fig. S2.2e): a bimodal distribution is observed during the transition season (with two peaks centered around $CI = 0.5$ and 1). Conversely, for the wet (dry) season, a unimodal distribution centered around $CI = 1.2$ (0.5) is observed. As a result, the cloud radiative forcing is most negative during the wet season, intermediate during the transition season and limited between June and August (Fig S2.2f). These results show that probability density functions of cloud radiative properties can be used to identify seasons.

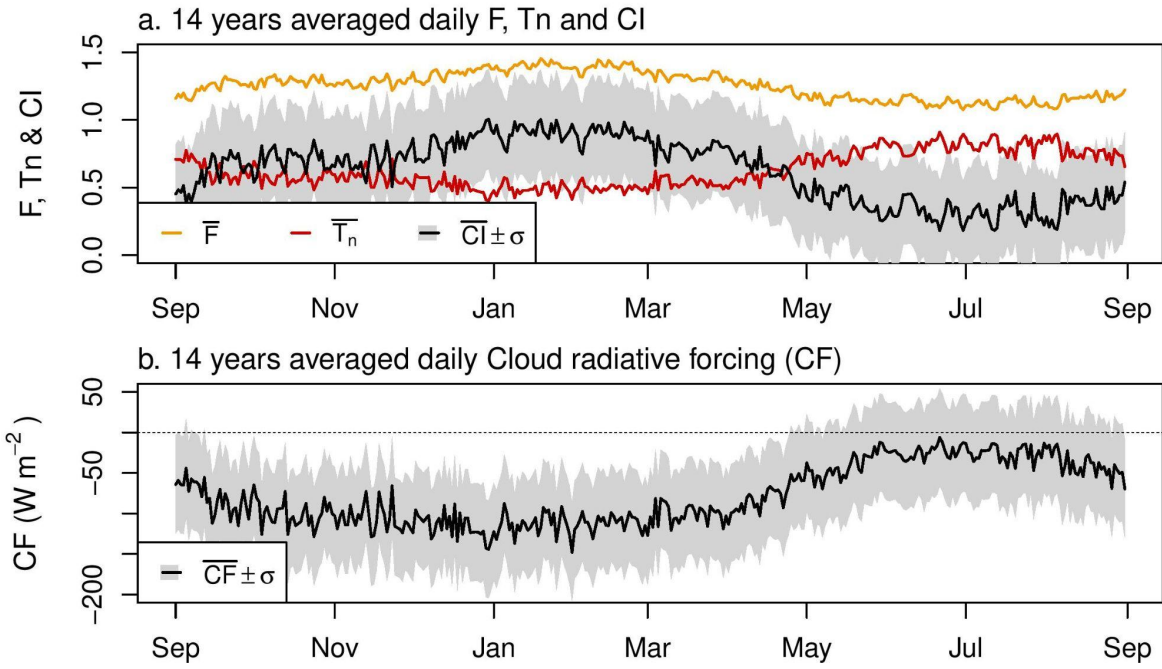


Figure S2.1. 14 year average daily values of cloud lowwave emission and bulk transmissivity factors along with the cloud index ($CI \pm \sigma$, plot a) and long term average daily cloud radiative forcing ($CF \pm \sigma$, plot b).

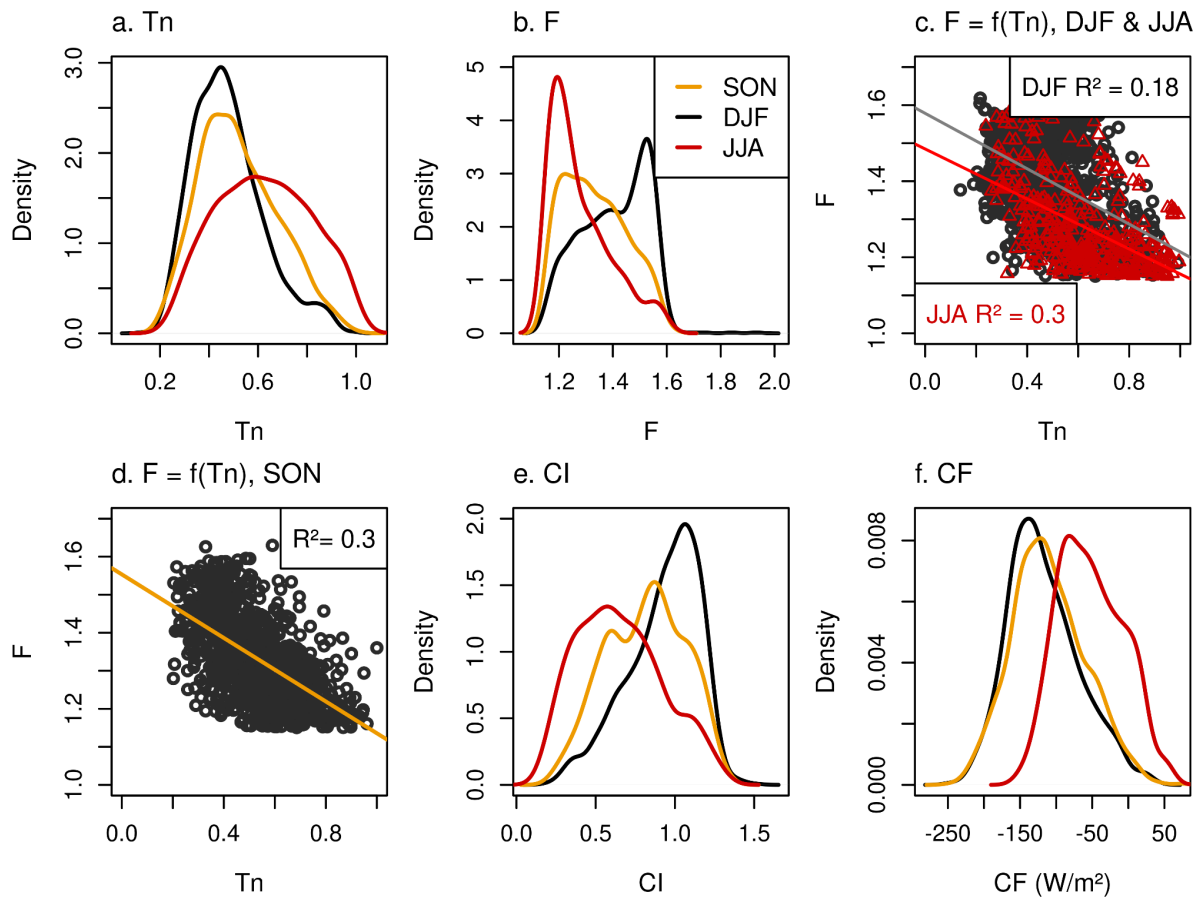


Figure S2.2. Probability density functions of T_n and F (a & b), linking F and T_n for the dry and wet seasons (c) and the transition season (d) along with the cloud index (e) and cloud radiative forcing (f) pdfs. The black lines are for the wet season (DJF), the red ones for the dry one (JJA) and the yellow ones for the transition period (SON). 14 years of cloud radiative properties between 1999/00 and 2016/17 were used for the plots.

Supporting information for the Chapter 4.5



Journal of Geophysical Research Atmospheres

Supporting Information for

Climate controls on the interseasonal and interannual variability of the surface mass and energy balances of a tropical glacier (Zongo Glacier, Bolivia, 16°S): new insights from the multi-year application of a distributed energy balance model

P. Autin^{1†}, J. E. Sicart¹, A. Rabatel¹, A. Soruco² and R. Hock^{3,4}

¹Univ. Grenoble Alpes, CNRS, IRD, Grenoble-INP, Institut des Géosciences de l'Environnement (IGE, UMR 5001),
F-38000 Grenoble, France

²Facultad de Ciencias Geológicas, Universidad Mayor de San Andrés, La Paz, Bolivia

³Department of Geoscience, Oslo University, Oslo, Norway

⁴Geophysical Institute, University of Alaska, Fairbanks, AK, United States of America

Corresponding author: Philémon Autin (philemon.autin@univ-grenoble-alpes.fr)

†Institut des Géosciences de l'Environnement, Bâtiment Glaciologie, 54, rue Molière, 38400 Saint Martin d'Hères – France

Contents of this file

Text S1

Figures S1 to S4

Table S1

Introduction

This supporting Information provides an overview of the operating periods of the automatic weather stations used in this study along with a detailed gap-filling methodology. It also provides simulation results for all years considered in this study along with those of the sensitivity studies.

Text S1. Automatic Weather Station data timelines and gap-filling methodology

Figure S1 shows the operating timelines of the three automatic weather stations on and around Zongo glacier. For the sake of simplicity, only the major data gaps (i.e., 10 days or more) are shown on the timeline. There were several overlapping operating periods (Fig. S1), which made it possible to compare measurements at different stations. Thus, in order to identify the variables measured at the ORE and at the PLATAFORMA that could be used to fill in data gaps at SAMA, correlations between the variables in the same operating periods were studied and the main results are presented below. It is worth noting that, apart from the hydrological year 2016/17, only the data measured at the ORE were required to fill in gaps in measurement made at SAMA.

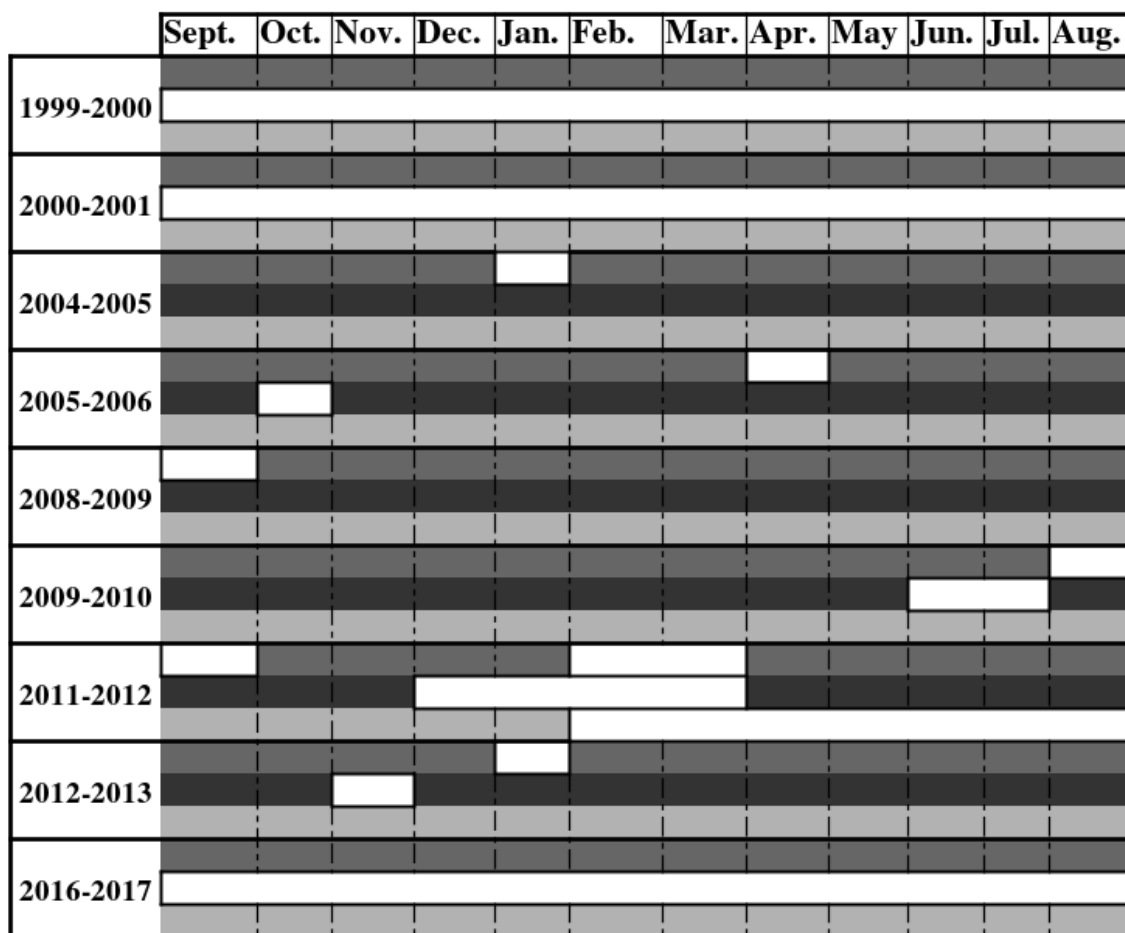
It was possible to replace relative humidity data as the correlation between the measurements at the two AWS is very high ($R^2=0.93$). Similarly, nighttime temperatures were highly correlated and consequently, was used. However, the daytime temperatures did not fit because of differing glacier surface types (moraine and snow/ice), hence, the missing day-time temperatures were taken from the PLATAFORMA and brought to the AWS altitude by applying a $-0.55\text{K}/100\text{m}$ lapse rate.

Regarding the radiation components, it was possible to use both the incoming short and longwave radiation from the ORE to fill in the gaps ($R^2 > 0.8$). Regarding outgoing longwave radiation, it was found that if the values measured at the ORE above 315.6 W m^{-2} were replaced by 315.6 W m^{-2} , the measurements from the ORE could be used to replace missing values at SAMA. However, it was necessary to limit the values to 315.6 W m^{-2} for the on-glacier measurements as the surface temperature cannot exceed 0°C .

Between May and August 2005, the incoming longwave radiation measurement at SAMA was interrupted, consequently the incoming longwave radiation was reconstructed according to the equation parameterized by Sicart et al. (2010) at the daily time scale and was assumed to remain constant throughout the day.

Regarding precipitation, the amounts measured at the ORE and at SAMA differed significantly. The ORE was equipped with a GEONOR rain gauge located on the moraine and was consequently affected by wind, and thus showed a significant undercatch (40%) less than the amounts measured at SAMA. When gaps at SAMA were identified, first, in order to confirm that precipitation events actually took place, the measured albedo at the AWS was analyzed as precipitation events increased the albedo value. In this case, the precipitation measured at the ORE was increased by 40% and used to fill the gap. Because the ORE no longer existed for the hydrological year 2016/17, the precipitation amounts measured at the PLATAFORMA were increased by 50% and used to fill in the gaps in this year. Note that the 50% increase was obtained by comparing the measured precipitation amounts on the glacier and at the PLATAFORMA over several years.

Due to the high spatial heterogeneity of wind speed in mountainous areas, the measurements made at each automatic weather station were poorly correlated. For data gaps of less than a few hours, a linear extrapolation was used. For bigger data gaps, the gap was filled with the mean values of measurements at SAMA over the same period in other years.

**Legend:**

	SAMA	Operational for all the years
	ORE	Operating period: 25/08/03-12/03/2015
	Plataforma	Operational for all the years
		Represents the month with data gaps > 10 days

Figure S1. Operating periods of the three automatic weather stations on and around Zongo glacier (Fig. 1) for each of nine simulated mass-balance years. The white boxes represent months with data gaps > 10 days. Note that numerous shorter periods ranging from a few hours to a few days with missing data also occurred (not shown).

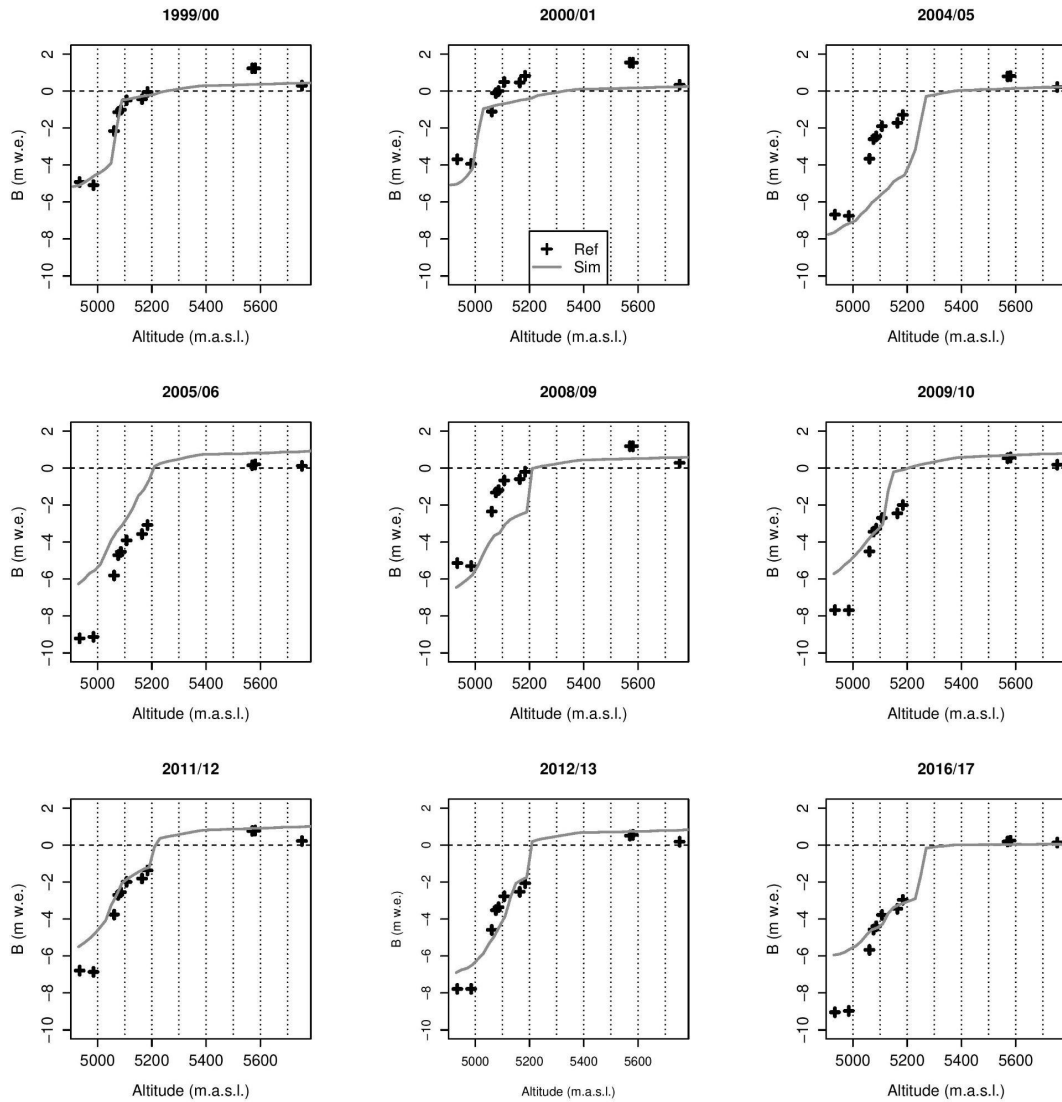


Figure S2. Surface mass balance as a function of altitude. The black crosses are the reference measurements. The gray lines represent the mean simulated B (20 m elevation bands). This figure highlights one of the main drawbacks of considering a single calibration for all the years: it is globally robust but, the melt in the ablation zone for some years was underestimated (e.g. 2005/06) while for others, it was overestimated (e.g. 2004/05).

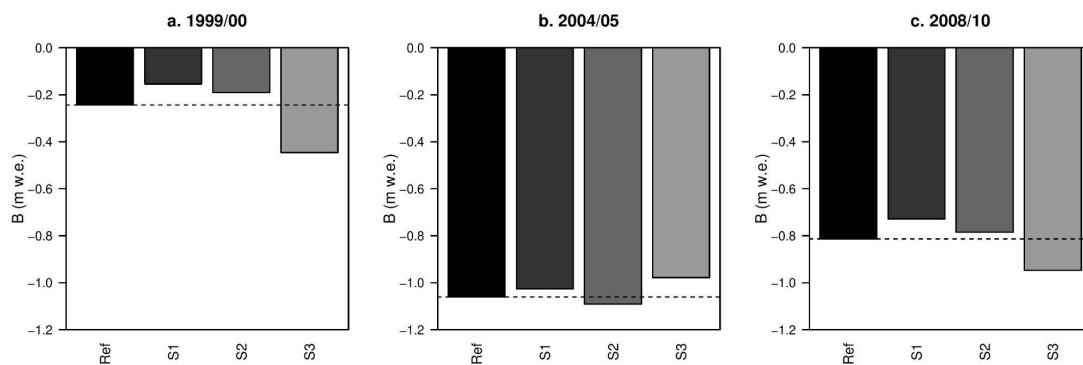


Figure S3. Impact of scenarios S1-S3 on the glacier-wide surface mass balance over the transition

period of mass-balance years 1999/00 (a), 2004/05 (b) and 2008/09 (c). The dashed line shows the surface mass balance in the reference season.

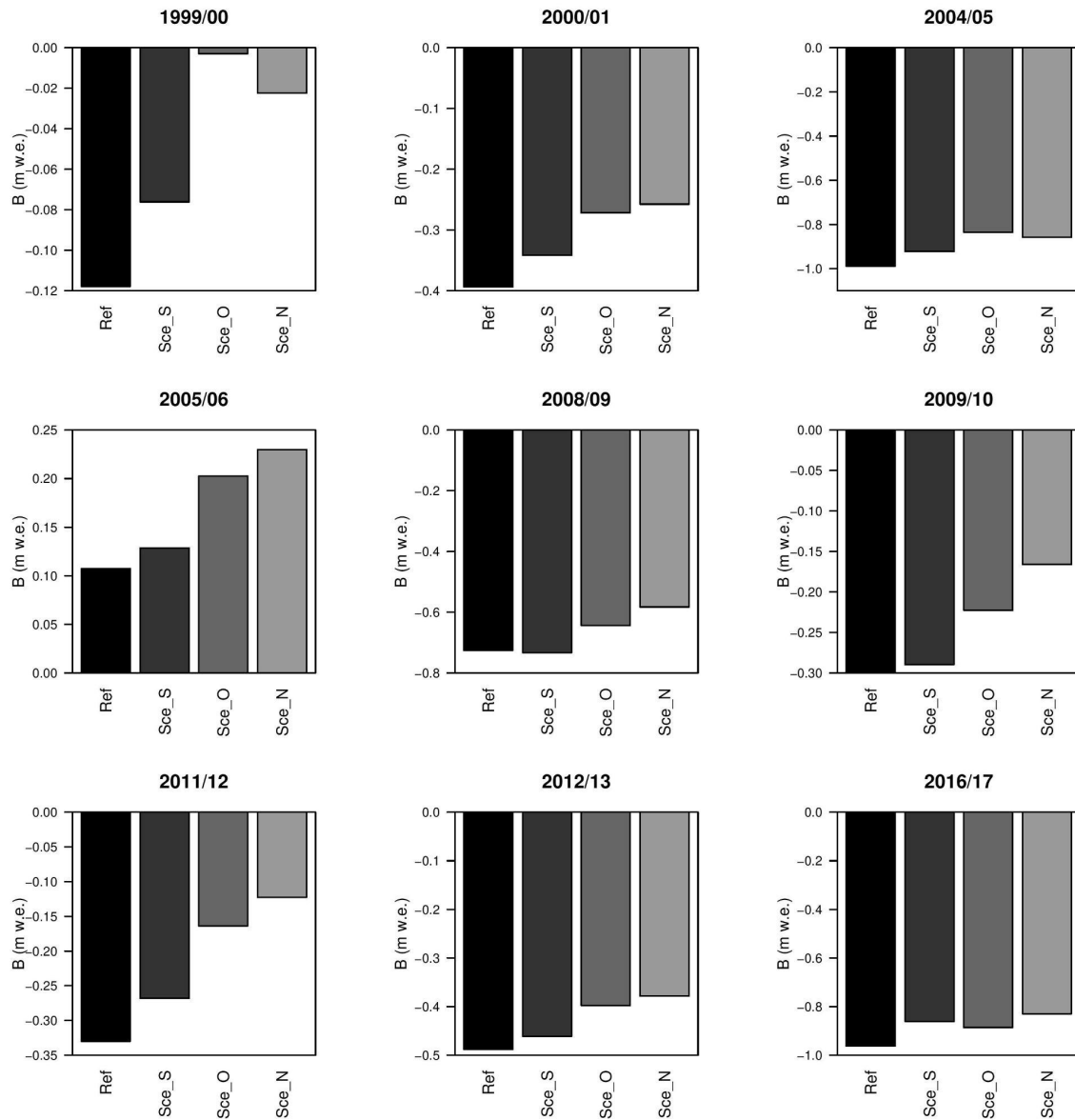


Figure S4. Impact of the cloud scenario on the surface mass balance during the transition period for the nine years considered.

Table S1. Impact of precipitation scenario S1 on the surface mass balance of September, October, November, the three-month period and the annual scale. The years in bold are those in which S1 increases the drop in surface mass-balance. The bold and italic font on the bottom right shows the mean impact on the melt at both the seasonal and annual scale.

Year	Time-scale	B ref (m w.e.)	B S1 (m w.e.)	Year	Time-scale	B ref (m w.e.)	B S1 (m w.e.)
1999/00	September	0.02	0.1	2009/10	September	-0.09	-0.03
	October	-0.02	-0.05		October	-0.19	-0.12
	November	-0.12	-0.1		November	-0.02	-0.07
	SON	-0.12	-0.05		SON	-0.3	-0.23
	Annual	-0.21	-0.16		Annual	-1.85	-1.8
2000/01	September	-0.22	0.02	2011/12	September	-0.03	-0.12
	October	0.06	-0.06		October	-0.13	-0.13
	November	-0.23	-0.12		November	-0.17	-0.14
	SON	-0.39	-0.16		SON	-0.33	-0.39
	Annual	-0.05	0.18		Annual	-0.89	-0.94
2004/05	September	-0.33	-0.29	2012/13	September	-0.2	-0.17
	October	-0.38	-0.35		October	-0.16	-0.16
	November	-0.27	-0.37		November	-0.13	-0.17
	SON	-0.99	-1.01		SON	-0.49	-0.5
	Annual	-2.48	-2.49		Annual	-0.97	-1.01
2005/06	September	0.02	0.06	2016/17	September	-0.33	-0.29
	October	0.08	0.1		October	-0.25	-0.26
	November	0.01	0.06		November	-0.38	-0.34
	SON	0.11	0.22		SON	-0.96	-0.9
	Annual	-0.36	-0.2		Annual	-1.62	-1.55
2008/09	September	-0.19	-0.12	<i>Period</i>	<i>Mean difference (S1-Ref.)</i>		<i>σ</i>
	October	-0.21	-0.25	SON	12%		18%
	November	-0.33	-0.32		Annual	5%	
	SON	-0.73	-0.69				
	Annual	-1.16	-1.14				

Appendix A - Scientific diffusion and training

Publications

Autin, P., Sicart, J. E., Rabatel, A., Soruco, A., & Hock, R. (2022). Climate controls on the interseasonal and interannual variability of the surface mass and energy balances of a tropical glacier (Zongo Glacier, Bolivia, 16°S): New insights from the multi-year application of a distributed energy balance model. *Journal of Geophysical Research: Atmospheres*, 127, <https://doi.org/10.1029/2021JD035410>

Autin, P., Sicart, J. E., Rabatel, A., Hock, R., & Jomelli, V. (2022, under review). Climate reconstruction of the Little Ice Age maximum extent of the tropical Zongo Glacier (16°S) using a distributed energy balance model. *C.R. Geoscience*.

Armijos, E., Crave, A., Espinoza, R., Fraizy, P., Dos Santos, A.L.M.R., Sampaio, F., De Oliveira, E., Santini, W., Martinez, J. M., **Autin, P.**, Pantoja, N., Oliveira, M., & Filizola, N. (2017). Measuring and modeling vertical gradients in suspended sediments in the Solimões/Amazon River. *Hydrological Processes*, 31(3), 654-667. doi: 10.1002/hyp.11059

Chardon, J., Hingray, B., Favre, A. C., **Autin, P.**, Gailhard, J., Zin, I., & Obled, C. (2014). Spatial similarity and transferability of analog dates for precipitation downscaling over France. *Journal of Climate*, 27(13), 5056-5074. doi: 0.1175/JCLI-D-13-00464.1

Presentations

- International Union of Geodesy and Geophysics (IUGG, 2018), Montreal, Canada: *Application of distributed surface energy mass balance model over a tropical glacier: Zongo, Bolivia (16°S)*
- Alpine Geography Meeting (AGM, 2021), online: *Analysis of the Climatic Factors Controlling the Surface Mass Balance of Zongo Glacier, Bolivia using nine years of data by application of a Distributed Energy Model.*
- Société Hydrotechnique de France (SHF, 2021), online: *Analysis of the Climatic Factors Controlling the Surface Mass Balance of Zongo Glacier, Bolivia using nine years of data by application of a Distributed Energy Model.*

Summer schools

- Mountain Research School (Ecrins Massif, OSUG, ITEM) a transdisciplinary school on research in mountain environments (sociology, tourism, glaciology and geosciences, 5 days)
- Autour du 2°C (Autrans, France, IRD) a pluridisciplinary training on the societal changes and trajectories required to maintain global warming below 2°C (5 days)

Appendix B: Data availability

DEBAM: <https://regine.github.io/meltmodel/>

Current Climate

Data used in the paper published in the Journal of Geophysical Research: Atmospheres (includes the 9-year hourly dataset used in the simulations, the precipitation and cloud cover scenarios along with the digital elevation models for the simulated years):

<https://glacioclim.osug.fr/335-Energy-balance-on-a-tropical-glacier-in-Bolivia>

Little Ice Age

Data is available upon request